Dual Thermal System for Power and Fresh water Production

A thesis submitted in fulfilment of the requirements for the degree of

Doctor of Philosophy

Anna Khaghani
B.Eng.

School of Aerospace, Mechanical and Manufacturing Engineering
Science, Engineering and Technology Portfolio
RMIT University
2013

Declaration

I certify that except where due acknowledgement has been made, the work is that of the author alone; the work has not been submitted previously, in whole or in part, to qualify for any other academic award; the content of the thesis is the result of work which has been carried out since the official commencement date of the approved research program; any editorial work, paid or unpaid, carried out by a third party is acknowledged; and, ethics procedures and guidelines have been followed.

Anna Khaghani

March 2014

Acknowledgement

This project could not have completed without the support of RMIT University for the endorsement and financing of the project. I am greatly indebted to the following supervisors and guides who graciously lent me their technical expertise and encouragement throughout the project:

- Prof. Aliakbar Akbarzadeh my first supervisor for his guidance in testing, analysis, thesis writing and journal publications
- Associate Professor John Andrews. my second supervisor for his guidance in analysis, thesis editing, and resources provision
- Dr Abhijit Date as a guide for his comments and recommendations during the presentations on this topic at RMIT

Gratitude is expressed the following people for their contribution to the project:

- Patrick Wilkins and David Goodie RMIT University for the production of the test rig and turbine prototypes and modification
- All RMIT University Bundoora East Workshop staff
- All members of Energy CARE Group

Special thanks to my parents for supporting me all the way from distance every single day.

Abstract

Within most areas of Australia the supply of natural fresh water is being stretched to breaking point in order to meet the increasing demand for agricultural, industrial and domestic uses. The commercially favoured reverse osmosis (RO) technology for fresh water production from saline water requires large amounts of energy in the form of electricity. At the same time, electricity is presently being generated from predominantly non-renewable and polluting fossil fuels. Furthermore, electricity generation is largely centralised, resulting in high transmission losses and overall inefficiencies. Like water, the demand for electricity is also increasing, requiring expansion of electricity generation capacity. Environmental considerations relating to climate change and resource depletion are driving demand for sustainable and lower-emission technologies as well as system efficiency improvement via distributed generation. Geothermal energy will be part of the renewable solution, offering base load power from decentralised generation facilities. The International Energy Agency has shown that geothermal power production has one of the lowest generation cost at US$20-100/MWh compared with conventional and other forms of renewable energy [1] and can meet 10% of Australia's power demand using hydrothermal resources located in fractured or porous rock, generally at depths of 0.1 km to 4.5 km [2]. To date there has been very little commercial exploitation of these low heat sources for electricity generation despite their abundance and no known exploitation for combined desalination and power generation.

As it has been searched, there is no technology which can provide the combined solution for fresh water production and power generation together. Therefore, the primary aim of this project is to develop a dual geothermal system that uses hot saline water from geothermal reservoirs in Australia and can simultaneously produce fresh water and electrical power. The development of low cost and high performance simple reaction water turbine which will be used in Combined Desalination and Power generation (CDP) unit to directly convert the energy of geothermal hot water to electricity is another aim of this research.

In this thesis, two new innovative designs of simple reaction water turbine are presented and the performance characteristics of their prototypes are investigated

experimentally and graphically presented. The theoretical analysis of the simple reaction turbine presented in this thesis highlights the potentials and intrinsic characteristics of simple reaction turbine. The governing equations for ideal situation without losses and practical situation with losses are presented in this thesis. Further, the theoretical model for optimum turbine diameter is presented followed by the theoretical analysis of phase change phenomenon in the nozzle.

This thesis explains the systematic procedure of manufacturing turbine rotors for both the innovative new designs. Thesis further illustrates the experimental test rig and its instrumentation used for testing the prototypes of the new turbine designs. Experimental procedures are explained with illustrative pictures of test rig and its instrumentation.

The performance characteristics like turbine power output, electrical power output, turbine efficiency and overall efficiency verses rotational speed for different supply temperature and isentropic efficiencies is also presented with examples and illustrative discussion for all new turbine designs.

A case study of the potential low head hydro site in Victoria, Australia is presented with detail turbine sizing and water intake system for small creek using natural stone weir. Simple costing of the entire low head micro hydroelectric installation is presented towards the end of this thesis.

In the conclusion of this research, an optimised low cost and high performance simple reaction turbine design has been developed and presented to be used for electricity production from low head hydro sources.

Table of content

List of Figures

List of Tables

Nomenclature

A	area (m^2)
C_p	specific heat capacity (J kg^{-1} K^{-1})
D	diameter (m)
g	Acceleration due to gravity (m/s^2)
h	specific enthalpy (kJ/kg)
h_f	sensible heat of water (kJ/kg)
h_{fg}	latent heat of vaporization (kJ/kg)
H	Height of condenser branch (m)
I	current (A)
I	mass moment of inertia (kg/m^2)
K	stiffness factor (N/m)
LMTD	Log Mean Temperature Difference (ºC)
$\dot{m}$	mass flow rate (kg/s)
m	mass (kg)
N	rotational speed (RPM)
N	number of branches for condenser
P	pressure (Pa)
Power	power (W)
$\dot{Q}$	rate of heat transfer (W)
Q	heat transfer (J)
r	radius (m)
R	turbine radius (m)
R	gas constant (J/mol K)
s	specific entropy (kJ/kg K)
t	time (s, min)
T	temperature (ºC)
T_H	temperature of heat source (ºC)
T_L	temperature of sink (ºC)

T_C	temperature of condenser (ºC)
T	torque (Nm)
V	voltage (Volts)
V	velocity (m/s)
V	volume (m^3)
$\dot{V}$	volumetric flow rate (m^3)
W	work (J)
w	relative velocity (m/s)
$\dot{W}$	mechanical power (W)
x	length (m)
x	dryness fraction
z	height (m)

List of Greek Letters

η_{tri}	trilateral cycle efficiency
η_{isc}	isentropic expansion efficiency
γ	mass per unit volume (kg/m^3)
ν	specific volume (m^3/kg)
ρ	density (kg/m^3)
ω	rotational speed (rad/s)

List of short letters

act	actual
adia	adiabatic
atm	atmosphere
ex	external
f	
isen	isentropic
Nu	Nusselt number
Pr	Prantel Number
Re	Reynolds number
sat	saturated
th	thermodynamic
tri	trilateral
rel	relative

List of Acronyms

CDP	Combined Desalination an Power generation
DX	Direct eXchange
ED	Electro Dialysis
EGS	Engineered Geothermal System
GAB	Great Artesian Basin
GEL	Geothermal Exploration Lease
GHP	Geothermal Heat Pump
HDR	Hot Dry Rock
HFR	Hot Fractured Rock
HR	Hot Rock
HSA	Hot Sedimentary Aquifer
KE	Kinetic Energy
LDR	Liquid Dominated Reservoir
MEB	Multi Effect Boiling
MEE	Multi Effect Evaporation
MSF	Multi Stage Flashing
MVC	Mechanical vapor compression
NCG	Non Condensable Gases
ORC	Organic Rankine Cycle
PV	Photo Voltaic
RES	Renewable Energy Resources
RO	Reverse Osmosis

SDRT	Spiral Disk Reaction Turbine
SEC	Specific Energy Consumption
SHE	Spiral Heat Exchanger
TFC	Trilateral Flash Cycle
TLC	Trilateral Cycle
WHO	World Health Organization

Chapter 1 Introduction

1.1 Motivation and Introduction

With the growing understanding of global warming and climate change, it has been acknowledged that traditional dependence on fossil fuel extracts a heavy cost from the environment. Consequently, the benefits of the use of renewable energy have gained recognition. At the same time the rapid economic growth of developing economies including China, India, Brazil, Vietnam, and the Philippines has raised world energy consumption to record levels [3] .The electricity demand is expected to increase at a faster rates than the overall energy supply. At present the majority of electricity is produced from thermal power plants which use coal, gas or oil as the energy source[4]. There are growing global concerns about the global warming caused by carbon dioxide emissions from the use of fossil fuels, which creates a question about the long-term use of this energy resource.

The 20th century brought unprecedented development in human history with major breakthroughs in all scientific and technical fields. However, those breakthroughs have not been free, and in some cases, and from certain points of view, the price paid has been excessive. During the last 100 years, the human population has multiplied four fold (from 1.6 billion people in 1900 to over 6 billion at present). However, water consumption has multiplied by nine in the same period and energy consumption by sixteen, with very significant associated degradation of the environment and natural resources. Water and energy, along with air we breathe, are the three elements essential to life and civilization. At present there is a clear consensus on the impact that this overexploitation of resources is having on the fragile ecosystem of our planet, stretching to the limit the possibilities for sustainability that the planet can offer. Therefore, this development, which has been and continues to be clearly unsustainable, must become environmentally friendly as sustainable development that which is able to fulfil our needs without endangering those of future generations [5].

Renewable technologies are considered to be clean sources of energy and optimal use of these resources can minimize environmental impacts, produce minimum secondary

wastes and is sustainable based on current and future economic and social societal needs. The Sun is the source of all conventional and renewable energies. The primary forms of solar energy are heat and light. Sunlight and heat are transformed and absorbed by the environment in a multitude of ways. Some of these transformations result in renewable energy flows such as biomass and wind energy. Renewable energy technologies provide an excellent opportunity for mitigation of greenhouse gas emission and reducing global warming through substituting conventional energy sources. Renewable energy sources (RES) supply 14% of the total world energy demand [6]. RES include biomass, hydropower, geothermal, solar, wind and marine energies. The renewable are the primary, domestic and clean or inexhaustible energy resources [7]and [8]. Large-scale hydropower supplies 20 percent of global electricity. Wind power in coastal and other windy regions is a promising source of energy [7]and [9]. The proportion of RESs is expected to increase very significantly (30–80% in 2100)[9]. The global renewable energy scenario up to 2040 is presented in Table 1-1.

Table 1-1Global renewable energy scenario by 2040 (9)

	2001	2010	2020	2030	2040
Total Consumption(million tons oil equivalent)	10,038	10,549	11,425	12,352	13,310
Biomass	1080	1313	1791	2483	3271
Large hydro	22.7	266	309	341	358
Geothermal	43.2	86	186	333	493
Small hydro	9.5	19	49	106	189
wind	4.7	44	266	542	688
Solar Thermal	4.1	15	66	244	480
Photovoltaic	0.1	2	24	221	784
Solar Thermal electricity	0.1	0.4	3	16	68
Marine	0.05	0.1	0.4	3	20
Total Renewable energy Sources	1,365.5	1,745.5	2,964.4	4,289	6,351
Renewable Energy Source Contribution (%)	13.6	16.6	23.6	34.7	47.7

The last decade has shown catastrophic effects of rapid climate change caused by global warming and a consequence increase in awareness of the importance of a sustainable environment [10]. The role of renewable energy in tomorrow's world is of great significance for global environmental stability. Sun, wind and flowing or stored hydro (water) are considered to be the most common renewable energy sources for power generation. Out of these three renewable energy resources, the advantage of geothermal energy is that it can continuously supply energy and can serve as a base power source [11].

Keeping in mind that the world is currently heavily dependent on non-renewable energy sources (fossil fuels) such as coal, oil and natural gases, which are rapidly diminishing and becoming increasingly more expensive, the role of renewable energy has been recognized to be significantly important in sustainable future development. Hydropower is a good example of renewable energy and its present use and potential application to future power generation cannot be underestimated [12].

In addition to high demand for using renewable sources for sustainable energy production, producing the fresh water is also becoming more critical. Within most areas of Australia the supply of natural fresh water is being stretched to breaking point in order to meet the increasing demand for agricultural, industrial and domestic uses. The commercially favoured reverse osmosis (RO) technology for fresh water production from saline water requires large amounts of energy in the form of electricity[13]. For example, a typical RO desalination plant consumes approximately 4.6 kWh of electricity for each kL of fresh water produced[14]. At the same time, electricity is being generated from predominantly non-renewable and polluting fossil fuels. Furthermore, electricity generation is largely centralised, resulting in high transmission losses and overall inefficiencies. As with water, the demand for electricity is also increasing, requiring expansion of electricity generation capacity. Environmental considerations relating to climate change and resource depletion are driving demand for sustainable and lower-emission technologies as well as for system efficiency improvement via distributed generation. Geothermal energy will be part of the renewable solution, offering base load power from decentralised generation facilities. The International Energy Agency has shown that geothermal power production has one of the lowest generation cost at US$20-

100/MWh compared with conventional and other forms of renewable energy and can meet 10% of Australia's power demand using hydrothermal resources located in fractured or porous rock, generally at depths of 0.1 km to 4.5 km[15].

To date there has been very little commercial exploitation of these low heat sources for electricity generation despite their abundance and there is no known exploitation for combined desalination and power generation.

The Combined Desalination and Power (CDP) generation project at RMIT has shown that it is possible to generate electricity and produce fresh water in a single unit from low temperature saline water heated by renewable sources [16]. By generating two valuable products concurrently, commercially viability promises to be improved over generating each individually. The present performance of CDP as a water desalinator is satisfactory. However, its efficiency needs to be increased several times as a power generator. Means for this improvement are studied and presented in this thesis. By improving power extraction efficiency to the targeted level (half the theoretical limit), CDP will become a technology of great importance with potentially high commercial value and wide application.

The thermodynamic process which takes place in the CDP is based on expanding hot saline water inside an expander in order to produce power. The resulting vapour is condensed and thus fresh water is produced. Considerable research has been carried out on development of two-phase turbines for power production alone from solar and geothermal resources. Those turbines have generally been of screw expander type and the thermodynamic process closely follows a trilateral cycle. However, no research so far has examined the possible simultaneous fresh water production and power generation in a single unit as in the CDP proposed in the present research project.

1.1.1 Significance and innovation

Innovation

The dual geothermal system to be developed is innovative in that two useful products, namely fresh water and electricity, are generated in a single process and from a low-temperature heat source. To achieve this, a novel approach is required as the existing

geothermal systems such as “flushed steam” and “binary” produce only power and no fresh water.

In the proposed dual geothermal system incorporating the CDP concept as shown in **Error! Not a valid bookmark self-reference.** saline hydrothermal water is drawn into a chamber that is initially evacuated and its pressure maintained at a low level (4 kPa to 5 kPa absolute) by running cooling water through coil. Hot geothermal saline water enters the central rotor through a mechanical seal installed at the base of the tank. It flows through the central rotating hollow shaft to which hollow cylindrical arms are attached at the upper end. The hot water then flows outward towards converging-diverging (CD) nozzles installed at the end of each arm. As the water approaches the throat of the nozzle its pressure increases because of the centrifugal effect caused by the rotation of the arm. After passing through the throat, the pressure drops abruptly and becomes equal to or slightly higher than the chamber pressure at the nozzle exits. As a result flashing occurs and the hot liquid salt water is converted into a mixture of liquid water at higher salinity and fresh water vapour. At this stage the supplied hot water has been converted in to a two-phase fluid at a lower temperature (ideally the same as or slightly above the chamber temperature).The latent heat required for the phase change is derived mainly from the reduction of sensible heat initially available in the hot saline water. The rate of vapour production will be 10% for feed water at 90ºC and 17% for feed water at 150ºC. The fluid (now a mixture) expands in volume in the nozzle by several thousand times and produces very high velocity jets (150m/s to 200m/s) relative to the nozzle and issuing tangentially to the circle traced by the rotor arm. These jets exert a reaction force on the rotor causing it to rotate at high speed. The turbine is

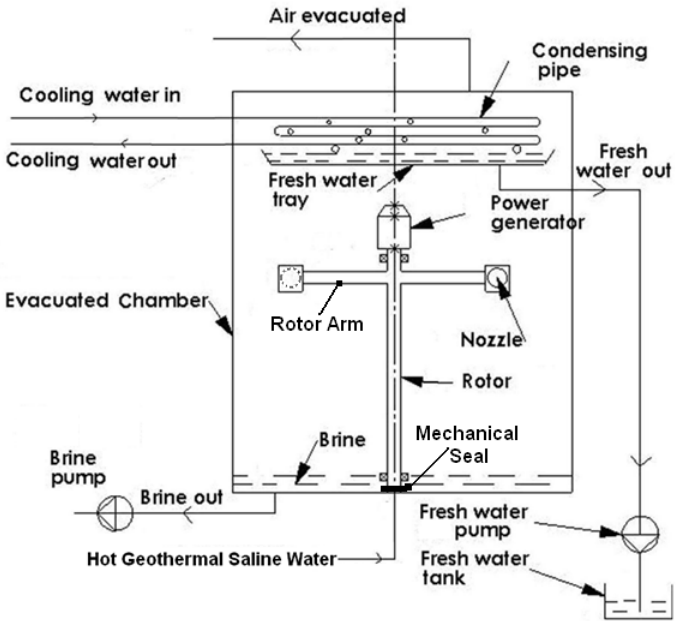

Figure 1-1 Schematic layout of CDP system

mechanically connected to an electric generator for production of electrical power. The produced vapour is condensed and the condensate is collected in a tray as shown in Figure 1.1 and pumped out as fresh water. The liquid part of the mixture, with its higher salt content is collected at the bottom of the chamber and is pumped out for re-injection into the ground or further applications such as mineral extractions. The total amount of auxiliary power required for pumping and intermittent operation of the vacuum pump is minimal compared with the amount of electrical power produced by the electrical generator. This two-phase reaction turbine is a conceptually simple device that is expected to be manufactured using standard CNC fabrication techniques. The turbine and overall system should also be readily scaled up to larger sizes.

An innovative part of the proposed CDP is that the input salt water alone is used as the working fluid, unlike machines such as Rankine Cycle Engines [17]which employ organic fluids (such as isopentane, isobutane, and R123a) and the Kalina Cycle [18]which normally uses ammonia. In addition, in the proposed CDP system, it is the geothermal water that expands in the turbine, so that need for a heat exchanger for heat transfer between the geothermal water and the working fluid is eliminated. These points will make the CDP concept both environmentally and economically attractive.

The use of a reaction turbine as the prime mover of the unit as shown in **Error! Not a valid bookmark self-reference.** further simplifies the system. Unlike in screw expanders where the working fluid passes through a complex path formed by the helical surfaces of the screw expanders, in the CDP unit water flows through simple nozzles that can be in the form of simple grooves easily machined in the rotor.

Previous research [19],[20] has found that the configuration of a simple rotor in the form of two cylindrical arms with nozzles attached to their tips, although highly effective for the proof of the concept is very inefficient for power generation. Thus, while the rate of production of fresh water in the experiments carried out at RMIT has been very close to the thermodynamic theoretical limits for such systems, the CDP unit has been very inefficient for power generation (only some 10% of the theoretical limit, and 20% of the target efficiency). This low performance for power generation can be attributed to the rapid flashing of the mixture mostly outside the nozzle and not within the

nozzle resulting in a low exit velocity of the mixture from the nozzle as compared with the expected value based on consideration of isentropic expansion of the fluid. The key to maximising the efficiency is to design carefully the profile of the passage for the fluid downstream of the nozzle throat in such a way that all the possible phase change of liquid water into the mixture and the resulted volumetric expansion occurs within the nozzles. The above requires the replacement of the arms by a disk type rotor in which grooves can be machined to form the optimum nozzle geometry. This will then maximise the velocity of the exit jets of the mixture relative to the nozzles, which in turn will enhance the thermodynamic efficiency of the turbine. The design of such an efficient two-phase turbine will require thorough knowledge and understanding of the thermodynamics of two- phase nozzles. Although there have been investigations done on such nozzles for temperatures above 220°C [21, 22] in relation to high temperature geothermal sources, there is virtually no relevant information available for the lower temperature range of 90°C to 150°C, which is the temperature of most of the hydrothermal resources in Australia. It is noted that some limited information has recently become available as the result of the preliminary research work carried out at RMIT for the temperature range of 60°C to 90°C [23, 24]. Therefore there is a need for a comprehensive research on two-phase nozzles for the temperature range of 90°C to 150°C, which is the temperature range of the geothermal resources considered in this research project. Additionally, the drag force resulting from high rotational speeds of the turbine needs to be reduced by further development.

The research in this project involves combined fluid dynamic and thermodynamic analysis and modelling (mathematical and computer) of two-phase fluid flows in the turbine accompanied by experimental investigation of different nozzles and rotor shapes and sizes for the reaction turbine in the CDP unit for applications in the temperature range of 90°C to 150°C as found in Australian hydrothermal resources.

This work develops new understanding of:

- The thermodynamic characteristics of two-phase nozzles (water as working fluid) for a temperature range of 90°C to 150°C.

- Effect of salt concentration on the phase change from liquid saline water (up to 3% salt) into a mixture of fresh water vapour and brine produced through flashing.
- Effective extraction of fresh water and electric power from hydrothermal resources
- Suitable materials for turbine construction to withstand high rotational speeds of the rotor for the temperature range of this investigation (90°C to 150°C) in a corrosive environment (salt) and assuring the quality of the fresh water produced

Significance

The dual geothermal system using CDP will be a very simple machine for simultaneous production of fresh water and electrical power from saline hydrothermal resources. Producing fresh water and power can also be achieved from hydrothermal resources separately by using conventional thermal water desalination system such as multi-effect evaporation (MEE) [25] and heat engines such as an organic Rankine cycle (ORC) and Kalina [26-28]. However, the dual geothermal system proposed in this application offers the possibility of producing both fresh water and power simultaneously in a single system. The simplicity of CDP used in a dual geothermal system offers very strong potential for producing fresh water and power at much lower costs compared with the case of running MEE and ORC independently for utilisation of the hydrothermal resource. The proposed research will therefore compare the CDP concept with these alternatives in terms of technical performance, economics and environmental impacts

This dual geothermal system promises to help utilise salty hydrothermal sources to meet Australia's increasing demand for both water and electricity through a simple system. The production of fresh water alone from salty hydrothermal sources without this new two-phase turbine using conventional desalination systems is achievable but has little appeal because of the requirement for electrical energy and high cost. The generation of power from low temperature hydrothermal sources via existing technology is also possible but is only marginally economical because of the high capital cost of ORC engines ($12000 to $15000 per kW) due to the complexity of the system. However,

the combined generation of electricity and fresh water via dual geothermal systems incorporating CDP may substantially improve the overall economic viability compared with electricity generation alone. The target considered here is to reduce the capital cost of CDP to less than $10000 per kW capacity. Considering that the production of fresh water using the CDP concept is already proven with the possible maximum yield indicates a very attractive additional product at no extra cost. Since the CDP concept is very simple, provided that the proposed research program is developed further, there is every reason to believe that the desired improvements in the efficiency of energy conversion can be made. The fact that part of the geothermal water is converted to fresh water (10% for feed water at 90ºC and 17% for feed water at 150ºC) also means that less water needs to be injected back to the ground meaning lower parasitic power losses and less water handling. A targeted cost for a small commercial-scale dual geothermal system of 100kWe incorporating CDP with fresh water production of 80kL per day will be approximately $1 million (excluding geothermal extraction costs).

This research contributes to the achievement of Australia's mandatory target for renewable and low emission power generation and has the potential to decentralise power generation. The CDP system is also applicable to other low-grade heat sources, such as waste heat recovery and solar thermal sources. This research is directly in line with the National Research Priority relating to An Environmentally Sustainable Australia. It addresses at least three of the associated priority goals: water - a critical resource, reducing and capturing emissions in transport and energy generation, and developing deep earth resources.

It is the aim of this project to develop an economically-viable dual geothermal system for utilising hot salty water in geothermal reservoirs in Australia for production of fresh water and power. Achievement of this aim would thus open up the exploitation of the geothermal resources that are not currently being utilised, and hence contribute to the national and international efforts to reduce greenhouse gas emissions. The manufacture of such engines by Australian industry would also offer a significant domestic and export market opportunity.

The project outcomes have strong direct benefits to regional communities in Australia, because the dual geothermal system when developed will offer an independent source of fresh water and power supply from renewable sources.

1.1.2 National benefit

This project offers significant social, economic, environmental and technological benefits to Australia. It will encourage the development of the geothermal industry within Australia. The dual geothermal system would make a very significant contribution to increasing the percentage of electricity in Australia generated from renewable energy sources, reducing fossil-fuel usage and thereby reduce national greenhouse gas emissions. It will help make the transition towards a sustainable national energy supply system. Considering the potential application of geothermal energy in Australia indicates that 40% of Australian energy can be produced by this renewable energy source [29]. This indicates the potential impact of development of dual geothermal systems as proposed in the application. When properly developed and managed, geothermal systems are uniquely reliable, with conventional hydrothermal power stations typically achieving much higher load factors compared to hydro and wind power stations. It also offers an alternative technology for distributed or decentralised power generation and freshwater production.

The market prospects for the dual geothermal system within Australia would involve wealth creation through manufacturing, engineering, project management, sales, marketing and future R&D as well as in the operation and maintenance of dual geothermal systems within the water and electricity industries.

Social benefits to Australia will ensue with the creation of jobs in each of these areas. Other social benefits will be realised from the viable production of fresh water and electricity in rural areas of Australia, supporting the expansion of regional populations.

The opportunity for export of dual geothermal systems and related technologies is substantial, for use with the massive geothermal resources worldwide. This will greatly amplify the economic and social benefits to Australia.

1.2 Aim and objectives

The available data on geothermal resources in Australia indicate that most of the geothermal waters (hydrothermal) in Australia are saline (up to 2% salt) and are at a temperature range of 90°C to 150°C, encountered at depths of 2 km to 4 km. The aim of this project is to develop a dual geothermal system that uses hot saline water from geothermal reservoirs in Australia and can simultaneously produce fresh water and electrical power. The development of low cost and high performance simple reaction water turbine, which will be used in a Combined Desalination and Power generation (CDP) unit to directly convert the energy of geothermal hot water to electricity, is another aim of this research.

The aim can be broken down into the following task-oriented objectives:

- Conduct a literature review to better understand the current developments.
- Further, enhance the theoretical analysis of simple reaction water turbines following the current body of knowledge.
- Develop a theoretical model to predict phase change phenomena and conceptualise ways to utilize it for speed governing.
- Develop a computer model to simulate the performance of a dual geothermal system incorporating CDP for system design, sizing for lab scale and power plant scale.
- Design and develop a stationary nozzle experimental set up for nozzle optimization in the turbine and validation system.
- Design and develop a lab scale experimental arrangement of a dual geothermal system for optimization and model validation.
- Build a new innovative simple reaction water turbine prototype based on manufacturing simplicity.
- Improve the turbine performance making suitable modifications in the developed turbine designs.

- Identify potential high temperature hydropower sites in Victoria, Australia through an online survey and conduct a case study for one of these sites for technical and economic feasibility.

The project will develop a more efficient two-phase turbine (hot liquid water as input and a mixture of low temperature water vapour and liquid water as output) in a laboratory-scale CDP prototype, to produce both fresh water and electrical power. The entire CDP system will be specifically targeted for use with saline geothermal water sources, which are prevalent in Australia and represent a vast and essentially untapped resource.

1.3 Research question and method

The specific research questions addressed in this thesis are:

1. What is the relation between rotational speeds, output power and the thermodynamic efficiency of the system?
2. What are the effects of temperature and expansion rate on phase change dynamics for the working fluids?
3. What is the best rotor configuration in order to increase the thermodynamic efficiency of the system?
4. How to remove Non-condensable gases from geothermal water in a sustainable way?
5. What would be a system configuration of the CDP system for MW scale power generation for lowest cost and ease of manufacture
6. What are the environmental impacts of the CDP system utilizing geothermal energy and how can these impacts be minimized?

The methodology that has been followed in order to meet the aims and address the research questions in this thesis is given in Table 1-2:

Table 1-2:Methodology of the research project

Step No.	Title of activity	Activity description & relation to research questions
1	Literature review	Analysis of published literature on fresh water and electricity production from renewable resources, available technologies for utilizing geothermal energy, and the use of a simple reaction turbine to enhance the power generation. (addresses research questions 1 and 2)
2	Development of theory and a computer model	Development of an improved theoretical analysis of phase change phenomena in the turbine, and a mathematical simulation model of a two phase nozzle based on this theory using combined fluid dynamic and thermodynamic analysis and modelling (mathematical and computer) of two-phase fluid flows in the turbine (addresses research questions 1- 3)
3	Design Phase	Designing the experimental facility based on the theoretical analysis (addresses research questions 1- 3)
4	Experimental apparatus and testing different prototypes	Build the experimental facility based on designing parts and performing the number of repeatable tests for different conditions (addresses research questions 1-3)
4	Performance measurement	Collecting the experimental data through performed tests and do the analysis and comparison for all the conditions in order to improve the design (addresses research question 1 and 2)
5	Model testing	Validation of model using experimental data. Comparison of model predictions with experimentally measured performance. Refinement of the model if necessary (addresses research question 1 - 3)
6	System analysis and evaluation	Analysis of the operation of the designed reaction turbine for application in a geothermal system. Evaluation of the system for a demonstration unit (addresses research question 4-6)
7	Performance enhancement	Identification of CDP components or design features requiring further research and development. (addresses research question 5 and 6)
8	Thesis writing	Preparing and writing the thesis

1.4 Scope

The thesis focusses on developing a dual geothermal system that:

- Uses geothermal hot saline water
- Incorporates an innovative simple reaction turbine
- Use a trilateral flash cycle to enhance the utilization of the geothermal water
- Produces power and fresh water simultaneously
- Has detailed design with manufacturing simplicity

In addition the main application for CDP considered throughout the thesis is in Hydrothermal- geothermal systems for remote area power supply. Further explanation of the selected scope for the thesis is provided later in chapter 2.

1.5 Outcomes

At the outset of this research work, the outcomes expected were the following:

1. A two-phase turbine suitable for power generation from hot saline geothermal water
2. An integrated system design and laboratory-scale CDP prototype for geothermal sources
3. A computer model that can be used for development of demonstration and commercial-scale systems, and performance prediction
4. Cost estimates (both capital and operational) for the whole system

After successful completion of this research project the outcomes will be used to manufacture, install and test a prototype in a field trial of the technology by the partner organisation at a geothermal site in Australia for performance monitoring and demonstration (20 kW electrical power and 15 000 litres per day fresh water output – sufficient for 20 families).

1.6 Organisation of dissertation

The reminder of this dissertation is organised as follows:

Chapter 2 introduces a background and literature review of different power generation and desalination methods using renewable energy resources.

Chapter 3 describes the geothermal energy in Australia, its potential, resources, challenges, the sector and also current available technologies that use geothermal energy. In addition this chapter introduces the current geothermal resources specifically in Vitoria.

Chapter 4 explains the theoretical analysis of the novel combined desalination and power generation system by description and comparison of different thermodynamic cycles, turbines and heat exchangers.

Chapter 5 describes the design of the simple reaction turbine that operates in CDP by going through the phenomenon of two-phase flow and maximizing its efficiency.

Chapter 6 presents the development of the computer model that provides the prediction of the whole system performance that each operator can simply use and redesign the system based on the criteria and different input situations.

Chapter 7 explains the turbine experimental rig and the procedure of the experimental tests, which have been done at RMIT University.

Chapter 8 discusses the results of the experimental tests that used to improve the design and validate the computer model.

Chapter 9 studies the theoretical and experimental aspects of removing non-condensable gases from geothermal water which is an important issue in a real case of geothermal planet by introducing the sustainable way of this removal in a system such as CDP.

Chapter 10 purposes the demonstration CDP unit design for a 25kW geothermal planet with its cost analysis.

Finally, chapter 11 concludes the complete work highlighting the main contributions and future work required in this research.

1.7 Publications

1. **Sustainable removal of non-condensable gases from geothermal waters,** Anna Khaghani, AbhijitDate, Aliakbar Akbarzadeh. Renewable and Sustainable Energy Reviews 21 (2013) 204–214.
2. **Investigate the potential of using trilateral flash cycle for combined desalination and power generation integrated with salinity gradient solar pond,** Anna Khaghani, Abhijit Date, Firoz Alam, aliakbar Akbarzadeh. Procedia Engineering, Volume 49, 2012, Pages 42-49.
3. **Sustainable way of removing non-condensable gases from waters**, Anna Khaghani, AbhijitDate, Aliakbar Akbarzadeh DOI: 10.2316/P.2011.756-049, (756) Power and Energy Systems and Applications - 2011.
4. **Sustainable non-condensable gas removal from geothermal water and its comparison with available technologies,** Anna Khaghani, AbhijitDate, Aliakbar Akbarzadeh. the Solar 2010 conference (48th ANZSES Conference) ,Canberra 1st-3rd of December 2010.
5. **Prospective of trilateral cycle for power generation and fresh water production utilizing geothermal resources in Australia,** Anna Khaghani, AbhijitDate, Aliakbar Akbarzadeh .Renewable energy journal
6. **Experimental performance of a rotating two-phase turbine for initially sub-cooled hot water for combined desalination and power generation: Part A,** AbhijitDate, Anna Khaghani, Sara vahaji, Aliakbar Akbarzadeh. submitted to Applied Thermal Engineering
7. **Experimental performance of a rotating two-phase turbine for initially sub-cooled hot water for combined desalination and power generation: Part B,** AbhijitDate, Anna Khaghani, Sara vahaji, Aliakbar Akbarzadeh. submitted to Applied Thermal Engineering

8. **Investigate the potential of using trilateral flash cycle for combined desalination and power generation from geothermal resources,** AbhijitDate, Anna Khaghani, Aliakbar Akbarzadeh ready to submit

Chapter 2 Background and literature review

2.1 Introduction

Water and energy are two of the most important topics on the international environment and development agenda. The social and economic health of the modern world depends on sustainable supply of both energy and water. Many areas worldwide that suffer from fresh water shortage are increasingly dependent on desalination as a highly reliable and non-conventional source of fresh water. Therefore the desalination market has greatly expanded in recent decades and that is expected to continue in the coming years. The integration of renewable energy resources with desalination and water purification is becoming increasingly attractive [30].

Power and water supply are widely recognised as the two major issues humankind will have to face and solve during this century. While it is clear that, in the next few decades, oil will cease to dominate, it is not yet clear today which source of energy will replace it. At the same time, water scarcity, already a serious global problem will become critical during the first half of this century. Of all the current environmental problems, those related to energy and water are probably the hardest to approach scientifically, and those that will have the worst long-term consequences. Problems associated with water scarcity, and the gradual destruction and contamination of fresh water resources are becoming more pressing in many areas of the planet, causing concern even in countries, which, so far, have not experienced such problems [30].

2.2 Different ways of power production and desalination

2.2.1 Power production using renewable energy resources

During 1990–2050, primary energy consumption is expected to increase by 50% according to the most environmentally conscious scenario and by 275% according to the highest growth rate scenario. In the environmental scenario, carbon emissions are expected to decrease slightly from 1990 levels, whereas the high growth-rate scenario

leads to a doubling of carbon emissions [31]. Global energy consumption in the last half century has rapidly increased and is expected to continue to grow in the future.

Existing power systems can be considered as a prime cause of current greenhouse or global warming effects as more than 75% of the energy is produced from fossil fuel. Therefore there is a critical need for a robust and sustainable power transmission and distribution system which is intelligent, reliable, environment friendly, and overcomes various problems associated with existing power systems [30].

Renewable energy resources will play an important role in the world's future. The energy resources have been split into three categories: fossil fuels, renewable resources and nuclear resources. Renewable energy sources are those resources which can be used to produce energy repeatedly, e.g. solar energy, wind energy, biomass energy, geothermal energy, etc. and are also often called alternative sources of energy [31]. The increasing concentrations of greenhouse gases such as CO2, CH4 , CFCs, halons, N2O, ozone, and peroxyacetylnitrate in the atmosphere are acting to trap heat radiated from the Earth's surface and are raising the surface temperature of the Earth [30].

World energy resources can be classified into two categories: fossil fuels and renewable resources.

- Fossil Fuels

With a view to meeting the future demand for primary energy in 2050 and beyond, it is important to know the extent of available reserves of conventional energy resources including fossil fuels and uranium, and the limitations posed on them by environmental considerations. Coal is the largest fossil resource available to us and the most problematic from environmental concerns. From all indications, coal use will continue to grow for power production around the world because of expected increases in China, India, Australia and other countries. From an environmental point of view, this would be unsustainable. Based on the known reserves of uranium, it is unlikely that nuclear power will be able to provide a significant part of our future energy [8].

- Renewable energy

Renewable energy sources are those resources which can be used to produce energy repeatedly, e.g. solar energy, wind energy, biomass energy, geothermal energy, etc. and are also often called alternative sources of energy [32]. Renewable energy sources that meet domestic energy requirements have the potential to provide energy services with zero or almost zero emissions of both air pollutants and greenhouse gases. Renewable energy system development will make it possible to resolve the presently most crucial tasks like improving energy supply reliability and managing the organic fuel economy; solving problems of local energy and water supply; increasing the standard of living and level of employment of the local population; ensuring sustainable development of the remote regions in desert and mountain zones; implementation of the obligations of the countries with regard to fulfilling the international agreements relating to environmental protection [31]. Development and implementations of renewable energy project in rural areas can create job opportunities and thus minimizing migration towards urban areas. Harvesting the renewable energy in a decentralized manner is one of the options to meet the rural and small scale energy needs in a reliable, affordable and environmentally sustainable way [8].

The ideal renewable energy source has no fuel cost and provides a high power density that is available most of the hours during a year (allowing for a high utilization of the power plant at full load). The importance of high availability is shown by the fact that investment costs for all electricity producing units are set by the rated power P [kW], while incomes are governed by the produced energy W [kWh]. A comparison of the renewable energy sources (data from the UN World Energy Assessment Report) shows the current electrical energy cost to be 2–10 US¢/kWh for geothermal and hydro, 5–13 US¢/kWh for wind, 5–15 US¢/kWh for biomass, 25–125 US¢/kWh for solar photovoltaic and 12–18 US¢/kWh for solar thermal electricity. Of the total electricity production from renewables of 2826 TWh in 1998, 92% came from hydropower, 5.5% from biomass, 1.6% from geothermal and 0.6% from wind. Solar electricity contributed 0.05% and tidal 0.02%. Comparing four “new” renewable energy sources (geothermal, wind, solar and tidal), shows 70% of the total electricity generated to come from geothermal which represents only 42% of the total installed capacity. Wind energy contributes 27% of the electricity, but has 52% of the installed capacity. Solar energy produces 2% of the

electricity and tidal energy 1%. Biomass constitutes 93% of the total direct heat production from renewables, geothermal 5%, and solar heating 2%. Heat production from renewables is commercially competitive with conventional energy sources. The current cost of direct heat from biomass is 1–5 US¢/kWh, geothermal 0.5–5 US¢/kWh, and solar heating 3–20 US¢/kWh. Geothermal energy, with its proven technology and abundant resources, can make a significant contribution towards reducing the emission of greenhouse gases [33].

It is clear that no single energy source is going to take over from the polluting fossil fuels in the new century. The integration of local energy sources in individual countries and regions into national/regional systems which make use of the best local and imported energy is important if we are to find solutions to regional and global energy problems. Proponents for renewable energy sources need to work together in the world energy market that is very conservative. In the following, the different renewable energy resources have been introduced briefly:

Solar Energy: As far as renewable energy sources are concerned, solar thermal energy is the most abundant one and is available in both direct as well as indirect forms. The Sun emits energy at a rate of 3.8×10^{23} kW, of which approximately 1.8×10^{14} kW is intercepted by the earth [5]. Electricity production cost through solar energy is significantly higher than that of conventional power stations. As far as carbon emission is concerned solar based power stations release almost zero carbon. Electrical energy is the pivot of all developmental efforts in both the developed and the developing nations because conventional energy sources are finite and fast depleting. Direct solar energy conversion to electricity is conventionally done using photovoltaic cells, which make use of the photovoltaic (PV) effect. The PV effect depends on interaction of photons, with energy equal to, or more than the band-gap of PV materials[30]. PV modules generate electricity directly from light without emissions, noise, or vibration. Sunlight is free but power generation cost is exceptionally high, although prices are starting to come down. Solar energy has low energy density: PV modules require a large surface area for small amounts of energy generation. The primary component in grid connected PV systems is the inverter, which converts DC power produced by the PV array into AC power consistent with the voltage and power quality requirement of the utility gird. In the case

of solar PV, it is naturally and practically evident that no PV technology will work during night time. Sometimes, this handicap is solved with the help of expensive storage technologies which do not improve the degree of utilization. In other words, storage technologies represent an extra investment cost which the electricity output seldom covers, leading to the conclusion that PV is one of the most expensive greenhouse gas abatement options, whilst recognising that it is one of the most important energy sources available since it is free of charge[34].

Wind Energy: from the renewable energy technologies applied to electricity generation, wind energy ranks second only to hydroelectric in terms of installed capacity and it is experiencing rapid growth. India is one of the most promising countries for wind power development in the world[35]. Wind power may prove practical for small power needs in isolated sites, but for maximum flexibility, it should be used in conjunction with other methods of power generation to ensure continuity [36].Wind energy potential studies show that the world-wide wind resources are abundant. The world-wide potential for wind energy is estimated to be 26,000 TWh/yr, although a capacity of 9000 TWh/yr may be utilized due to economical and other reasons[37].

Wind energy for electricity production today is a mature, competitive, and virtually pollution-free technology widely used in many areas of the world[36].Wind technology converts the energy available in the wind to electricity or mechanical power through the use of wind turbines. The function of a wind turbine is to convert the motion of the wind into rotational energy that can be used to drive a generator. Wind turbines capture the power from the wind by means of aerodynamically designed blades and convert it into rotating mechanical power. Wind turbine blades use airfoil sections to maximise mechanical power[37].

In the power-starved developing countries, wind power is a viable source of electricity, which can be installed and transmitted very rapidly, even in remote, inaccessible and hilly areas. Electricity generation from wind never depletes and never increases in price. The electricity produced by these systems could save several billion barrels of oil and avoid many million tons of carbon and other emissions [38].

Wind energy potential is not easily estimated because, unlike solar energy, it depends on the site characteristics and topography to a large degree, as wind speeds are influenced strongly by local topographical features[39].

Wave Energy: Generating electricity from waves is predicted to be a new source of renewable energy conversion expanding significantly, with a global potential in the range of wind and hydropower. Several wave power techniques are on the edge of commercialisation, and thus evoke questions of environmental concern. Conservation matters are to some extent valid independent of technique but the main focus is on point absorbing linear generators. The theoretical potential for wave- and tidal energy conversion is immense in parts of the world with long oceanic coastlines [40]. The physical properties of waves make them a very interesting source of energy, being better in comparison with e.g. wind and solar power, due to higher energy density and more predictable occurrence (solar influx is converted to wind that in its turn is converted and stored as waves) [41]. Wave power along the European west coast has been estimated to be able to cover all of the Western European electrical energy consumption[40] . Recently, there have been estimations on wave energy conversion even in milder climate sea areas indicating a greater worldwide availability for wave power [43]. Although the techniques are generally not yet advanced, it is likely that wave power will become at least as important as wind and hydropower are today. Several in-sea-trials have demonstrated the importance of coping with excessive wave power, for instance during a storm. Many installations have been destroyed by the harsh ocean weather. From an economical point of view, it can be noted that the large waves dictate the costs while the small and medium waves provide the income. If a wave energy converter is to survive the peak powers in the ocean, it must have large safety margins. This usually raises the total costs of the system without giving a corresponding increase of the income. One way of reducing this problem is to place the converter underwater or at the seabed, thereby reducing the impact of large waves on the equipment [42, 43].

Geothermal Energy: Geothermal energy for electricity generation has been produced commercially since 1913, and for four decades on the scale of hundreds of MW both for electricity generation and direct use. The utilization has increased rapidly during the last three decades. In 2000, geothermal resources have been identified in over 80

countries and there are quantified records of geothermal utilization in 58 countries in the world. The worldwide use of geothermal energy amounts to 49 TWh/a of electricity and 53 TWh/a for direct use. Electricity is produced with geothermal steam in 21 countries spread over all continents. Five countries obtain 10–22% of their electricity from geothermal energy. Only a small fraction of the geothermal potential has been developed so far, and there is ample space for an accelerated use of geothermal energy both for electricity generation and direct applications[44].

The worldwide use of geothermal energy amounts to about 49 TWh/a of electricity and 53 TWh/a for direct use. A new estimate of the geothermal potential of the world, gives the total potential for the resources suitable for electricity generation (resource temperature in excess of 150°C) as 11,000±1300 TWh/a, and the total potential resources for direct use (resource temperature lower than 150°C) in excess of 1400 EJ/a (390,000 TWh/a heat). These figures for the potential cover both known and unidentified resources. Stefansson [45]estimates the identified geothermal resources to be 2000±140 TWh/a for electricity generation, and in excess of 7000 TWh/a heat for direct use. There is certainly space for an accelerated use of geothermal energy both for electricity generation and direct use in the near future. Electricity is produced with geothermal steam in 21 countries spread over all continents. The top ten countries in 1999 were (showing MWe in brackets): USA (2228), Philippines (1909), Italy (785), Mexico (755), Indonesia (590), Japan (547), New Zealand (437), Iceland (170), El Salvador (161), and Costa Rica (143). The most progressive country at present, the Philippines, plans to add 526 MWe to the installed capacity during 2002–2008. About 22% of the electricity in the Philippines is generated with geothermal steam. Other countries generating 10–20% of their electricity with geothermal energy at present are Costa Rica, El Salvador, Iceland and Nicaragua. Two new countries have recently commissioned their first geothermal power stations, Ethiopia (9 MWe) and Guatemala (33 MWe)[46].

The electric generation cost is variable, but commonly around US¢4/kWh. The lowest cost is obtained with co-generation of electricity (US¢2/kWh) and hot water for district heating (US¢0.5/kWh) in two high temperature fields in Iceland [47].

Direct application of geothermal energy can involve a wide variety of end uses, such as space heating and cooling, industry, greenhouses, fish farming, and health spas. It uses mostly existing technology and straightforward engineering. The technology, reliability, economics, and environmental acceptability of direct use of geothermal energy have been demonstrated throughout the world. The main types of direct use are bathing/swimming/balneology (42%), space heating (35%, thereof 12% with geothermal heat pumps), greenhouses (9%), fish farming (6%), and industry (6%) [30].

Direct application can use both high- and low-temperature geothermal resources and is therefore much more widespread in the world than electricity production. The production cost/kWh for direct utilization is highly variable, but commonly under US¢2/kWh [47].

The number of countries producing geothermal power and the total worldwide geothermal power capacity under development appear to be increasing significantly in the first decade of the 21st Century. The number of countries producing power from geothermal resources could increase 120%, from 21 in 2000 to as many as 46 in 2010. Total geothermal capacity on-line could increase over 55%, from 8,661 MW in 2000 to 13,500 MW or more [48].

Therefore geothermal resource uses can be divided into two categories:

- Direct use of energy, for example heating and bathing;
- Electricity generation

There are two important aspects of the utilisation of geothermal resources:

(a) with cascading and combined uses it is possible to enhance the feasibility of geothermal projects and (b) the resource temperature may limit the possible uses. Cascading of geothermal fluids to successively lower temperature applications may increase the overall thermodynamic efficiency of the resource use, and can thereby improve the economics of the entire system. However, care needs to be taken not to decrease the long-term sustainability of the system. Uses of geothermal resources, after being used for power generation, can include space or district heating, greenhouse heating, and aquaculture pond and swimming pool heating, or by use of absorption

chillers, district cooling. The site specifics are a major factor in achieving the cascading of the resource, with the various applications required to be near to each other [46].

Resources can be broadly classified as low temperature (less than 90 °C), moderate temperature (90 °C – 150 °C), and high temperature (greater than 150 °C). Low temperature resources at economically drillable depth are not only much larger, in terms of the absolute volume (km3) of resource, than high temperature resources but, geographically much more widely distributed. At the same time high temperature resources can generally be utilised more efficiently and economically. For these reasons large scale use of geothermal resources for electricity generation has traditionally been restricted to countries where high temperature resources occur close to the surface, usually related to magmatic activity. Technological developments have now reached the point where such restrictions on depth, temperature and the natural occurrence of fluid may no longer be so critical.

The two main categories of geothermal resources may be explained as:

- Direct use

Direct heat use is one of the oldest, most versatile and also the most common form of geothermal energy utilisation by mankind. Examples include bathing, district heating, agricultural applications and desalination. There are many possible uses of geothermal fluids at different temperatures, with the addition of electricity generation from binary cycles.

The main types of direct applications of geothermal energy are space heating 52% (thereof 32% using heat pumps), bathing and swimming (including balneology) 30%, horticulture (greenhouses and soil heating) 8%, industry 4%, and aquaculture (mainly fish farming) 4%. Figure 2-1 shows the direct applications of geothermal energy worldwide by percentage of total energy use. The main growth in the direct use sector during the last decade has been the use of geothermal (ground-source) heat pumps. This is due, in part, to the ability of geothermal heat pumps to utilise ground-water or ground-coupled temperatures anywhere in the world [49].

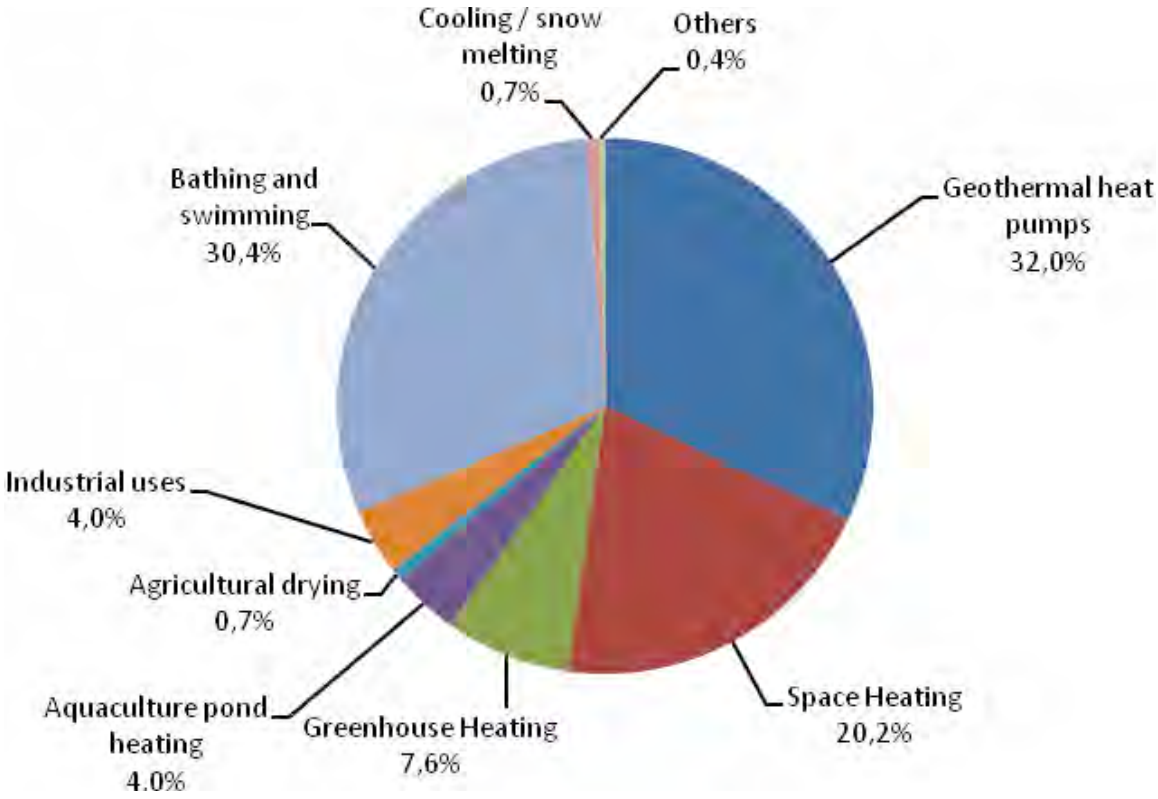

Figure 2-1 Direct applications of geothermal worldwide in 2004 by percentage of total energy use [50].

Space heating, of which more than 80% is district heating, is among the most important direct uses of geothermal energy. The preferred water delivery temperature for space heating is in the range 60- 90°C and commonly the return water temperature is 25-40°C. Conventional radiators or floor heating systems are typically used, but air heating systems are also possible. If the temperature of the resource is too low for direct application, geothermal heat pumps can be used. Space cooling can also be provided by geothermal systems. Geothermal heat pumps can heat and cool with the same equipment.

Lower temperature sources produce the energy equivalent of 100M BBL per year. Sources with temperatures from 30-150 C are used without conversion to electricity for as varied as district heating, greenhouses, fisheries, mineral recovery, industrial process heating and bathing in 75 countries. Heat pumps extract energy from shallow sources at 10-20 C in 43 countries for use in space heating and cooling. Home heating is the fastest-growing means of exploiting geothermal energy, with global annual growth rate of 30% in 2005 and 20% in 2012 [50].

Approximately 270 petajoules (PJ) of geothermal heating was used in 2004. More than half went for space heating, and another third for heated pools. The remainder supported industrial and agricultural applications. Global installed capacity was 28 GW, but capacity factors tend to be low (30% on average) since heat is mostly needed in winter. Some 88 PJ for space heating was extracted by an estimated 1.3 million geothermal heat pumps with a total capacity of 15 GW [51].

Heating is cost-effective at many more sites than electricity generation. At natural hot springs or geysers, water can be piped directly into radiators. In hot, dry ground, tubes or down hole heat exchangers can collect the heat. However, even in areas where the ground is colder than room temperature, heat can often be extracted with a geothermal heat pump more cost-effectively and cleanly than by conventional furnaces. These devices draw on much shallower and colder resources than traditional geothermal techniques. They frequently combine functions, including air conditioning, seasonal thermal energy storage, solar energy collection, and electrical heating. Heat pumps can be used for space heating essentially anywhere.

Iceland is the world leader in direct applications. Some 93% of its homes are heated with geothermal energy, saving Iceland over $100 million annually in avoided oil imports. Reykjavik, Iceland has the world's biggest district heating system. Once known as the most polluted city in the world, it is now one of the cleanest [50].

- Electricity generation

Conventional geothermal energy developments provide 9,700 MWe of electricity generation world-wide and have a track record of over 100 years of successful development and a 3% growth rate . It can be conservatively predicted that over 1000 MWe of new generation will be installed worldwide within the next five years using current technology. A recent major study for the US Government by the Massachusetts Institute of Technology (MIT 2006) has pointed out that a relatively modest investment in research and development (R&D) (equivalent to the cost of building one large coal-fired power plant) could lead to technical breakthroughs whereby geothermal could provide a substantial proportion of the USA’s non-transport energy needs[51] .

The majority of power generation is typically undertaken with high temperature resources (220-340 °C) and the most economical results are from higher temperatures and shallower resources. However, the lowest temperature power plant in the world is currently operating at only 74 °C in Chena, Alaska. The Birdsville plant in Australia operates on 99 °C fluid [52].

As geothermal energy resources are the main source of providing renewable energy addressed in this research, the available technologies which use geothermal resources for power generation has been studied worldwide.

Geothermal electrical plants were traditionally built exclusively on the edges of tectonic plates where high temperature geothermal resources are available near the surface. The development of binary cycle power plants and improvements in drilling and extraction technology enable enhanced geothermal systems over a much greater geographical range. Demonstration projects are operational in Landau-Pfalz, Germany, and Soultz-sous-Forêts, France, while an earlier effort in Basel, Switzerland was shut down after it triggered earthquakes. Other demonstration projects are under construction in Australia, the United Kingdom, and the United States of America [48].

The thermal efficiency of geothermal electric plants is low, around 10–23%, because geothermal fluids do not reach the high temperatures of steam from boilers. The laws of thermodynamics limit the efficiency of heat engines in extracting useful energy. Exhaust heat is wasted, unless it can be used directly and locally, for example in greenhouses, timber mills, and district heating. System efficiency does not materially affect operational costs as it would for plants that use fuel, but it does affect return on the capital used to build the plant. In order to produce more energy than the pumps consume, electricity generation requires relatively hot fields and specialized heat cycles. Because geothermal power does not rely on variable sources of energy, unlike, for example, wind or solar, its capacity factor can be quite large – up to 96% has been demonstrated. The global average was 73% in 2005 [53].

Geothermal energy comes in either vapour-dominated or liquid-dominated forms.

- Liquid-dominated plants

Liquid-dominated reservoirs (LDRs) are more common with temperatures greater than 200 °C and are found near young volcanoes surrounding the Pacific Ocean and in rift zones and hot spots. Flash plants are the most common way to generate electricity from these sources. Pumps are generally not required, powered instead when the water turns to steam. Most wells generate 2-10MWe. Steam is separated from liquid via cyclone separators, while the liquid is returned to the reservoir for reheating/reuse. As of 2013, the largest liquid system is Cerro Prieto in Mexico, which generates 750 MWe from temperatures reaching 350 °C (662 °F). The Salton Sea field in Southern California offers the potential of generating 2000 MWe [54].

The principle of flash steam power plant has been shown in Figure 2-2.

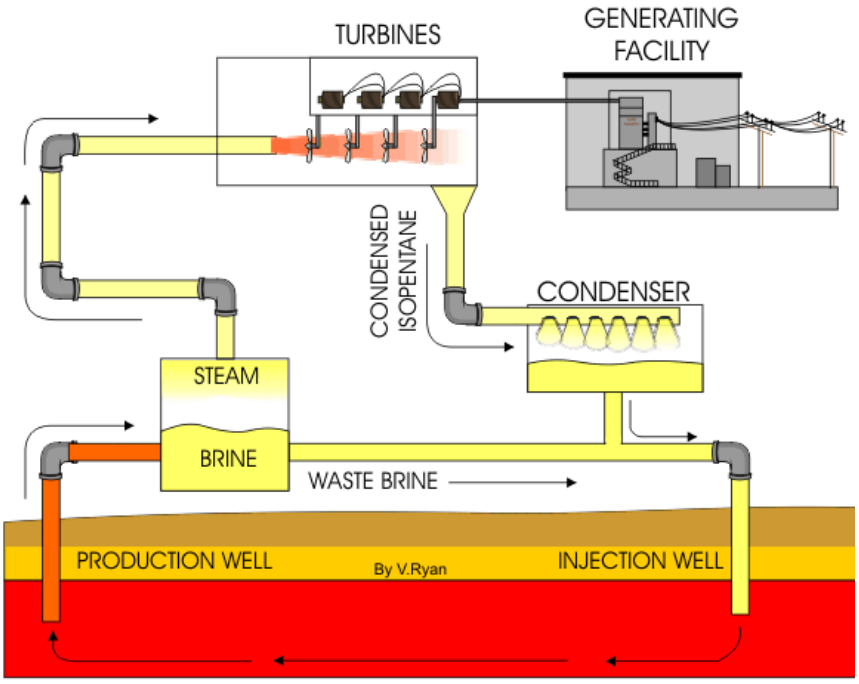

Figure 2-2 Geothermal Flash steam power plant

The most attractive geothermal fields for developers have been those with higher resource temperatures and production fluid enthalpies. In general as the resource temperature increases the proportion of steam available from the geothermal fluids at the

surface also increases and so too its pressure. These conditions provide for more efficient operation of condensing steam turbines, and hence lower electricity production costs. For low enthalpy resources (i.e. lower resource temperatures), a low plant operating pressure is needed to maximise the amount of available steam, equipment is larger and hence more expensive, and a significant proportion of the available energy in the production fluid is rejected unused in the separated brine.

Lower temperature LDRs (120-200 C) require pumping. They are common in extensional terrains, where heating takes place via deep circulation along faults, such as in the Western US and Turkey. Water passes through a heat exchanger in a Rankine cycle binary plant. The water vaporizes an organic working fluid that drives a turbine. These binary plants originated in the Soviet Union in the late 1960s and predominate in new US plants. Binary plants have no emissions[51]. The working principle of binary plants is shown in Figure 2-3.

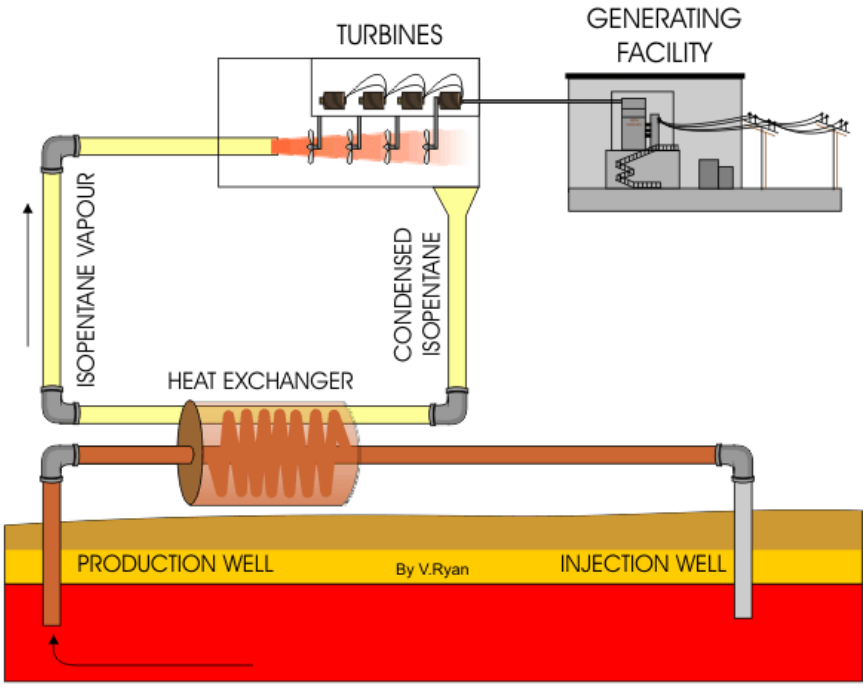

Figure 2-3 Geothermal binary power plant

Generating electricity from low-to-medium temperature geothermal fluids (85-170 °C) and from the waste hot water coming from separators in water-dominated geothermal fields, has made considerable progress since improvements were made in binary fluid technology known as Organic Rankin cycle (ORC).

Turboden from Italy offers ORC technology. Although it has designed, manufactured and supplied a number of ORC plants, it has produced only one geothermal power plant, a 1 MWe development at Altheim, Austria. Plant capacities are in the 0.3 to 1.5 MWe range.

Barber-Nichols, who have also been in the business of binary geothermal power plants in the late 1970s and early 1980s, produced numerous ORC systems for converting solar and geothermal energy to electrical power and air conditioning. These plants generally have a capacity less than 1.5 MWe15.

United Technologies (part of the Carrier Corporation) is a newcomer to the geothermal ORC market. They have a 400kW demonstration plant at Chena Hot Springs in Alaska. United Technologies are actively pursuing larger plant sizes and hope to have a 1 MWe package available in the near future [55]. These are based on adapting Carrier air conditioning units, using a commercial refrigerant. They may be applicable to lower temperatures ranges than typical ORC units and be particularly suitable for Hot Sedimentary Aquifer (HAS) applications in Australia, provided a suitable means of cooling is available.

The widespread use of binary plants overseas, market competition and their ready commercial availability mean that there is probably little advantage in undertaking fundamental R&D on such systems in Australia.

Another technology which has been used for liquid dominated reservoirs is the Kalina system.

In more detail, The Kalina Cycle is a variant of the closed Rankine binary cycle, but uses an ammonia-water mixture as the motive fluid. The basic process was developed by Dr. Alex Kalina and patented during the 1980's. A 3.2 MWe demonstration plant

operated for around 7,000 hours at the US DOE research facility at Canoga Park in the 1990's. Two other Kalina plants have been constructed and are currently in operation:-

- a 2 MWe plant operating on geothermal brine at Husavik, Iceland, which entered service in 2000.
- a 4 MWe unit at Sumitomo Metals in Japan using low grade process waste heat, operating since 1999.

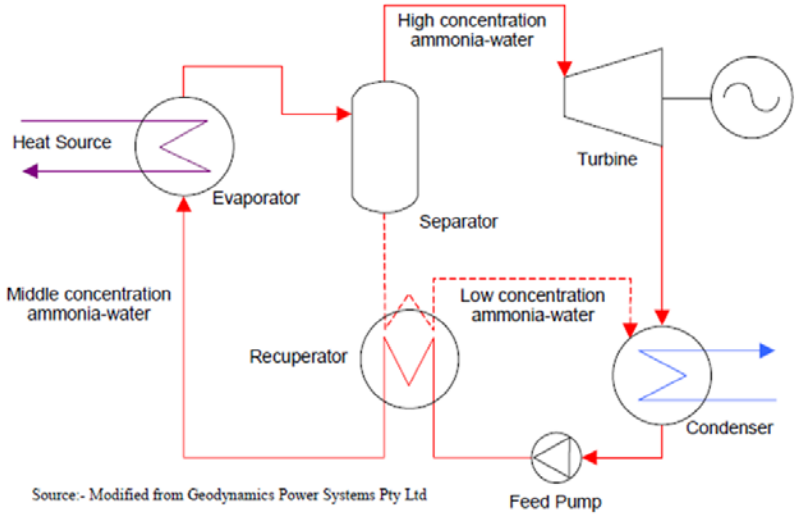

Figure 2-4 schematic of Kalina cycle

There are several prospective Kalina Cycle projects under consideration at the present time, but none is under construction.

Process Description

The Kalina Cycle offers improved energy recovery efficiency over organic Rankine cycles through optimisation of the motive fluid vaporising and condensing characteristics to best match the available resource conditions. The inherent variable boiling point characteristic of a mixture allows the temperature profile through the motive fluid side of the evaporator to achieve a closer overall approach to that of the heat source fluid. This results in more effective heat transfer as the heat duty is not restricted by a single "pinch" point, as it is for a single component ORC fluid, boiling at a constant temperature. In addition, by varying the working fluid composition at several points in the cycle (by separating and later recombining streams), selected unit operations can take

place under more advantageous thermodynamic conditions, further increasing cycle efficiency.

The Kalina Cycle typically uses an ammonia-water solution of around 80 wt% ammonia, though individual streams in the cycle are richer or leaner to alter thermo-physical properties. At the condenser outlet the liquid is saturated at the condenser pressure. The feed pump then increases the stream pressure to above turbine inlet conditions. The high-pressure fluid is pre-heated to recover heat from the lean liquid exiting separator before entering the evaporator. In the evaporator the ammonia water solution is partially vaporised by heat exchange with the geothermal fluid. The mixed phase fluid is separated into rich vapour (high ammonia concentration) and lean liquid (low ammonia concentration) components in the separator.

The working fluid vapour from the separator is expanded through the turbine to produce electricity. Conventional steam turbines, which are highly developed and readily available, are appropriate for this service. The liquid from the separator is cooled in the preheater, as noted earlier. The turbine exhaust vapour and lean liquid are cooled and condensed in the condenser, which can be water- or air-cooled. The recombined, cool liquid then passes to the feed pump to complete the cycle.

Increased cycle efficiency can be obtained by using a low temperature recuperator (not shown in diagram) upstream of the condenser to transfer heat from the turbine exhaust vapour and lean separator liquid exchange heat to the cold working fluid from the feed pump. This additional heat recovery step was incorporated into the Kalina plant built in Iceland.

- Vapor dominated

Naturally occurring vapor-dominated geothermal systems are rare but highly efficient at producing electricity. Many reservoirs may contain vapour-dominated zones, particularly at shallow depth or if they are located in high relief areas, but very few undisturbed reservoirs do not have liquid reservoirs below sea level elevation. The Geysers (northern California, USA), Larderello (Italy), and Kamojang, Darajat (both in central Java, Indonesia) are the four fields with published pressure data confirming

vapor-dominated pressures profiles at substantial depth in their reservoirs. Vapor-dominated sites offer temperatures from 240-300 C that produce superheated steam.

The Geysers in California is the largest and best known vapor dominated reservoir. Here, steam is obtained by drilling wells from 7,000 to 10,000 feet deep. In a dry steam reservoir, the natural steam is piped directly from a geothermal well to power a turbine generator. The spent steam (condensed water) can be used in the plant's cooling system and injected back into the reservoir to maintain water and pressure levels. The Geysers has 1517 MW of active installed capacity with an average production factor of 63% (955 MW) [48]. Steam used at The Geysers is produced from a greywacke sandstone reservoir, that is capped by a heterogeneous mix of low permeability rocks and under laid by a silicicintrusion [56].

The Geysers electrical plant reached peak production in 1987, at that time serving 1.8 million people. Since then, the steam field has been in gradual decline as its underground water source decreases. Currently, the Geysers produce enough electricity for 1.1 million people.

Techniques developed from Enhanced Geothermal Systems research will increase the production of the region in the future. By re-injecting grey water from the nearby city of Santa Rosa, existing wells will be recharged. This water will be naturally heated in the geothermal reservoir, and be captured by the existing power plants as steam. The project should increase electrical output by 85 MW, enough for about 85,000 homes[51].

Other uses being developed include the use of geothermal resources for water desalination, via an evaporation and condensation loop process. With the increasing requirements for energy intensive applications (standard reverse osmosis desalination plants, hydrogen fuel development) and a preference for sustainable and clean energy sources, there is increasing scope for the use of geothermal energy in many applications.

Environmental Issues for Geothermal water:

Geothermal fluids contain a variable quantity of gas, largely nitrogen and carbon dioxide with some hydrogen sulfide and smaller proportions of ammonia, mercury, radon and boron. The amounts depend on the geological conditions of different fields.

Most of the chemicals are concentrated in the disposal water which is routinely re-injected into drill holes and thus not released into the environment. The concentrations of the gases are usually not harmful, and the removal of e.g. hydrogen sulphide from geothermal steam is a routine matter in geothermal power stations where the gas content is high.

The range in CO2 emissions from high-temperature geothermal fields used for electricity production in the world is 13–380 g/kWh, whereas the CO2 emissions are 453 g/kWh for natural gas, 906 g/kWh for oil and 1042 g/kWh for coal. Sulfur emissions are also significantly less for geothermal than for fossil fuel electric power stations [55].

The gas emissions from low-temperature geothermal resources are normally only a fraction of the emissions from the high-temperature fields used for electricity production. The gas content of low-temperature water is in many cases minute, as in Reykjavik (Iceland) where the CO2 content is lower than that of the cold groundwater. In sedimentary basins, such as the Paris basin, the gas content may be too high to be released. In such cases the geothermal fluid is kept under pressure within a closed circuit (the geothermal doublet) and re-injected into the reservoir without any de-gassing taking place. Conventional geothermal schemes in sedimentary basins commonly produce brines which are generally re-injected into the reservoir and therefore never released into the environment (CO2 emission zero). Geothermal utilization has reduced CO2 emissions in Iceland by 1.9 million tonnes/a compared to the burning of fossil fuels. The total release of CO2 in Iceland is 2.2 million tonnes/a. The reduction has significantly improved Iceland's position globally in this respect. Many countries could reduce their emissions significantly through the use of geothermal energy [52].

2.2.2 Water Desalination systems using renewable energy resources

The origin and continuation of mankind is based on water. Water is one of the most abundant resources on earth, covering 75% of the planet's surface. However, approximately 97% of the earth's water is salt water in the oceans, and just 3% is fresh water. This small percentage of the earth's water, which supplies most of human and animal needs, exists in ground water, lakes and rivers. The only nearly inexhaustible sources of water are the oceans, which, however, are of high salinity. Thirty percent of all fresh water is underground, most of it in deep, hard-to-reach aquifers. Lakes and rivers together contain just a little more than 0.25% of all fresh water; lakes contain most of that. It would be feasible to address the water-shortage problem with seawater desalination; however, the separation of salts from seawater requires large amounts of energy which, when produced from fossil fuels, can cause harm to the environment. Therefore, there is a need to employ environmentally friendly energy sources in order to desalinate seawater[14].

Renewable energy provides a variable and environmental friendly option and supports national energy security at a time when decreasing global reserves of fossil fuels threaten the long-term sustainability of the global economy.

The integration of renewable resources into desalination and water purification is becoming increasingly attractive. This is justified by the fact that areas of fresh water shortages have plenty of solar energy and these technologies have low operating and maintenance costs [57].

Man has been dependent on rivers, lakes and underground water reservoirs for fresh water requirements in domestic life, agriculture and industry. Approximately 70% of total water consumption is used by agriculture, 20% is used by the industry and only 10% of the water consumed worldwide is used for household needs [57].

Less than 1% of fresh water is within human reach. Despite technological progress, renewable fresh water reserves on earth will be only 0.3% of the world water. Agriculture uses two-third of available fresh water.

The proportion of irrigated surface was expected to increase by 1/3 in 2010 and by 50% in 2025. Industrial and domestic water use increases at twice the rate of population increase [59]. However, rapid industrial growth and the worldwide population explosion have resulted in a large escalation of demand for fresh water, both for household needs and for crops to produce adequate quantities of food. Added to this is the problem of pollution of rivers and lakes by industrial wastes and the large amounts of sewage discharged. In total, water demand doubles every 20 years, so that the water emergency situation is certainly very alarming [58].

Desalinize in general means to remove salt from seawater or generally saline water. According to World Health Organization (WHO), the permissible limit of salinity in water is 500 parts per million (ppm) and for special cases up to 1000 ppm, while most of the water available on Earth has salinity up to 10,000 ppm, and seawater normally has salinity in the range of 35,000–45,000 ppm in the form of total dissolved salts [60].

Desalination processes require significant quantities of energy to achieve separation of salts from seawater. The dramatic increase of desalinated water supply will create a series of problems, the most significant of which are those related to energy consumption and environmental pollution caused by the use of fossil fuels. Renewable energy provides a variable and environmental friendly option and national energy security at a time when decreasing global reserves of fossil fuels threaten the long-term sustainability of global economy. The integration of renewable resources in desalination and water purification is becoming increasingly attractive.

Production of fresh water using desalination technologies driven by renewable energy systems is thought to be a viable solution to water scarcity in remote areas characterized by lack of potable water and conventional energy sources like heat and electricity grids. Worldwide, several renewable energy desalination pilot plants have been installed and the majority has been successfully operated for a number of years. Virtually, all of them are custom designed for specific locations and utilize solar, wind or geothermal energy to produce fresh water. Operational data and experience from these plants can be utilized to achieve higher reliability and cost minimization. Although renewable energy powered desalination systems cannot compete with conventional

systems in terms of the cost of water produced, they are applicable in certain areas and are likely to become more widely feasible solutions in the near future.

Water desalination is feasible using different techniques that can be generally classified into two categories:

1. Thermal process: In this technique, a thermal energy resource is being used in order to desalinate the seawater. This thermal energy might be acquired from conventional resources such as fossil fuel sources, nuclear energy, etc. or from non-conventional (Alternative) resources such as solar, geothermal, wind or marine (wave, tidal) energy.

The operating principle of thermal processes entails reusing the latent heat of evaporation to preheat the feed while at the same time condensing steam to produce fresh water. The energy requirements of these systems are traditionally defined in terms of units of distillate produced per unit mass (kg) of steam or per 2326 kJ heat input which corresponds to the latent heat of vaporization at 73 ◦C [59]. Commercial desalination processes based on thermal energy are multi-stage flash (MSF) distillation, multiple effect boiling (MEB) and vapor compression (VC), which could be thermal (TVC) or mechanical (MVC). MSF and MEB processes consist of a set of stages at successively decreasing temperature and pressure. The MSF process is based on the generation of vapor from seawater or brine due to a sudden pressure reduction when seawater enters an evacuated chamber. The process is repeated stage by stage at successively decreasing pressures. This process requires an external steam supply, normally at a temperature around 100 ◦C. The maximum temperature is limited by the salt concentration to avoid scaling and this in turn limits the performance of the process. On MEB, vapors are generated due to the absorption of thermal energy by the seawater. The steam generated in one stage or effect is able to heat the salt solution in the next stage because the next stage is at a lower temperature and pressure. The performance of the MEB and MSF processes is proportional to the number of stages or effects. MEB plants normally use an external steam supply at a temperature of approximately 70 ◦C. On TVC and MVC, after

initial vapor is generated from the saline solution, this vapor is thermally or mechanically compressed to generate additional production.

The irst MSF planet was built in 1957 in Kuwait. Kuwait is considered a leading country in the production of freshwater from seawater with the MSF technology. The first commercial MSF unit ever installed was 40 years ago at Shuwaikh near Kuwait's harbor. The plant consisted of four units, each with a production capacity of 0.5 MIGD. These were followed by a 1 MIGD capacity unit a few years later. By the mid-1960's, 2 MIGD capacity units became available, and before the end of that decade the 4 MIGD capacity became more common[60].

In 1979, Kuwait was still the world's leading country in use of MSF technology, where the capacity of freshwater production with this technology reached 102 MIGD. Twenty years later (1999), Kuwait has a total of 40 operating MSF units, with a total production capacity of 234 MIGD. This capacity can be increased to 257 MIGD through higher temperature operation [60].

2. Membrane processes: In this process, the high-pressure pumps are mechanically driven or salts contained in the seawater are ionized using electricity. The operating principle of membrane processes invites direct production of electricity from solar or wind energy, which is used to drive the plant. Energy consumption is usually expressed in kWhr/m^3. These are the reverse osmosis (RO) and electro-dialysis (ED) processes. The first requires electricity or shaft power to drive the pump that increases the pressure of the saline solution to a required level. The required pressure depends on the salt concentration of the resource saline solution and it is normally around 70 bar for seawater desalination. ED also requires electricity for the ionization of water which is cleaned by using suitable membranes located at the two appositively charged electrodes. Both of RO and ED are used for brackish water desalination, but only RO competes with distillation processes in seawater desalination [61].

The projects which are in operation using RO for desalination are as below:

- In Israel at Ashkelon on the Mediterranean coast, the world's largest reverse osmosis plant is producing 320,000 cubic metres of water a day at around possibly $0.50 USD per cubic metre [62].
- In Sindh Province Pakistan the provincial government has installed 382 RO plants out of which 207 are installed in backward areas of Sindh which includes districts of Thar, Thatta, Badin, Sukkur, Shaheed, Benazirabad, Noshero, Feroz, and others while 726 are on the final stage of their completion [63].

They are also some under construction as:

- In China a desalination plant will be built for Tianjin, to produce 100,000 cubic metres of desalinated seawater a day.
- In Spain 20 reverse osmosis plants will be built along the Costas, expecting to meet slightly over 1% of Spain's total water needs.
- In Pakistan South Asia's biggest RO plant is Under Construction in Dadu to treat the effluent of RBOD for irrigation and drinking purposes[63].

The dominant processes are MSF and RO, which account for 44 and 42% of worldwide capacity, respectively [64]. The MSF process represents more than 93% of the thermal processes and RO process represents more than 88% of the membrane processes.

As has been introduced in the first chapter, the main aim of this research was to develop a dual geothermal system that uses hot saline water from geothermal reservoirs in Australia and can simultaneously produce fresh water and electrical power. Geothermal energy has been selected as a main source of energy, because geothermal energy is independent of weather contrary to solar, wind, or hydro applications. It has an inherent storage capability and can be used both for base load and peak power plants. However, in most cases, it is more economical to run the geothermal plants as base load suppliers. Geothermal energy, with its proven technology and abundant resources, can make a significant contribution towards reducing the emission of greenhouse gases worldwide. International forecasts predict that the share of renewable energy sources in

the world energy mix will increase very significantly in the new century (to 30–80% in 2100). How large the share of geothermal energy will be in the world energy scenario at the end of the new century is much dependant on the actions of the geothermal community and on the countries leading geothermal development.

2.3 Conclusion

As a results, the benefits of using geothermal energy over other sources of renewable energy are that the geothermal resource

- has the potential to provide clean, reliable and renewable electricity
- is an emerging ‘green’ energy industry [independent of climate; base-load; 98% efficiency on an annual basis]
- supports projects with a small ‘footprint’ , with minimal environmental and visual impacts
- has the potential to help reduce greenhouse gas emissions and improve energy efficiency. [Federal Government MRET scheme aims to increase energy generated from renewable sources to 20% by 2020]
- industry development will promote development in rural and regional centres [44]

In the next chapter the geothermal resources in Australia will be introduced and different technologies for utilizing these resources will be discussed to develop the most efficient suitable method for simultaneously producing electricity and fresh water from Australia’s geothermal resources.

Chapter 3 Geothermal energy in Australia

3.1 Introduction

Geothermal energy has not until now played a significant role in Australia's energy mix, nor has Australia been significantly involved in the global geothermal community. In the last decade however, interest in geothermal energy has increased significantly due to the combination of two major drivers. Firstly, further research into Hot Rock (HR) and Hot Sedimentary Aquifers (HAS) resources has provided a better understanding of Australia' large geothermal potential. Secondly, the imminent risks posed by climate change and the need to reduce Australia's carbon footprint are increasingly being reflected in government policy [65].

Australia's vast HSA and HR resources have the potential to provide secure renewable base load power for the future. Preliminary work carried out by Geoscience Australia has suggested that by extracting 1% of the available geothermal energy that exists between a maximum 5km depth and the upper depth at which a temperature of 150 °C occurs could yield approximately 1.2 billion petajoules which is equivalent to 26,000 times Australia's primary electrical energy usage over the 2004-2005 financial year[66].

It is envisioned that there is a proof of concept HR development in Australia in early 2009. A report prepared for the Australian Geothermal Energy Association suggests that the Australian geothermal energy industry could provide up to 2,200 megawatts of base load capacity by 2020, with the cost of generating electricity from geothermal resources moving rapidly down the cost curve to approximately $90 per megawatt hour for commercial scale plants by 2020 [65].

3.2 Australia's geothermal energy resources

The accessible geothermal energy in Australia exists in two forms, which present different technical and economic opportunities and challenges.

3.2.1 Hot rock

The first type is Hot Rock (HR), which includes Hot Fractured Rock (HFR) and Hot Dry Rock (HDR). HR resources are found mainly in high heat producing granites. These granites accumulate heat from the decay of radioactive elements or from the absorption of heat from material below. The temperature of these granites can reach 250°C at economically drillable depths. These deep resources generally require stimulation to have sufficient connected permeability to constitute a viable reservoir. As a result, geothermal projects of this type will need careful development optimisation in order to be economically viable, especially when located in remote regions. Figure 3-1 illustrates the concept of a power plant harnessing HR geothermal energy.

A feature of the Australian HR resources, as exemplified in the Cooper Basin on the border between Queensland and South Australia, is extremely high fluid pressures. It is not yet clear whether this will apply in other locations in Australia. Similar pressures have not been encountered in other HR projects elsewhere in the world. This is a positive feature since it means that wells will self-discharge and no fluid must be added, but it does present some unique challenges for well and surface plant design.

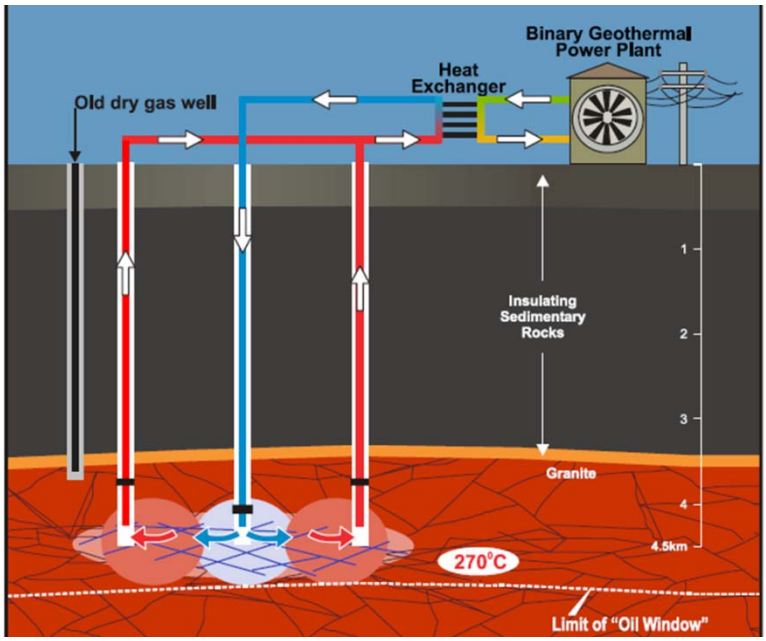

Figure 3-1 HDR system

The HR geothermal resource in Australia is poorly understood, in terms of location, quality and yield potential, due to a lack of accurate data on temperature and stress regimes at the depths in question. Known HR areas exist in the Cooper Basin and in Western Australia and Tasmania, but further exploration is needed[47].

Although there has been considerable research into the use of engineered geothermal systems (EGS) applied to HR resources over the past 35 years, notably in Europe, the USA and Japan, nowhere have such systems yet been brought into commercial production. There are technical, economic and other challenges to overcome. In many respects, Australia is now leading the world in developing and commercialising this technology and as such, is breaking new ground with limited relevant overseas experience to draw on.

3.2.2 Hot sedimentary aquifers

Hot Sedimentary Aquifers (HSA) are closer to 'conventional' forms of geothermal energy in that they exhibit naturally convective fluid systems. HSA resources tend to be shallower and cooler than the HR systems, but will yield large volumes of hot water without stimulation. The only existing geothermal power plant in Australia, at Birdsville in Queensland, uses HSA.

The Great Artesian Basin (GAB) is the world's largest artesian groundwater basin, underlying about 22 percent of the Australian continental landmass (see Figure 3-2). Groundwater from the GAB comes out at wellheads at temperatures ranging from 30°C to 100°C and, in most cases, has to be cooled before it can be used as town or stock water. The sheer size and temperature of the underground water resource makes it an attractive geothermal target [67].

The challenges in these systems are more economic, requiring incremental technological development rather than major technological breakthroughs. HAS systems are being brought into production around the world, and there is a good deal of technology development taking place upon which Australia can draw. Initial estimates from our industry partner for one of their sites shows the source temperature to be around 130°C with a geothermal fluid flow rate of around 20kg/s. Such a site with heat sink

temperature of 30 to 40°C would have a potential to deliver around 7MW of thermal energy rate.

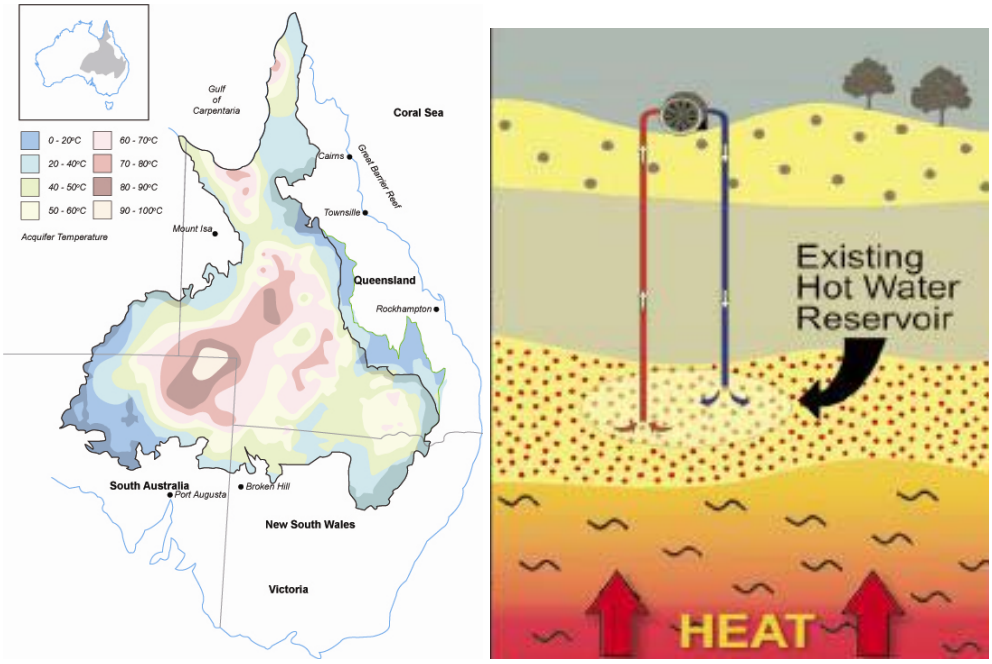

Figure 3-2 Ground Water Temperatures in the GAB and a typical HAS system

Both HR and HSA geothermal energy are generally classed as renewable energy sources on the basis that when extraction of heat ceases, the resource regenerates, albeit at different time scales in different geological contexts.

3.3 The Potential for Geothermal Energy in Australia

Australia's geothermal energy resources have the potential to become a significant source of secure, renewable and low-emission base load power for the future. Preliminary resource evaluation work has suggested that extracting just one percent of the energy from rocks hotter than 150°C and shallower than 5,000m would yield approximately 190 million PJ of energy or about 26,000 times Australia's primary power usage in 2005 [68].

To date, geothermal energy has played a minimal role in Australia's energy mix, with only one small remote plant in operation in Birdsville, Queensland. During the last decade, however, interest in geothermal energy has increased significantly because of

two major factors. Firstly, research into Australia's geothermal resources has provided evidence that electricity generation from geothermal sources is possible in Australia. Secondly, the challenge posed by climate change has become a significant driver for policy development by Australian governments at all levels [69].

As a result, there has been significant growth in the number of private sector companies seeking to produce geothermal energy in Australia. Industry is confident that there could be a:

- proof of concept Hot Rock (HR) development in Australia by 2008, and demonstration of the capacity for commercial power generation by 2012.

3.3.1 Potential new uses for geothermal energy

There are a number of conceivable uses for geothermal energy, supplementary to direct electricity generation. Several of these have already been adopted elsewhere in the world, but not yet in Australia. These additional uses can be broadly divided into three separate topics:

• Direct use: resource then used in recreation, agriculture, & industry;

• Geothermal Heat Pumps: involving drilling merely tens of metres – resource then utilised for building heating & cooling; and

• Secondary use: involving the use of geothermal energy, already utilised in electricity generation, for additional direct use type applications.

- Direct use

Further investment and development may occur in Australia especially within the direct use applications of geothermal resources to enhance agricultural and aquaculture productivity and, with the expansion of geothermal resource utilisation (including space heating/cooling applications), in new building projects.

As a means to assist Australia's increasing efforts to reduce its carbon emissions, there is potential for the direct use of low temperature geothermal hot water for drying coal, prior to its combustion during electricity generation. As an example, it is believed that water temperatures of around 150 °C may be available at depths of 3 to 4 km in

Victoria's Latrobe Valley. This resource could be utilised to dry coal at existing brown coal fired power stations in the vicinity, a process that increases the coal's efficiency in energy release during combustion, ultimately lowering the absolute requirement for coal combustion [70].

The envisaged coal drying process was originally intended to utilise condenser water as the source of energy to heat air that in turn would be used to dry the coal. Due to the low water temperature, the equipment was going to be very large and expensive. The use of close to 150 °C geothermal source water would drastically reduce the size and cost of coal drying plant, and thereby increase its efficiency. Once proven, this coal drying process could then be retrofitted to existing power stations in the region.

This positive contribution towards reducing greenhouse gas emissions at coal fired power stations would be significant, as it could continue for the remainder of the power station's operational life, which in many cases is expected to be several decades.

A pilot plant and a geothermal bore are required to test the patented coal drying process, and determine its capabilities. Should it prove to be successful, it could be fitted to the existing power stations relatively quickly. Should it prove unsuccessful, the geothermal hot water could still be used for power generation via a Kalina cycle, or other similar technology, if water flows are as high as expected. This scenario allows geothermal heat to start providing solutions to the greenhouse gas problem in the very short term, while other geothermal technologies, such as hot rock, are perfected and brought into commercial operation.

With increasing demands for potable water, the use of geothermal resources for the desalination of water will also be an area of focus. Further development of existing prototypes is expected to allow feasible use of this technology. That could be applied to seawater, if geothermal resources are located close to the coast, or to the hot saline ground waters themselves, provided issues such as subsidence due to fluid withdrawal can be satisfactorily addressed.

Material recovery from geothermal brines remains an intriguing possibility. That has been done on various scales and with various degrees of success elsewhere in the world to recover substances as diverse as dry ice (Turkey), zinc (USA), boric acid (Italy)

sodium and potassium chloride and other salts (Mexico). Gold and lithium have been recovered on an experimental scale. With the complex chemistry and possibly high degree of mineralisation of fluids that may occur in deep Australian HR resources, recovering other minerals or elements may be feasible.

Such projects are unlikely to be the prime driver for geothermal developments in Australia, but could provide a valuable economic boost to otherwise marginal projects.

A significant limitation to recovering minor constituents such as gold from geothermal fluids has been the precipitation of the major constituents such as silica. Preventing silica and other scales depositing on flashing or cooling is however the focus of research for enhancing energy extraction, which could have the synergistic effect of making mineral recovery more feasible.

The different applications for direct-use of geothermal energy vary according to temperature, as illustrated by the Lindal diagram in Figure 3-3[71].

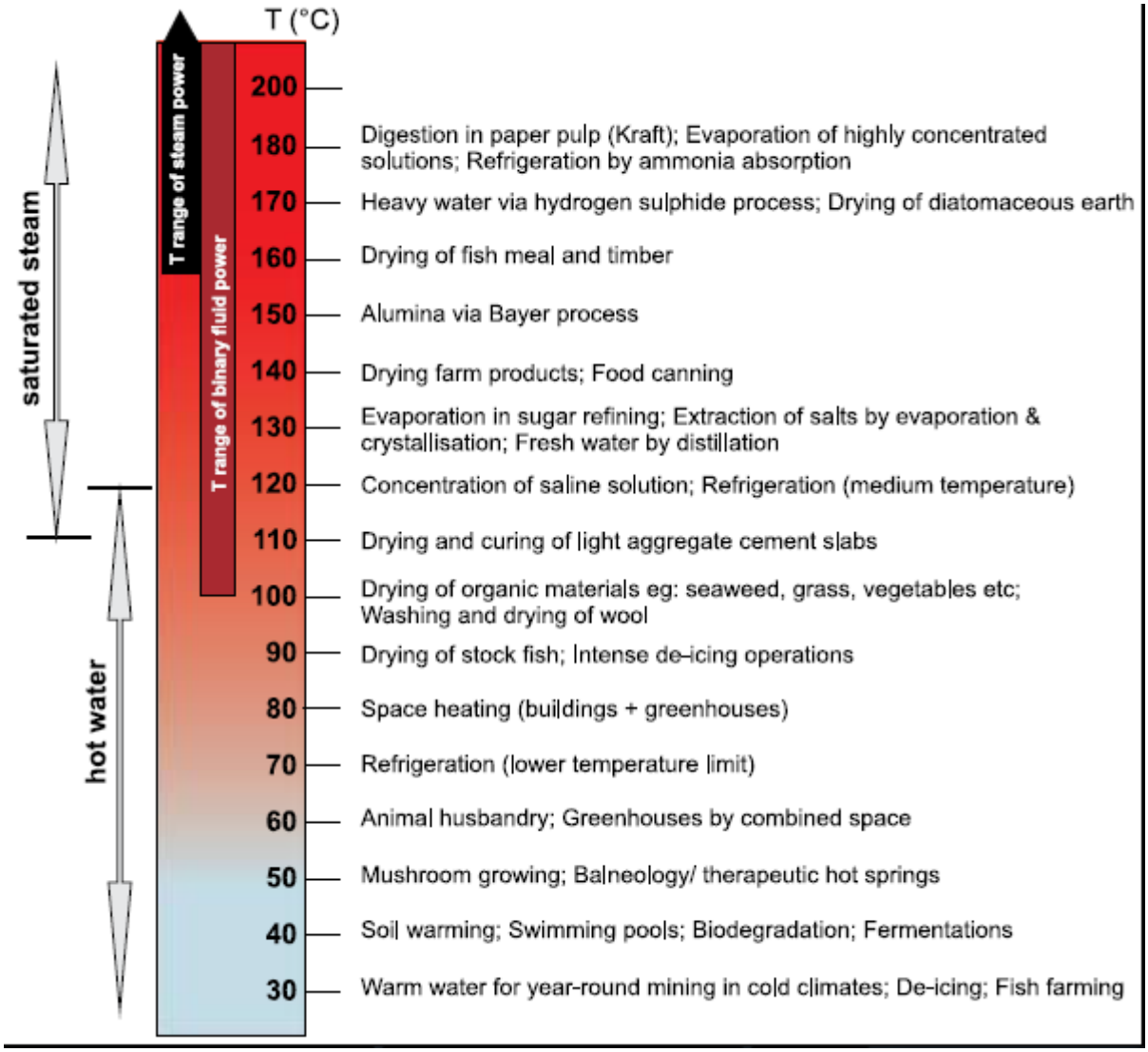

Figure 3-3 Examples of direct use applications for geothermal energy [71]

Direct use is typically associated with lower-temperature geothermal resources (those with temperatures less than 150°C), though some applications may require higher temperatures. In Australia, geothermal heat could be used in agriculture for greenhouse heating or crop drying as well as in aquaculture and space heating. It could also be used for industrial processes such as concrete curing, milk pasteurisation, chemical extraction, refrigeration, drying organic materials (seaweed, grass etc), desalination, wool processing and pre-heating of water in coal-fired power stations. Cascading use, whereby the same water is used in successive processes at progressively lower temperatures, is possible within a single geothermal operation. This can improve efficiency and economic feasibility.

Why use geothermal heat directly?

There are economic, environmental and energy efficiency benefits associated with the direct use of geothermal energy, including:

- Lower heating costs by reducing electricity, oil or gas consumption;
- Reduced emissions of CO2 and oxides of nitrogen and sulphur, by reducing consumption of fossil-fuel-generated electricity;
- Better use of resources, with reduced consumption of a high-grade fuel (such as natural gas) for low-grade heating; and,
- Minimal ongoing costs after installation.

In addition, at the lowest end of the temperature spectrum, ground source heat pumps can be used almost anywhere in the world to provide heating and cooling for buildings [50].

Direct-use of geothermal energy normally requires accessing heated groundwater that is naturally circulating through sedimentary strata or fractured rock (a hydrothermal system, Figure 3-4). This type of geothermal resource is found wherever sufficient quantities of groundwater come into contact with heated rocks. Hydrothermal systems can be high or low temperature depending on the type of heat source and its proximity to the groundwater. High temperature hydrothermal systems with circulating fluids as hot as 350°C are restricted to locations near active or recent volcanism, such as New Zealand or Iceland, and are usually exploited for electricity generation. Hydrothermal systems with fluids less than 150°C are more widespread and are suited to direct-use applications. Heat sources for low-temperature hydrothermal systems in Australia include high-heat-producing basement rocks, or geologically recent volcanic systems [15].

Australia's Great Artesian Basin has large, low-temperature hydrothermal systems, with aquifers containing groundwater that comes to the surface as warm as 98°C. There are likely to be many other locations in Australia where warm groundwater is present and could be used for direct-use applications.

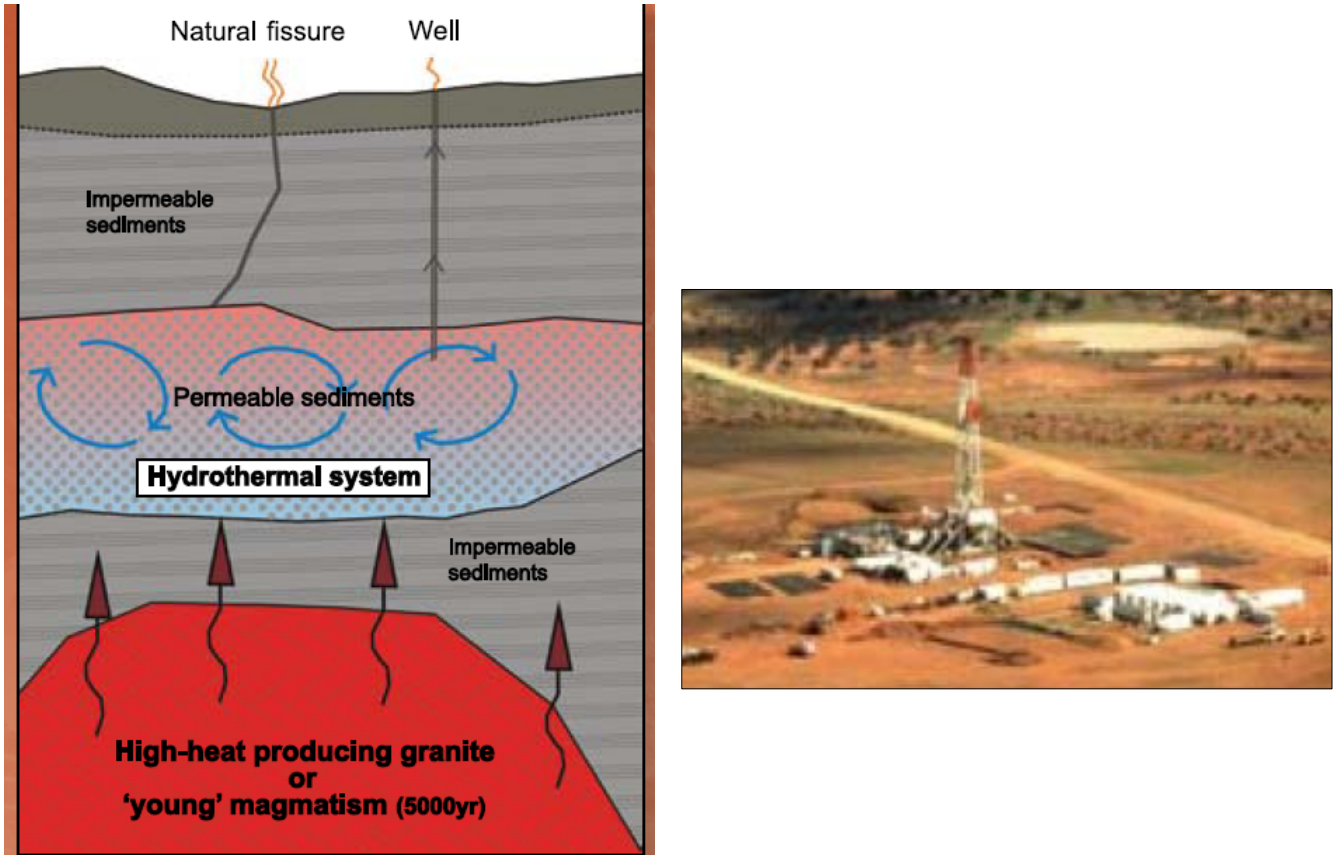

Figure 3-4 Hydrothermal system and Australia's Great Artesian Basin [47]

Heated water or wet steam from a hydrothermal system is extracted through a bore and passed through pipes or coils at the surface to provide energy for a particular process. The cooled fluid is then often recirculated back into the aquifer through a second bore to maintain a sustainable system. In some cases, the warm/hot water may be passed through a heat exchanger to transfer its heat to what is termed a working fluid, which then delivers the heat to where it is required [47].

- Geothermal Heat Pumps

Geothermal heat pumps (GHPs), are devices used to provide heating and cooling (air conditioning) of buildings. The technology requires the transfer of heat between the building and the ground or groundwater. GHP's do not rely on elevated or anomalous geothermal temperatures and hence do not have the same geographic restrictions that apply to geothermal electricity generation and direct use applications and, unlike hot dry rock technologies, GHPs are currently economically attractive. The use of GHPs is growing, particularly in areas with continental climates where there are large temperature

variations between summer and winter. In the year 2000, there were around 2,000 geothermal heat pumps operating in Australia. Typical unit sizes range from 5 to 20 kW for domestic use, and in excess of 150 kW for commercial or institutional installations. GHPs rely on the relatively constant temperature of the Earth and the groundwater present within 100 m of the surface [47]. In areas with continental climates the Earth is warmer than the overlying atmosphere in winter and cooler in the summer. GHPs take advantage of this situation by transferring heat stored in the Earth into a building in winter, and transferring it back into the ground in summer. The Earth is therefore a heat source in winter and a heat sink in summer. GHPs are technically simple, comprising an earth connection subsystem (usually a series of pipes or loops buried in the ground), a heat pump, and a distribution subsystem which is typically a conventional ducted system that moves heated or cooled air throughout the building. There are number of alternative arrangements for exchanging heat with the Earth, "ground-coupled heat pumps" operate in a "closed-loop" configuration, whereby water is recirculated through pipes buried in the ground. The transfer of heat is improved if the loop is immersed in water and hence efforts are often made to ensure that the closed loop is below or partially below the water table. The less common Groundwater Heat Pumps operate in an "open loop" arrangement, pumping groundwater through the unit.

Ground source heat pumps typically circulate fluid through a shallow closed-loop piping system in the earth or a water body (Figure 3-5), to use the relatively constant temperature of the rocks or water as a heat source or a heat sink. High temperatures are not needed, and these systems can be applied almost anywhere. In winter, cold liquid pumped into the ground absorbs heat from the surrounding rocks, and the warmed liquid that is returned to the surface can be used to heat buildings. Conversely, warm liquid pumped into the ground in summer will lose heat to the relatively cooler surrounding rocks, and can be used to cool buildings [72].

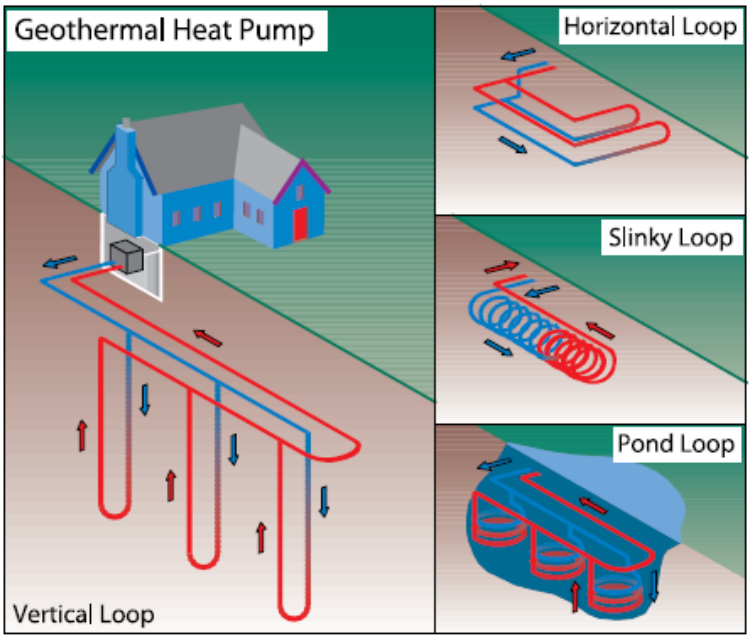

Figure 3-5 Various closed-loop configuration of ground source heat pumps

When the temperature difference between the ground and air temperatures is at a maximum, which usually occurs at the height of summer and winter, the ground source heat pumps run most efficiently and provide the greatest potential for cooling or heating. The example has been shown in Figure 3-6.

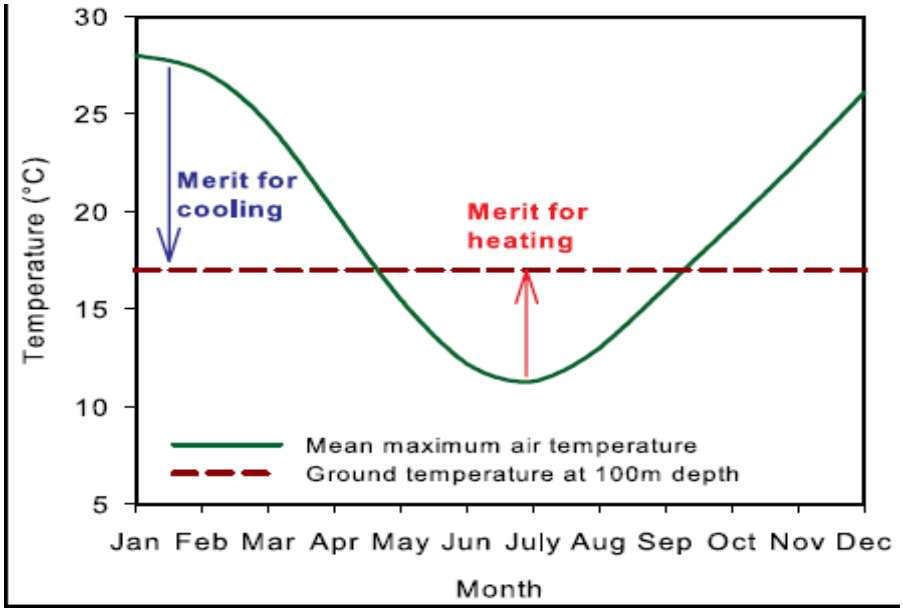

Figure 3-6 Seasonal air temperature variations in Melbourne compared to ground temperature at 100 meter depth [73].

Although ground source heat pumps are electrically-powered, they are used only to move heat, not to produce heat. As a result, they are energy efficient and usually have Coefficients of Performance (a measure of energy efficiency) greater than three. This means that for every unit of electrical energy consumed, three units of energy are delivered in the heating or cooling process.

- Existing direct-use applications in Australia

Direct-use of geothermal energy in Australia currently includes building and district heating systems (eg: Portland, Victoria), spa developments (Mornington Peninsula, Victoria and Mataranka, Northern Territory), artesian baths (Moree, Lightning Ridge artesian baths, and Pilliga Hot Artesian bore, inland New South Wales) and swimming pool heating (Challenge Stadium, Western Australia) [70]. Geothermal heat pumps have been installed in several locations, including at Geoscience Australia's office building in Canberra, the Integrated Energy Management Centre and the Antarctic Centre in Hobart, and the Hobart Aquatic Centre.

Using up to 75% less electricity than conventional systems, Geothermal Heat Pumps (GHPs) are a cost-effective and highly efficient alternative for space heating, cooling, and water heating in various building applications. GHPs operate reliably and quietly, providing better humidity control and improved zone-level temperature control than conventional forms of building heating and cooling.

GHPs achieve this high level of energy efficiency by using the ground rather than ambient air as a heat source and sink, as ground temperatures are lower than the air temperature during summer and warmer during winter.

In non-residential buildings, GHPs typically save 15% of total building energy use; in residential buildings savings can be as high as 45%. In a US study involving 4000 houses retro-fitted with GHPs, annual electrical energy savings of approximately 6,400 kWh per house or 32% were recorded. Summer peak electric demand for the area was reduced by 6.7 MW, or over 40% [71].

In Australia, GHPs have been installed at several non-residential locations, including Geoscience Australia's office building in Canberra, the Integrated Energy Management Centre and the Antarctic Centre in Hobart, and the Hobart

Aquatic Centre. Direct Exchange (DX), refrigerant-based, closed-loop GHP systems are now available in Australia, which can offer benefits in terms of the width and depth of the required drilling. Australia's current GHP capacity is estimated to be 5.5 MWth or 10 GWh/yr.

- Secondary use

In addition to its utilisation as a source of energy for electricity generation, a geothermal resource has the potential to be utilised for any number of secondary or tertiary applications, such as those described in the sections immediately above.

However, with water being such a scarce commodity throughout Australia, it would require substantial planning of the geothermal production to re-injection loop, in order to ensure that the optimal utilisation of the resource is realised.

3.4 The geothermal sector in Australia

The geothermal industry in Australia is presently in a phase of resource exploration and is yet to demonstrate proof of concept of sustainable commercial power generation. The technical proof of concept requires the successful circulation of thermally conductive fluid through the underground heat exchanger, transfer of that heat energy to the surface and then successful operation of an above ground heat exchanger and use of the extracted heat energy to drive power generating plant, such as a steam turbine. Commercial proof of concept, such as is required to attract project finance, would require demonstration that the long run marginal costs associated with the development and operation of such a power plant are competitive, given whatever support mechanisms may be in place, with plant using conventional generation technologies and that the longevity of the heat resource is demonstrated to be sufficient to provide a return on the investment in the form of interest and capital repayment.

In anticipation of the potential to demonstrate proof of concept, the first Geothermal Exploration Lease (GEL) was granted in Australia in 2001. Nationally, 33 companies have applied for 282 licences with work programs investment over the period to 2002-13 estimated by the industry to be worth $832 million[69]. Much of this effort is focused on HR resources. The largest share of the geothermal activity is occurring in South Australia, where 22 companies hold 223 licenses with an estimated related work program of $667 million. Of the 33 companies with exploration licenses in Australia, ten are listed on the Australian Stock Exchange [69].

Only a small number of geothermal companies have commenced drilling and exploration. Of the geothermal companies that have commenced drilling, there are two companies that have announced they intend to develop demonstration plants within the next 5 years.

3.5 The cost of geothermal electricity generation in Australia

In traditional Australian power economics, coal has proved to be the most financially viable resource for base load generation, and gas for use in the intermediate and peaking generation roles. Australian Government policies such as the Renewable Energy Target, for twenty percent of Australia's electricity generation to come from renewable sources by 2020, representing an additional 45,000 gigawatt hours, and the Carbon Pollution Reduction Scheme, will significantly improve the economic case for renewable energy in Australia, including geothermal energy [69].

A number of recent studies have sought to estimate the cost of renewable energy generation.

McLennan Magasanik Associates (MMA) (2006) noted that:

• A number of new technologies can provide emission abatement competitively for base load power at $30/tCO2e post 2020.

• Some of these resources such as geothermal may be limited by transmission cost and available resources.

• Coal with carbon capture can compete with nuclear for base load generation on currently projected cost profiles.

• Gas in NSW and Victoria and brown coal IDGCC in Victoria can compete for intermediate roles.

• Other renewables (PV, solar thermal) should be able to compete if the full cost of carbon emission exceeds $40 tCO2e.

A 2008 report for the Australian Geothermal Energy Association, also by MMA, suggested that the cost of generating electricity from geothermal resources is expected to move rapidly down the cost curve through to 2020 – through learning, experience and economies of scale outcomes commencing at around $120 /MWh at small scale (10 MW to 50 MW) and decreasing to around $90/MWh at large scale (300 MW or greater) by 2020 [66].

A 2006 MIT study concluded that an industry learning curve will drive down the cost of geothermal generation in the US through deployment of a series of modest sized binary power plants. The modelling suggested that geothermal generation would be cost competitive with 100 MWe installed at US$0.060/kWh (AUD$67/MWh at AUD$=90c). Over 10 years, with the installation of a total of 200 MWe, the cost was modelled to drop to US$0.045/kMh (AUD$50/MWh).

In its 2007 annual planning report, the Electricity Supply Industry Planning Council (ESIPC) calculated the cost of geothermal generation to lie in the region of $70 - $130/MWh [66].

3.6 Challenges for geothermal energy development in Australia

Both HR and HSA differ from the kinds of geothermal energy developments seen overseas, as Australian resources require deep drilling to access and are not associated with magmatic activity. There is, however, much valuable knowledge available worldwide in 'conventional' geothermal developments, and to a lesser extent in HSA developments, but the nature of Australia’s geothermal resources means that not all of it is directly applicable.

These differences suggest that the industry will face more technical challenges and probably lead to larger calls on funding in the HR type of system than the HSA type. However, for both types of system there is also considerable work required on resource location and definition.

There are also a number of non-technical barriers and constraints to exploitation of Australia's geothermal energy as a commercially viable renewable energy source. These constraints range from availability of resources to undertake exploration and scheme implementation (financial, labour, engineering, scientific, technical and equipment such as drilling rigs) through to environmental, cultural, energy market and fiscal barriers. In the Australian context, there may be significant regulatory challenges in the future usage of HSA resources, as water rights are tightened in response to drier conditions in many areas.

There are overlaps between technological and other constraints that cannot be divorced. Some problems such as the need for development of improved down hole packers and measurement tools are straight technical constraints that will have to be overcome for the industry to be feasible. Other requirements, such as improving power plant efficiency are not absolute technical constraints, but are improvements that will change the economic feasibility of projects and so have a large effect on what can be considered economically viable resources.

Other issues are necessary for the proof of concept of geothermal energy in Australia. For example, the industry is confident of the technical feasibility of generating power from HR, but the financial market will respond more strongly once an HR demonstration project proves its practicality.

In practical terms, all of these constraints will require some technological development to overcome.

3.7 Current technologies utilizing geothermal energy in Australia

Several different plant types have been used for geothermal electricity generation worldwide, with the most appropriate type depending on the specific fluid characteristics. Generally speaking, the capital, and, to a lesser extent, the operating costs will increase, in a more than linear fashion, as the enthalpy of the resource decreases.

There are also some economies of scale in geothermal power plants,al though once over a certain size, plants effectively become modular and further economies are limited. That point will be at approximately 100 MWe for condensing steam turbines, and 10 MWe for binary plants. This is by no means a hard and fast relationship, and there are notable exceptions.

3.7.1 The potential of different power plant types in Australia

3.7.1.1 Steam turbines

Initially, electricity generation from natural high temperature resources was mainly produced by conventional condensing steam turbines. These systems still represent the largest proportion of generation worldwide and remain the lowest cost option per MWe at sizes generally above 10 MWe, provided the resource characteristics are suitable, which will rarely be the case in Australia. Condensing steam turbine plants require a supply of relatively high pressure steam, which implies a high reservoir temperature (generally over 240 °C unless dry steam is present), abundant fluid, and the use (in this part of the scheme) of the flashed fraction only. In a sense these plants work by “high grading” the resource, and so coupled with factors such as very shallow wells, have permitted the use of geothermal generation in the face of extremely low electrical energy prices in countries such as New Zealand. However, this will not be the case in Australia where, due to the nature of the resources, the economics of geothermal generation are more marginal [65].

Condensing steam plants are typically used for resource temperatures in excess of 175°C. If boiling water at 175°C is flashed down to a pressure of 2 bar (abs), the steam fraction is only 10.7 % by weight.

Australian hydrothermal resources generally do not provide the high fluid temperatures required for economical use of steam Rankine cycle generation.

There are several experienced and competent providers around the world for steam-turbine-based geothermal power plants and component equipment. Unit sizes are typically in the 20-80 MWe range, but are offered from less than 5 MWe up to 110 MWe [69]. Most often such plants use direct contact condensers with evaporative wet cooling towers, and surplus condensate going to reinjection wells. Again this will not be appropriate for use in arid areas in Australia where there is a requirement for full injection. Such systems can be air cooled, but this results in a significant loss of efficiency. Research and development is needed, possibly including diurnal thermal storage.

Incremental improvements in efficiency will be carried out by plant manufacturers, principally Japanese, as part of the normal course of commercial development. Apart from the cooling circuit (which is common to any power plant type) there are no particular technology developments on steam turbines required for use in Australia and therefore no technological development on this power plant type has been recommended in the Roadmap.

3.7.1.2 Binary plants

Binary plants utilise a secondary working fluid, usually an organic fluid (typically n-pentane: hence the name Organic Rankine Cycle or ORC), that has a low boiling point and high vapour pressure at low temperatures when compared to steam. The secondary fluid is operated through a conventional Rankine cycle: the geothermal fluid yields heat to the secondary fluid through heat exchangers, in which the secondary fluid is heated and vaporises; the vapour produced drives a normal axial flow turbine, is then cooled and condensed, and the cycle begins again. The schematic is shown in Figure 3-7.

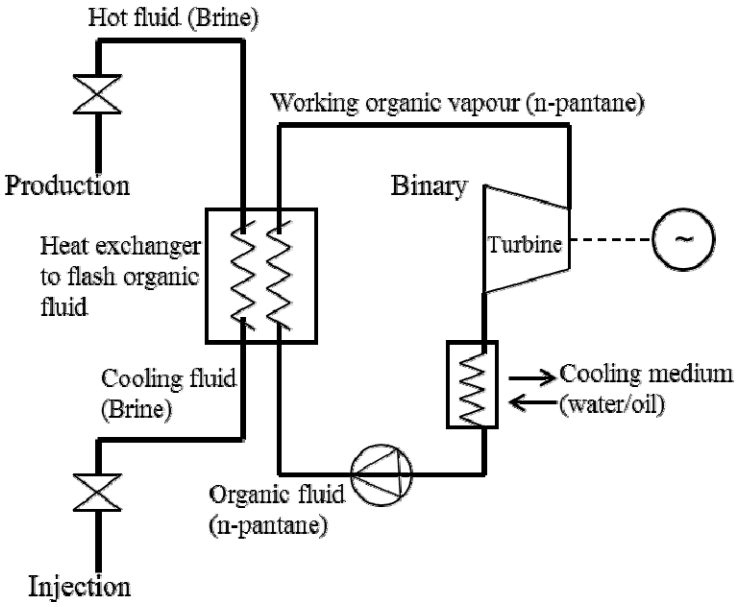

Figure 3-7 Schematic of geothermal binary power plant in Birdsville

The most common type of geothermal binary plant uses a hydrocarbon working fluid, as at Birdsville. Such plants are available from several manufacturers worldwide, of which the largest and best known is an Israeli/USA company, OrmIndustries, though there are other suppliers in Europe and the USA. Many hundreds of MWe of these plants have been installed worldwide, sometimes in combination with back pressure steam turbines. The standard Ormat configuration is to use air cooling which is suited to Australian conditions but may lose efficiency when ambient air temperatures are high. The maximum size ORC turbine, which is commercially available, is about 15 MWe capacity but smaller units are more common and larger plants are built up from numerous smaller modules [70].

3.7.1.3 The Kalina system

A recent variation on the binary plant is the Kalina scheme. The Kalina power cycle is claimed to be a more thermodynamically efficient technology for converting mid to low temperature heat sources into electricity. In simple terms, the Kalina cycle is a Rankine cycle that uses an ammonia-water mixture as its working fluid instead of organic hydrocarbons used in conventional organic Rankine applications. The key points of differentiation of the Kalina cycle are:

• The varying boiling temperature of the working fluid when heated at constant pressure;

• The ability to vary working fluid composition within the cycle and hence optimise heat transfer; and

• The ability to operate more efficiently on low temperature fluids. This makes it of particular interest for HAS projects in Australia, or others where a high degree of efficiency is required.

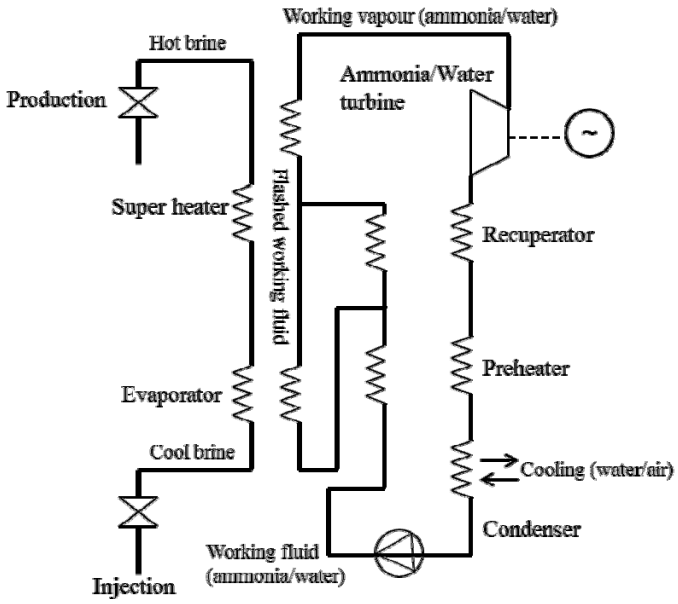

Figure 3-8 Schematic of geothermal Kalina power plant

For the Kalina Cycle, Geodynamics has claimed that the capital cost per kW could be lower than that of a comparable ORC plant. This is largely on the basis of higher efficiency, which increases the power generated from a given amount of input heat. The only public domain data identified was a reference to Exergy's bid price for the Husavik plant being equivalent to US$ 905 /kW (OCEES, 2003). At face value this is a very attractive price, but it must be recognised that this plant has a seawater cooling system with very low water temperature. An air-cooled system in Australia would be significantly more expensive due to the condenser cost, and the higher condensation temperature would reduce the "bottom line" – the power generated from an equivalent sized plant to Husavik. Furthermore, it is possible that the price offering for the Husavik plant may have been particularly keen in order to get the first geothermal Kalina plant

constructed. There are a number of different versions of the general Kalina Cycle, which have different process schemes and hence capital costs.

Since the nature of the constituent equipment items of the two cycles are quite similar, it is to be expected that operating and maintenance costs and issues would be broadly comparable.

Kalina cycle generation is not yet in widespread commercial use. The system is currently more expensive per MWe installed, but whether this translates to being more or less expensive per MWh generated has not as yet been demonstrated, and is the subject of some controversy [68].

In Australia, Geodynamics Limited, through its 25% owned associate Exorka International Limited (EI), has access to the Kalina power cycle technology. EI is a global sub-licensee for the Kalina power cycle technology. EI has exclusive rights in Australia and New Zealand for technology transfer related to Kalina and non-exclusive rights to use the Kalina patents in all countries. EI is working to commercialise Kalina with prospective customers, both in waste heat and geothermal applications. There is one 2 MWe plant in operation in Iceland, and EI is working on delivering a demonstration plant at the San Jacinto geothermal project in Nicaragua [66].

3.7.2 Current geothermal power plant in Birdsville, Australia

Readily accessible geothermal temperatures in Australia are generally too low for economic generation of electricity. Accordingly there are few examples of geothermal electricity generation in Australia. There are however two examples of Organic Rankine Cycle engines (ORC) that have been developed by Enreco Pty Ltd at Birdsville and Mulka Station [65]. The location is shown in Figure 3-9.

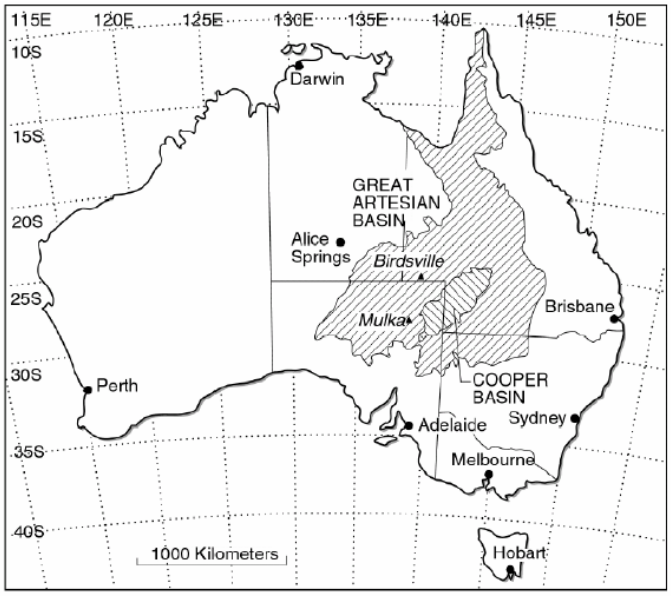

Figure 3-9 Location of geothermal plants in Australia [76]

Mulka Cattle Station is located on the Birdsville Track in northern South Australia. A 15 kW ORC engine was constructed and installed in 1986 with funding provided by the South Australian Government. The plant uses water from a deep bore tapping the aquifers of the Great Artesian Basin. The bore, originally drilled in 1904, is approximately 1300 m deep and produces about 10 L/s of water at 86°C. After use as a heat source for the ORC plant the geothermal water was further cooled and used in the ORC condenser before being used for stock watering purposes [74].

Commissioned in 1986, the ORC plant operated continuously for about three and a half years before the property was sold. It is believed to be the first operational geothermal power plant in Australia. Rated at 15 kW, the ORC plant output declined to about 10 kW during the summer when high ambient temperatures reduced the plant efficiency. The gross electricity conversion efficiency was 8% with a net 6% obtained when parasitic loads were accounted for [67].

Following the successful demonstration of small scale electricity generation at Mulka Station, Enreco Pty, Ltd, installed a similar but larger plant in the town of Birdsville (population 100) in western Queensland. The plant was funded by the National Energy Research and Demonstration Council, an agency of the federal government. Hot water is supplied to the plant from a 150 mm diameter bore drilled to a depth of 1220 m

in the Great Artesian Basin. The bore had been flowing under artesian pressure for 45 years prior to the installation of the ORC plant. Its production rate is approximately 27 L/s at a temperature of 98°C and a shut in wellhead pressure of 1215 kPa. The water is cooled to about 80°C in the ORC heat exchangers and is used in the Birdsville town water supply after use in the plant [74]. Figure 3-10 shows a schematic of the Bridsville power plant and Figure 3-11 shows the station.

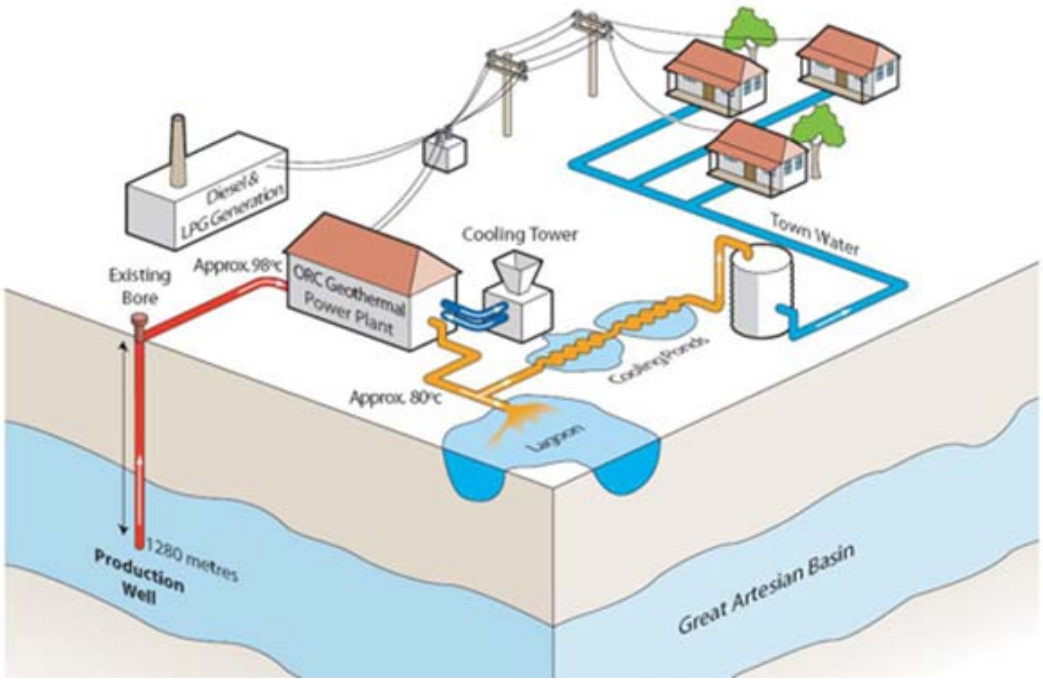

Figure 3-10 Schematic of Birdsville power plant

Figure 3-11 Birdsville power station

The ORC plant commenced operation in 1992. Rated at 150 kW it achieved only a modest net output of about 60 kW and an average parasitic load of almost 40 kW. Following substantial plant modifications in 1999, including the replacement of Freon (R114) by the more environmentally acceptable isopentane, the plant was returned to operation in June 1999 and has been operating successfully, albeit at low efficiency, since that time [67]. Gross plant output is still well short of the rated plant output of 150 kW and overall conversion efficiency is about 6% [74].

The town's peak electricity demand has been estimated as about 250 kW. The ORC plant is able to meet the town's power demand at night and during the winter and it works in combination with a conventional diesel generator at other times. It is understood that the ORC plant has reduced the town's diesel consumption by about 160,000 Litres per year representing an annual fuel saving of $135,000 and a reduction of about 430 tonnes of greenhouse gas emissions each year. The capital cost of the low temperature ORC units has been estimated at about $4000/kW increasing to about $6000 - $7000/kW after production bore refurbishment, water reticulation and civil works are included[75] .

3.8 Geothermal Resource in Victoria

As has been described earlier, geothermal energy in Victoria is derived from natural heat within the earth and can be classified into two categories:

- Hot Dry Rock (HDR), where the direct heat of the rock is used
- Hydrothermal which utilises hot water and steam generated in the ground

Both energy sources can be used for direct heat and power generation.

Victoria has limited Hot Dry Rock resources which are at depths that may currently preclude commercial energy generation. The hydrothermal property of geothermal bores in Victoria has potential for geothermal direct use applications.

Geothermal temperatures in Victoria increase on average between 3 and 4ºC per 100 metres from the surface. Whilst Australia has great potential for developments in the

use of Hot Dry Rocks for energy generation, it does not have many Hot Dry Rock resources [74].

The feature of the geothermal systems in Victoria of most interest is the highly productive aquifers in the unconsolidated basin sediments at depths of up to 1000 metres. These aquifers provide uniformly highly productive geothermal bores.

Applications that take advantage of the geothermal resources in Victoria can be found in the form of geothermal heat pumps, space heating and district heating, bathing and swimming pool heating, aquaculture pond heating, greenhouse heating, industrial uses, cooling and air conditioning, and agricultural drying.

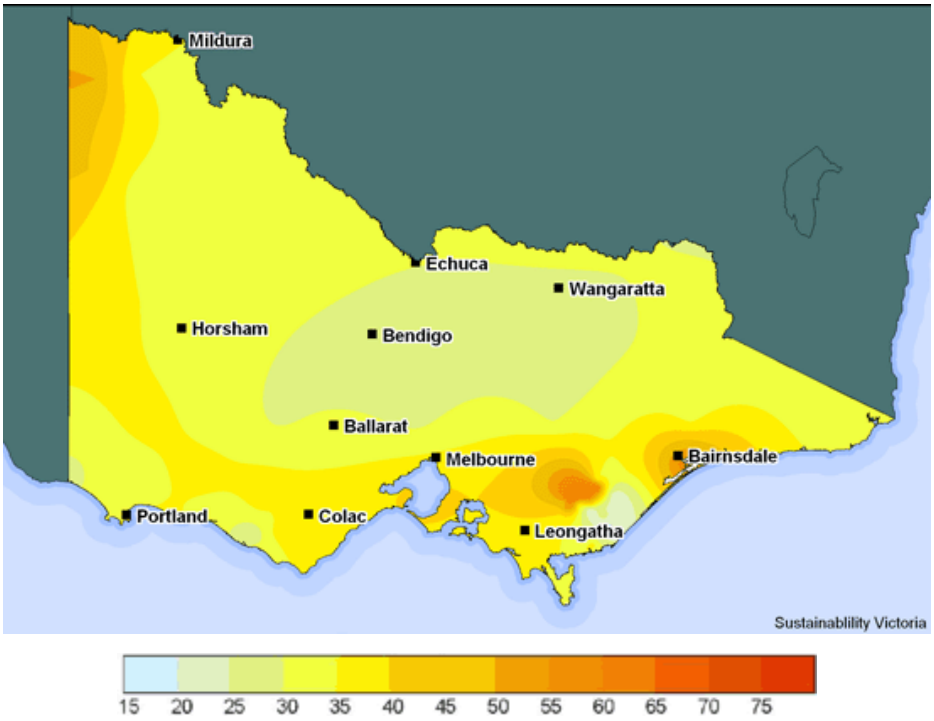

Figure 3-12 Sub-surface temperature at 500m below ground level (degrees Celcius)

The Figure 3-12 shows the temperature below the surface at 500m depth. This resource assessment was developed in partnership with Sinclair Knight Merz and Professor Jim Cull, Monash Geoscope [76].

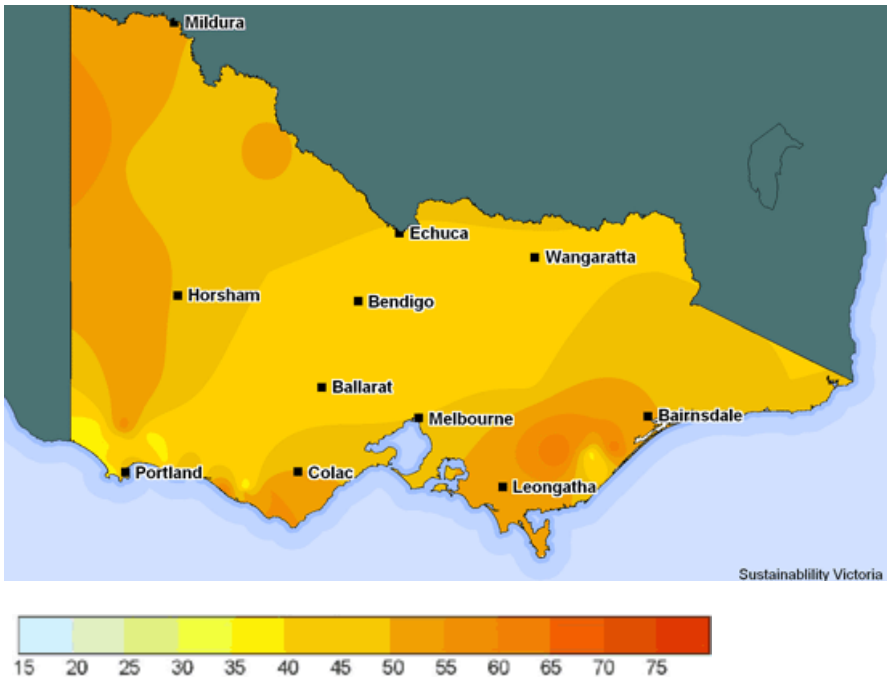

Figure 3-13 Sub-surface temperature at 1000m below ground level (degrees Celcius)

Figure 3-13 shows the temperature below the surface at 1000m depth. This resource assessment was developed in partnership with Sinclair Knight Merz and Professor Jim Cull, Monash Geoscope [76].

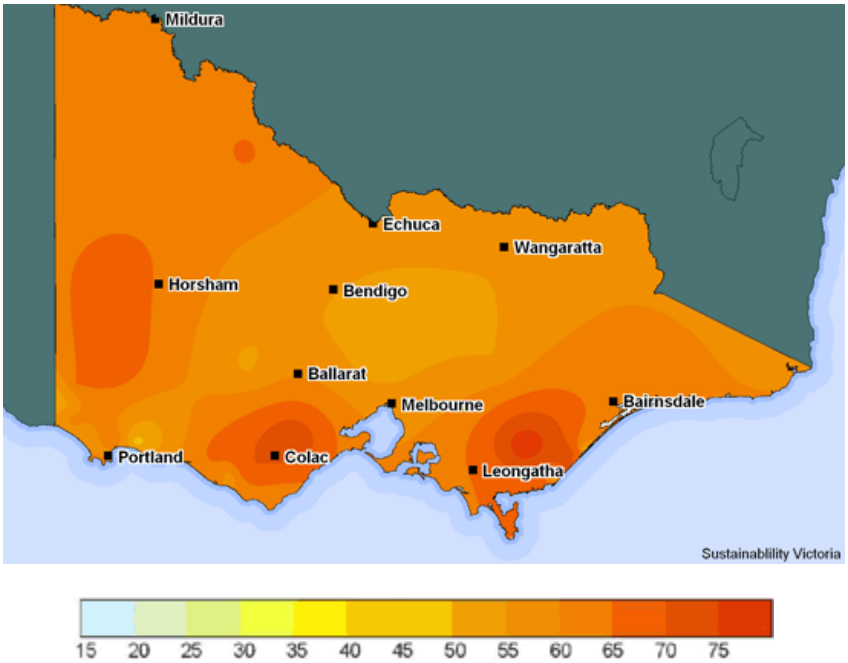

Figure 3-14 Sub-surface temperature at 1500m below ground level (degrees Celcius)

The Figure 3-14 shows the temperature below the surface at 1500m depth. This resource assessment was developed in partnership with Sinclair Knight Merz and Professor Jim Cull, Monash Geoscope [76].

Average geothermal gradients in the sedimentary basins (i.e. the Gippsland, Otway and Murray Basins) were found to be between 3 and 4ºC per 100 m depth which is marginally above the worldwide average background level of 3ºC/100 m. An obvious hot spot in the geothermal gradients appears to be present in the Latrobe Valley in the Gippsland Basin where geothermal gradients are as high as 7.3ºC/100 m. The high gradients are associated with relatively high measured temperatures (up to 70ºC) in bores that are less than 800 m in depth. The reason for this anomaly is not well understood but is believed to be associated with the thick coal measures present at this location. The elevated geothermal gradients are only observed in bores that are less than 800 m deep. At greater depths the temperatures appear to revert to the average geothermal gradient of the Gippsland Basin [76].

The maps of geothermal temperature presented in this section indicate that temperatures between 30 and 60ºC, are present over much of the state at depths of 500 to 1500 m. The feasibility of extracting geothermal waters at these temperatures is strongly influenced by the geology and hydrogeology of the deep sedimentary basins. Experience at drilling deep groundwater bores has demonstrated that substantial volumes of water can be obtained from the aquifers within the thick unconsolidated Tertiary age sediments found in the Gippsland, Otway and Murray basins. Bores that penetrate into the underlying basement rocks rely on encountering fractures and faults in the rock mass to obtain production. Accordingly, the chances of a bore delivering useable quantities of geothermal water from depth depends on whether the unconsolidated sediments extend to sufficient depth for the required temperature. The assessment of geothermal resources in this environment should therefore be accompanied by maps of the surface of the deep bedrock to help define deep drilling targets for production bores.

Geothermal water easily accessible in Victoria can be used for a number of direct uses. The temperature of water easily accessible within 1000 m of the surface over much of the state is ideal for numerous applications, such as space heating, including the

heating of greenhouses, bathing (both in spas and heated swimming pools), aquaculture pond heating and agricultural drying.

The geothermal waters of the Otway Basin are currently being used to great advantage in a district heating scheme in Portland. The system, jointly operated by Glenelg Shire Council and Portland Coast water provides water and space heating to municipal and administrative buildings, swimming pools, hotel and hospital. The scheme has been operational since the early 1980's and has provided substantial savings in fuel costs while at the same time reducing greenhouse gas emissions. It is a clear demonstration of an appropriate use of the resources that are present throughout the entire basin [77].

The temperature of geothermal water within 2000 m of the surface in Victoria is not sufficiently high for generating electricity in a conventional steam turbine. Organic Rankine Cycle and Kalina Cycle electricity generation technologies could possibly be applied in Victoria. However the expected plant efficiencies at temperatures less than 100ºC are so low that such developments are unlikely to be economical. Similarly, geothermal temperatures in that depth region easily accessible by drilling are generally too low to be able to support a successful Hot Dry Rock development under current economic conditions and with currently proven technologies. Local, thermal anomalies identified in the Gippsland and Otway Basins could however represent exploration targets for potential Hot Dry Rock developments [77].

Few bores have been drilled in Victoria for the express purpose of exploring or developing geothermal resources. Most of the deep bores that have been drilled were aimed at minerals and petroleum exploration and production and at defining, monitoring and producing groundwater.

The majority of geothermal temperature data have been obtained from wells drilled in the Otway and Gippsland sedimentary basins. The relatively high concentration of bores and temperature measurements in these areas reflects the location of oil, gas and minerals exploration and the existence of thick, permeable sediments from which substantial quantities of groundwater can be obtained. Deep bores and geothermal temperature measurements are scarce in the Murray Basin reflecting the lack of

petroleum and deep mineral exploration carried out in the region. Similarly, no deep geothermal temperatures have been found in the Central Highland area where thick sedimentary sequences and the potential for deep groundwater production are absent. The absence of deep measured temperatures in the central and northern parts of the state does not necessarily reflect poor geothermal potential [74].

For space heating, hot geothermal water is either circulated directly through the buildings or is used as a heat source for a separate closed-loop heating system, depending on available temperature, flow and water quality.

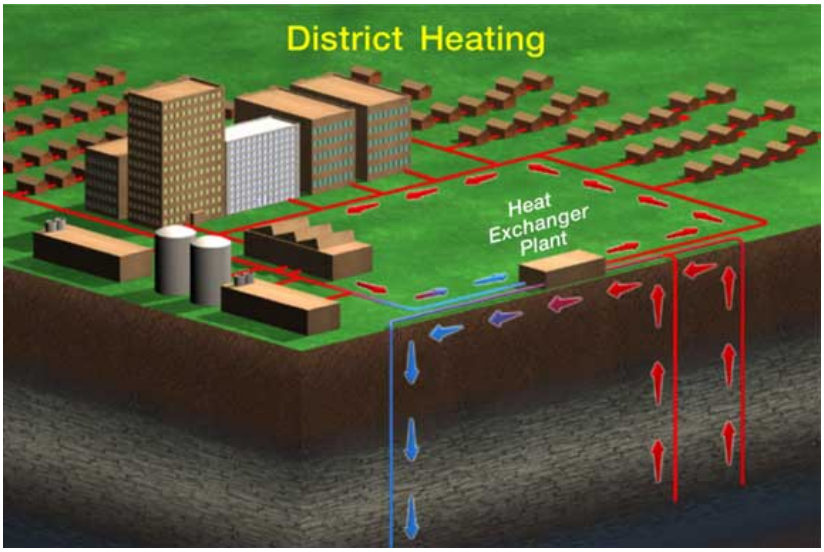

Figure 3-15 District heating system

Space heating and district heating are likely to be more economically attractive in areas where ambient temperatures are low for a substantial proportion of the year. In much of Victoria it is unlikely that space heating would be required for more than a few months each year. Facilities such as hospitals have a more substantial heat demand, however, including hot water. Low-grade heat demand for a modern, integrated health-care facility would be in the range 3 to 4 kWth/bed. A wide range of resource temperatures can be used, but the preferred range would be 70-80°C.

Geothermal hot water is used extensively for hot springs, spas and municipal swimming pools. Depending on water quality and temperature, the geothermal fluid may be used exclusively, mixed with town water, or used as a heating medium for town water. Supplemental heating can be provided to boost final water temperature, where necessary.

Figure 3-16 Hot spring in Portland

The pool temperature for such applications ranges from around 25 to 40 °C. Geothermal fluid temperatures of between 40 and 60°C are commonly used.

The municipal swimming pool at Portland in Victoria has used 58°C geothermal water for heating since 1985. A spa complex to be fed by 47°C geothermal water is currently under construction on the Mornington Peninsula near Melbourne.

Figure 3-17 District heating in Portland

The geothermal resources in the city of Portland have been used to heat a public swimming pool and a number of buildings in the city since the early 1980's. A description of the installed heating facilities and an assessment of the total available energy are presented by King et al.1987 a summary of which is presented in the following paragraphs[78].

Deep groundwater bores, currently owned and operated by Portland Coast Water for the purpose of municipal water supply for the city of Portland, produce groundwater at temperatures between 57 and 60°C. Before reticulation in the city water supply the water is cooled in forced draught cooling towers. Water is extracted from the aquifers of the Dilwyn Formation of the Wangerrip Group at depths ranging between 1200 and 1400 m [78].

Water produced from Portland 14 (also known as the Henty Park Bore) is used for geothermal heating purposes. Drilled in 1982, Portland 14 free flows under artesian pressure at approximately 90 L/s from a production interval between 1254 and 1365 m below ground level. In 1985 it delivered about 22 L/s of hot water to a number of heat exchangers to heat the city's swimming pool complex, arts centre, civic centre, municipal offices (now occupied by the Glenelg Shire Council) and elderly citizen's centre (King et al, 1987). The estimated cost savings associated with the use of geothermal energy for heating in 1985 was approximately $120,000 per year [78].

Since publication of King et al, 1987 [76], the geothermal space heating system has been expanded to incorporate more municipal and private buildings. The geothermal heat is now used in the following buildings:

- Portland and District Hospital
- Police Station
- Fawthrop Centre
- Public Swimming Pool Complex
- Municipal Offices
- CEMA Arts Centre
- Civic Hall
- Library
- Richmond Henty Hotel
- State Emergency Services Offices

 Maritime Discovery Centre.

The system is believed to currently use 60 – 70 L/s of hot water (~58°C) extracted by the Henty Park Production Bore. Unfortunately the production rates and temperatures are not being monitored and hence details of the geothermal water flow and temperature are only estimates.

Water is pumped from the production bore through a 225 mm diameter supply line connecting all of the utilisation sites. At each facility water is extracted from the main via 50 mm and 100 mm diameter offtakes. After heat is removed from the water in the heat exchangers it is pumped into a return line that parallels the main distribution pipe and the used geothermal water is piped back to the Henty Park production bore site where it is cooled further in forced draught cooling towers [76].

Chapter 4 Theoretical study of a novel combined desalination and power generation system using a simple reaction turbine incorporated in a trilateral cycle

4.1 Introduction

Following the introduction of technologies which can be used to produce electricity and fresh water and considering their potential for use in Australia, two of these technologies which are better suited to the available conditions are discussed in the first part of this chapter. Through thermodynamic comparison of these cycles, the advantages and disadvantages of both have been studied in order to select the most efficient one for analysis and as a basis for designing a reaction turbine and a CDP system. In the next section of this chapter, reaction turbines and expanders are introduced and the basis for selecting a simple reaction turbine is discussed. Also the analysis which has been used in design and prediction of power generation and freshwater production based on the previous two sections is discussed in detail.

The next section presents analysis related to designing the simple reaction turbine and heat exchangers for the CDP. In the last section, the methods of defining and measuring the efficiency both of the turbine and the CDP system are discussed.

4.2 Power cycles used in geothermal power plant and the potential for using a trilateral cycle for combined power generation and fresh water production

Conversion of heat to power is a long-standing challenge for which the basic physical principles have been established in the 19th century by Carnot and Rankine [79]. Presently, there is rapidly growing interest in technologies for conversion of heat at low or moderate temperatures which is available for example as solar, geothermal, biogenic

or waste heat. For conversion of this heat to power one can consider ClausiuseRankine cycles with organic working fluids.

For Rankine cycles (ORC), Kalina cycles, and trilateral cycles (TLC); in relation to the large number of publications about them, the references given are regarded as incomplete. Whilst ORC and Kalina processes are used already in existing power plants, the TLC are still in a state of technical development and are less well known.

As TLC are less similar to Carnot cycles than ClausiuseRankine cycles it is expected that TLC will have lower thermal efficiency than ORC at the same maximum and minimum cycle temperatures. The advantage of the TLC, however, is more efficient heat transfer from the heat carrier to the working fluid of the cycle. Therefore, in order to make a practically relevant comparison of ORC and TLC it is necessary to perform model calculations for systems which include heat transfer from the heat carrier to the working fluid, the cycle process, and the heat transfer from the working fluid to the cooling agent. For comparison of the systems efficiencies the inlet temperatures of the heat carrier and of the cooling agent must be the same for the TLC- and the ORC systems.

It was estimated by Löffler [80] that TLC - systems have efficiencies which are 50%-100% higher than those of ORC - systems. Model calculations for comparison of TLC - and ORC – systems have been published by Zamfirescu and Dincer [81] They considered a heat carrier inlet temperature of 150 C and a cooling air temperature of 25C. The TLC working fluids were ammonia-water mixtures and the ORC working fluids were pure R141b, R123, R245ca, and R21. They found that the exergy efficiency based on the ratio of power production to the incoming exergy flow of the heat carrier is approximately 2-3 times higher for the TLC than for the ORC. It is known that the power output of ORC systems can be remarkably increased by using higher pressures which are slightly subcritical or supercritical [82]. For such pressures the isobar of the working fluid during heating matches much better the isobar of the heat carrier. Hence, a comparison of higher pressure ORC with TLC remains a challenging task.

4.2.1 Carnot Cycle

From elementary thermodynamics, it is known that the ideal closed power cycle in terms of thermal efficiency is the Carnot cycle, which was devised by Sadi Carnot in 1824. Carnot's ideal cycle produces the highest thermal efficiency of any cycle operating between a heat source at a temperature TH and a sink at a temperature TL. It is important to remember, however, that the Carnot cycle is stipulated to operate between two constant-temperature heat reservoirs, i.e. a heat source and a sink which are thermally so large that they can deliver or accept any amount of thermal energy without changing their own temperatures.

Furthermore, Carnot's remarkable finding applies only to a cycle composed of reversible processes (i.e. no thermodynamic irreversibilities). Carnot's conclusion stems from what is usually called Carnot's theorem, namely, that the efficiency of the ideal thermodynamic cycle can depend only on the temperature of the heat source, TH, and the temperature of the heat sink, TL, measured on the absolute thermodynamic temperature scale[79].

The stipulation of reversible processes means that all heat transfer and work processes must be thermodynamically perfect. For heat transfer, this means that there must be zero temperature difference between the heating (or cooling) medium and the cycle working fluid at every point in the heat exchanger. For work processes, there must be no heat loss and no increase in the entropy of the working fluid which would arise from friction or any other dissipative mechanisms within the system. It is impossible, of course, for any real, practical cycle to conform to these constraints.

The Carnot cycle consists of the four reversible processes shown in Figure 4-1, a so-called T–S diagram having the temperature, T, on the ordinate and the entropy, S, on the abscissa.

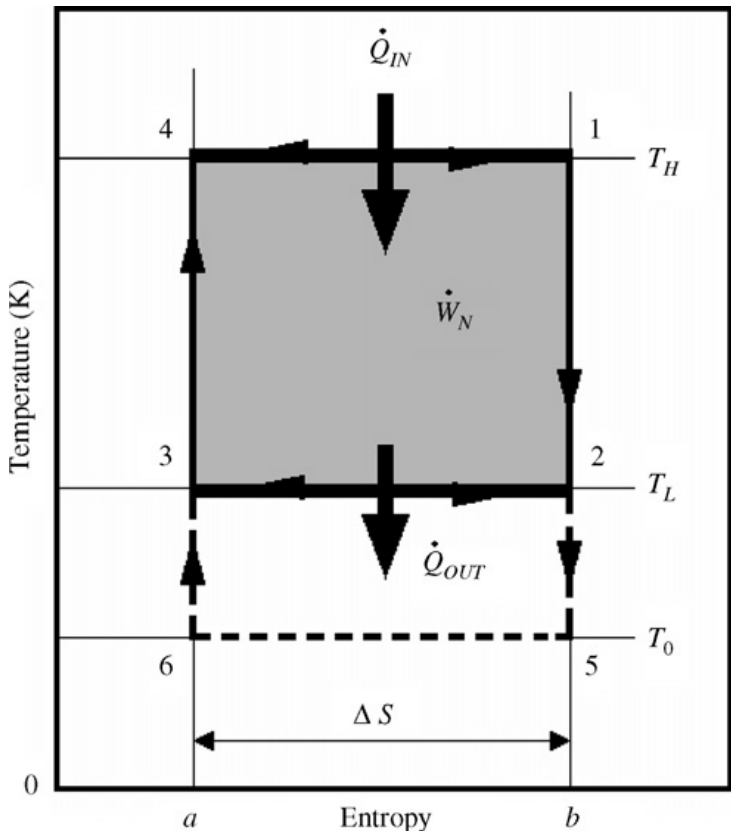

Figure 4-1 Ideal Carnot cycle

The processes are:

• 1→2: Isentropic expansion during which work is produced by the cycle working fluid

• 2→3: Isothermal heat rejection from the working fluid to a cooling medium

• 3→4: Isentropic compression during which work is performed on the cycle working fluid

• 4→1: Isothermal heat addition to the working fluid from a heating medium.

As can be seen from the figure, the temperatures of the heating medium and of the cooling medium are identical to those of the working fluid during the processes 4→1 and 2→3, respectively.

While the working fluid changes from states 4 to 1, the heating medium changes from states 1 to 4, and while the working fluid changes from states 2 to 3, the cooling medium changes from states 3 to 2. This is a practical impossibility for real cycles since

there must be a finite temperature difference to drive the heat transfer from one system to the other. Furthermore, the two isentropic work processes (1→2 and 3→4) are unrealistic; irreversibilities, such as generated by friction, can never be completely eliminated and will cause increases in entropy, even if the systems are perfectly insulated (another practical impossibility). Thus, real cycles have lower efficiencies than the ideal Carnot cycle.

The temperature labeled T_0 is the lowest available temperature of the surroundings, also known as the "dead-state" temperature. It constitutes the lowest temperature that could be used for the heat rejection process, i.e. the lowest sink temperature.

The shaded area 12341 in Figure 4.1. represents the net useful work that can be generated by the cycle. The rectangular area 1ba41 lying beneath the process 4→1 down to absolute zero represents the heat input to the cycle. This area property of the T–S diagram is one of the basic consequences of the second law of thermodynamics.

4.2.1.1 Thermodynamics of the Carnot process, when supplied by a hot fluid stream which is cooled from T_H to T_L

The efficiency and power produced in a Carnot cycle can be described as :

$$Power_{carnot} = \dot{Q}_{carnot}\,\eta_{carnot} = \dot{m}c_p(T_H - T_L)\eta_{carnot} = \dot{m}c_p(T_H - T_L)\frac{T_L - T_0}{T_L} \tag{4.1}$$

Therefore the example of a typical geothermal condition with 150ºC feed water and 30ºC exit water will be as below:

$$\Rightarrow \frac{Power_{carnot}}{\dot{m}} = c_p(T_A - T_B)\frac{T_B - T_c}{T_B} = (150-140)\frac{140-30}{140+273}c_p = 10\times 0.266\times 4.2 = 11.17\ \ kJ/kg$$

4.2.2 Organic Rankine Cycle (ORC) for producing power

The working fluid operates in a contained, closed-loop cycle and is completely segregated from the heat source fluid. There are a number of possible variants of the cycle, in terms of heat exchange configuration, turbine configuration, etc., which may be selected as appropriate to the temperature and physical state(s) of heat source fluid. A simplified schematic diagram of a typical ORC power plant is presented in Figure 4-2.

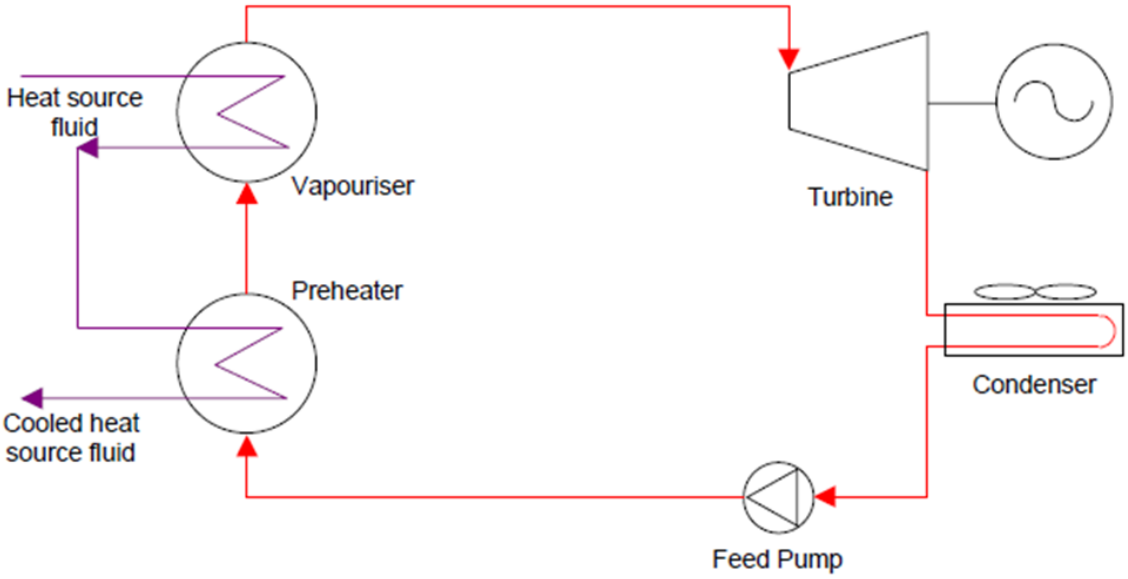

Figure 4-2 Simplified Schematic of ORC Power Plant

The working fluid absorbs heat from a heat source, in this case the hot geothermal fluid, via one or more shell-and-tube heat exchangers. This heat causes the working fluid to evaporate, producing the high-pressure vapour that is then expanded through a turbine-generator. The high-pressure motive fluid vapour passes through a liquid separator located on top or downstream of the vaporiser, prior to flowing into the turbine. The separator is required to remove entrained liquid droplets and to prevent impingement on the turbine blades.

The low pressure turbine exhaust vapour is then condensed, using either air-cooled heat exchangers ("fin-fan exchangers"), or a water-cooled, shell-and-tube condenser. Air cooling is appropriate in locations with limited water supplies, although the motive fluid outlet temperature is then limited by the prevailing ambient dry-bulb,

rather than wet-bulb, temperature. This increase in “sink temperature” reduces the overall thermodynamic efficiency of the power cycle.

From the condenser, the liquid working fluid is pumped to high pressure and returned to the preheater to close the cycle. It is also possible to incorporate an additional heat exchanger into the cycle, normally known as a recuperator. In this exchanger, residual sensible heat in the low-pressure turbine exhaust stream is used for initial preheating of the cold liquid from the motive fluid pump, thus increasing the cycle efficiency. The decision to incorporate a recuperator into the cycle depends on the quantity of available heat in the turbine exhaust.

The heat source fluid can be liquid, vapour or two-phase. By virtue of the complete segregation of the working fluid from the heat source fluid, the ORC cycle also finds application at geothermal fields where the geothermal fluids would be difficult to handle in a conventional steam turbine (eg. corrosive fluid or with high non-condensible gas content).

4.2.2.1 Thermodynamics of the ORC process

The Rankine cycle is an idealised vapour power cycle, which is the main basis for modern power generation plants. Various types of heat source can be used for these power plants, including combustion of coal, natural gas or oil, nuclear fission and solar thermal energy [79].

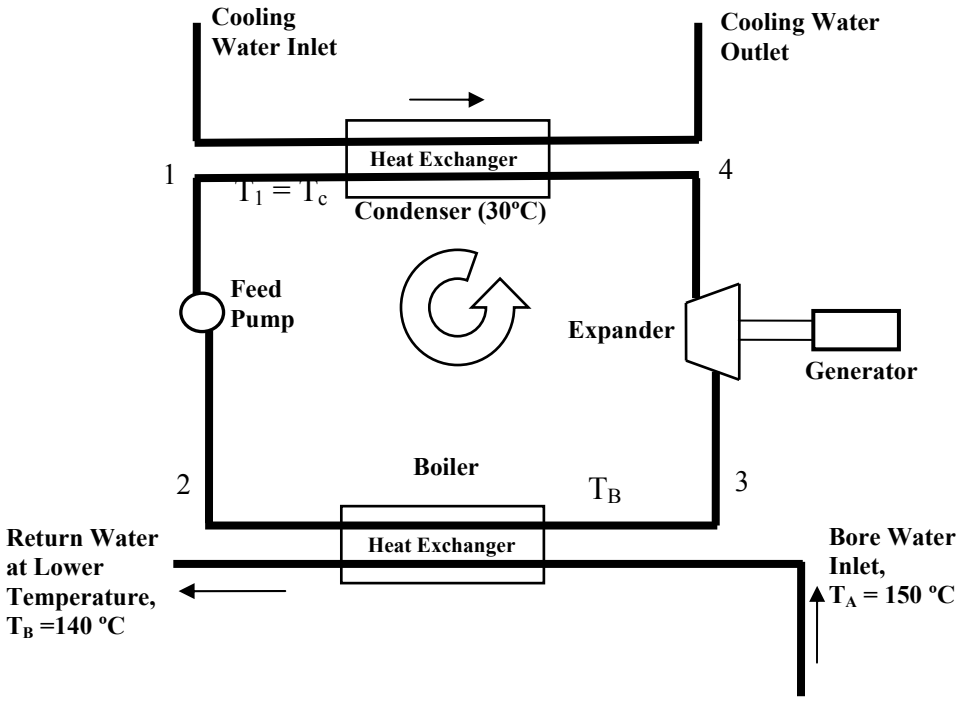

Figure 4-3 Schematic of power plant that works under Carnot or Rankine cycle

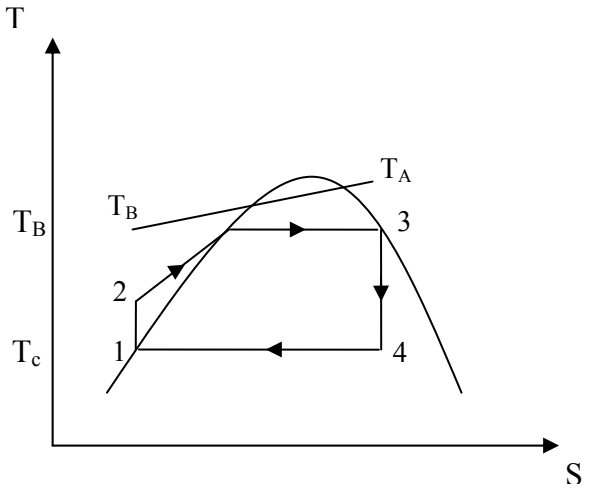

Figure 4-4 T-S diagram of a typical Rankine cycle

The following notations are used:

T_A = source fluid inlet temperature

T_B = source fluid outlet temperature

T_c = condensing temperature

$$Power_{rankine} = \dot{Q}_{rankine}\,\eta_{rankine} = \dot{m}\,c_p\left(T_A - T_B\right)\eta_{rankine} \tag{4.2}$$

$$\eta_{rankine} = 1 - \frac{T_c}{\bar{T}_{in}} \tag{4.3}$$

Where $\bar{T}_{in}$ is the mean effective temperature of the heat addition process (i.e. 2 – 3), which is to be calculated.

Since the process from 2 to 3 is isobaric (constant pressure), the following equation is applied, taking advantage of the Second Law of Thermodynamics:

$$Tds = dh \qquad \Rightarrow \int_2^3 Tds = \Delta h = h_3 - h_2 \tag{4.4}$$

The left hand side of the above equation is essentially the total area enclosed under the curve 1-2-3-4, which can be represented by $\oint Tds$.

Let T_m denote the mean effective temperature, such that $T_m \Delta s$, or $T_m\left(s_4 - s_1\right)$ will be equal to $\oint Tds$.

Therefore,

$$\bar{T}_{in} = T_m = \frac{\oint Tds}{\Delta s} = \frac{\Delta h}{\Delta s} = \frac{h_3 - h_2}{s_4 - s_1} \tag{4.5}$$

This requires the thermodynamic properties of the working fluid at all states, 1, 2, 3 and 4.

Following is the sample calculation for the above,

$T_1 = T_c = 30$ ºC

$s_1 = s_{1,f} = 0.4368$ kJ/kg K

$h_1 = h_{1,f} = 125.74$ kJ/kg

$T_2 \approx T_1 = 30$ ºC

$h_2 \approx h_1 = 125.74$ kJ/kg (assuming minimum work done by the feed pump)

$T_3 = T_B = 140$ ºC

$s_3 = s_{3,g} = 6.9294$ kJ/kg K

$h_3 = h_{3,g} = 2733.5$ kJ/kg

$T_4 = T_c = 30$ ºC

$s_4 = s_3 = 6.9294$ kJ/kg K

Therefore,

$$\bar{T}_{in} = \frac{h_3 - h_2}{s_4 - s_1} = \frac{2733.5 - 125.74}{6.9294 - 0.4368} = \frac{2607.76}{6.4926} = 401.65\,K = 128.65\,^{o}C$$

$$\Rightarrow \frac{Power_{rankine}}{\dot{m}} = c_p\left(T_A - T_B\right)\left(1 - \frac{T_c}{\bar{T}_{in}}\right)$$

$$= \left(150 - 140\right)\left(1 - \frac{30 + 273}{401.65}\right)c_p$$

$$= 10 \times 0.2456 \times 4.2 = 10.31\ kJ/kg$$

4.2.3 Trilateral cycle for producing power and fresh water

When geothermal binary plants are considered, it is recognized that the heating medium is not an isothermal source, but rather a fluid (e.g. a hot brine) which cools as it transfers heat to the cycle working fluid. The ideal cycle appropriate for such a case is a modification of the rectangular cycle shown, namely, one of a triangular shape as shown in Figure 4-5. It is clear that the triangular cycle 1231 must have a lower thermal efficiency than the ideal Carnot cycle for a given pair of temperatures, T_H and T_L.

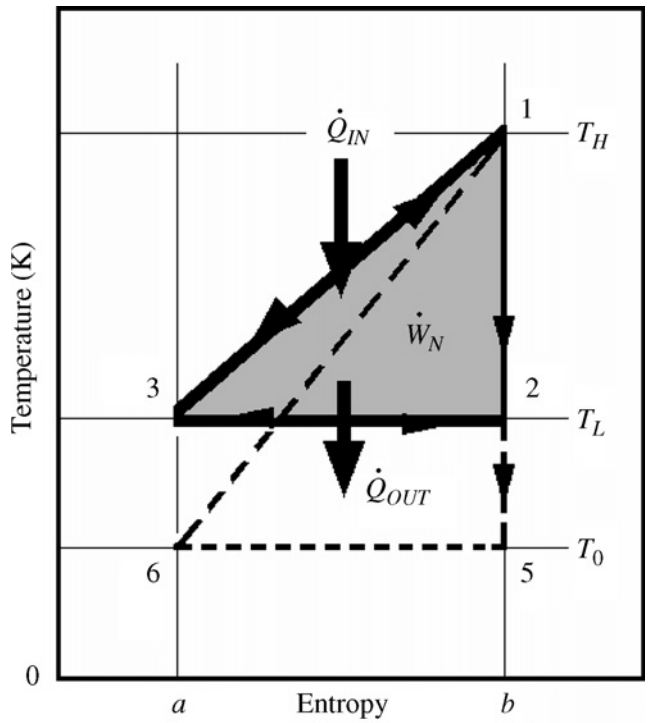

Figure 4-5 Ideal trilateral cycle

In Figure 4-5, the cycle 1231, sometimes called the "trilateral" cycle (Smith, 1993; Brown and Mines, 1998), is composed of three processes, 1→2, 2→3 and 3→1, the first two of which are the same as in the ideal Carnot cycle. Process 3→1 represents the heating process for the cycle working fluid and, in the opposite direction (1→3), the cooling process for the heating medium. This is justified because in the ideal case of reversible heat transfer, as mentioned earlier, there can be no temperature difference between the heating medium and the cycle working fluid at any point along this process. The discharge temperature of the brine, T_3, can be no lower than the condensing temperature of the working fluid, T_L. In the ideal case, these two temperatures are equal.

The TLC-system as shown in Figure 4-6 consists of the trilateral cycle to which heat is supplied from the heat carrier and removed by the cooling agent.

The TLC-plant consists of a pump, a heater, a two-phase expander and a condenser. In state 1 the working fluid is saturated liquid water with temperature T_1 at the vapour pressure p_1.

Then the pressure of the liquid is increased by the pump to p_2 at state 2 in the homogeneous liquid. Thereafter, the liquid water enters the heater where it is heated up

just to its boiling point at pressure p_2 which is state 3. The temperature T_3 is the boiling temperature at pressure p_2. At state 3 the fluid enters the two phase expander. In the expander the liquid expands into the wet vapour region down to pressure p_1 and arrives at state 4 with temperature T_1 and vapour content x. During this process step the working fluid delivers work[83].

Finally, starting from state 4 the wet vapour is completely condensed until it reaches state 1.

As described previously, the heat is supplied to the TLC-plant from a heat carrier which enters the heater at temperature T_5 and leaves it at temperature T_6. The heat is removed by a cooling agent which enters the condenser at temperature T_7 and leaves it at temperature T_8.

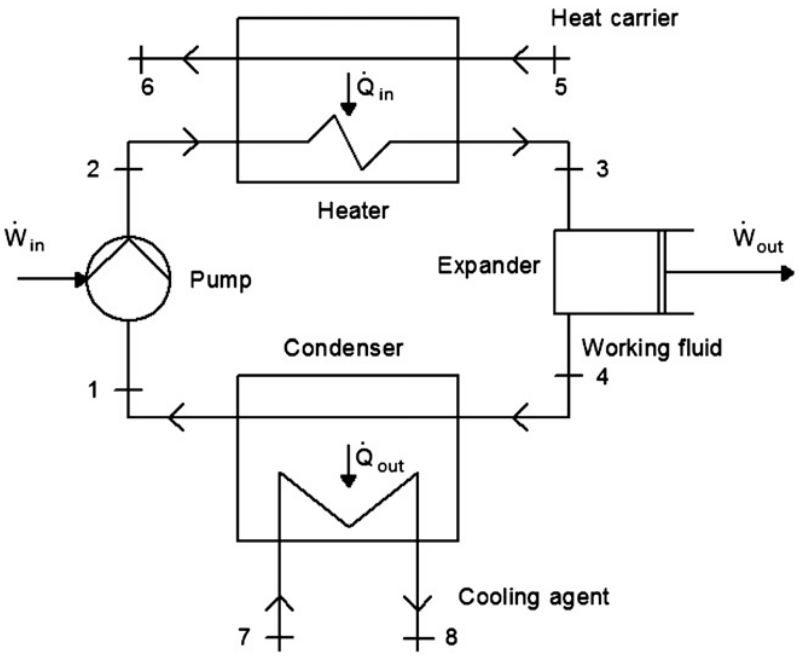

Figure 4-6 Configuration of TLC system

in the next section, the thermodynamics underlying this system is discussed for a typical power plant.

4.2.3.1 Thermodynamics of the TLC-process

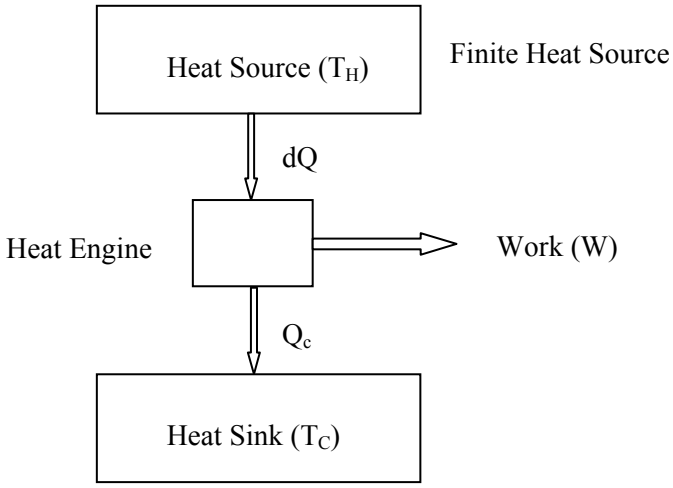

Figure 4-7 Schematic of a Heat Engine

To start with, it is necessary to work out the cycle efficiency of a trilateral flash cycle. Figure 4-7 shows a simple schematic of a typical heat engine, with dQ denoting the infinitesimal amount of heat supplied from a finite heat source of temperature T, which can be given by:

$$dQ = m\, c_p\, (-dT) = -\, m\, c_p\, dT \tag{4.6}$$

where '-' indicates a drop in the heat source temperature.

If the trilateral cycle efficiency is η, then

$$\eta = \frac{dW}{dQ}$$
$$\Rightarrow dW = \eta dQ \tag{4.7}$$

At this infinitesimal segment of the trilateral cycle, the maximum efficiency is that of the Carnot cycle. That is,

$$\eta = \frac{T - T_C}{T}$$
$$\Rightarrow dW = \eta dQ = \frac{T - T_C}{T}\left(-mc_p dT\right) \tag{4.8}$$

where Tc is the condenser temperature, or the heat sink temperature

Then, the total amount of work done is obtained from the integral of the Eq. (4.9) between T_H and T_L, which are the initial and end temperature of the working fluid.

$$\begin{aligned} W &= \int_{T_H}^{T_C} \frac{T_C - T}{T} mc_p dT \\ &= mc_p \int_{T_H}^{T_C} \left(\frac{T_C}{T} - 1\right) dT \\ &= mc_p \left[T_C \ln T - T\right]_{T_H}^{T_C} \\ &= mc_p \left[T_C \left(\ln T_C - \ln T_H\right) - \left(T_C - T_H\right)\right] \end{aligned}$$
$$\Rightarrow W = mc_p \left[T_C \ln \frac{T_C}{T_H} - \left(T_C - T_H\right)\right] \tag{4.9}$$

Therefore, the overall efficiency of the trilateral flash cycle, η_{tri}, can be derived as follows:

$$\eta_{tri} = \frac{W}{Q_{total}} = \frac{W}{mc_p\left(T_H - T_C\right)}$$
$$\eta_{tri} = \frac{mc_p \left[T_C \ln \frac{T_C}{T_H} - \left(T_C - T_H\right)\right]}{mc_p\left(T_H - T_C\right)}$$

$$\Rightarrow \eta_{tri} = 1 + \frac{T_C}{T_H - T_C} \ln \frac{T_C}{T_H} \tag{4.10}$$

Substituting typical operating parameter values for the CDP unit (T_H = 150 ºC and T_L = 30 ºC), into the above equation gives:

$$\eta_{tri} = 1 + \frac{T_C}{T_H - T_C}\ln\frac{T_C}{T_H} = 1 + \frac{30+273}{(150+273)-(30+273)}\ln\frac{30+273}{150+273} = 0.157 = 15.7\%$$

Alternatively, another method can be used to calculate the trilateral cycle efficiency, explained by [84], which is shown below in Figure 4-8 .

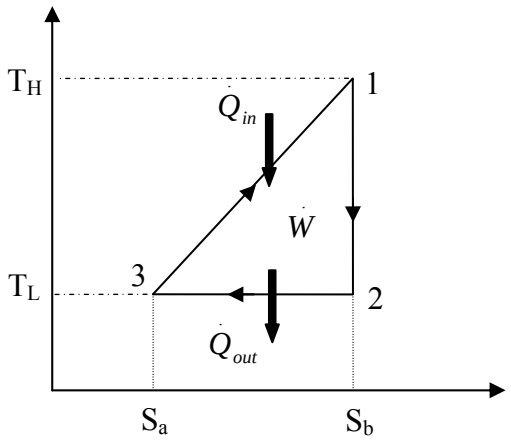

Figure 4-8 T-S diagram of ideal trilateral cycle

Note: T_H denotes a heat source temperature, and T_L means heat sink temperature

The work output $\dot{W}$ is given by the area under the triangle $1 \to 2 \to 3$, A_{123}. Also, the heat input $\dot{Q}_{in}$, is equivalent to the area, A_{12ba31} in the T-S diagram. That is:

$$\dot{W} = \frac{1}{2}(S_b - S_a)(T_H - T_L) \tag{4.11}$$

and,

$$\begin{aligned}\dot{Q}_{in} &= \frac{1}{2}(S_b - S_a)(T_H - T_L) + (S_b - S_a)T_L \\ &= (S_b - S_a)\left(\frac{1}{2}(T_H - T_L) + T_L\right) \\ \Rightarrow \dot{Q}_{in} &= \frac{1}{2}(S_b - S_a)(T_H + T_L)\end{aligned} \tag{4.12}$$

Therefore, the trilateral efficiency, η_{tri}, can be given by:

$$\eta_{tri} = \frac{\dot{W}}{\dot{Q}_{in}} = \frac{\frac{1}{2}(S_b - S_a)(T_H - T_L)}{\frac{1}{2}(S_b - S_a)(T_H + T_L)} = \frac{(T_H - T_L)}{(T_H + T_L)} \tag{4.13}$$

Using the same parameters as above, (T_H = 150ºC and T_L = 30 ºC), yields:

$$\eta_{tri} = \frac{T_H - T_L}{T_H + T_L} = \frac{(273+150) - (273+30)}{(273+150) + (273+30)} = 16.5\ \%$$

This result agrees with the result obtained using the previous formula that is 15.7 %.

Equation 4.13 is derived by assuming an ideal trilateral cycle. In reality, power plants designed to follow the trilateral cycle as closely as possible may be compared with the maximum trilateral limit case in terms of a relative efficiency, η_{rel}, which is defined as:

$$\eta_{rel} = \frac{\eta_{th,act}}{\eta_{tri}} \tag{4.14}$$

where $\eta_{th,act}$ is the actual thermal efficiency of the system.

The Figure 4-9 shows a schematic of a power plant which works under a trilateral cycle.

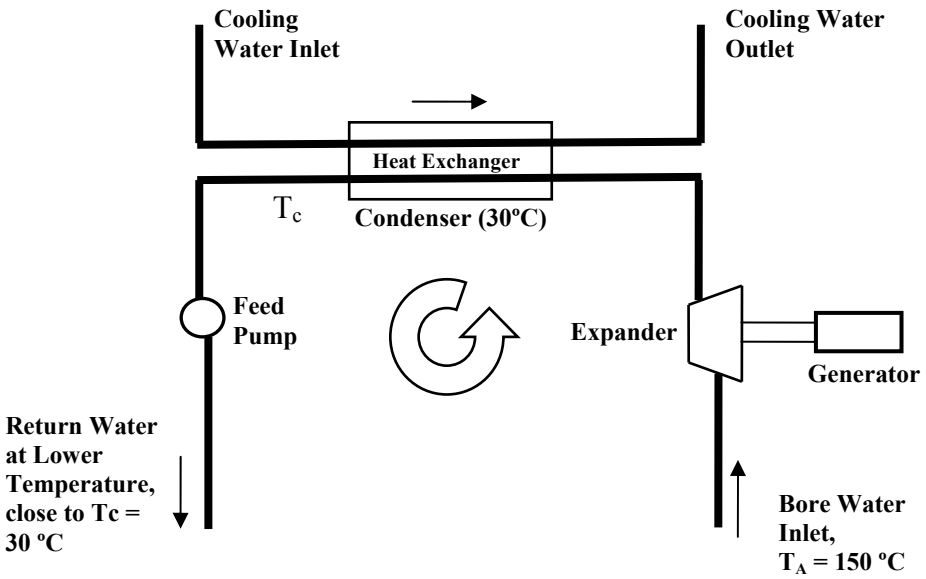

Figure 4-9 Schematic of power plant that works under trilateral cycle

$$Power = \dot{Q}_{tri}\,\eta_{tri} = \dot{m}\,c_p\left(T_A - T_c\right)\eta_{tri} \qquad (4.15)$$
$$= \dot{m}\,c_p\left(T_A - T_c\right)\left(1 + \frac{T_C}{T_A - T_C}\ln\frac{T_C}{T_A}\right)$$

$$\Rightarrow \frac{Power}{\dot{m}} = c_p\left(T_A - T_c\right)\left(1 + \frac{T_C}{T_A - T_C}\ln\frac{T_C}{T_A}\right) = \left(150 - 30\right)\left(1 + \frac{30 + 273}{\left(150 + 273\right) - \left(30 + 273\right)}\right)c_p$$
$$= 120 \times 0.158 \times 4.2 = 79.46 \text{ kJ/kg}$$

4.2.4 Comparison of the ORC and TLC

It can be shown that a TLC has the potential to recover more power from a low-temperature single-phase heat source than conventional cycles such as Carnot and Rankine cycles. The main reason for this is the minimization of irreversibility in the heat transfer process between the source and the working fluid. The recoverable heat therefore increases almost linearly with a rise in source temperature. The associated gain in power output per unit source mass flow rate is even greater because the additional heat is transferred at a higher temperature. It is thus converted into work more efficiently [83].

Although the cycle efficiency is lower than those of Carnot and Rankine cycles, the overall conversion efficiency from thermal energy of the heat source to mechanical energy is greater. This is because of the superior ability of the TFC to extract sensible heat compared with a single Carnot cycle when the heat source has finite thermal capacity. An example follows to illustrate this comparison.

Figure 4-10 shows a simple schematic representation of a conventional geothermal binary power plant operating with a finite heat source, the temperature of which drops from 150 ºC to typically 100 ºC – 140 ºC as the flow is returned, depending on the flow rate of the heat source fluid. The condensing temperature is maintained at 30 ºC by the cooling water.

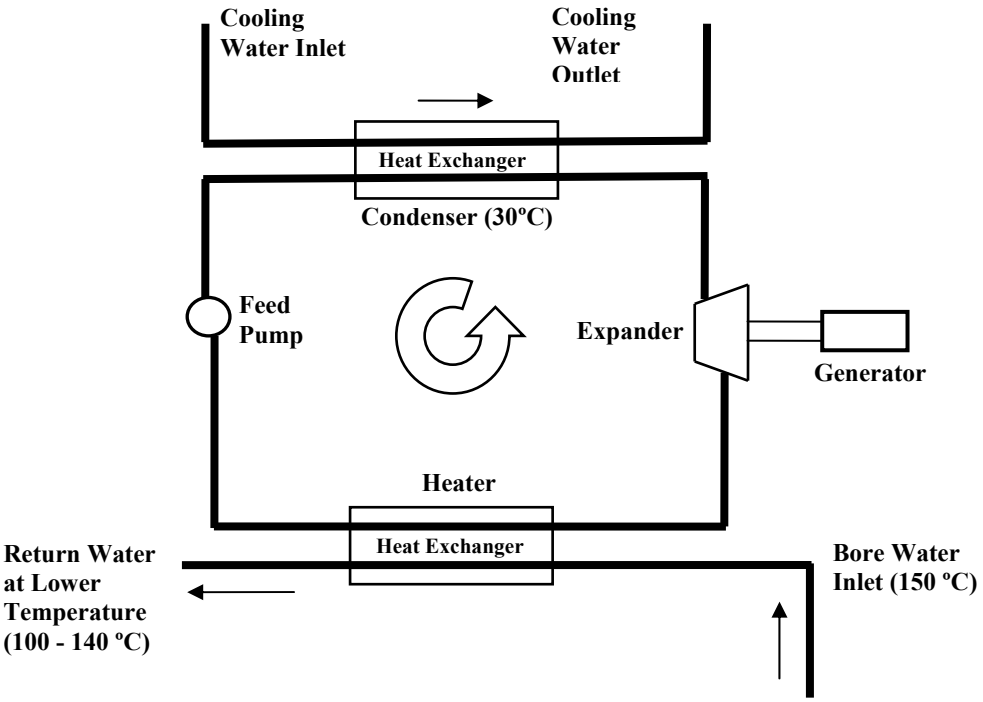

Figure 4-10 Schematic diagram of a geothermal power plant

Figure 4-11 to Figure 4-13 illustrate the T-S diagrams for the cycles under consideration, including the Carnot cycle (on the left), and the trilateral flashing cycle, or TFC (on the right). The shaded areas on each graph represent the extent of irreversibility of the cycle. It can be seen that, as the temperature drop in the heat source becomes greater associated

with a decrease in its flow rate, the temperature matching between the source and working fluid becomes worse for the Carnot cycle, which increases the extent of irreversibility. In comparison, the extent of irreversibility is reduced for the TFC, which is attributed to improved temperature matching. Therefore, with heat sources of limited capacity and flow rate, as illustrated in Figure 4-11, for the same amount of heat extraction, the ability to make use of this heat is clearly greater for the TFC. This demonstrates why the TFC is favored as the model for geothermal binary power plants [84].

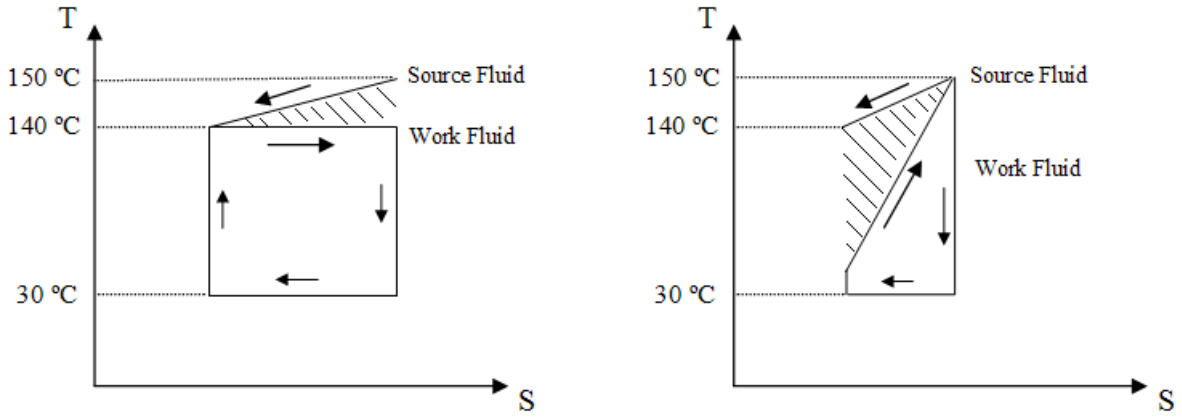

Figure 4-11 T-S diagram for Carnot Cycle (Left) and TFC (Right), with heat source fluid of high flow rate.

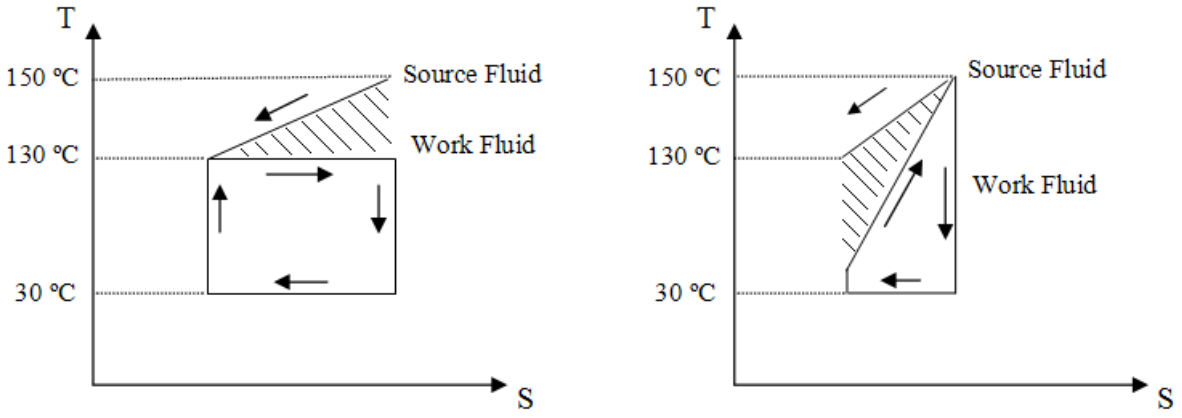

Figure 4-12 T-S diagram for Carnot Cycle (Left) and TFC (Right), with heat source fluid of medium flow rate

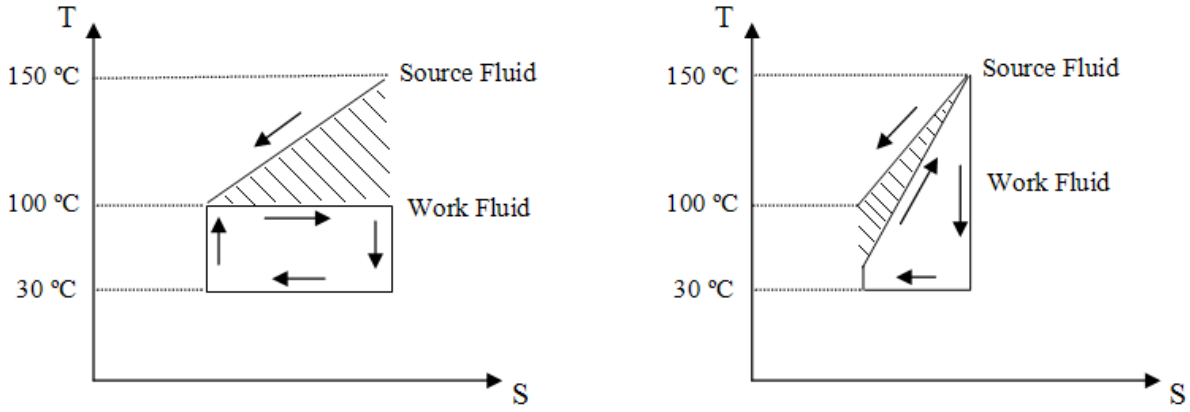

Figure 4-13 T-S diagram for Carnot Cycle (Left) and TFC (Right), with heat source fluid of low flow rate

Comparison of theoretical efficiencies and specific energy production for Carnot, Rankine and Trilateral cycles is presented in the following figures. The comparisons are made based on theoretical performances of the cycles for a constant sink temperature and varying feed water temperature,

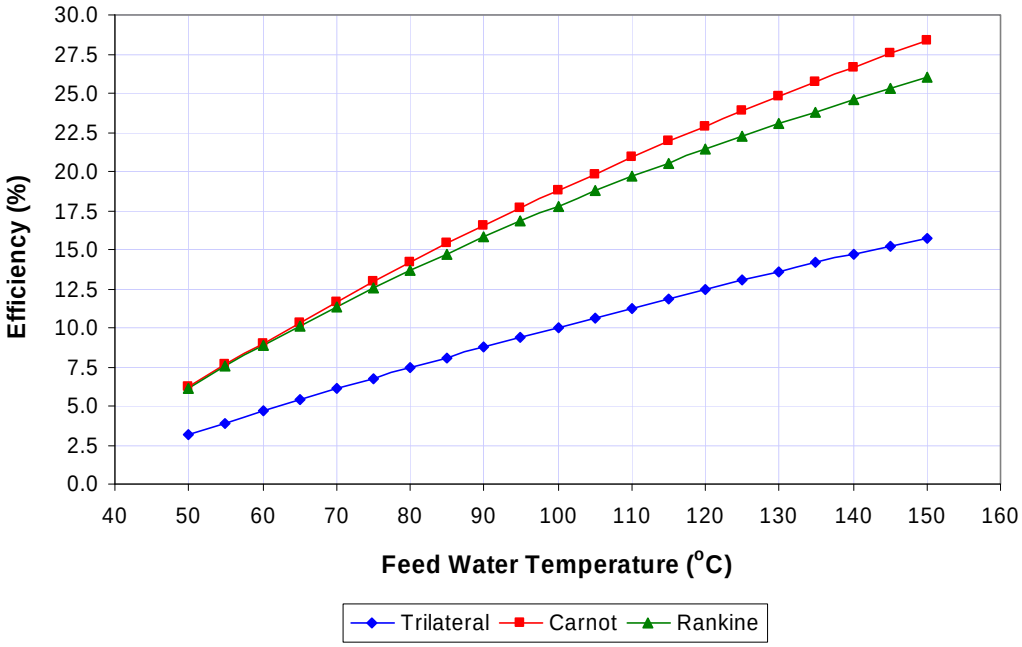

Figure 4-14 Cycle efficiency as a function of feed water temperature (condenser temperature = 30 °C)

As seen in Figure 4-14 which has been produced based on the preceding analysis of the cycle's efficiency, at any given feed water temperature and a fixed condenser temperature, the trilateral cycle has the lowest efficiency compared with the other two cycles: the Carnot cycle and the Rankine cycle. The Rankine cycle efficiency is the next highest, which closely follows the Carnot cycle efficiency especially at the lower feed water temperature. It can also be observed that the efficiency difference between the trilateral and the other two cycles becomes greater at a higher feed water temperature.

As it can be seen from Figure 4-15 which has been produced based on the power production analysis discussed earlier, although the cycle efficiency of the trilateral cycle is inferior to that of conventional thermodynamic cycles such as the Rankine cycle, it has been shown that it enables better utilization of the heat source. Consequently, with a given heat source temperature and mass flow rate, more power can be extracted by heat engines which work under a trilateral cycle. The basis of the advantage of the trilateral cycle is that the heat source fluid also acts as the working fluid and can be introduced directly to a two-phase expander, and condensed at the condenser temperature. In a Rankine cycle heat engine, the heat source fluid is used to supply heat to the working fluid through heat exchangers and experiences a much lower temperature drop, and consequently a lower enthalpy drop.

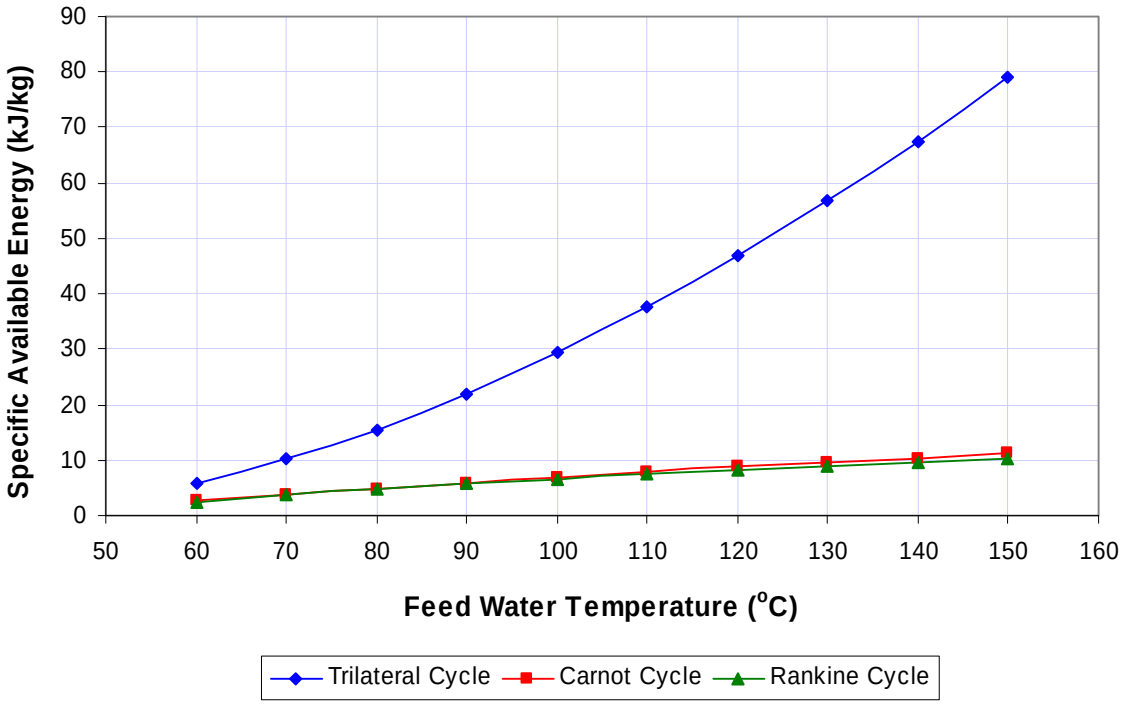

Figure 4-15 Specific Energy available for extraction, as a function of feedwater temperature, for condenser temperature at 30 °C

4.3 Thermodynamics underlying the trilateral cycle used in the experimental CDP rig

The trilateral cycle process, introduced earlier, is shown in Figure 4-16. In the laboratory case the feed water was heated to reach to point 2 although the process started from point 1 whereas in the geothermal case the process starts at point 2 as the water is already at 150 °C. The liquid saline water feed at atmospheric pressure (Point1) is heated close to saturation temperature (Point2) and then passes through a nozzle and ideally experiences an isentropic expansion after which the mixture leaves the nozzle. Process 2-3 shows the ideal isentropic expansion process which would provide the maximum power production. Process 2-3" indicates a constant enthalpy process from which the maximum fresh water would be produced as the result of maximum vapor production but with no work production. This is similar to single stage flash desalination using a stationary nozzle. Realistically the process of expansion will

be somewhere between the two limits where the end point of the process is shown as point 3 prime.

,

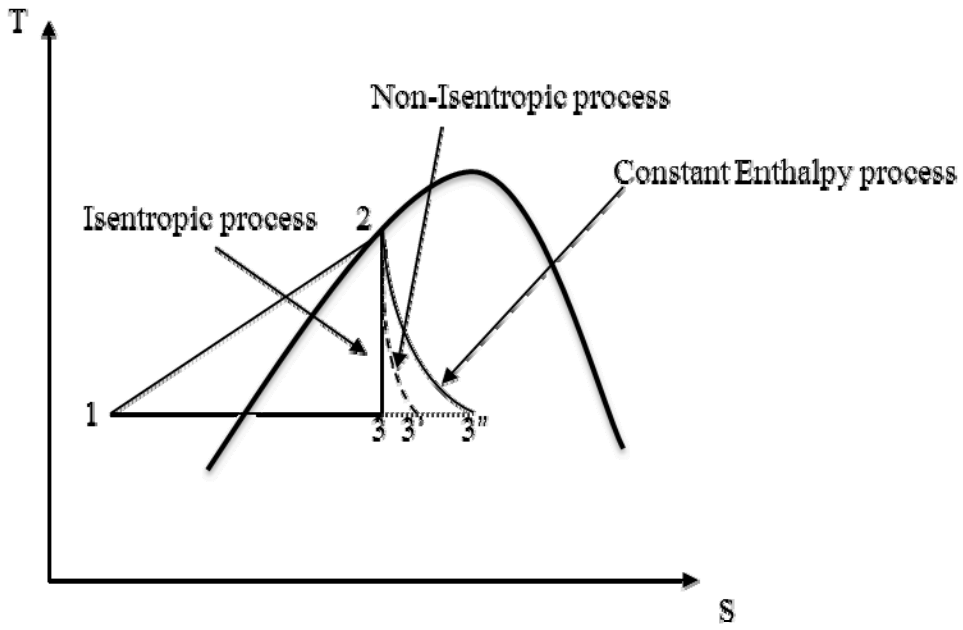

Figure 4-16 T-S diagram for trilateral cycle of CDP

Going through the thermodynamic analysis of the process, the thermodynamic properties of point 2 are available:

$$s_2 = s_{f2} \tag{4.16}$$

$$h_2 = h_{f2} \tag{4.17}$$

$$\dot{V}_2 = \dot{m} \times v_{f2} \tag{4.18}$$

Where the values of s_{f2} and h_{f2} which are the specific entropy and specific enthalpy of the hot feed liquid water and can be found from the table of water properties[85].

Considering the isentropic expansion, points 2 and 3 have the same entropy, therefore:

$$s_2 = s_3 \Rightarrow s_3 = s_{f2} = s_{f3} + x s_{fg3} \tag{4.19}$$

Knowing the temperature at 3 (assumed to be the same as the condenser temperature), the corresponding S_f and S_{fg} can be found. Hence the quality of the mixture at point 3 can be calculated by:

$$x = \frac{s_3 - s_{f3}}{s_{fg3}} \tag{4.20}$$

Having x from above, specific enthalpy h_3, specific volume v_3 and the volumetric flow rate of the mixture at the exit of the nozzle can be calculated as:

$$h_3 = h_{f3} + xh_{fg3} \tag{4.21}$$

$$v_3 = v_{f3} + xv_{fg3} \tag{4.22}$$

$$\dot{V}_3 = \dot{m} \times v_3 \tag{4.23}$$

In the real situation, the cycle has an isentropic efficiency less than one as defined in Eq (4.24) which means that the quality of the mixture at point $3'$ will be different from that at point 3.

$$\eta_{isentropic} = \frac{h_2 - h_{3'}}{h_2 - h_3} \tag{4.24}$$

Using Eq. (4.24), $h_{3'}$ can be found as shown in Eq. (4.25).

$$h_{3'} = h_2 - \eta_{isentropic}(h_2 - h_3) \tag{4.25}$$

Assuming that an estimate of the isentropic, efficiency is in available

then $h_{3'}$ can be calculated from the above equation.

Considering the isentropic process (2-3) and using above equation, the isentropic efficiency would be 1 . For a constant enthalpy process, the isentropic efficiency would be zero.

The quality of the mixture in a real non isentropic process and using the value of the specific enthalpy of the product as calculated by Eq. (4.25) would be:

$$x' = \frac{h_{3'} - h_{f3}}{h_{fg3}} \tag{4.26}$$

Knowing x' from above, specific volume $v_{3'}$ and the volumetric flow rate at the nozzles exits $\dot{V}_{3'}$ can be calculated as follows:

$$v_{3'} = v_{f3} + x'v_{fg3} \tag{4.27}$$

$$\dot{V}_{3'}(m^3/s) = \dot{m}(kg/s) \times v_{3'}(m^3/kg) \tag{4.28}$$

The relative velocity of the jet at the exit of the nozzle is:

$$V_r(m/s) = \dot{V}_3(m^3/s) \Big/ A_{nozzle}(m^2) \tag{4.29}$$

4.4 Turbine technologies for generating power

Man has attempted to develop mechanical machines working on the reaction principle for centuries, but it is only in the last two centuries that successful applications for power generation and aerospace technology have been developed. The developments in the technology came with two working principles for water turbines i.e. impulse and reaction principle [86]. Most of the conventional and modern day hydro turbines work on impulse or a combination of reaction and impulse principles. The turbine that was based on a pure reaction principle was forgotten for a long time and was considered obsolete. In late 17th century Barker an English engineer reinvented and modified the Hero's turbine design to work with the potential energy of water stored in dams or reservoirs. The modified turbine was called a Barker's mill [87]. Since then various inventors have developed new water turbines, which can produce large amount of energy, at different water heads, at high efficiencies. As stated water turbines are classified into two main categories according to their working principles, Impulse and Reaction.

4.4.1 Impulse Turbine

An impulse turbine consists of a rotor mounted on a shaft free to rotate on a set of bearings. The outer rim of the rotor carries a set of curved blades and a jet of fluid issuing from a nozzle impinges on the blades of the rotor. The change in momentum of the fluid as it hits the blades and causes the wheel to turn is defined as an impulse force [86]. The process described converts the kinetic energy of the fluid to mechanical work in the shaft producing power. The Pelton wheel is a good example of an impulse turbine as shown below.

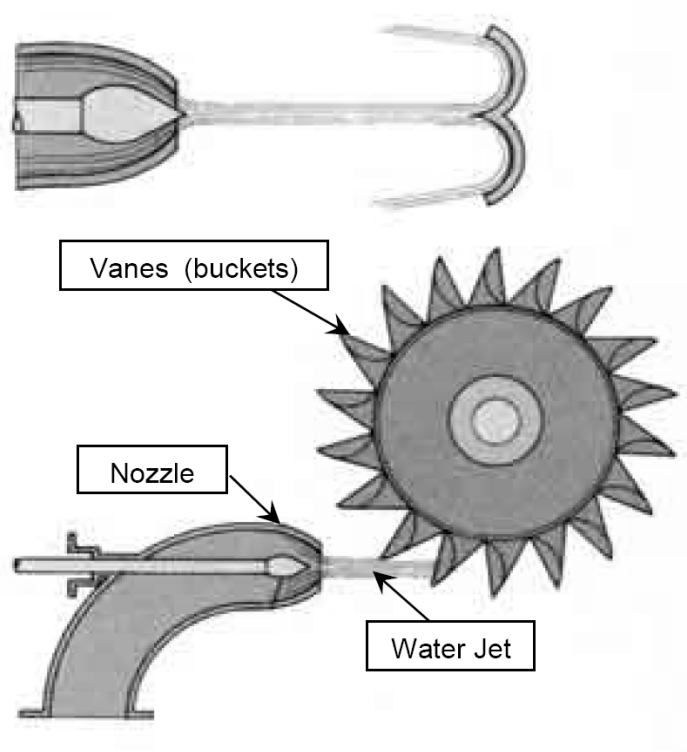

Figure 4-17 Pelton wheel [88]

Generally, impulse turbines are restricted to low volume high heads applications with low specific speeds. As said earlier the specific speed of a turbine is defined as the speed of an ideal, geometrically similar turbine, which yields unit power while supplied with unit head. In contrast, special designs such as the Turgo or crossflow turbines are examples of relatively high specific speed impulse units.

4.4.2 Reaction turbines

The earliest historically recorded outward-flow turbine is said to have been discovered almost 2000 years ago during the first century AD by Hero of Alexandria [87]. As shown in Figure 4.20 Hero's turbine consists of a hollow metal sphere with nozzles pointing in opposite directions tangentially to the sphere along the same axis. A sealed boiler generates the steam with two tubes connected to both the sphere and the boiler. This will cause the steam to flow into the sphere and come out of the nozzles therefore resulting in a rotation of the turbine. While the turbine did not produce power,

Hero demonstrated that steam power could be used to operate machinery. An illustration is shown below.

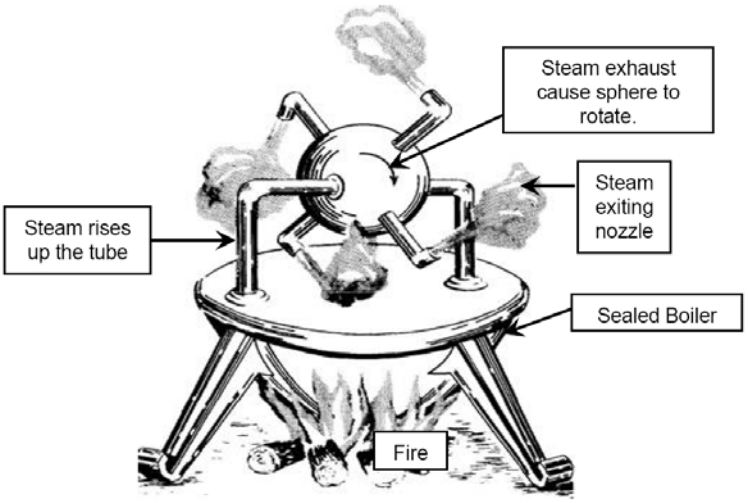

Figure 4-18 Hero's turbine [86]

The main reason for selecting a simple reaction turbine system was its flexibility to provide high expansion ratios. The combined desalination and power generation system, makes use of the trilateral flash cycle and the expander used in this system is a simple reaction turbine. As shown in the schematic of the CDP in Figure 4-19, hot saline water enters a flash tank through a radially outward flow two-phase reaction turbine. Initially the pressure inside the flash tank is between 5-6kPa absolute, this corresponds to water saturation temperature of approximately 32-36°C. The cooling water inlet temperature of the condenser is maintained between 18°C to 23°C. The hot (>60°C) saline water flash evaporates in the diverging section of the nozzle inside the reaction turbine and exits the turbine radially at a high velocity in the form of liquid-vapor mixture. The reaction force to this mixture flow makes the turbine rotate at very high speed and an electrical generator can be connected to this turbine to produce electrical power. The vapor part of the mixture flows to the condenser, where it is condensed and removed from the system as fresh water. The liquid part (brine) of the mixture is at higher salinity and falls to the bottom of the flash tank and is continuously removed from the tank.

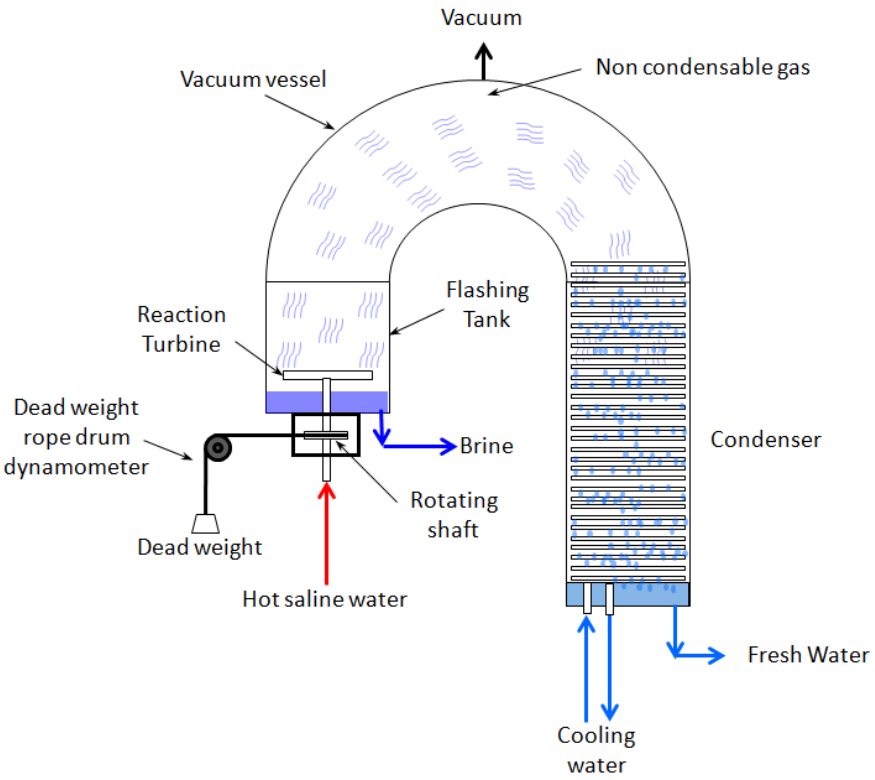

Figure 4-19 Schematic showing the principle of the CDP system

4.5 Estimating the output power of a simple reaction rotor using in CDP

4.5.1 Power output calculation

Power measurement of the CDP while the rotor is accelerating under the hot water feed is a significant aspect of the experiments in order to analysing the isentropic efficiency of the turbine and also mechanical and thermodynamic efficiency of the whole system. Therefore, determining a reliable means of analysing the potential for power generation by a CDP has been developed using the outcomes and observations of several experimental tests.

An important observation was uncertainties including losses which were the consequence of the friction and drag while the rotor was accelerating. Moreover, these

losses varied with increase in temperature of the inlet water as well as with the duration of the experiment. That was attributed to the change in expansion rate of the rotor and other components of the system such as bearings, seals and shaft. Therefore, calculating the actual power generated using the formula which is a function of rotational speed of the turbine that was measuring during the whole test would not give the correct amount of power generation potentiality of the CDP.

Another problem which has been faced through the experimental tests was the safety issue and the electrical uncertainty of using an electrical generator. These problems include mounting the generator coupled with the rotor and their balancing, efficiency of the generator itself and involving the electrical systems to put load on the rotor and to measure the corresponds current and voltage.

As a consequence, a method which can eliminate these uncertainties and sources of problems has been developed for power measurement of the experimental system. In this method, the rotor has been allowed to accelerate to a certain rotational speed and then the whole system was shutdown allow the rotor to decelerate. In this way, the deceleration rate can be used to determine the friction and losses of the system and subtracting it from the power which is during acceleration can provide the actual generated power. This method was found to be reliable and repeatable such that it could be used to determine the actual power generation of the CDP with reduced uncertainty and complexity.

The procedure of calculating the generated power and a detailed example of the measurement process is as follows:

In order to determine the power generated by the rotating turbine, the initial torque needed to start the turbine to rotate was measured by spring force measurement. However, as the initial torque will change as the rotor goes higher speed, it can be considered as a function of rotational speed or ω.

Therefore the power generated by the rotor through the thermodynamic process in the nozzles which is also a function of rotational speed of the turbine can be written as:

$$P(\omega) = T_o(\omega) \times \omega + \frac{d(KE)}{dt} + P_{ex} \tag{4.30}$$

Where $T_o(\omega)$ represents the torque caused by all the friction losses which can be a function of ω.

The kinetic energy of the turbine while it is rotating at the rotational speed of ω is:

$$KE = \int \frac{(r\omega)^2}{2} dm = \frac{\omega^2}{2} \int r^2 \, dm = \frac{\omega^2}{2} \int r^2 \rho dV \tag{4.31}$$

In which, $\int r^2 \, dm$ or $\int r^2 \rho dV$ is the moment of inertia for the turbine about the y axis which is its rotational axis and it is known as Iyy. Moment of inertia, also called mass moment of inertia, rotational inertia, polar moment of inertia of mass, or the angular mass, (SI units kg·m²) is a measure of an object's resistance to changes to its rotation. It is the inertia of a rotating body with respect to its rotational speed.

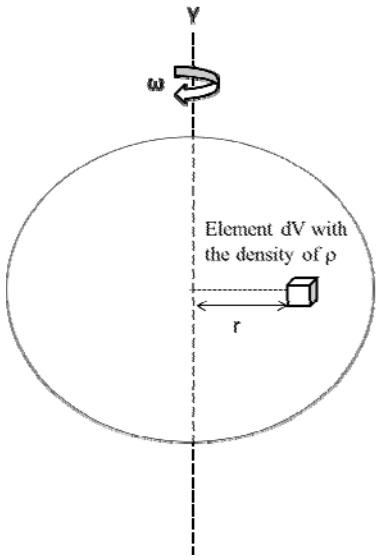

Figure 4-20 Element analysis of the rotary turbine

The moment of inertia plays much the same role in rotational dynamics as mass does in linear dynamics, describing the relationship between angular momentum and angular velocity, torque and angular acceleration, and several other quantities. The moment of inertia of an object about a given axis describes how difficult it is to change its angular motion about that axis. Therefore, it encompasses not just how much mass the object has overall, but how far each bit of mass is from the axis. The moment of inertia of an object

can change if its shape changes. Therefore, it can be found when the geometry of the disk or rotor is known. The moment of inertia of the rotor can be read for every axis by knowing its geometry.

Measuring the momentum of inertia experimentally

In order to measure the moment of inertia for the turbine and hollow shaft, an experimental facility has been prepared. The experimental method is based on when an object is subjected to torsion vibration about one fixed axis, the moment of inertia will have a direct relationship with the frequency of oscillation.

In the experiment, a known solid cylinder has been used as a calibration mass for measuring the period of oscillation. For this purpose, a piano wire has been mounted on the wall as shown in Figure 4-21 and the calibration mass has been hung from it. Then angular motion has been supplied uniformly to the mass and its period of oscillation has been measured using a stopwatch. The time for 15 oscillations has been measured by starting the mass oscillating, The time read on the stopwatch gives the period of the oscillation. The measurement has been repeated four times to find an average and to improve accuracy.

The frequency is found from the reciprocal of the period. As an example , if the period is two seconds, then the frequency is one half; the object makes one half of an oscillation per second.

For this system in torsional vibration, the period of oscillation T (s) is calculating using:

$$T = 2\pi\sqrt{\frac{I}{k}} \tag{4.32}$$

In which, I is momentum of inertia (kg/m2) and k is the stiffness of the wire (N/m).

For the known cylindrical calibration mass the moment of inertia can be calculated easily from:

$$I = \frac{1}{2}mr^2 \tag{4.33}$$

Where m (kg) is the mass of the solid which can be measured by weighing and r (m) is the radius of the cylinder.

Therefore from the T equation, as T (s) and I (kg/m2) are known, the stiffness of the wire can be calculated.

For the next step, the turbine for use in the CDP has been mounted with the hollow shaft on the wire and the same procedure has been done to measure the period of oscillation. This time, by knowing the T (s) and stiffness of the wire calculated from the calibration test, the moment of inertia for the turbine could be calculated.

Therefore the kinetic energy would be:

$$KE = \frac{\omega^2}{2} I_{yy} \tag{4.34}$$

Therefore using the kinetic energy definition and the associated discussion the power generated by the process can be calculated as:

$$P(\omega) = T_o(\omega) \times \omega + \frac{d}{dt}\left(\frac{\omega^2}{2} I_{yy}\right) + P_{ex} = T_o(\omega) \times \omega + \mathbf{I} \times \omega \times \frac{d\omega}{dt} + P_{ex} \tag{4.35}$$

The test which has been designed to calculate the power output of the turbine consists of two parts. The first part is to accelerate the turbine to a predetermined rotational speed and then close the hot water feed valve and allow the system to slow down itself which is referred to as the deceleration part. In the deceleration part, there is no power generated and the turbine decelerates because of frictional losses in the shaft, bearings and mechanical seals.

In both above tests no net power is extracted from the turbine, therefore $P_{ex} = 0$.

So in acceleration part:

$$P(\omega) = T_o(\omega) \times \omega + \mathbf{I} \times \omega \times \frac{d\omega}{dt} \tag{4.36}$$

And for the deceleration part:

$$T_o(\omega) \times \omega + I \times \omega \times \frac{d\omega}{dt} = 0 \tag{4.37}$$

Consequently:

$$T_o(\omega) = -\frac{1}{\omega} \times I \times \omega \times \frac{d\omega}{dt} = -I \times \frac{d\omega}{dt} \tag{4.38}$$

For the above equation $\frac{d\omega}{dt}$ can be obtained from the ω-t curve using the deceleration part.

Equation 4.38 simply states that the value of overall frictional torque for any ω can be found from the product of the mass moment of inertia I_{zz} and the rate of change of the angular velocity of the rotor in a decelerating test.

4.5.2 Measuring the Momentum Of Inertia (MOI) experimentally and analytically

In order to measure the momentum of inertia for the turbine and hollow shaft, an experimental facility has been prepared. The experimental method is based on when an object is subjected for torsion vibration about one fixed axis, the moment of inertia will have a direct relationship with the frequency of oscillation.

In the experiment, a known cylindrical solid has been considered as a calibration mass for measuring the period of oscillation. For this purpose, a piano wire has been mounted on the wall as shown in Figure 4-21.

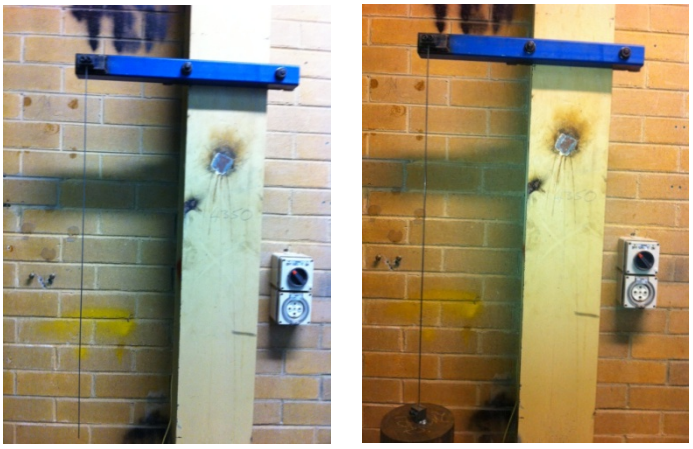

Figure 4-21 Experimental set up for measuring MOI for the simple cylinder

Then the calibration mass has been hung on it and angular motion has been supplied uniformly to the mass in order that the object's period of oscillation could been measured using a stopwatch. The time for 15 oscillations has been measured after starting the mass oscillating. The time read on the stopwatch allows calculation of the period of the oscillations. The steps have been repeated four times to find an average to improve accuracy.

The frequency is found from the reciprocal of the oscillation period. In the example above, if the period is two seconds, then the frequency is one half; the object makes one half of an oscillation per second.

As described earlier for this system in torsional vibration, the period of oscillation T (s) is calculated from:

$$T = 2\pi\sqrt{\frac{I}{k}}$$

In which, I is moment of inertia (kg/m2) and k is the torsional stiffness of the wire (N/m).

For the known cylindrical calibration mass the moment of inertia can be calculated easily using:

$$I = \frac{1}{2}mr^2$$

Where m (kg) is the mass of the solid which can be measured by weighing and r (m) is the radius of the cylinder.

Therefore from the T equation, as T (s) and I (kg/m2) are known, the stiffness of the wire can be calculated.

From the experiment which has been done for the calibration mass which is a stainless steel cylinder, 15 cycles were counted in 71.6 seconds, therefore:

$$T = \frac{71.6}{15} = 4.7\ s$$

The mass moment of inertia for the cylinder with radius of 170 mm and the mass of 42.55 kg is calculated as:

$$I = \frac{1}{2}mr^2 = \frac{1}{2} \times 42.55 \times (\frac{170}{2} \times 10^{-3})^2 = 0.1537\ kg.m^2$$

In order to increase confidence of measuring the mass momentum of inertia using numerical analysis, a model has been made in Solid Works as shown in Figure 4-22 and the mass moment of inertia from the solid file is also shown.

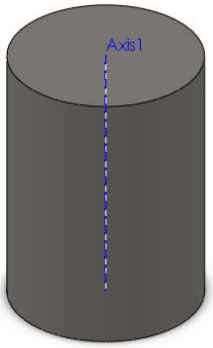

Moments of inertia: (kilograms * square meters)
Taken at the center of mass and aligned with the output coordinate system.

Lxx = 0.28	**Lxy = 0.00**	**Lxz = 0.00**
Lyx = 0.00	**Lyy = 0.15**	**Lyz = 0.00**
Lzx = 0.00	**Lzy = 0.00**	**Lzz = 0.28**

Figure 4-22 Analytical calculation of MOI for a simple cylinder using SolidWorks

As it can be seen the values are matched with each other.

So, the stiffness of the piano wire can be calculated as:

$$K = \frac{4\pi^2}{T^2} I = \frac{4\pi^2}{4.7^2} \times (0.1537) = 0.2744\ N/m$$

For the next step, the turbine for the CDP has been mounted with the hollow shaft on the wire and the same procedure used to measure the period of oscillation. Then, by knowing the T (s) and stiffness of the wire calculated from the calibration test, the moment of inertia for the turbine can be calculated.

MOI for Stainless steel turbine

The experimental facility has been used with the turbine with the assembled shaft hanging on the piano wire as shown in Figure 4-23. The figure shows the assembly of the turbine and the shaft hanging on the wire with the calibration mass at the side.

Figure 4-23 Experimental set up for measuring MOI of the turbine

This time, 15 cycles were counted in 133.9 seconds. Therefore, using the calculated stiffness of the wire, the mass momentum of inertia for turbine and shaft can be calculated as below:

$$T = \frac{133.9}{15} = 8.9\ s$$

$$I_{turbine+shaft} = \frac{T^2 K}{4\pi^2} = \frac{(8.9)^2 \times 0.2744}{4\pi^2} = 0.56\ kg.m^2$$

As the mass momentum of inertia has been measured using Solid Works for the calibration mass, the model for the turbine has also been made in solid work as shown in Figure 4-24:

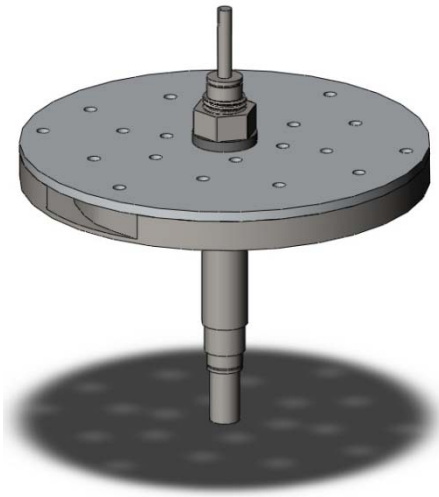

Moments of inertia: (kilograms * square meters)
Taken at the center of mass and aligned with the output coordinate system.
Lxx = 0.307 Lxy = -0.000 Lxz = 0.020
Lyx = -0.000 Lyy = 0.572 Lyz = -0.000
Lzx = 0.020 Lzy = -0.000 Lzz = 0.331

Figure 4-24 Analytical calculation of MOI for the turbine using SolidWorks

The material selected for the model was Aluminium for the top plate and stainless steel for the rest of the turbine and shaft. From this the mass moment of inertia has been calculated using Solid Works. The result is shown below:

As can be seen, the result from Solid Works matches the result based on the experimental measurement.

Figure 4-25 shows the acceleration and deceleration of the turbine during a test using the hot water at an average temperature of 95 °C and a volume flow rate of 10 l/min whilst maintaining the chamber pressure at 5kPa.

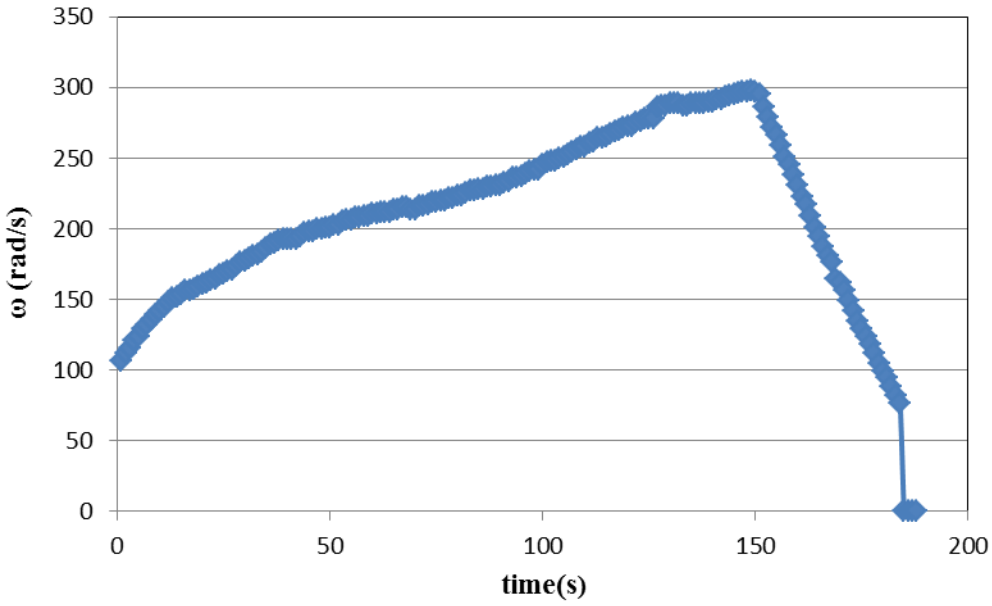

Figure 4-25 Experimental angular velocity vs. time

For the deceleration part and the corresponding trend line for the data of experiment, the deceleration rate of the rotor can be determined from the following graph.

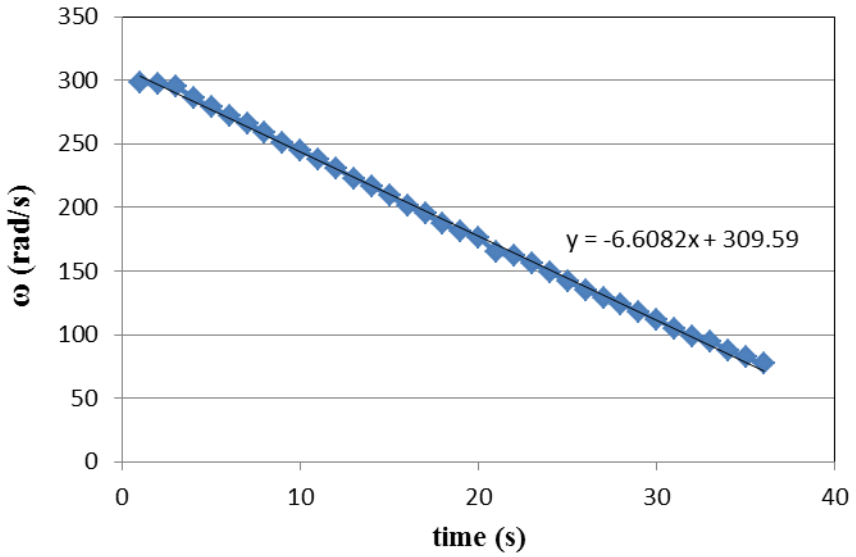

Figure 4-26 Trend line of the deceleration part of the process

Therefore, $\frac{d\omega}{dt}$ equals to -6.608 from the above figure and using the value of 0.168 for moment of inertia will give the initial torque of To=1.11 N.m.

Similar to calculations for the deceleration, the power generated from acceleration part can be calculated as Eq. (4.36):

$$P(\omega) = T_o(\omega) \times \omega + I \times \omega \times \frac{d\omega}{dt}$$

In which $\frac{d\omega}{dt}$ can be determined from acceleration part of ω-t curve as has been shown in the following figure.

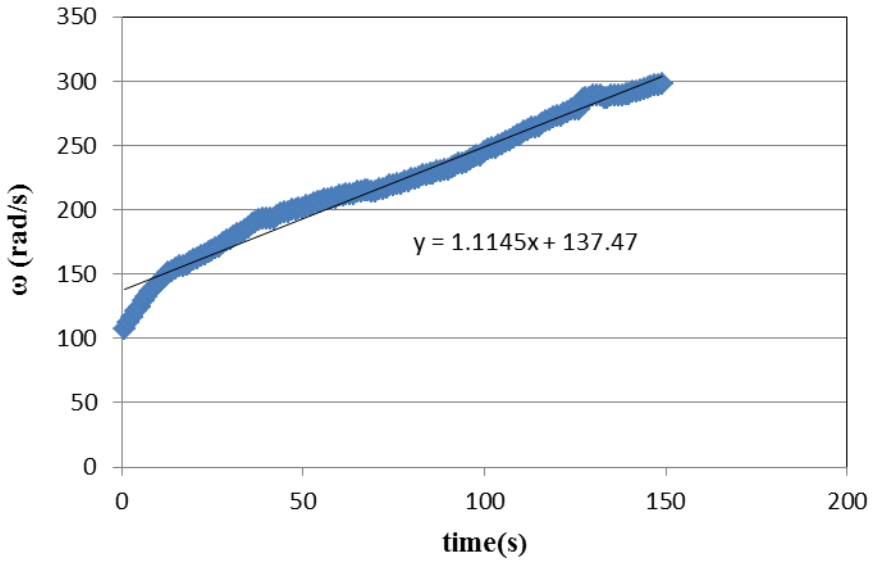

Figure 4-27 The trend line of acceleration part of the process

Which is 1.1145 rad/s from the above figure. Thus, the power output can be calculated for each rotational speed in anytime as shown in this figure:

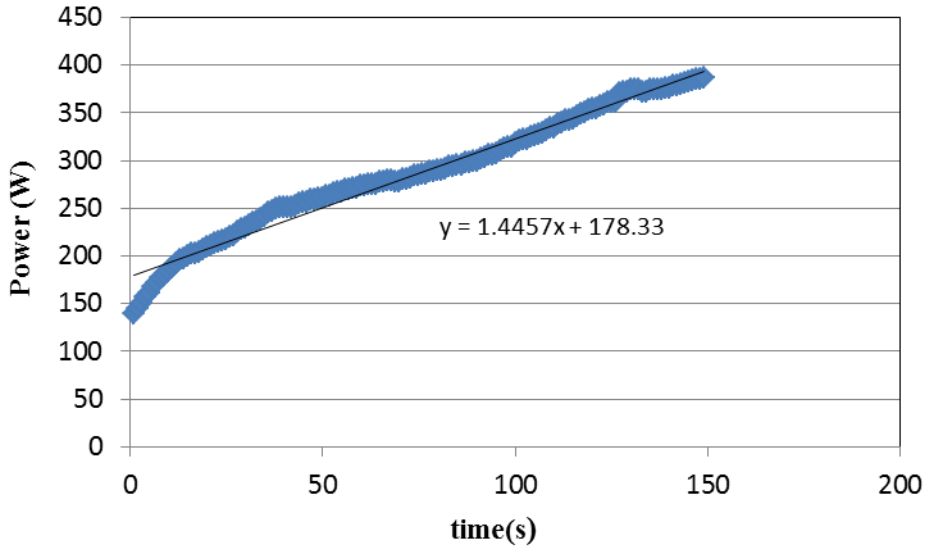

Figure 4-28 Power extracted VS. time

And the power versus rotational speed would be as shown:

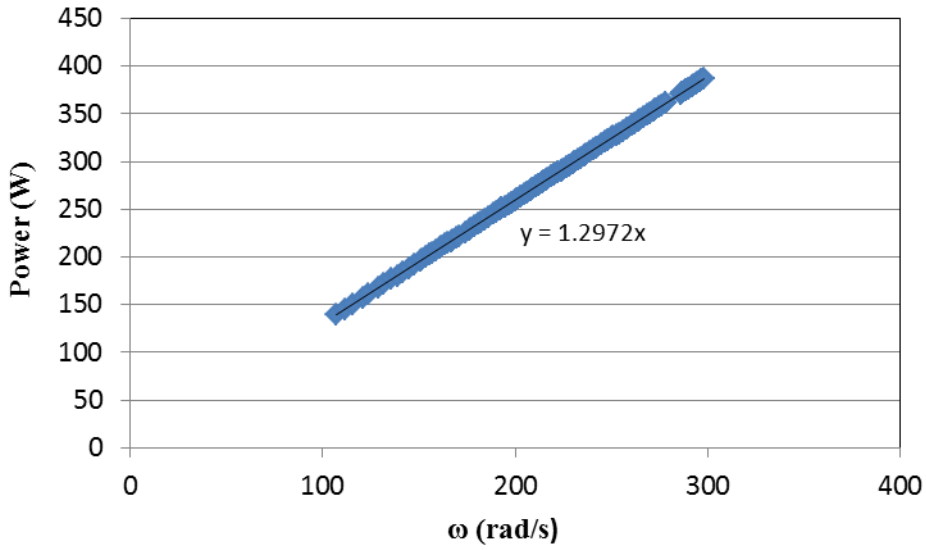

Figure 4-29 Power extracted VS. angular velocity

As it can be seen, for the test using a 5mm nozzle in the position close to the inlet of the rotor, and accelerating to 3000 rpm, a power of 386 W was generated by the turbine.

Instead of using the trend line for estimating the mean value of $\frac{d\omega}{dt}$, but using local $\frac{d\omega}{dt}$ for each rotational speed from the experiment results, the following figure shows the power generated by the rotor for each rotational speed.

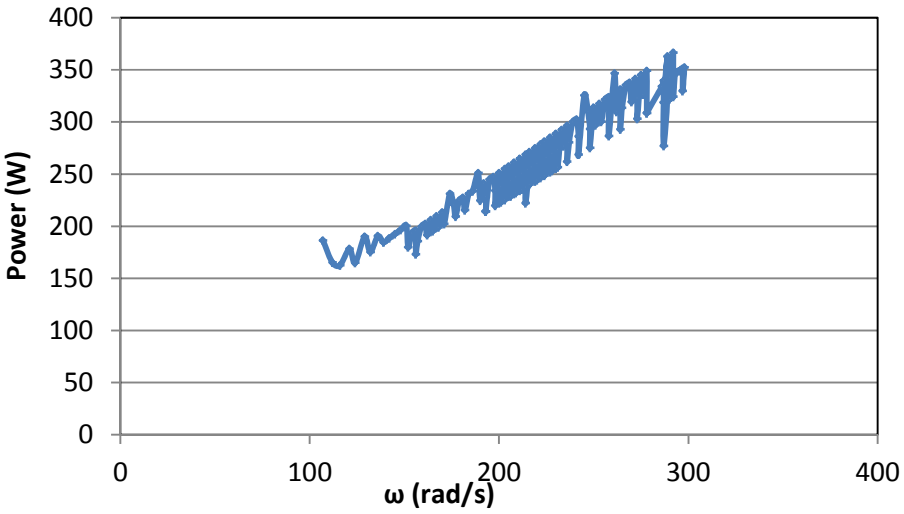

Figure 4-30 Power extracted VS. angular velocity using experimental acceleration

As it can be seen from the Figure 4-30 there are some fluctuations because of the continuous recording of the rotational speed. It is also acceptable that the power at maximum speed based on instantaneous measurements is consistent with that based on the mean acceleration rate.

4.6 Theoretical analysis of the heat exchanger

4.6.1 Condenser Design

Condensation occurs when the temperature of a vapor is reduced below its saturation temperature. In industrial equipment, the process commonly results from contact between the vapor and a cool surface. The latent energy of the vapor is released, heat is transferred to the surface, and the condensate is formed. Other common modes are homogeneous condensation where vapor condenses out as droplets suspended in a gas phase to form a fog, and direct contact condensation which occurs when vapor is brought into contact with a cold liquid.

There may be several complicating features associated with film condensation. The film originates at the top of the plate and flows downward under the influence of gravity. The thickness and the condensate mass flow rate increase with increasing the length because

of continuous condensation at the liquid-vapor interface which is at Tsat. There is then heat transfer from this interface through the film to the surface, which is maintained at Ts<Tsat. In the most general case the vapor may be superheated and may be part of a mixture containing one or more noncondensable gases. Moreover, there exists a finite shear stress at the liquid-Vapor interface, contributing to a velocity gradient in the vapor, as well as in the film.

4.6.1.1 Plate heat exchanger

Another type of heat exchanger is the plate heat exchanger. One form consists of multiple, thin, slightly-separated plates that have very large surface areas and fluid flow passages for heat transfer. This stacked-plate arrangement can be more effective, in a given space, than the shell and tube heat exchanger. Advances in gasket and brazing technology have made the plate-type heat exchanger increasingly practical. In HVAC applications, large heat exchangers of this type are called plate-and-frame; when used in open loops, these heat exchangers are normally of the gasket type to allow periodic disassembly, cleaning, and inspection. There are many types of permanently-bonded plate heat exchangers, such as dip-brazed and vacuum-brazed plate varieties, and they are often specified for closed-loop applications such as refrigeration. Plate heat exchangers also differ in the types of plates that are used, and in the configurations of those plates. Some plates may be stamped with "chevron" or other patterns, where others may have machined fins and/or grooves.

4.6.1.2 Plate fin heat exchanger

This type of heat exchanger uses "sandwiched" passages containing fins to increase the affectivity of the unit. The designs include cross flow and counter flow coupled with various fin configurations such as straight fins, offset fins and wavy fins.

Plate and fin heat exchangers are usually made of aluminium alloys which provide higher heat transfer efficiency. The material enables the system to operate at a lower temperature and reduce the weight of the equipment. Plate and fin heat exchangers are mostly used for

low temperature services such as natural gas, helium and oxygen liquefaction plants, air separation plants and transport industries such as motor and aircraft engines.

Advantages of plate and fin heat exchangers:

- High heat transfer efficiency especially in gas treatment
- Larger heat transfer area
- Approximately 5 times lighter in weight than that of shell and tube heat exchanger.
- Able to withstand high pressure
- Ease of Cleaning, The heat exchanger can be easily dismantled for inspection and cleaning (especially in food processing) and the plates are also easily replaceable as they can be removed and replaced individually.
- Temperature Control, The plate heat exchanger can operate with relatively small temperature differences. This is an advantage when high temperatures must be avoided. Local overheating and possibility of stagnant zones can also be reduced by the form of the flow passage.

Disadvantages of plate and fin heat exchangers:

- Might cause clogging as the pathways are very narrow
- Difficult to clean the pathways
- Aluminum alloys are susceptible to Mercury Liquid Embrittlement Failure
- There is a potential for leakage. The leaks that occur are sent to the atmosphere and not between process streams.
- The pressure drop that occurs through a plate heat exchanger is relatively high and the running costs and capital of the pumping system should be considered.

- When loss of containment or loss of pressure occurs, it can take a long time to clean and reinitialise this type of exchanger as hundreds of plates are common in larger builds.
- The narrow spacing between plates can become blocked by particulate contaminants in the fluid, for example oxide and sludge particles found in central heating systems.

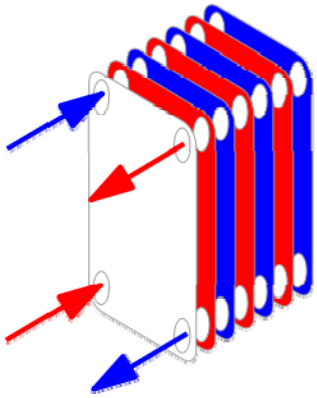

Figure 4-31 Plate and fin heat exchanger

This has a major advantage over a conventional heat exchanger in that the fluids are exposed to a much larger surface area because the fluids spread out over the plates. This facilitates the transfer of heat, and greatly increases the speed of the temperature change. Plate heat exchangers are now common and very small brazed versions are used in the hot-water sections of millions of combination boilers. The high heat transfer efficiency for such a small physical size has increased the domestic hot water (DHW) flow rate of combination boilers. The small plate heat exchanger has made a great impact in domestic heating and hot-water. Larger commercial versions use gaskets between the plates, smaller version tend to be brazed.

4.6.1.3 Spiral Heat Exchanger

A spiral heat exchanger (SHE), may refer to a helical (coiled) tube configuration, more generally, the term refers to a pair of flat surfaces that are coiled to form the two channels in a counter-flow arrangement. Each of the two channels has one long curved path. Pair

of fluid ports is connected tangentially to the outer arms of the spiral, and axial ports are common, but optional.

The main advantage of the SHE is its highly efficient use of space. This attribute is often leveraged and partially reallocated to gain other improvements in performance, according to well-known trade-offs in heat exchanger design. (A notable trade-off is capital cost vs operating cost.) A compact SHE may be used to have a smaller footprint and thus lower all-around capital costs, or an over-sized SHE may be used to have less pressure drop, less pumping energy, higher thermal efficiency, and lower energy costs.

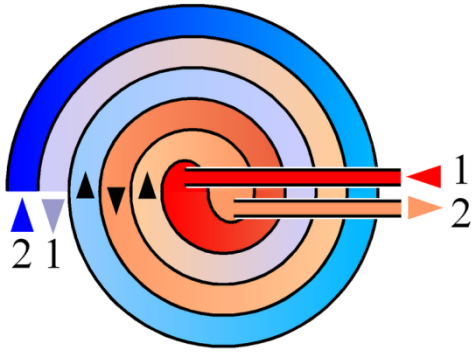

Figure 4-32 Spiral heat exchanger

Construction

The distance between the sheets in the spiral channels are maintained by using spacer studs that were welded prior to rolling. Once the main spiral pack has been rolled, alternate top and bottom edges are welded and each end closed by a gasket flat or conical cover bolted to the body. This ensures no mixing of the two fluids will occur. If a leakage happens, it will be from the periphery cover to the atmosphere, or to a passage containing the same fluid.

Self-cleaning

SHEs are often used in the heating of fluids which contain solids and thus have a tendency to foul the inside of the heat exchanger. The low pressure drop gives the SHE its ability to handle fouling more easily. The SHE uses a “self-cleaning” mechanism, whereby fouled surfaces cause a localized increase in fluid velocity, thus increasing the drag (or fluid friction) on the fouled surface, thus helping to dislodge the blockage and keep the heat exchanger clean. "The internal walls that make up the heat transfer

surface are often rather thick, which makes the SHE very robust, and able to last a long time in demanding environments." They are also easily cleaned, opening out like an oven where any build-up of foulant can be removed by pressure washing.

Self-Cleaning Water filters are used to keep the system clean and running without the need to shut down or replace cartridges and bags.

Flow Arrangements

There are three main types of flows in a spiral heat exchanger:

- Counter-current Flow: Fluids flow in opposite directions. These are used for liquid-liquid, condensing and gas cooling applications. Units are usually mounted vertically when condensing vapour and mounted horizontally when handling high concentrations of solids.
- Spiral Flow/Cross Flow: One fluid is in spiral flow and the other in a cross flow. Spiral flow passages are welded at each side for this type of spiral heat exchanger. This type of flow is suitable for handling low density gases which passes through the cross flow, avoiding pressure loss. It can be used for liquid-liquid applications if one liquid has a considerably greater flow rate than the other.
- Distributed Vapour/Spiral flow: This design is a condenser, and is usually mounted vertically. It is designed to cater for the sub-cooling of both condensate and non-condensables. The coolant moves in a spiral and leaves via the top. Hot gases that enter leave as condensate via the bottom outlet.

4.6.1.4 Shell and tube heat exchanger

Shell and tube heat exchangers consist of a series of tubes. One set of these tubes contains the fluid that must be either heated or cooled. The second fluid runs over the tubes that are being heated or cooled so that it can either provide the heat or absorb the heat required. A set of tubes is called the tube bundle and can be made up of several types of tubes: plain, longitudinally finned, etc. Shell and tube heat exchangers are typically used for high-pressure applications (with pressures greater than 30 bar and temperatures greater than 260°C). This is because the shell and tube heat exchangers are robust due to their shape.

There are several thermal design features that are to be taken into account when designing the tubes in the shell and tube heat exchangers. These include:

Tube diameter: Using a small tube diameter makes the heat exchanger both economical and compact. However, it is more likely for the heat exchanger to foul up faster and the small size makes mechanical cleaning of the fouling difficult. To prevail over the fouling and cleaning problems, larger tube diameters can be used. Thus to determine the tube diameter, the available space, cost and the fouling nature of the fluids must be considered.

Tube thickness: The thickness of the wall of the tubes is usually determined to ensure:

- There is enough room for corrosion
- That flow-induced vibration has resistance
- Axial strength
- Availability of spare parts
- Hoop strength (to withstand internal tube pressure)
- Buckling strength (to withstand overpressure in the shell)
- Tube length: heat exchangers are usually cheaper when they have a smaller shell diameter and a long tube length. Thus, typically there is an aim to make the heat exchanger as long as physically possible whilst not exceeding production capabilities. However, there are many limitations for this, including the space available at the site where it is going to be used and the need to ensure that there are tubes available in lengths that are twice the required length (so that the tubes can be withdrawn and replaced). Also, it has to be remembered that long, thin tubes are difficult to take out and replace.
- Tube pitch: when designing the tubes, it is practical to ensure that the tube pitch (i.e., the centre-centre distance of adjoining tubes) is not less than 1.25 times the tubes' outside diameter. A larger tube pitch leads to a larger overall shell diameter which leads to a more expensive heat exchanger.

- Tube corrugation: this type of tubes, mainly used for the inner tubes, increases the turbulence of the fluids and the effect is very important in the heat transfer giving a better performance.
- Tube Layout: refers to how tubes are positioned within the shell. There are four main types of tube layout, which are, triangular (30°), rotated triangular (60°), square (90°) and rotated square (45°). The triangular patterns are employed to give greater heat transfer as they force the fluid to flow in a more turbulent fashion around the piping. Square patterns are employed where high fouling is experienced and cleaning is more regular.
- Baffle Design: baffles are used in shell and tube heat exchangers to direct fluid across the tube bundle. They run perpendicularly to the shell and hold the bundle, preventing the tubes from sagging over a long length. They can also prevent the tubes from vibrating. The most common type of baffle is the segmental baffle. The semicircular segmental baffles are oriented at 180 degrees to the adjacent baffles forcing the fluid to flow upward and downwards between the tube bundle. Baffle spacing is of large thermodynamic concern when designing shell and tube heat exchangers. Baffles must be spaced with consideration for the conversion of pressure drop and heat transfer. For thermo economic optimization it is suggested that the baffles be spaced no closer than 20% of the shell's inner diameter. Having baffles spaced too closely causes a greater pressure drop because of flow redirection. Consequently having the baffles spaced too far apart means that there may be cooler spots in the corners between baffles. It is also important to ensure the baffles are spaced close enough that the tubes do not sag. The other main type of baffle is the disc and donut baffle which consists of two concentric baffles, the outer wider baffle looks like a donut, whilst the inner baffle is shaped as a disk. This type of baffle forces the fluid to pass around each side of the disk then through the donut baffle generating a different type of fluid flow [79].

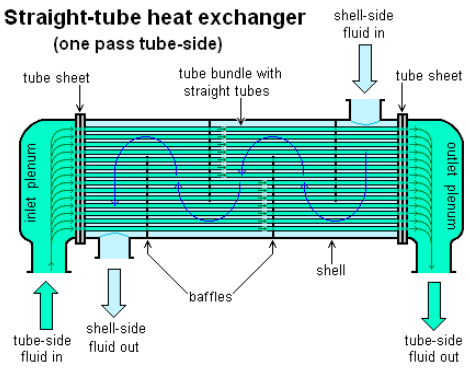

Figure 4-33 Shell and tube heat exchanger

Vertical Arrangement

In the vertical arrangement of the tubes the overall heat transfer coefficient may be calculated through the following procedure.

By knowing the chamber pressure, the saturation temperature of the vapor can be found using the saturation tables. The temperature of the condenser surface should be less than the saturation temperature of the vapor. Technically this difference can be assumed to be 5-6 °C. Therefore,

$$T_{Condenser\quad Surface} = T_{Chamber\quad Vapor} - 6 \tag{4.39}$$

As the input energy required and total mass flow rate of the cold water are known, the temperature of cooling water out would be:

$$T_{Cooling\,water\quad out} = \frac{Q}{\dot{m} C_p} + T_{Cooling\,water\quad in} \tag{4.40}$$

Considering the number of branches for the condenser (N),

$$Total\ mass\ \ flow\,rate\,in\,each\,branch = \frac{Total\ mass\ \ flow\,rate}{N} \tag{4.41}$$

Assuming the outer diameter and tube wall thickness for the tubes are known based on considering the design configuration, the inner diameter can be calculated as:

$$D_i = D_o - 2 \times t \tag{4.42}$$

The volume flow rate in each branch is:

$$v_1 = \frac{Total\ mass\ flow\ rate\ in\ each\ branch}{\rho} \quad (m^3/s) \tag{4.43}$$

And the velocity of cooling water in each branch:

$$V_1 = \frac{v_1}{A_i} \quad (m/s) \tag{4.44}$$

This velocity must be in the range of 1-3 m/s as air bubbles will appear if it is less than 1 m/s and some erosion will occur in the condenser if the velocity of water is more than 3 m/s. The values for Re, f, Pr and Nu may be calculated as below:

$$\mathrm{Re} = \frac{\rho v_1 D_o}{\mu} \tag{4.45}$$

And,

$$f = \{if\ \mathrm{Re} > 4000\} = 0.184 \times \mathrm{Re}^{-1/5} \tag{4.46}$$
$$= \{if\ \mathrm{Re} < 4000\} = \frac{64}{\mathrm{Re}}$$

Also,

$$\mathrm{Pr} = \frac{C_p \mu}{k_f} \tag{4.47}$$

Nusselt number,

$$Nu = 0.023 \times \mathrm{Re}^{4/5} \times \mathrm{Pr}^{2/5} \tag{4.48}$$

According to above calculation h_i would be:

$$h_i = \frac{k_f Nu}{D_i} \tag{4.49}$$

For vertical arrangement of the tubes, h_o is calculated using below equation:

$$h_o = 0.943\left[\frac{h_{fg} g(\rho_l - \rho_v)k_l^{\ 3}}{H(T_{sat} - T_s)}\right]^{1/4} \tag{4.50}$$

In which, H is the height of each branch and Ts is the condenser surface temperature. Therefore, the overall heat transfer coefficient is:

$$U = \frac{1}{\frac{1}{(\frac{r_i}{r_o})h_i} + \frac{r_o \ln(\frac{r_o}{r_i})}{k_{material}} + \frac{1}{h_o}} \tag{4.51}$$

Total surface area:

$$A_t = \frac{Q}{U \times (T_{Cooling\ water\ \ out} - T_{Cooling\ water\ \ in})} \tag{4.52}$$

According to the surface area, the total length is:

$$L = \frac{A_t}{3.14 \times D_o} \tag{4.53}$$

So the pressure drop in each branch can be found as:

$$\Delta P = \frac{f \times \rho \times V^2 \times L}{2 \times D_i} \tag{4.54}$$

Power loss in the tubes would be:

$$Power = v_1 \times N \times \Delta P \tag{4.55}$$

Horizontal Arrangement

The same procedure can be used for a horizontal arrangement with different definition of h_o:

$$h_o = 0.789\left[\frac{h_{fg} g\rho_l(\rho_l - \rho_v)k_l^{\,3}}{N\mu_l(T_{sat} - T_s)D_o}\right]^{1/4} \tag{4.56}$$

For liquid with relatively low enthalpies of phase change, such as many refrigerants, a correction is needed for the sub cooling term. The modified latent heat can be used in the equations as follows:

$$h_{fg}{}' = h_{fg} + (0.683 - \frac{0.228}{\mathrm{Pr}_l})C_{pl}(T_{sat} - T_s) \tag{4.57}$$

Based on the calculation provided, a computer model has been designed and used in order to design a heat exchanger with the required capacity and also appropriate arrangement. This model is discussed in chapter 6.

Chapter 5 Design of the simple two-phase flow reaction turbine operating in the CDP

5.1 Introduction

Following the theoretical analysis of simple reaction turbine presented in the previous chapter, here use is made of that analysis to design and configure prototypes of simple reaction turbines. This chapter describes how to design a simple water reaction turbine. In the case of a simple water reaction turbine the water enters the turbine axially from an intake pipe attached to the bottom of the turbine through a rotary seal and exits tangentially through nozzles located on the outer periphery of the turbine.

The main purpose of this study was to develop a simple design for a two-phase flow reaction turbine, and measure its performance characteristics using sub-cooled hot water as working fluid. This turbines purpose is use in a combined desalination and power generation system which operates on the thermodynamic trilateral flash cycle. The working principle of the combined desalination and power generation system is explained with the help of a system schematic and the governing equations. Design of the two-phase turbine used for this study is described with the help of part and assembly drawings, this is followed by description of the test facility and experimental procedure. Sub-cooled feed water at 96°C and under local atmospheric pressure was supplied to the turbine while the pressure at the turbine exit was maintained at approximately 6kPa absolute. The flow rate of feed water was controlled by the static pressure difference, throat area and the rotational speed of the turbine. The turbine under investigation had outer diameter of 412mm, throat diameter of 2.5mm and total nozzle exit area of 1320mm² for two curved nozzles. It was found that the best position of the throat for the turbine under study was approximately 34mm from the center of the turbine. Further it was found that when a flat head pin with 2.5mm diameter was placed in-line with the throat at 4mm distance from the throat the turbine performance improved significantly. The maximum power output of the two-nozzle turbine under investigation with pin is estimated to be approximately 160W with an isentropic efficiency of approximately 6%.

5.2 Previous work on flashing

Many researchers have studied flash boiling phenomena for a number of different applications, with most employing two-phase stationary nozzles [88],[89],[90],[91]. In 1986, Yoshiro, Hiroichi and Teruo conducted experiments to study flashing of superheated liquid jets of water and ethanol into vacuum chambers through stationary nozzles[90]. Experiments showed that two different patterns were formed depending on the superheat temperature. Complete flashing occurred when the temperature of the liquid was far above the bubble point, while breaking of liquid jet occurred at temperatures closer to the bubble point. They say that spraying is likely to occur when the nozzle is short.

In 1987, Gopalakrishna, Purushothaman and Lior studied the flash evaporation from a hot water pool[91]. This study was conducted with fresh water and with saline water (3.5% NaCl concentration) for initial temperatures from 25°C – 80°C and flash-down temperature differences from 0.5°C – 10°C. It was found that the flashed mass increases with Jakob number and pool depth.

In 1993, Ohta and Fujii used a thin wire in front of the throat of a converging and diverging nozzle to enhance the flashing process[92]. They found that the slip between the vapor and liquid along the diverging section and the maximum non-equilibrium pressure drop at the nozzle throat cause a decline in the nozzle efficiency. They did experiments on stationary nozzles with sub-cooled hot water at 136°C to 148°C.

In 1996, Bunch and team experimentally estimated performance of a stationary flashing flow nozzle using R134a in an energy system using geothermal high pressure hot water from a combination of thrust, flow, pressure and temperature measurements [93]. They found that seeding bubbles helped to improve the performance of the flashing nozzles and the nozzle efficiency was found to range from 33 to 47%.

In 2004, Brown and York studied the spray formation in a stationary nozzle during flashing process; critical superheat was found through this study [88]. Sprays from water and Freon-11 jets were experimentally analysed and the critical value of Weber number was found to be 12.5 for bubble growth of low viscosity liquids.

In 2009, Sami and Yasuyuki reported the influencing factors and their effects on the intensity of flash evaporation that occurs in the superheated water jets for stationary nozzles [94]. Through variety of experiments velocity of flow, initial temperature and degree of super-heat and injection nozzle diameter were investigated.

In 2009, Zhao, Akbarzadeh and Andrews proposed a novel system for simultaneous desalination and power generation which operate on trilateral flash cycle [16]. This system used flashing of sub-cooled hot water due to sudden depressurisation through a two-phase flow turbine. Initially a two arm rotor was used which showed that the power loss due to vapour drag was too high and hence a disk shaped rotor with curved nozzles should be used to improve the overall performance of the system. The hot working fluid forms a jet as it enters the low pressure diverging section of the converging-diverging nozzle within the turbine and now this superheated liquid jet starts to flash. The liquid and vapour part of the working fluid jet tend to separated more readily due to centrifugal, centripetal and coriolis forces acting on the fluid while turbine is rotating. The separation of liquid and vapour part cause loss in momentum and hence reduces the turbine efficiency. They suggested that early atomization of the superheated jet could help delay separation of liquid and vapour part and hence help improve the efficiency of the turbine. The present paper is a continuation of this research and is focused on improving the overall performance of the combined desalination and power generation system.

5.3 Characteristic of the reaction turbine used in the combined desalination and power generation system

As the concept of Combined Desalination and Power generation (CDP) has been introduced in Chapter 1, a radially outwards flow turbine was chosen in order to increase the output. This section discusses this matter in detail.

The ability to handle two-phase flow would allow a turbine to be coupled directly to a source of pressurized fluid containing, or flashing to, both a liquid phase and a gas

phase. It is considered that practical two-phase turbines would find substantial application in open or closed energy conversion cycles.

The theoretical thermal efficiencies of two fluid component, two-phase systems approach the Carnot cycle efficiency because of reheat of vapor by the liquid phase during expansion. This means that potentially considerably more mechanical or electrical energy can be generated from the same thermal energy from a heat source. Even for single component, two-phase turbine systems, the thermal efficiencies are higher than for comparable conventional Brayton or Rankine cycles.

In order to realize the full energy conversion potential of a two-phase turbine, it is necessary to design such a turbine, with high efficiency. In most of the development work on two-phase turbines in the past, substantial mechanical flow energy losses were experienced within the turbines. Demonstrated turbine efficiencies were at best in the range of 40%-45% for long lasting devices.

The concept of using a two-phase flow turbine in a CDP is shown in Figure 5-1.

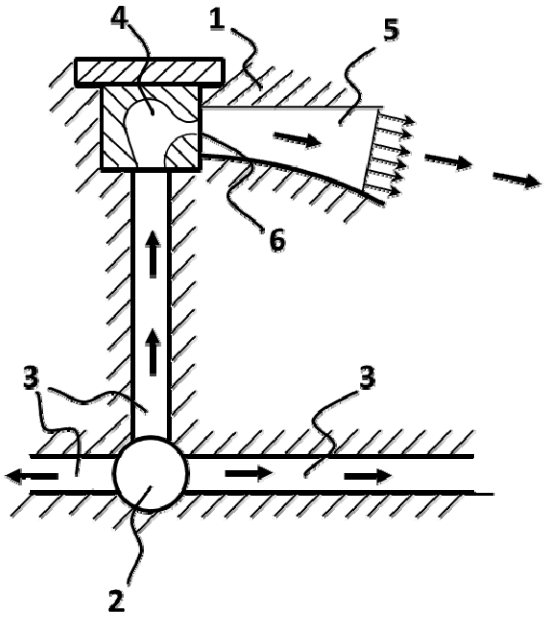

Figure 5-1 Schematic of principle of two phase flow turbine

Saturated hot water was introduced into the rotor through a hollow shaft 2. The saturated water then flowed radially outwardly through passages 3 and was flashed

through straight, short DeLaval nozzles tangentially to the rotor. The DeLavel nozzles consisted of two parts, a very short liquid converging nozzle 4 and a longer straight diverging two-phase nozzle 5. At the end of the liquid nozzle a discontinuous enlargement 6 of two or three times the cross-sectional area of the nozzle was used.

In rotating stepped DeLavel nozzles such as shown in Figure 5.1, severely delayed flashing has been found to occur. That is, as the saturated liquid travels from the center toward the outer radial edge of the rotor it becomes highly subcooled because of a very large pressure increase caused by the very substantial centrifugal accelerations of the order of several thousand g's. Flashing of highly subcooled liquid through very short nozzles yields low efficiency in such cases. Vapor nucleation sites are too small and do not have enough time to grow while the liquid passes quickly through the short converging part of the nozzle.

Another inefficiency of such devices is the existence of large lateral accelerations (of the order of multi thousands g's). This extreme lateral acceleration tends to separate the two phases and drastically increase the velocity slip loss. The slip loss causes loss of nozzle efficiency due to the vapor moving faster than the liquid.

Therefore, in the design of the two phase turbine for the CDP, these two main sources of inefficiency has been focused on. As one consideration, extended nozzles were contemplated having no substantial discontinuities in a converging diverging cross-sectional contour from near the center of a turbine rotor to its outer periphery. In this way, pressure in the nozzles drops gradually from the saturated or near saturated pressure at the hollow shaft to the discharge pressure. Thus, abrupt flashing is avoided.

In a second consideration, extended radially outward flow turbine nozzles are employed which are curved in such a way that the vectorial sum of all acceleration on the fluid within each nozzle has a minimal lateral component with respect to the local streamline direction of the nozzle. In this design, staging is employed such that separation of saturated liquid and saturated vapor occurs between stages with further expansion through two phase flow and vapor flow nozzles respectively.

5.4 Detailed description of the novel two phase reaction turbine

As has been introduced, the two major problems limiting the efficiency of two-phase reaction turbines are addressed in the preferred embodiment. These problems are two-phase flow separation in the rotating nozzles due to very large lateral centrifugal forces and abrupt flashing of highly subcooled liquid into two phase flow through short nozzles.

Nozzle 7 in Figure 5.2 illustrates a rotating radially outward flow, DeLaval nozzle. Through proper curvature, no overall component of acceleration lateral to the nozzle is experienced. In such a case, separation of the phases will be minimal. Figure 5-2 indicates accelerations which act on the fluid moving along the curved rotating nozzle.

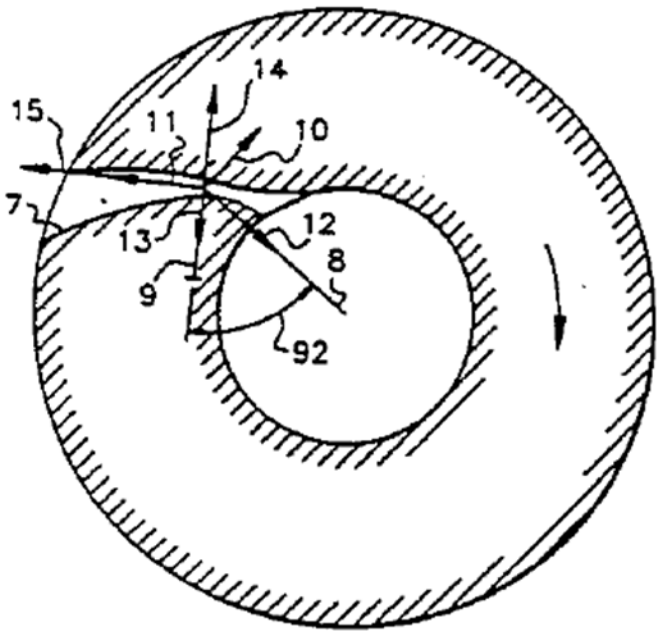

Figure 5-2 Schematic of the path of the nozzle

By selecting the local radii of curvature, one can balance out the lateral accelerations all the way along the nozzle. In other words the equation below should be satisfied all the way along the nozzle

$$\frac{w^2}{\rho} + \frac{u^2}{\rho}\cos\alpha - \frac{2uw}{R} = 0 \tag{5.1}$$

Using a computer model which predicts expansion of two-phase flow in a stationary DeLaval nozzle as well as the above equation, a numerical iterative procedure can be devised to obtain the exact shape and cross-section of the curved rotating nozzles.

A second feature is the design of the curved rotating nozzles such that gradual expansion or gradual pressure drop without any rise in pressure of the steam is achieved along an extended length of the nozzle as shown in Figure 5-3. In such a way, enough time is allowed for vapor nucleation sites to grow gradually so that abrupt, inefficient flashing is avoided.

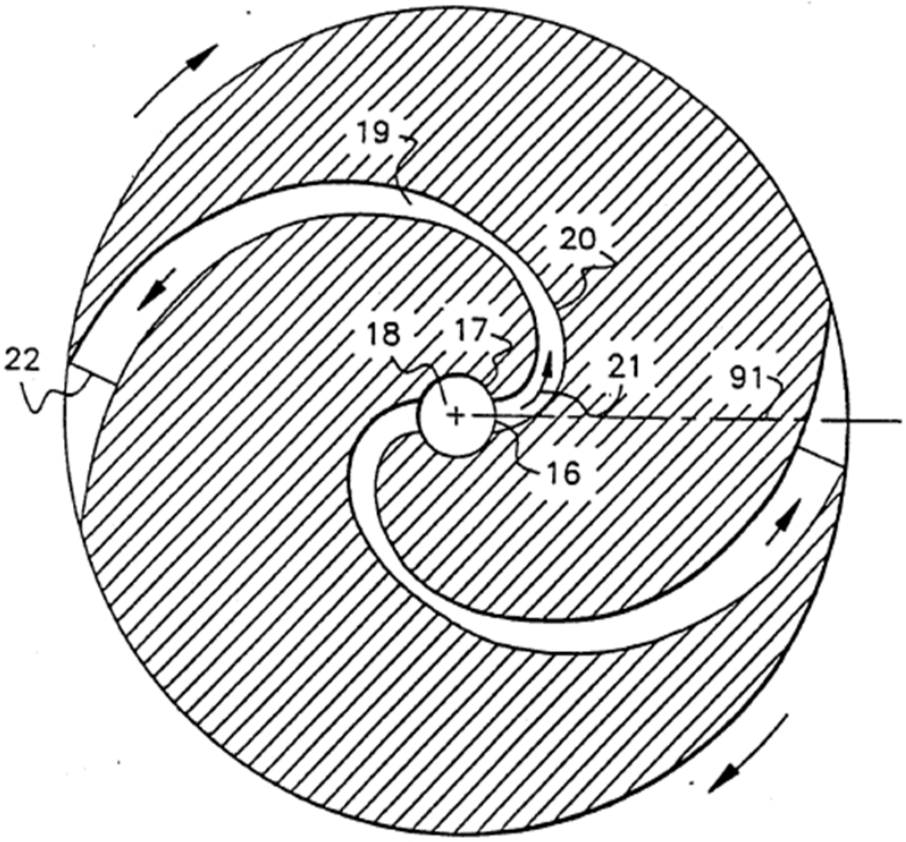

Figure 5-3 curved rotating nozzle

To achieve this result, the inlet 16 to the nozzle 19 should be placed at the outer radius 17 of the hollow shaft 18. Pressure of the fluid in the hollow shaft 18 is at saturation pressure or slightly higher. After entering the nozzle 19 at its entrance 16, the

fluid proceeds along the converging part 20 of the nozzle 19 as indicated by arrow 21. Line 91 indicates the radial direction at the nozzle entrance. The cross sectional area of the nozzle 19 changes from the nozzle inlet 16 to the nozzle outlet 22 in such a way that pressure decreases approximately uniformly per unit of length along the nozzle. In this way the pressure decrease and the expansion are very gradual.

By starting the pressure drop in the nozzle from close to the saturation pressure, the vapor nucleation sites, i.e. miniature bubbles in the liquid, are an order of magnitude larger than in a highly subcooled liquid. The size of a vapor nucleation site is of critical importance in the dynamics of the flashing process. The size of the nucleation sites can determine if flashing is in thermodynamic equilibrium (efficient propulsive flashing) or is in non-equilibrium (abrupt inefficient propulsive flashing).

The flashing fluid flowing through the nozzles 19 gradually decreases in pressure over time. The time during which this occurs is approximately two orders of magnitude longer than in the system depicted in Figure 5.1. This extended flashing also ensures that the expansion is in thermodynamic equilibrium.

A numerical procedure has been developed to generate the shape of the rotating nozzles. Fluid particles travelling with specified velocity along the nozzle need to experience no net or minimal force component normal to the streamline. In other words there would be no or minimal separation forces acting on the liquid. As discussed earlier the constraining equation is derived from the acceleration balance on a fluid particle that has relative velocity w (11) at a distance R (8) from the center of rotation. Local velocity of the rotor is u (10), and the radius of curvature of the nozzle is ρ (9).

The resulting equation is repeated here as:

$$\frac{w^2}{\rho} + \frac{u^2}{\rho}\cos\alpha - \frac{2uw}{R} = 0 \qquad (5.2)$$

If ω is the angular velocity of the rotor of a turbine then the Equation 5.3 relates the local rotor velocity to local radius.

$$u = R\omega \tag{5.3}$$

The procedure developed is an extensive iterative numerical computer method. It starts with an assumed relative velocity w profile in a rotating system as a function of distance along the nozzle measured from the nozzle inlet. The velocity w profile is actually obtained by running the stationary nozzle computer code for specified nozzle inlet conditions and using the resulting exit bulk velocity (V_b) in the energy equation between two points along a passage in a rotating system. The bulk velocity is defined as a local cross-sectional average fluid velocity (for both phases) as predicted by the computer code.

Knowing w (the relative velocity) at any point, geometry and constraining equations are used to advance in small steps until the outer diameter of the rotor is reached. The nozzle overall length is found at this point as well as the corresponding relative velocity. If this discharge velocity differs from what was prescribed by the stationary nozzle run, then the velocity profile is changed and iterations are continued until agreement is reached.

The equation used to calculate the relative velocity in a rotating passage requires the value of enthalpy drop Δh between a reference point (entrance to the nozzle) and any other point along the passage. An estimate of Δh can be retrieved from the stationary nozzle code run converting V_b at the point into the enthalpy change.

For simplicity a linear velocity profile was selected with the maximum velocity at discharge V_{bmax} the same as predicted by the stationary nozzle run. So for a point N along the passage:

$$V_{bN} = \frac{V_{b\max} S_N}{S_{\max}} \tag{5.4}$$

w

where V_{bN} is the relative velocity at a local point N of an equivalent stationary nozzle, S_N is the distance along the nozzle from the nozzle entrance to the point N and S_{max} is the total length of the nozzle.

The relative velocity in the rotating nozzle, at a point equivalent to a point in a stationary nozzle, can now be calculated as below

$$w_n^2 = w_o^2 + (u_n^2 - u_o^2) + 2\Delta h_n \tag{5.5}$$

$$\Delta h_n = \frac{1}{2} V_{bN}^2 \tag{5.6}$$

$$u_n = \omega R_n \tag{5.7}$$

Also w_o and u_o have knowns value at the reference point which is the entrance to the nozzle. Figure 5-4 shows a method for finding appropriate local radii of curvature of the rotating nozzle. Local point N is on radial distance Rn from the center of the rotor. Points N-1 and N+1 are located at incremental distances upstream and downstream of the point N. the incremental distance in the stream wise direction between two points is denoted by ΔS. The rotor radii at appropriate nozzle points are R_n , R_{n-1} and R_{n+1}. Radii of nozzle curvature at appropriate points are ρ_n , ρ_{n-1} and ρ_{n+1}.

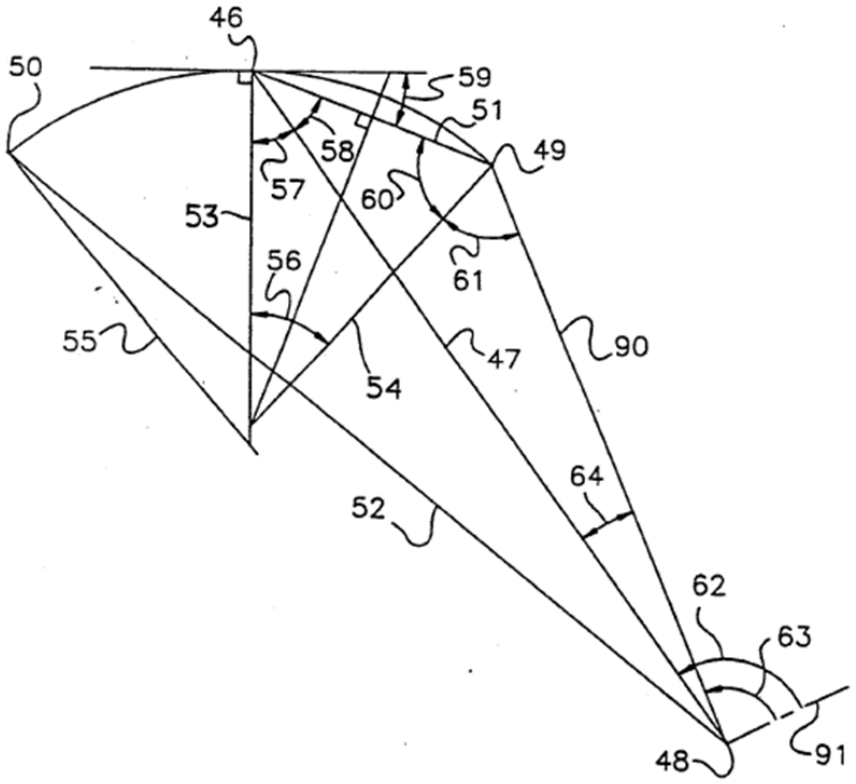

Figure 5-4 Method for finding appropriate local radii of curvature of the rotating nozzle

Indicated angles are $2\beta_n$, α_n, γ_n, β_n, $90-\beta_n$, α_{n-1}, θ_n, θ_{n-1} and $\Delta\ \theta_n$. Knowing the relative velocity of the fluid along the nozzle at the upstream point N-1 and solving the constraining equation for the radius of curvature, the Equation 5.8 can be generated:

$$\rho_{N-1} = \frac{w_{N-1}^2}{[\omega(2w_{N-1} - u_{N-1}\cos\alpha_{N-1})]} \tag{5.8}$$

Then from the geometry of a triangle N, N-1,O,

$$\beta_{N-1} = SIN^{-1}\frac{\Delta S}{2\rho_{N-1}} \tag{5.9}$$

R_n can be found from the cosine law for a triangle N, N-1, O:

$$R_n = \sqrt{\Delta S^2 + R_{n-1}^2 - 2R_{n-1}\Delta S \times SIN(\beta_n - \alpha_{n-1})} \tag{5.10}$$

Also θ_n is found from the sin law for the same triangle

$$\Delta\theta_n = SIN^{-1}\frac{\Delta S \times COS(\alpha_{n-1} - \beta_n)}{R_n} \tag{5.11}$$

Now α_n can be found as required for the next step.

$$\alpha_n = 90 - \gamma_n - \beta_n = 90 - [180 - (\Delta\theta_n + (90 - \beta_n + \alpha_{n-1}))] - \beta_n = \alpha_{n-1} - 2\beta_n + \Delta\theta_n \tag{5.12}$$

Then for the next step S, θ and N are increased:

$$S=S+1 \tag{5.13}$$

$$\theta= \theta+ \Delta\theta$$

$$N=N+1$$

And then w at the new point is evaluated.

Once the nozzle trajectory, based on a given V_b profile, has been generated, the program checks agreement between the exit relative velocity prescribed and the one that was calculated at the outer radius of the rotor using the numerical routine. If a discrepancy is found a new value is assigned for the nozzle length and a new velocity profile (this time having the prescribed exit velocity at the end of the new trajectory length) is used for the next run. This scheme repeats itself until agreement is reached.

5.5 Design of the path of the groove in the CDP rotor

The first rotor which was designed was a split reaction rotor which has a semi circular path. Figure 5 shows the exploded assembly of a Split Disk Reaction Turbine (SDRT). This turbine is made from four pieces with an outer diameter of 412mm; all the other main dimensions are shown in the Figure 5-5. The throat of the turbine nozzle is made from inserts which can be located at four different locations as shown in Figure 5-5. The throat orifice diameter in the tests was 2.5mm. Placing throat inserts at different locations allows the radial distance (radius) of the throat from the center to be varied, as well as the length of the diverging section of the nozzle after the throat, as shown in Figure 5-5. Radial outward flow simple reaction turbines exhibit centrifugal pumping effect as discussed by researchers developing similar turbines [95]. Centrifugal pumping of working fluid is influenced by changing the position of the throat. Meanwhile, by varying the diverging nozzle length, the time available for the working fluid to flash (change the phase) within the turbine will change.

One of the objectives of this research program was to develop a simple design for a two-phase reaction turbine. The nozzle path is formed by two identical interchangeable nozzle guide vanes placed at 180° to each other. These nozzle guide vanes are made from multiple semi-circles and hence are believed to be easy to design and manufacture. With this design the power output of the turbine can be varied easily by changing the nozzle guide vanes and throat inserts. Figure 5-6 shows the actual turbine and the 2.5mm diameter orifice insert that has been used in the present experimental tests. At the exit of the diverging nozzle the cross section was 33mm x 20mm for each nozzle. The mass moment of inertia of the present turbine rotary system was experimentally estimated to be 0.21 $kg.m^2$.

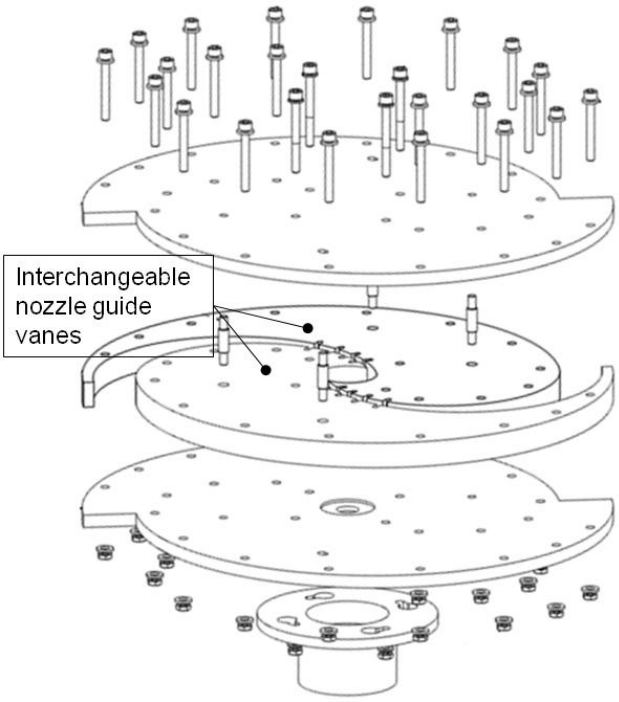

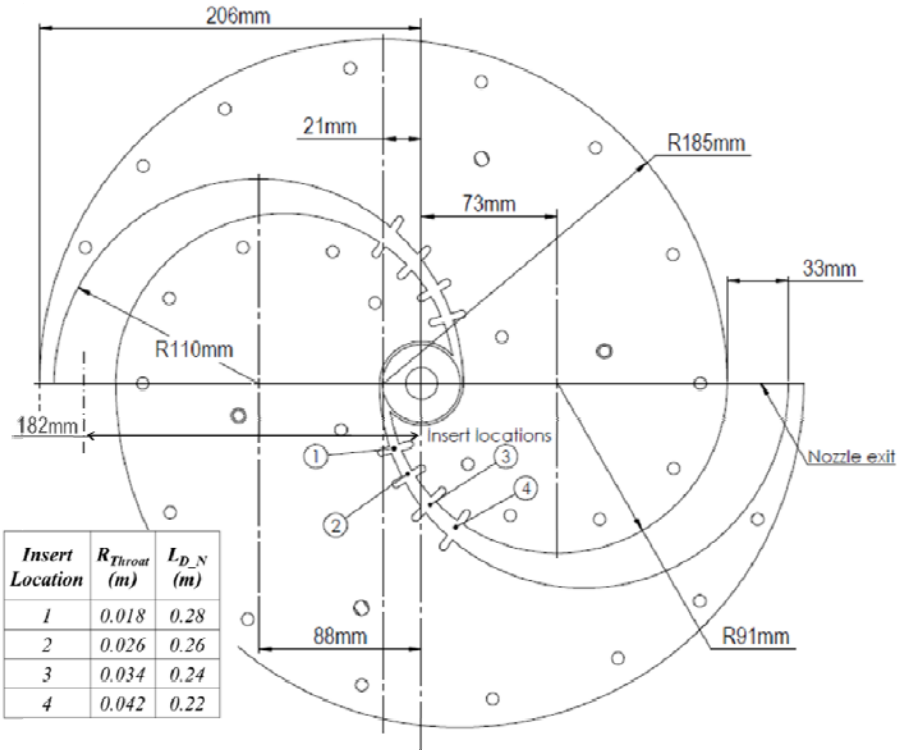

Insert Location	R_{Throat} (m)	L_{D_N} (m)
1	0.018	0.28
2	0.026	0.26
3	0.034	0.24
4	0.042	0.22

Figure 5-5 SDRT exploded assembly

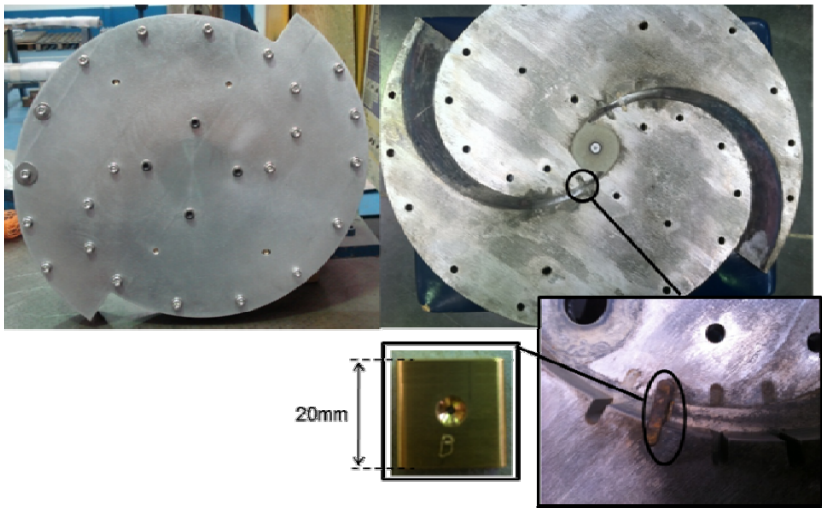

Figure 5-6 Photos of SDRT and brass insert

In configuration tests the position of orifice insert was changed and for each location of the insert the turbine was allowed to accelerate to the maximum rotational speed while maintaining driving temperature difference and then allowed to decelerate. The acceleration and deceleration rates were monitored, recorded and analyzed to estimate the gross shaft power produced by the turbine. The results of the design changes are discussed in details in chapter 8.

From the experimental results for the first turbine with simple semi-circular curved nozzles it was found that the turbine power output and hence the turbine efficiency was very low compared to the theoretical predictions [96]. On the other hand the fresh water production was a close match to the theory. Such behaviour of the CDP system was attributed to a delay in flashing of the fluid and/or separation of the two-phases. In the rotating nozzles, a large lateral acceleration tends to separate the two phases, which drastically decrease the nozzle efficiency due to the vapour moving faster than the liquid. Therefore the nozzle curvature of the second turbine was redesigned based on the suggestions made by Fabris in his 1993 patent [97]. Figure 5-7 illustrates the different acceleration components that are acting on a particle of fluid. The lateral acceleration components that tend to separate the two phases of the fluid are coriolis acceleration $a_{coriolis}$, centripetal acceleration relative to motion $a_{cpt-rel}$ and centripetal acceleration with respect to the centre of the turbine a_{cpt}. While the turbine is stationary

these three acceleration components do not exist and the largest acceleration component is due to the change in the relative motion of the fluid within the nozzle a_{stream}.

$$a_{coriolis} = \frac{2 \times U_{loc} \times V_{r-loc}}{R_{loc}} \tag{5.14}$$

$$a_{cpt-rel} = \frac{V_{r-loc}^2}{r_{loc}} \tag{5.15}$$

$$a_{cpt} = \frac{U_{loc}^2}{R_{loc}} \tag{5.16}$$

Here U_{loc} is the local tangential velocity of the turbine, V_{r-loc} is the local relative fluid velocity inside the nozzle, R_{loc} is the local radius of the turbine, r_{loc} is the local radius of curvature of the nozzle. To estimate the optimal curvature of the two-phase rotating nozzle the pressure drop along the length of the diverging nozzle is assumed to be linear. And the change in relative velocity of fluid along the length of nozzle is also assumed to be linear. The maximum relative velocity at the exit of the nozzle is calculated assuming an isentropic efficiency of 100% for the turbine geometry and proposed test conditions [98]. In theory, the two phases will not separate if the lateral acceleration components balance each other and there is zero resultant lateral acceleration. The curvature of the nozzle for the second turbine is estimated through an extensive iterative process described by Fabris, using the following acceleration balance equation. The operating rotational speed to estimate the curvature of the nozzle of the second turbine is assumed to be 20,000rpm.

$$a_{cpt} + a_{cpt-rel} - a_{coriolis} = \frac{U_{loc}^2}{R_{loc}} + \frac{V_{r-loc}^2}{r_{loc}} - \frac{2 \times U_{loc} \times V_{r-loc}}{R_{loc}} = 0 \tag{5.17}$$

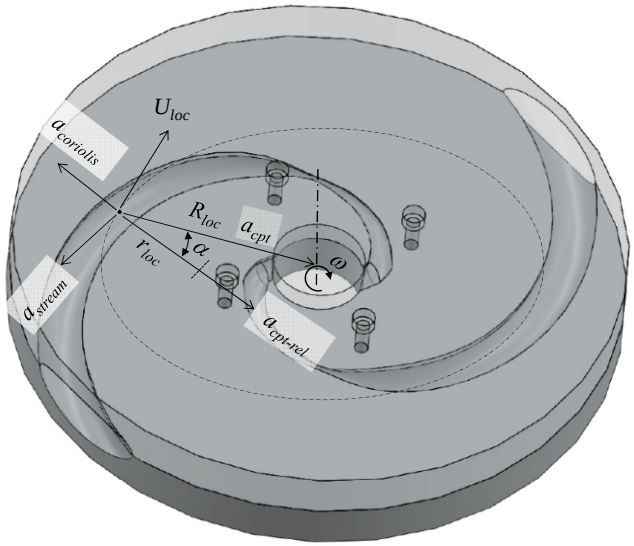

Figure 5-7 Localised lateral acceleration forces acting on a particle of fluid flowing within rotating turbine

Figure 5-8 and Figure 5-9 show the curved nozzle profile, coordinates and radius of nozzle cross section along with photos and drawings of the second turbine under investigation. This turbine was made from 7075-T6 series aluminium alloy to withstand the centrifugal forces that are generated at high rotational speeds. The turbine assembly was made from two plates with curved nozzle grooves machined as mirror images. The turbine had outer diameter of approximately 300mm and total thickness of approximately 40 mm. The turbine was attached using a flanged coupling to a hollow shaft that carried the hot feed water. The throat had a cross sectional diameter of 2mm and the nozzle exit diameter was 25 mm. All radial outward flow simple reaction turbines exhibit centrifugal pumping effect as discussed by researchers developing similar turbines [99, 100]. The throat was located at 59 mm distant from the centre of the turbine to generate enough centrifugal pressure to prevent unintended boiling before the throat which can cause chocking. The mass moment of inertia of this turbine shaft assembly was experimentally estimated to be 0.12 kg-m².

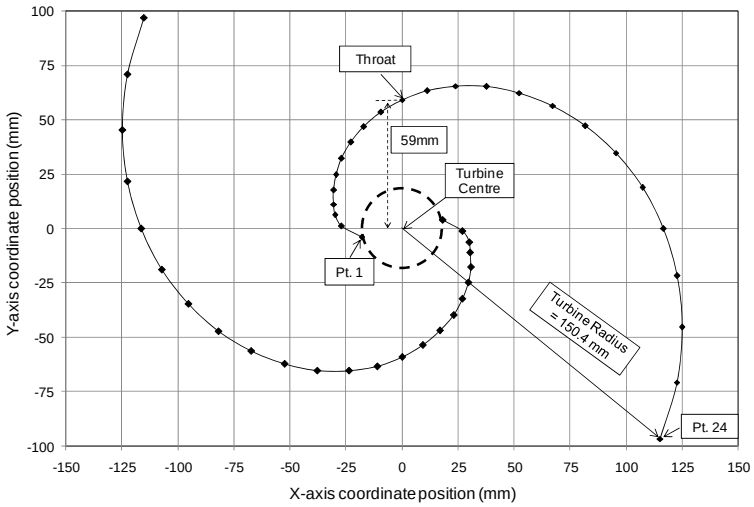

Figure 5-8 Curved nozzle profile of the turbine under investigation

Point No.	X – coordinate (mm)	Y - coordinate (mm)	Radius of nozzle c/s $R_{c/s\ (mm)}$
1	-18	-4	6
2	-27	1.16	5.95
3	-29.94	6.21	5.95
4	-30.54	11.12	5.4
5	-30.61	17.67	4.85
6	-29.5	24.75	4.25
7	-27	32.17	4
8	-22.9	39.66	3.2
9	-17.08	46.92	2.65
10	-9.44	53.55	2.1
Throat	0	59.15	1
12	11.16	63.27	3.25
13	23.82	65.46	5
14	37.7	65.29	6.35
15	52.36	62.4	7.5
16	67.28	56.46	8.5
17	81.87	47.27	9.25
18	95.43	34.73	9.5
19	107.24	18.91	10
20	116.56	0	10.5
21	122.66	-21.63	11.5
22	124.85	-45.44	12
23	122.53	-70.74	12.5
24	115.24	-96.7	12.5

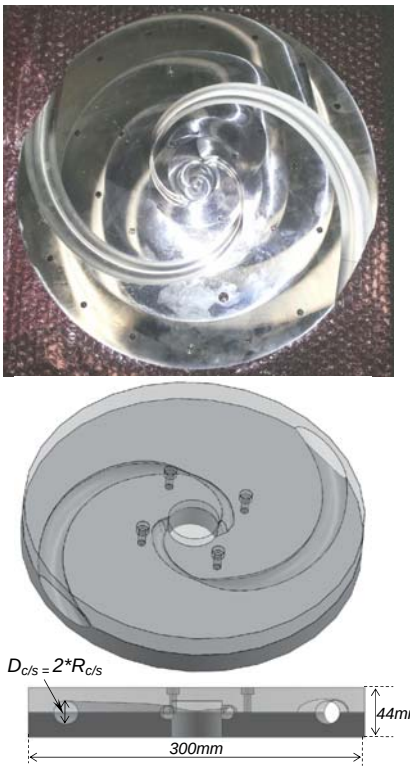

Figure 5-9 Coordinates, radius of nozzle cross section at each point and photo of turbine

Chapter 6 Development of computer model and the theoretical prediction of the CDP performance

6.1 Introduction

In this chapter, the process is discussed for developing the advanced and user-friendly computer model which can be used for designing the Dual system for Power generation and Desalination. In addition, some prediction of the CDP performance is provided in order to indicate the computer model capabilities.

6.2 The procedure of developing the computer model

Based on the analysis which has been done on the trilateral cycle using a simple reaction turbine as has been discussed in chapter 4, section 4.2.2 , the advanced computer model has been developed. This computer model is capable of predicting the performance of the CDP system for different boundary conditions.

Considering the process in the turbine with one central inlet and two outlets shown in Figure 6-1, the energy balance equation can be written for the control volume considered.

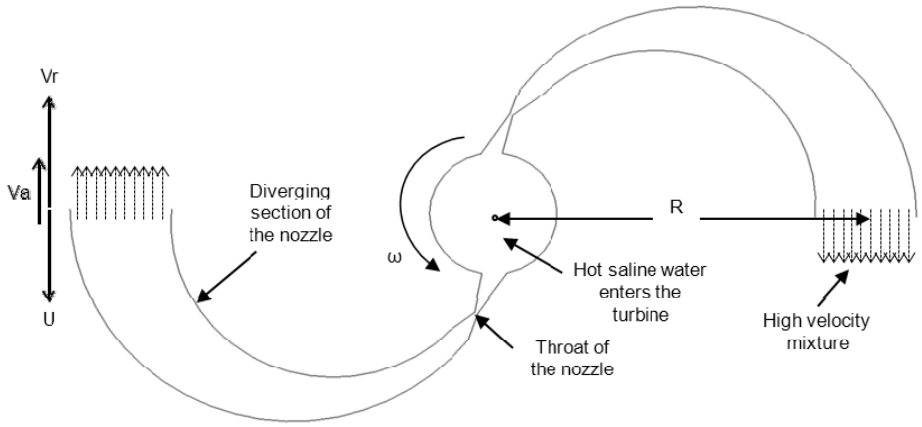

Figure 6-1 Schematic of simple reaction turbine nozzle

$$\dot{m}(h_i + \frac{1}{2}V_i^2 + \rho g z_i) = \dot{m}(h_o + \frac{1}{2}V_o^2 + \rho g z_o) + \dot{Q} + \dot{W} \tag{6.1}$$

Where subscripts i and o refer to the inlet and outlets of the control volume. Because of the very low velocity at the inlet in comparison with the exit velocity, V_i in the above equation can be ignored, and because of the small or zero height difference between the inlet and outlet $z_i = z_o$ and by considering the process as an adiabatic one, $\dot{Q} = 0$. Therefore, the energy balance equation becomes:

$$\dot{m}(h_i - h_o) = \frac{1}{2}\dot{m}V_a^2 + \dot{W} \tag{6.2}$$

Where, Va is the absolute velocity of the mixture leaving the exits of the nozzles and $\dot{W}$ is the rate of mechanical power production by the rotor of the turbine. The torque and the power which are generated by the jet leaving the rotor can be expressed as:

$$\begin{aligned} T(N.m) &= \dot{m}(kg/s) \times V_a(m/s) \times R(m) \\ Power(W) &= T(N.m) \times \omega(1/s) \end{aligned} \tag{6.3}$$

Where ω =2πN /60and N is the rotational speed (RPM).

Therefore $\dot{W}$ can be also calculated as follow:

$$\dot{W} = T\omega = \dot{m} V_a R\omega \tag{6.4}$$

$$V_a = V_r - R\omega \tag{6.5}$$

In addition, the total area of the exit of the nozzle can be found as follow:

$$\dot{m} = \rho_o A V_r = A V_r \frac{1}{v_o} \Rightarrow A = \frac{\dot{m} v_o}{V_r} \tag{6.6}$$

By using, Eqs (6.2), (6.3) and (6.4) $\dot{W}$ can be calculated:

$$\dot{W} = \dot{m} R\omega \left[\sqrt{R^2\omega^2 + 2(h_i - h_o)} - R\omega \right] \tag{6.7}$$

Eliminating V_a and V_r between Eqs. (6.4), (6.5) and (6.6) and substituting $\dot{W}$ from (6.7):

$$A_{exit} = \frac{\dot{m} v_o}{\sqrt{R^2\omega^2 + 2(h_i - h_o)}} \tag{6.8}$$

In addition, from Eqs. (6.6) and (6.8), V_r and Va can be calculated:

$$V_r = \frac{v_o \dot{m}}{\dot{m} v_o} \sqrt{R^2\omega^2 + 2(h_i - h_o)} = \sqrt{R^2\omega^2 + 2(h_i - h_o)} \tag{6.9}$$

$$V_a = \sqrt{R^2\omega^2 + 2(h_i - h_o)} - R\omega \tag{6.10}$$

The overall efficiency of the heat engine is defined as:

$$\eta_{engine} = \frac{Power}{\dot{Q}_H} = \frac{\dot{W}}{\dot{Q}_H} = \frac{\dot{m} R\omega\left[\sqrt{R^2\omega^2 + 2(h_i - h_o)} - R\omega\right]}{\dot{m} C_p (T_i - T_o)} = \frac{R\omega\left[\sqrt{R^2\omega^2 + 2(h_i - h_o)} - R\omega\right]}{C_p (T_i - T_o)} \quad (6.11)$$

Where $\dot{m}$ is the mass flow rate of the feed saline water and T_i is the related temperature at the turbine inlet. To refers to the temperature in the chamber which is assumed to be the condenser temperature. Also, the rate of fresh water production can be obtained from the mass flow rate and the quality of the mixture as $\dot{m} \times x$.

Therefore the recovery ratio becomes:

$$\text{Recovery Ratio} = \frac{Rate\ \ of\ \ fresh\ water\ \ produced}{Rate\ \ of\ \ feed\ salt\ water} = \frac{\dot{m} \times x}{\dot{m}} = x \quad (6.12)$$

In which x is the quality of the mixture at the exit of the nozzles.

6.3 Characteristic of the computer model and performance prediction

The designer of a CDP system can simply enter the input data such as Temperature and mass flow rate of the feeding water, the diameter of the rotor which is going to be used in the system and the desired vacuum pressure of the chamber in the computer model. The output of the model will provide the exit area of the nozzles, the amount of power generation and fresh water production and the isentropic efficiency of the process as well as the thermal efficiency of the system. In addition, from the available thermal energy calculated by the model, the user is able to size the whole system and have access to the properties of the heat exchanger suitable for the designed CDP.

User Input Data		
ational Speed(rad	ω	300
Radius(m)	R	0.2
Description	Temperature (°C)	User Input Data
Turbine Inlet	T2	150
Nozzle Exit	T3	30
Description	Efficiency (%)	User Input Data
Isentropic eff. 1	High	100%
Isentropic eff. 2	Low	50%
Description	Mass flow rate (kg/s)	User Input Data
Input flow rate	m	120

Figure 6-2 Snap shot of input data in the developed computer model

Figure 6.2 shows a sample of asset of input data for the computer model. It can be seen that, by entering the inlet and outlet temperatures, the radius of the rotor, the desired vacuum pressure and the flow rate of the available saline water, all the properties of the water are estimated based on the saturated properties of water, which has been coded into the computer model. Then, based on the analysis in section 6.2 the exit area of the nozzles, power which has been produced for different isentropic efficiencies, fresh water production and the efficiency of the system will be calculated and indicated as the output of the computer model.

Calculated Data					
For Isentropic efficiency =		100%	For Isentropic efficiency =		50%
Description	Quality (x)	Calculated	Description	Enthalpy (kJ/kg)	Calculated
Point 3	x3	0.175	Point 2	h2	632.25
			Point 3'	h3'	591.98
Description	Enthalpy (kJ/kg)	Calculated			
Point 2	h2	632.25	Description	Quality (x)	Calculated
Point 3	h3	551.72	Point 3'	x3'	0.192
Description	Specific Vol. (m³/kg)	Calculated	Description	Specific Vol. (m³/kg)	Calculated
Point 3	V3	5.7652713	Point 3'	V3'	6.310161
Description	Vol. Flow rate. (m³/s)	Calculated	Description	Vol. Flow rate. (m³/s)	Calculated
Point 3	Vdot exit	691.8325557	Point 3'	Vdot exit	757.2193168
Description	Power (kW)	Calculated	Description	Power (kW)	Calculated
Isentropic Power	W	9664.02	Non-isentropic Power	W'	4832.01

Figure 6-3 Snap shot of calculated data in the developed computer model

Having a full specification of point 3' which has been shown in the T-S diagram of the trilateral cycle in Figure 6-4, enables prediction of the performance of the turbine including power generation and fresh water production capacity, the size of the required turbine for that specific initial condition including the exit area of the nozzle, the length of the nozzle and the isentropic efficiency of the designed turbine.

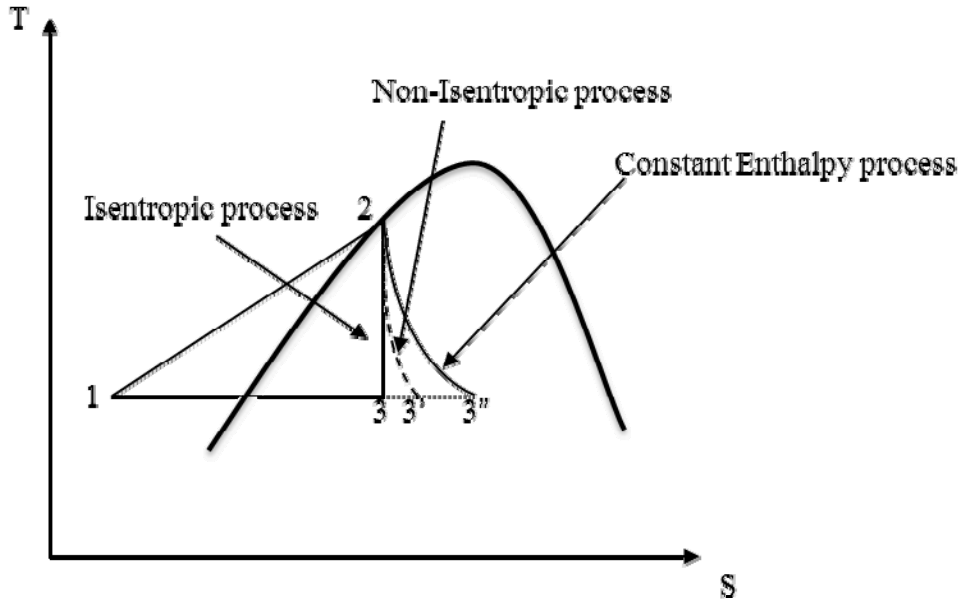

Figure 6-4 T-S diagram of trilateral cycle inCDP

Figure 6-5 and Figure 6-6 show the theoretical performance predictions using the computer model of a dual geothermal system with 400kW thermal input.

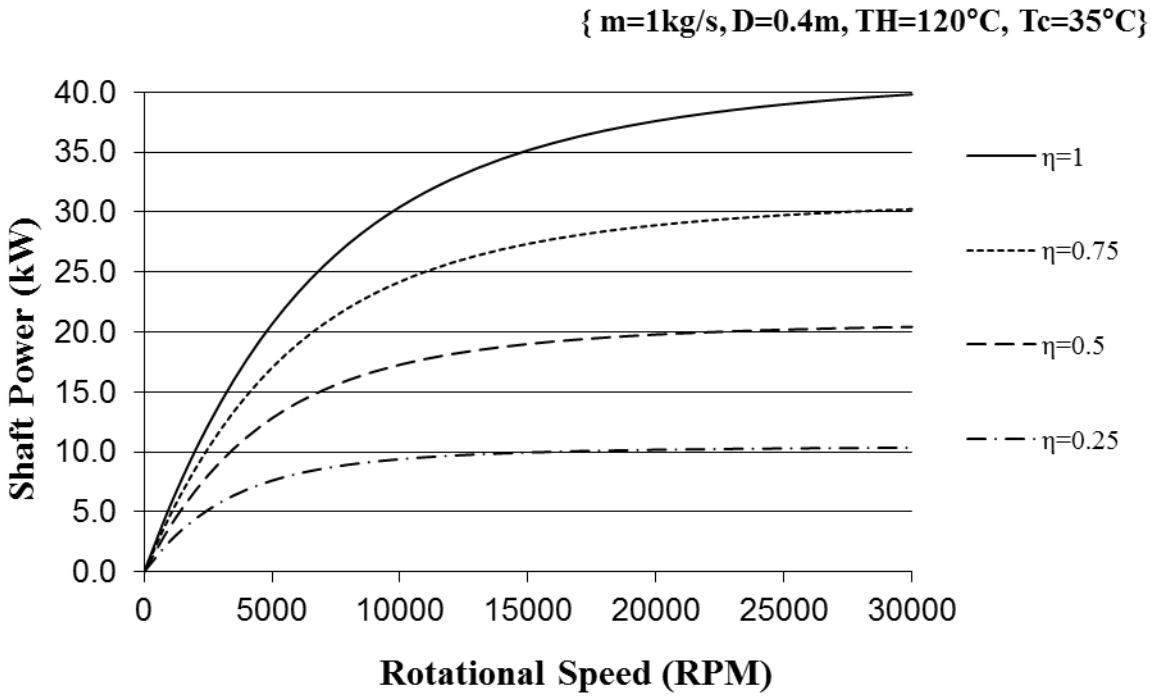

Figure 6-5 Theoretical shaft power output at different rotational speeds and isentropic efficiencies of dual geothermal system

As it can be seen from the predictions for power output, for rotational speeds greater than 20000 RPM, there is very little change in the power production. Therefore, this speed may be reasonably taken as the optimum operating speed.

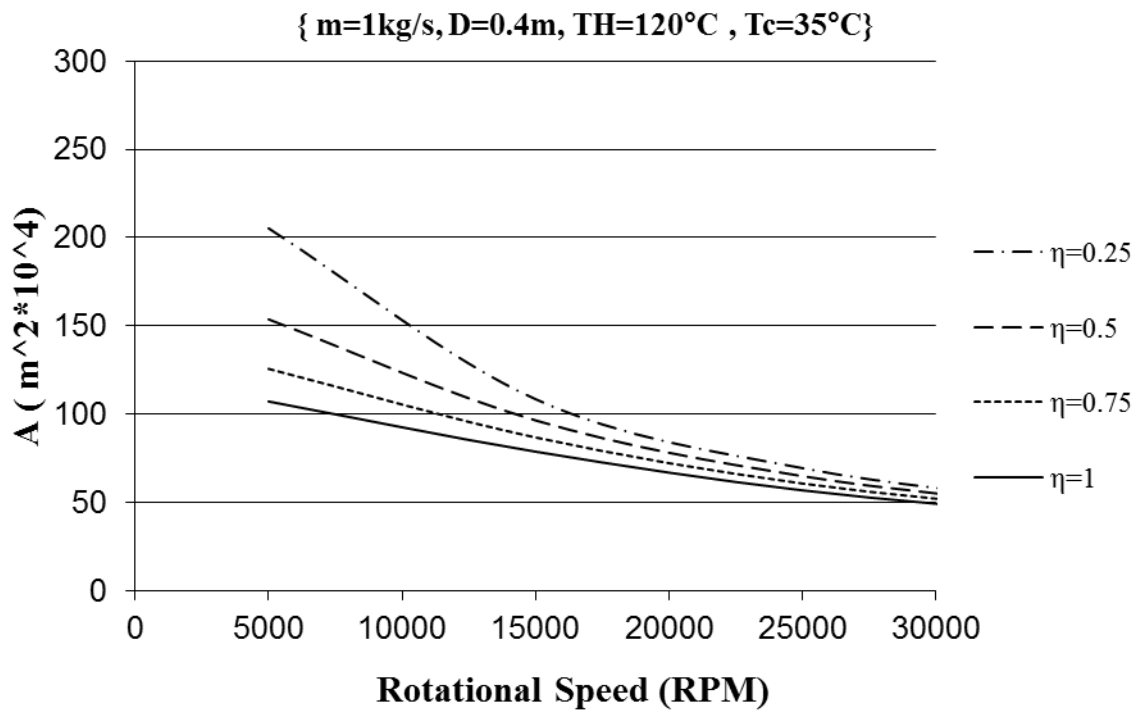

Figure 6-6 Optimum exit area of the two phase nozzle for dual geothermal system turbine

As has been shown in Figure 6-6, the exit area of the nozzle can be predicted for the optimum rotational speed and the desired isentropic efficiency.

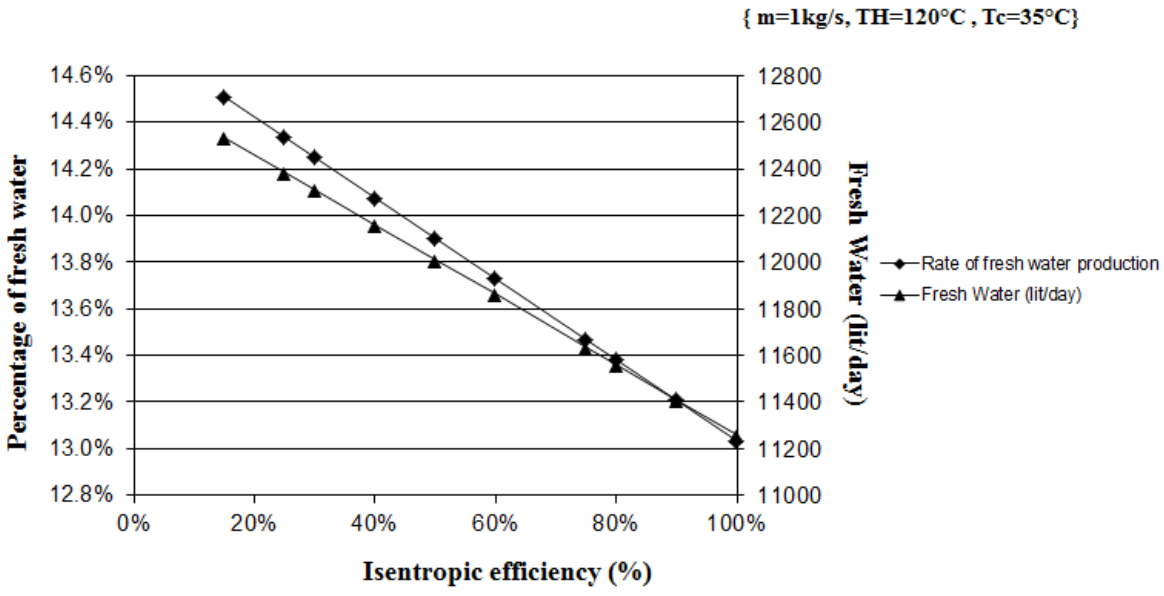

Figure 6-7 Fresh water production at different isentropic efficiencies for dual geothermal system turbine

The fresh water production can also be predicted using the required input characteristics of the system. As the isentropic efficiency of the system increases, the amount of fresh water production decreases. As a result, the optimization for both should be considered to enhance the combined power generation and fresh water production.

Another capability of the computer model is that the initial torque which has been discussed in Chapter 4 to enhance the extracted power from the turbine can be considered in the model. Therefore, the user can easily put T_o as zero which means considering no power loss or enter a value for it based on the geometry of the rotor to allow for the power loss. In order to provide an example of this capability, the following graph shows the effect of considering T_o using the computer model for an isentropic efficiency of 25%.

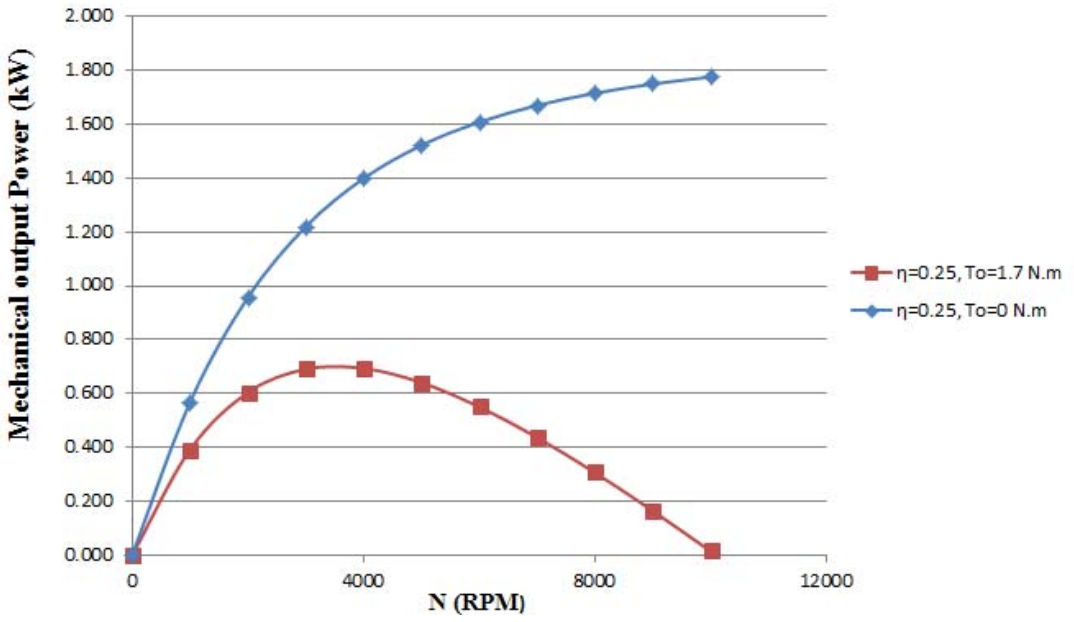

Figure 6-8 Comparison of considering initial torque for power loss in the computer model

As it can be seen from the result, considering the power loss based on the friction, leads to the optimum rotational speed for maximum output power whereas considering T_o=0 the power increases as the rotational speed increases.

As described in this chapter, the developed computer model can be used for different conditions of the input data and the rotor can be designed with the associated predicted performance including power and fresh water production for the designed CDP system.

Chapter 7 Turbine experimental rig and test procedure

In this chapter, the experimental rig which has been installed at RMIT University is introduced in detail. Therefore, all the CDP parts and measurement devices are explained individually with their specifications. In addition, the procedure of conducting the experimental test is explained in order to enhance the user-friendly processes for carrying out tests and collecting the required data.

7.1 Hot water heating system

For the purpose of providing hot water to feed into the CDP system and because two condition were considered in running the experiments on different rotors, two water heating system have been designed and used based on the required input energy and the available resources.

The first heating system (hot water tank) provided hot water at temperatures below 100 °C, while the second hot water system (a modified steam generator) provided liquid hot water that at temperatures above 100 °C.

7.1.1 Hot water tank

Figure 7-1 shows the hot water tank used for the experiments which had a volume of 400L. Normally mains supply water at approximately 25°C was used in the tank and heated to commencement of boiling with 3 × 3kW immersion heaters. Typically, it took around 4hrs for the water to boil. Because of the limitations in the available 3phase electric power points in the thermal laboratory, the capacity of the immersion heaters was limited to 9kW.

Figure 7-1 Hot water tank

Figure 7-2 shows the 3 on-off switches for the three heating elements of the hot water tank which enabled control of the temperature of the water in the tank.

Figure 7-2 Switches for the heating elements

7.1.2 Modified steam generator

A Clayton steam generator as shown in Figure 7-3 was modified to supply liquid hot water at temperatures above 100°C using a maximum heat input of 100kW.

Figure 7-3 Boiler

The water was pressurised using a centrifugal pump to approximately 800kPa (gauge). Pressurised mains water was fed to two flat plate steam to water heat exchangers connected in series. Steam at 165°C was used to heat the mains (feed) water to temperatures above 100°C. The temperature of the feed water was adjusted by controlling the flow rate of steam through the control panel shown in Figure 7-4. The maximum feed water temperature was around 150°C which was still sub-cooled at approximately 900kPa absolute pressure, which was maintained by the feed pump and monitored by the operator.

Figure 7-4 Pressure controller

7.2 Turbine and Condenser

The CDP system which contained the rotor and condenser consisted of 3 separate aluminum parts. This configuration has been based on the limited capacity according to the size of the rotor and RMIT laboratory. In addition, this arrangement has been designed to facilitate efficient change procedure of the different rotors. Therefore, several experiments with different rotors size and shape were conducted involving disassembling and reassembling the first two parts. The drawing of the configuration is shown in Figure 7-5

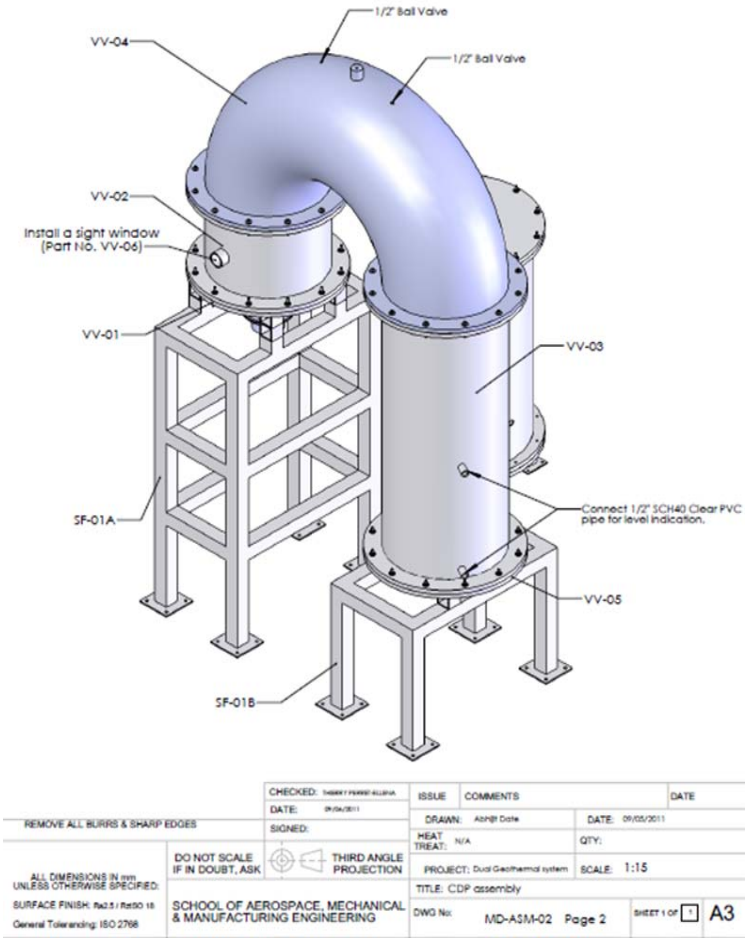

Figure 7-5 CDP unit set up

The first section which is the turbine housing is the 400mm×600 mm tank which includes the rotor that has been installed on the shaft.

The bottom plate of the turbine housing on which the shaft and turbine were sat, is shown in Figure 7-6.

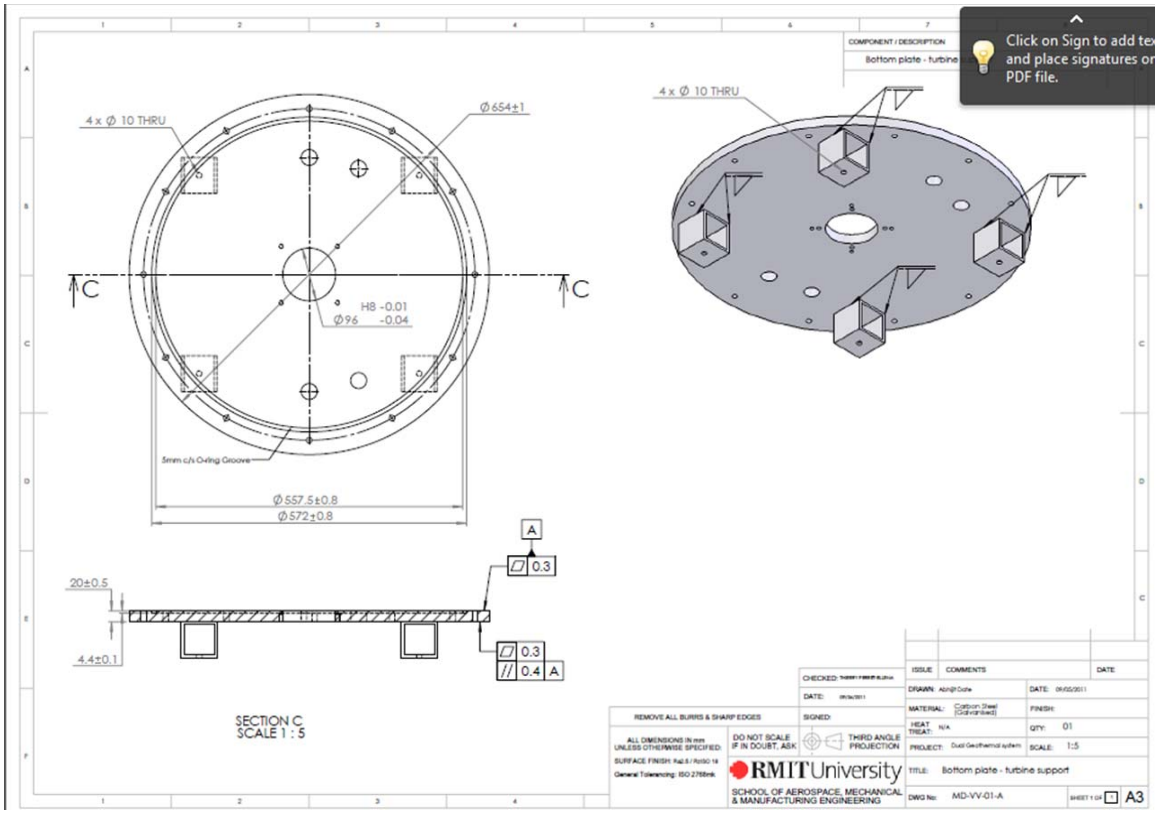

Figure 7-6 Bottom plate of turbine housing

There were also plugs designed in order to drain the brine water, and for installing the thermocouples for measuring the temperature inside the tank .

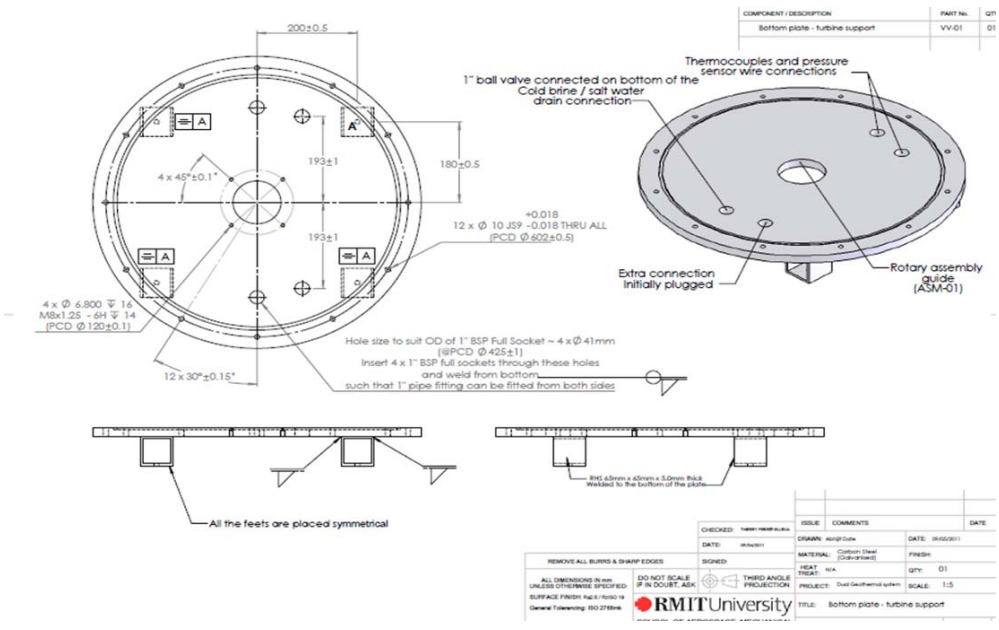

Figure 7-7 Connections of the bottom plate of the turbine housing

The detailed design of the rotor shaft which passed through the bottom plate and held the different rotors used in the experiments is shown in Figure 7-8.

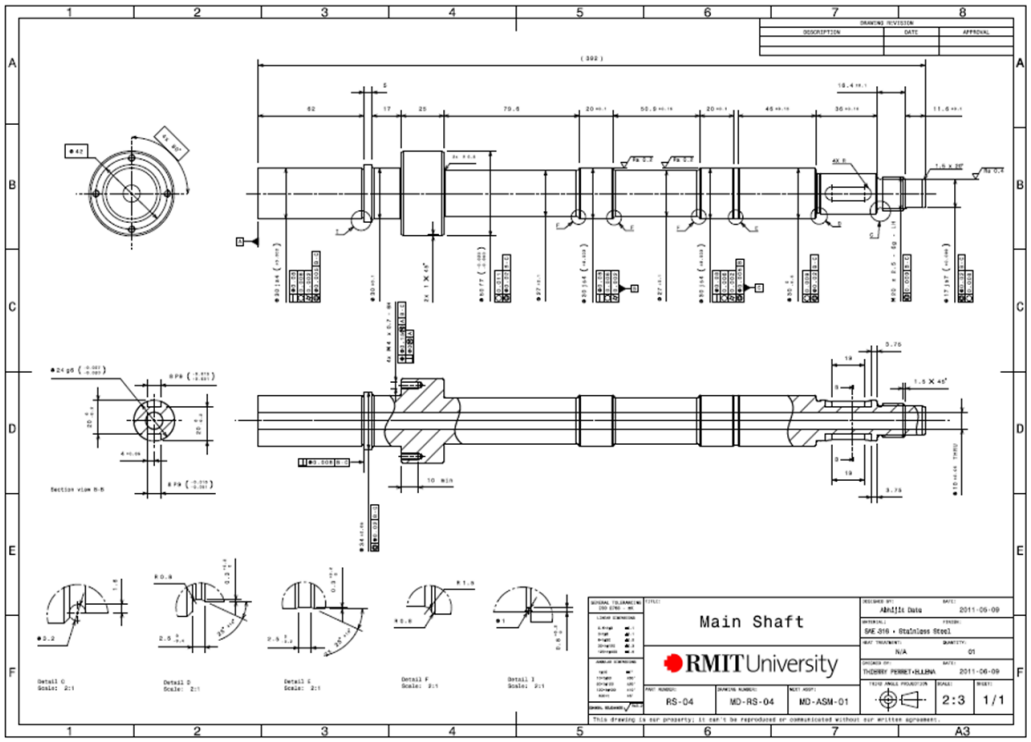

Figure 7-8 Shaft design

The main shaft and bearing housing has been designed according to the requirement of accommodating different rotors which is shown in the following Figure.

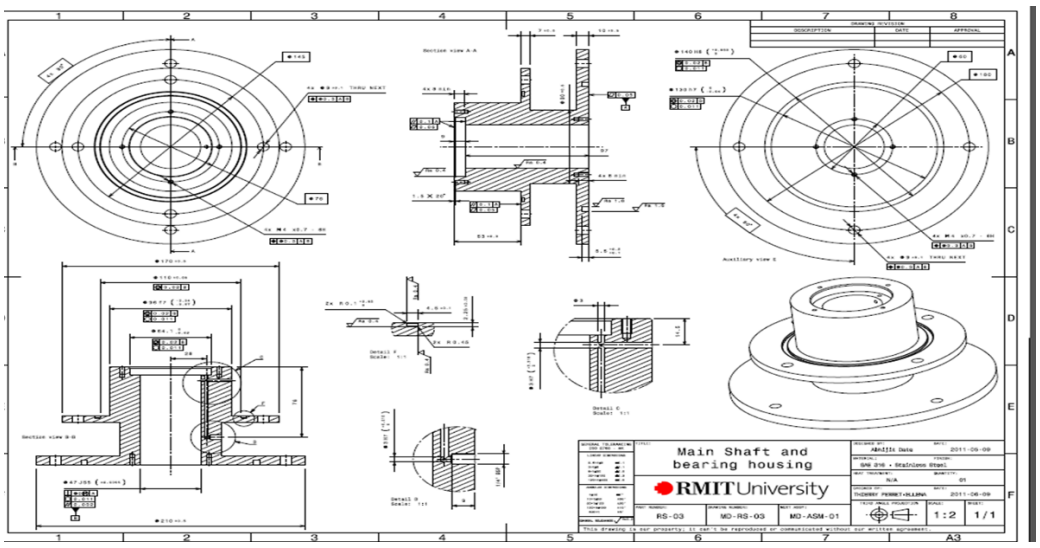

Figure 7-9 Shaft and bearing housing

The design if the main shaft assembly has been shown in Figure 7-10,

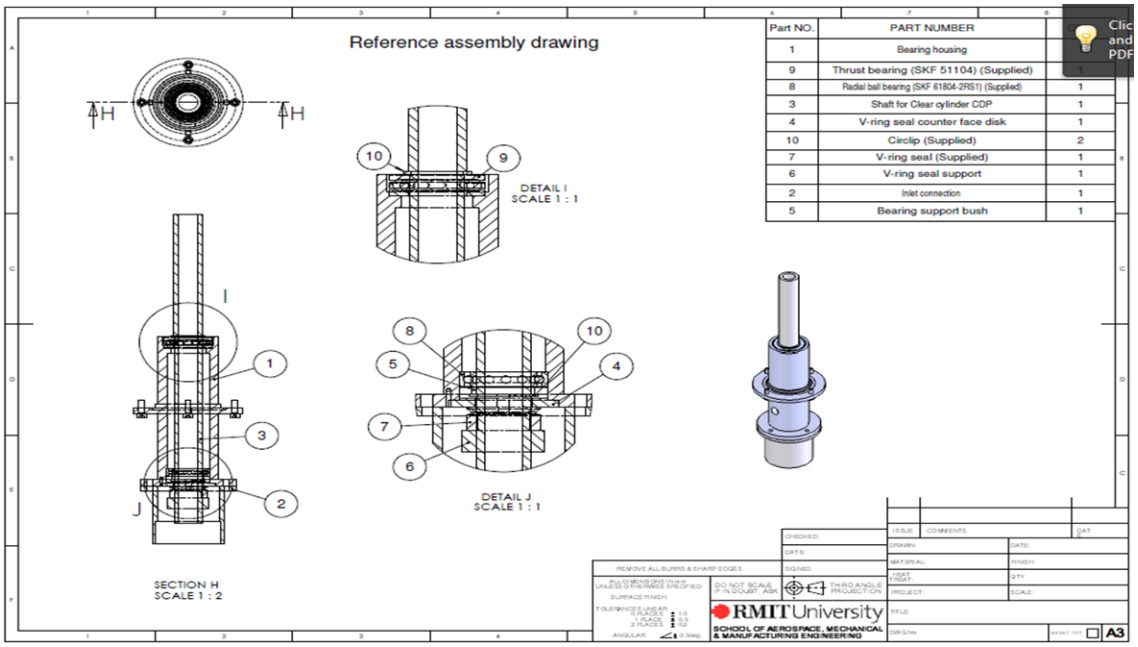

Figure 7-10 Shaft assembly

Therefore the whole assembly for the rotary shaft is as shown in a detailed design drawing,

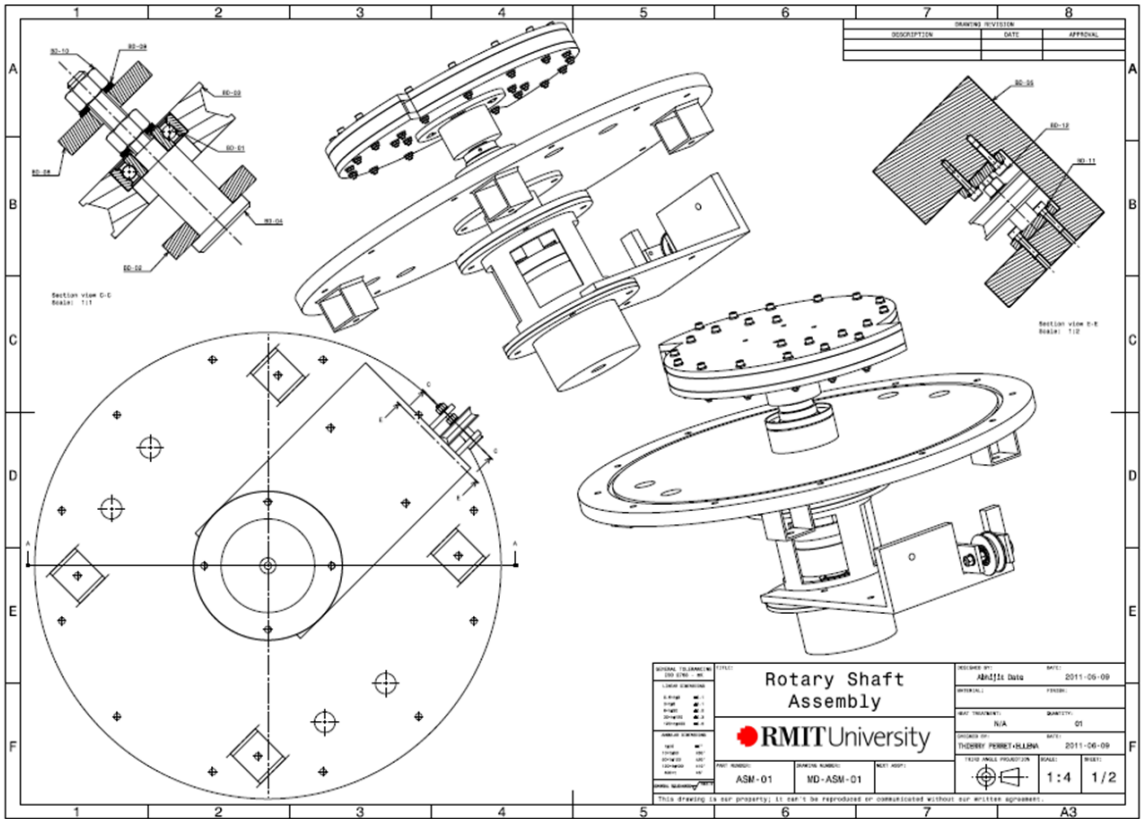

Figure 7-11 Assembly of the shaft and turbine in turbine housing

The turbine housing which contains the above parts has been constructed as shown in following drawing.

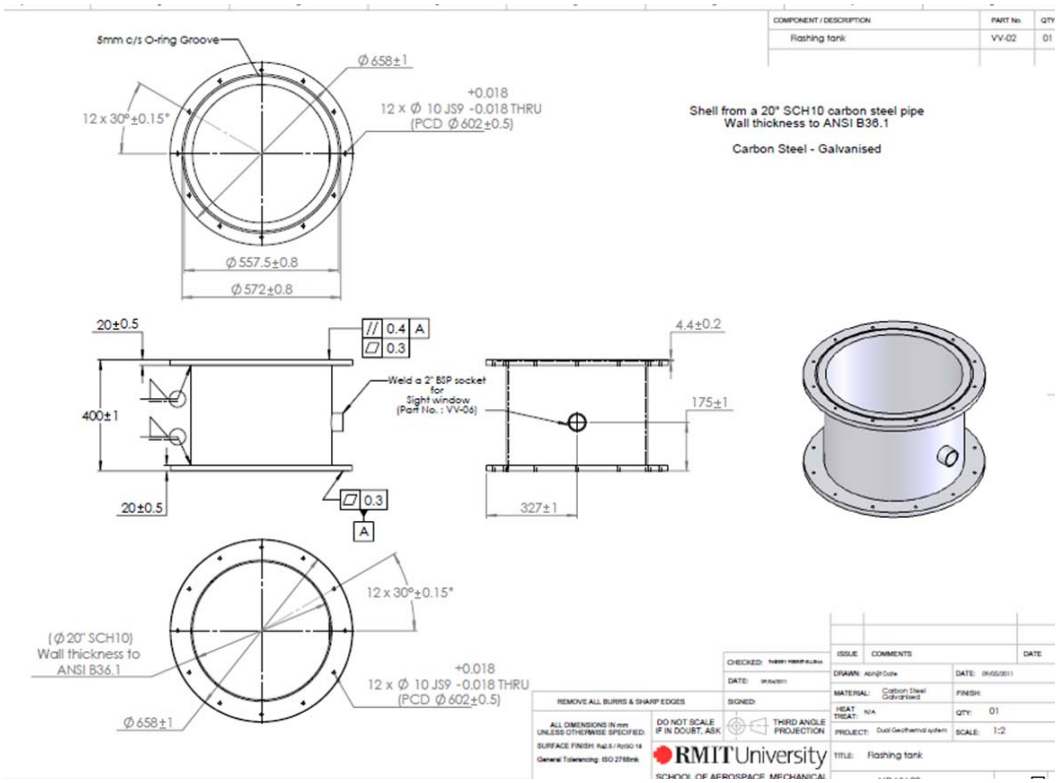

Figure 7-12 Turbine housing drawing

.

Figure 7-13 Turbine housing

The Figure 7-14 shows the stand that each rotor has been installed on and coupled to the shaft which is inside the turbine housing section.

Figure 7-14 shaft and bearing housing

The second section is the curved aluminum tank which is a vapour transfer duct and connects the turbine housing that contains the rotor to the third part that contains the condenser. This configuration has been considered based on the volume of the vapour produced based on the theoretical analysis of the phase change process to allow the vapour to travel smoothly without loss directly to the condenser for producing the maximum capability of fresh water. The detailed is shown in Figure 7-15

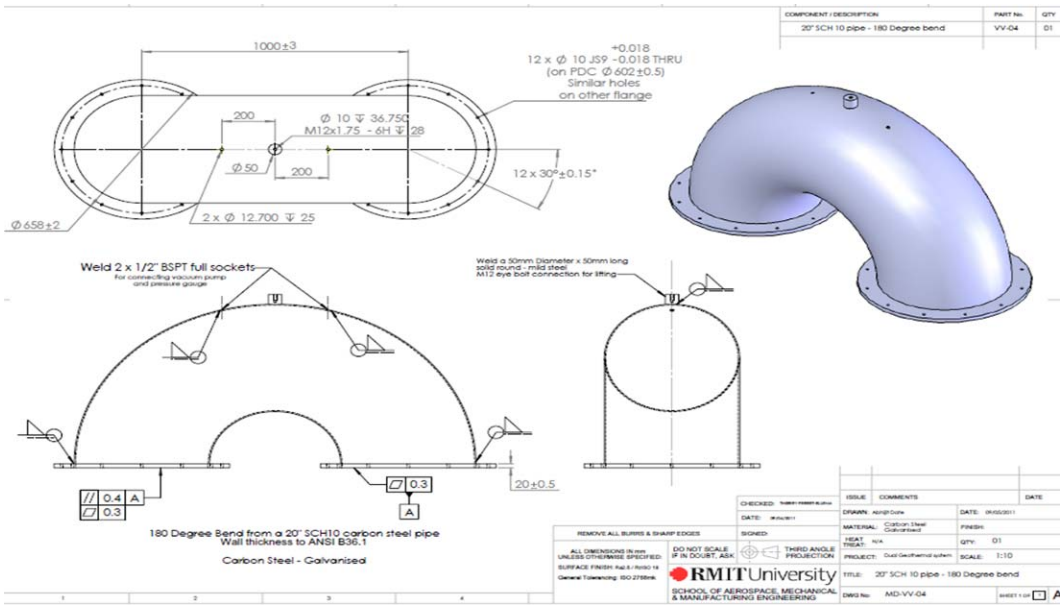

Figure 7-15 vapor transfer duct drawing

The first two parts of the turbine and condenser set were as shown in Figure 7-16.

Figure 7-16 Turbine housing and vapor transfer duct

The third section which is a condenser housing was a 110 mm × 600 mm aluminum tank which contained the 3 layer heat exchangers performing as condenser to produce the fresh water.

The bottom plate of this component contained four plugs for inlet and outlet of the cooling water for the condenser and e for draining the fresh water produced and one extra plug which has been used to install the thermocouples for monitoring the required temperature as been shown in Figure 7-17.

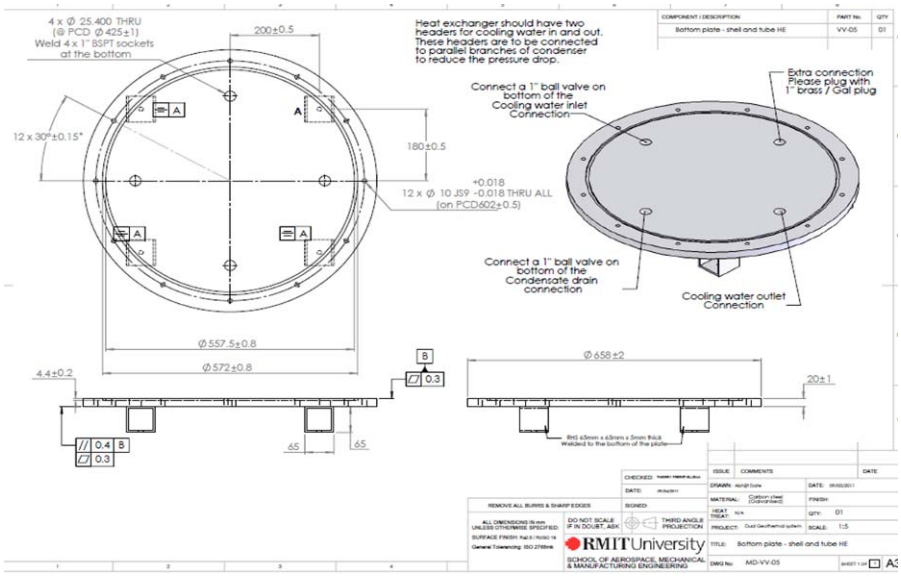

Figure 7-17 Bottom plate of condenser housing drawing

Figure 7-18 shows the container in which the condenser was installed.

This part also contained the clear PVC pipe to indicate and monitor the level of fresh water production.

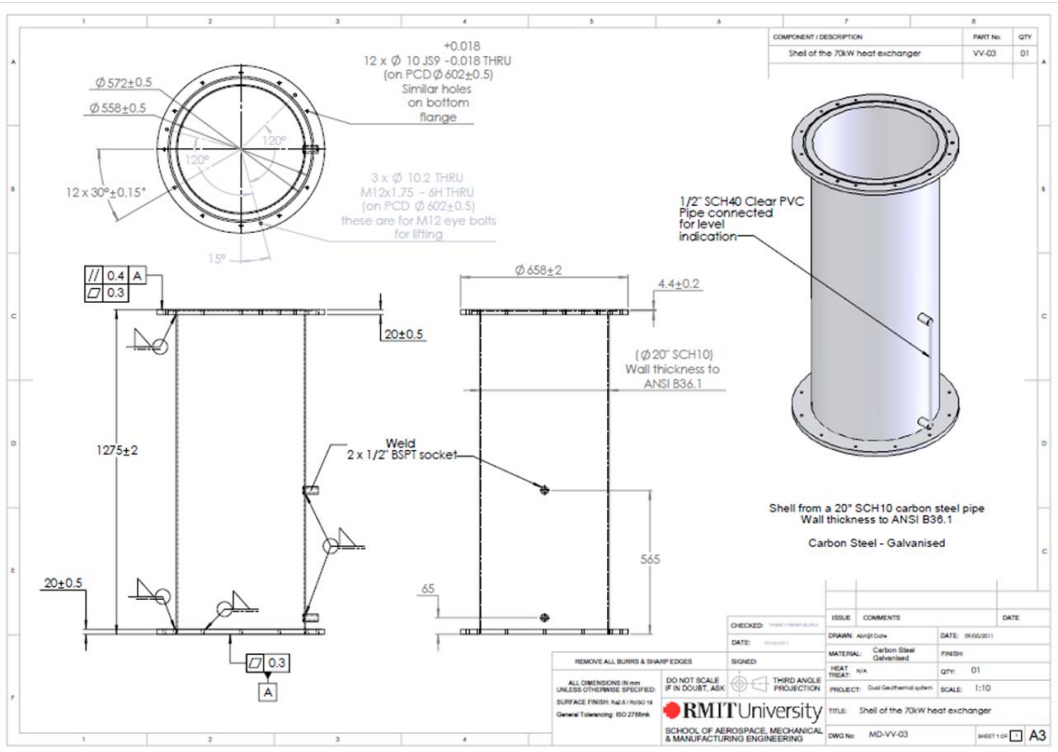

Figure 7-18 Condenser housing drawing

The housing is shown in Figure 7-19.

Figure 7-19 Condenser housing

In Figure 7-20, the bottom plate of the third part is shown with the connections of the condenser as is e discussed in the condenser section.

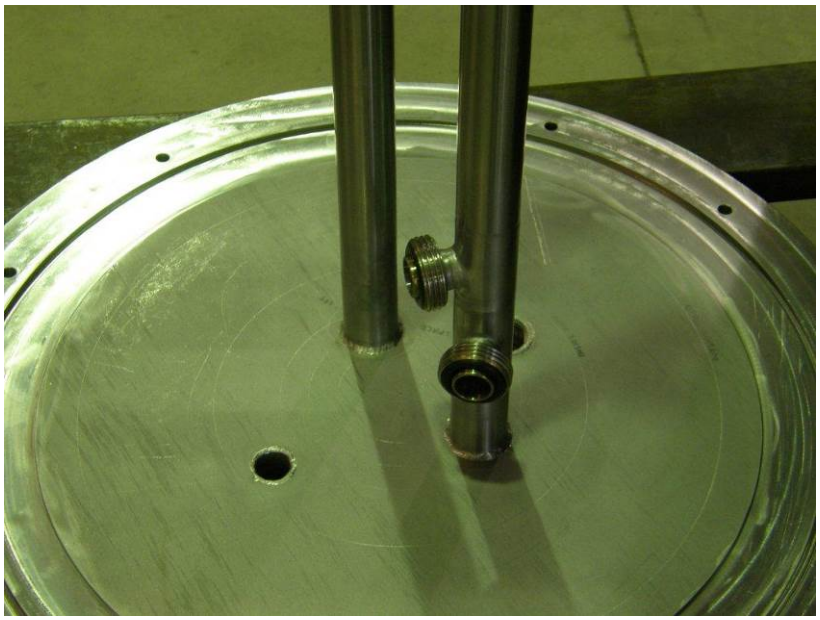

Figure 7-20 Bottom plate of condenser housing

Figure 7-21 shows a detailed drawing of the turbine and condenser configuration.

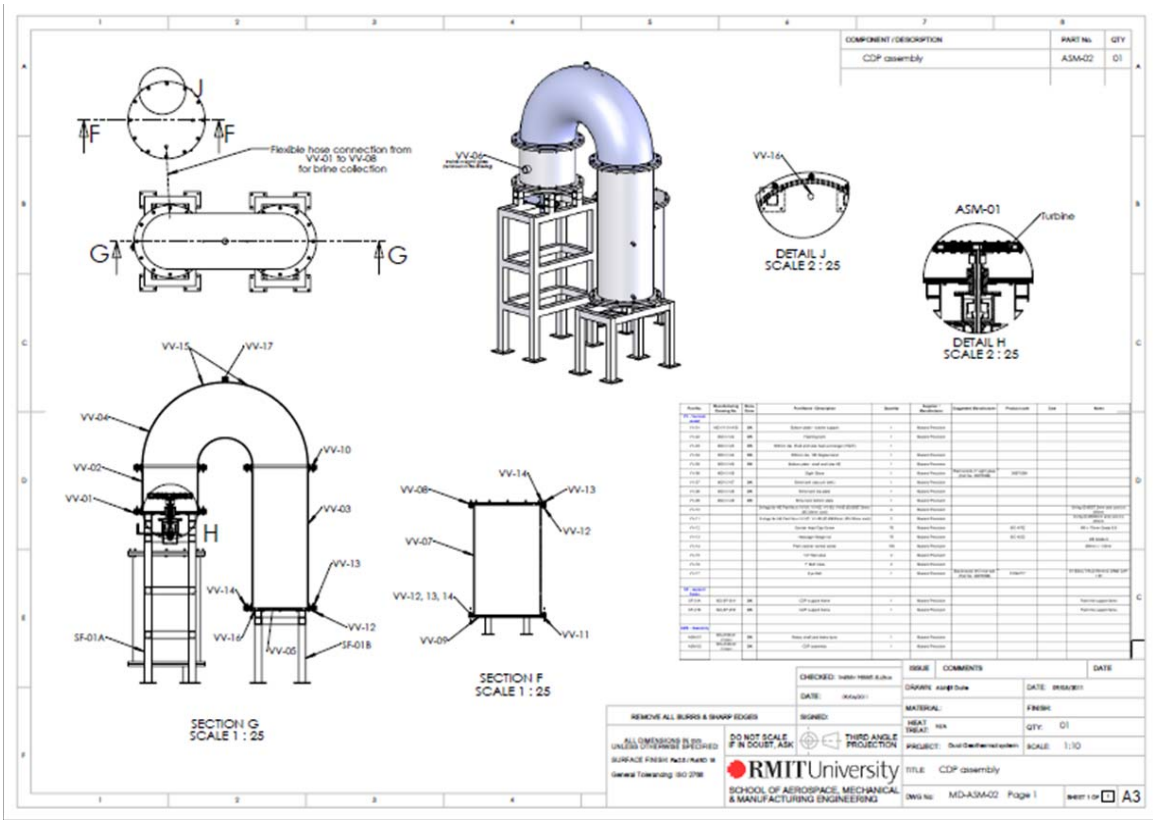

Figure 7-21 Turbine and condenser configuration

Therefore the total manufactured configuration of the turbine and condenser set was as shown in Figure 7-22.

Figure 7-22 Turbine and condenser configuration

For changing the rotor, the first and the second part were disassembling using a cable crane. After disassembling the old rotor, and attaching the new rotor to the shaft, these two parts were reassembled ready for testing.

7.3 Turbine

Three sample two phase turbine rotors were designed and manufactured in the project. For each rotor, several tests were performed to enhance understanding of the two phase flow phenomena and towards improving further designs by validating the computer model based on the achieved repeatable data.

7.3.1 Spilt rotor

The first rotor design as shown in figure 7.22 is referred to as a two-phase split reaction rotor and has very simple design with 4 main parts. This turbine was made from 7000 series aluminum alloy. As shown in Figure 7-23 the top and bottom plates sandwich the nozzle passage inserts to form the diverging section of the nozzle. The position of the throat area (i.e. where the converging section ends) can be varied by placing the throat insert in one of the four grooved locations while the turbine is assembled. This arrangement facilitated varying the feed water flow rate while maintaining the operating pressure difference. Further, this type of arrangement facilitated manufacture of the turbine as the top and bottom plates can be mass produced while the nozzle passage inserts and the throat inserts can be custom made for individual geothermal site conditions. After design and manufacture of this turbine it were complete, it was concluded that this could be one of the potential configurations of making the two-phase reaction turbines.

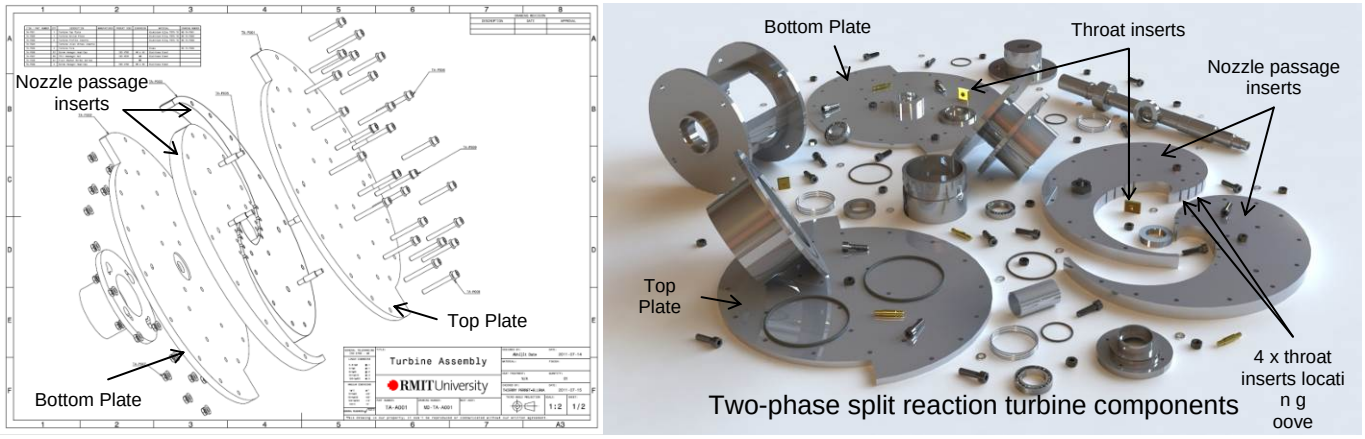

Figure 7-23Two-phase split reaction turbine

Also the Figure 7-24 shows the detailed design of the split turbine path with the inserts.

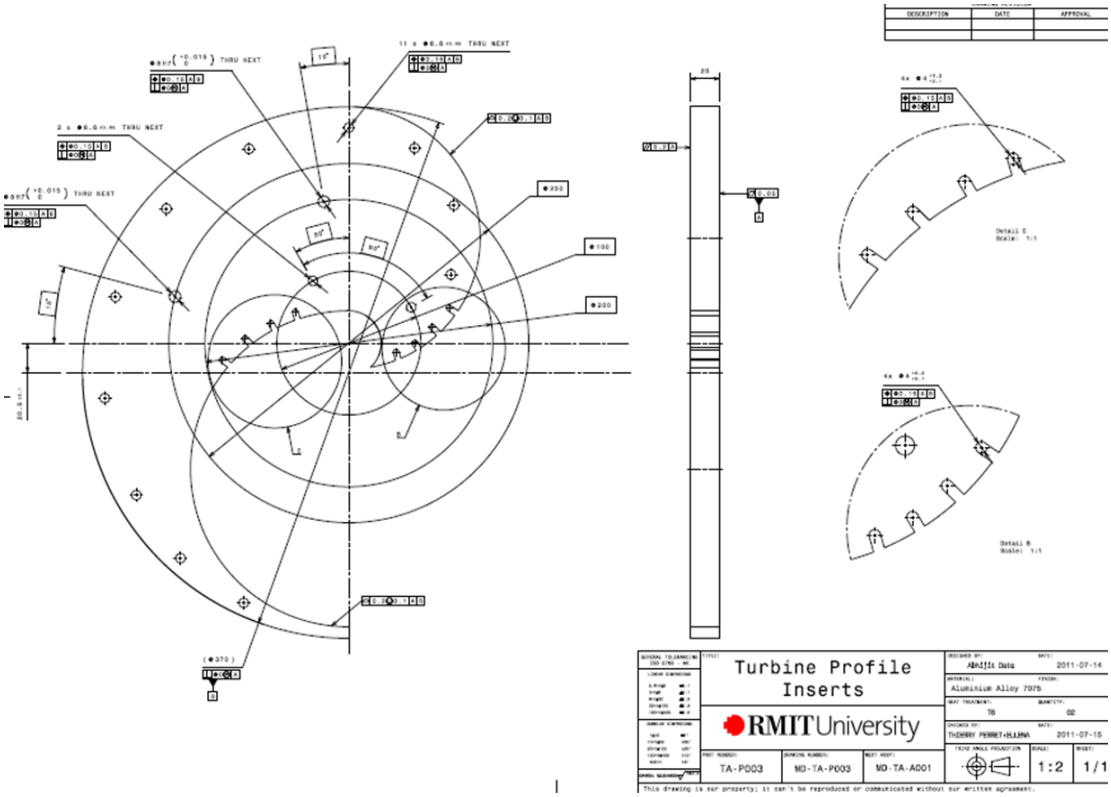

Figure 7-24 Spilt rotor nozzle inserts drawing

The rotor insert detailed design is as shown in Figure 7-25.

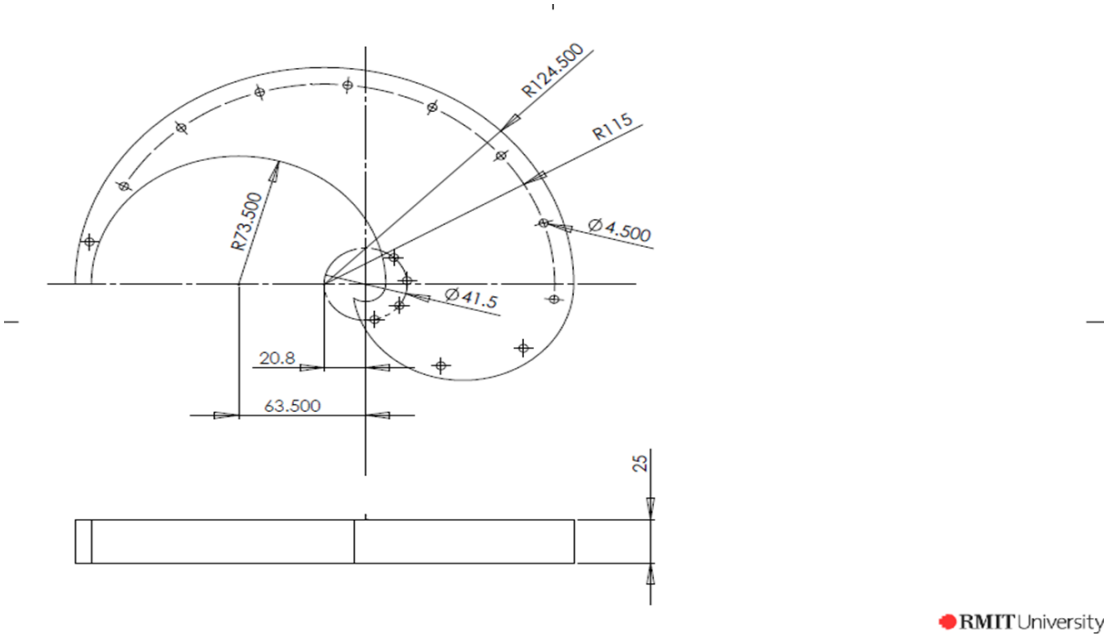

Figure 7-25 Spilt rotor drawing

The bottom and top plates of this split rotor are as shown in Figure 7-26.

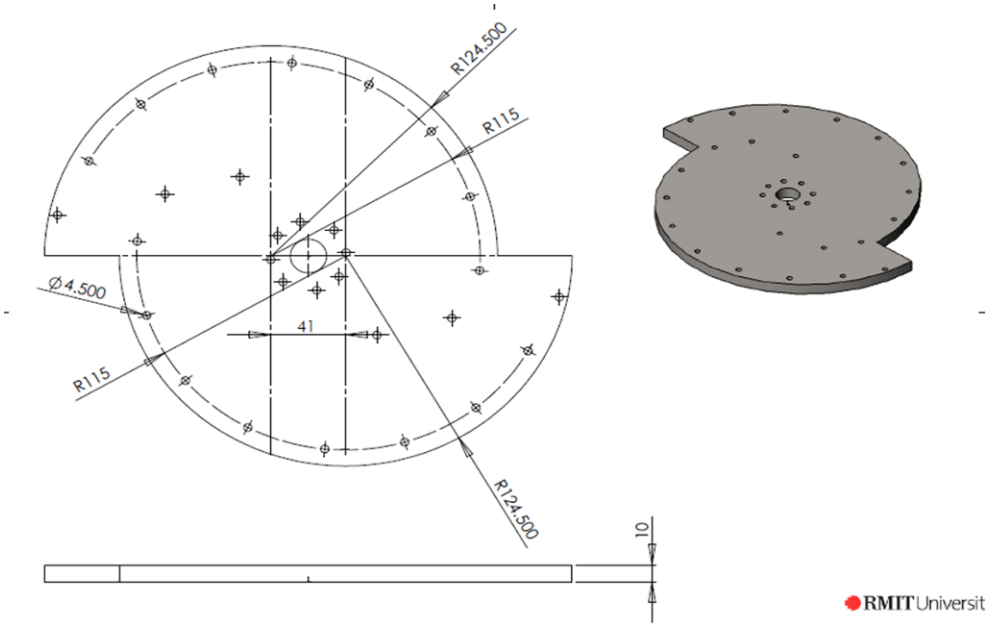

Figure 7-26 Bottom plate of the split turbine drawing

The assembly of the split rotor is shown in Figure 7-27.

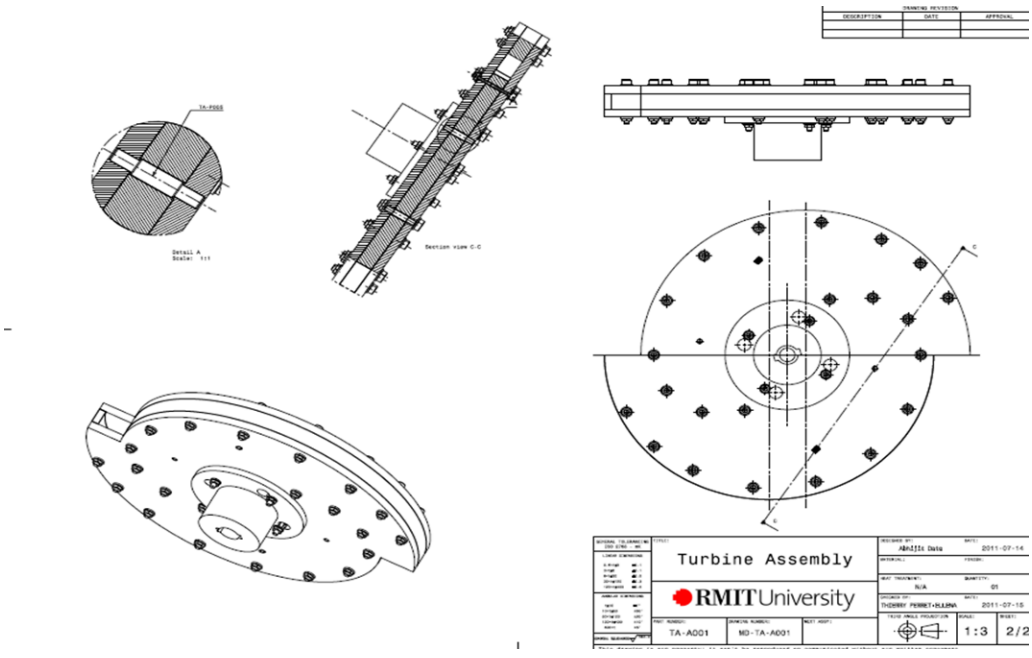

Figure 7-27 Assembly of the split rotor

As it can be seen from Figure 7-28, there are 4 different configurations which have been considered to investigate different length of the nozzle and therefore assess the influence of nozzle length on the performance of the system.

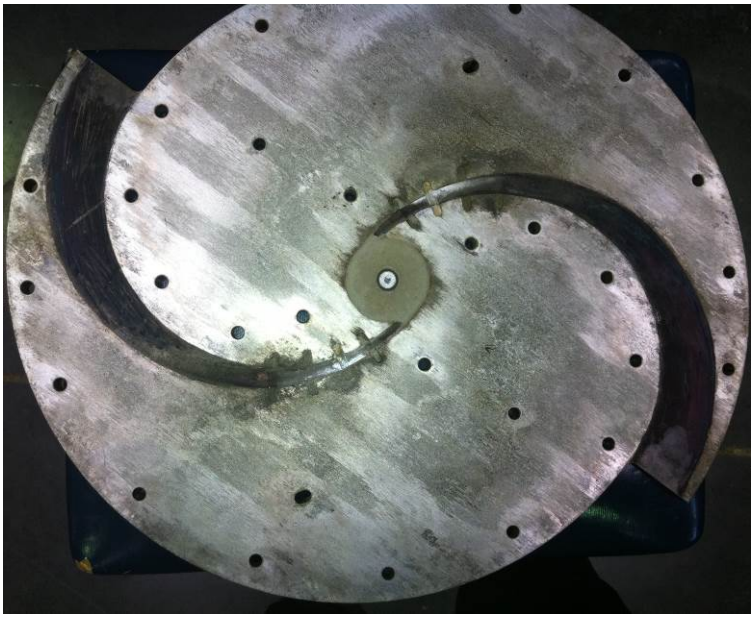

Figure 7-28 Spilt turbine with nozzle inserts

Some inserts have been designed to investigate different orifice sizes in order to assess the effects of the orifice size on the efficiency and performance of the system. Figure 7-29 shows one of these inserts which can be placed in the different designed positions.

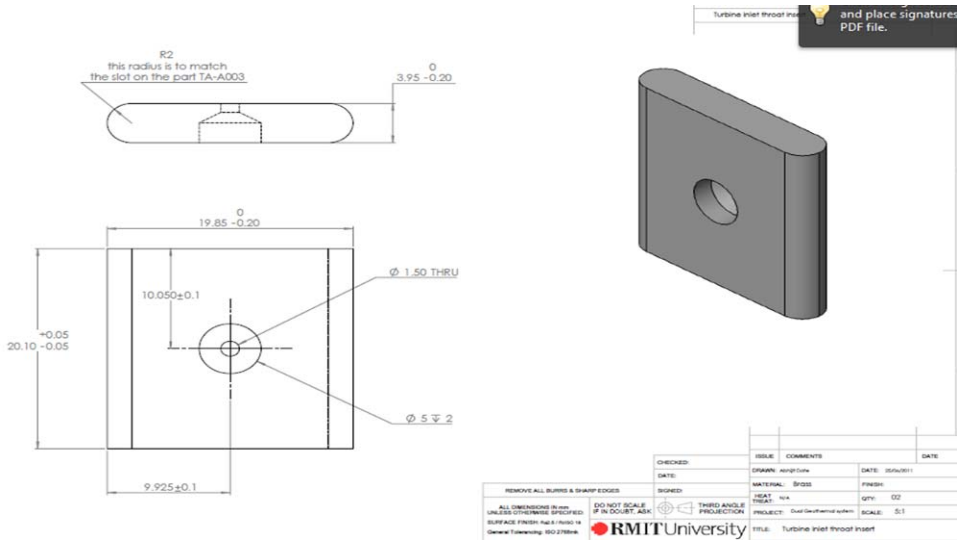

Figure 7-29 Insert for the split rotor

The inserts have been manufactured from brass with different orifice sizes as shown in Figure 7-30.

Figure 7-30 Nozzle insert and its position on the split rotor

This experimental design facilitates improvement of the rotor design as it enables of study of different positions and size of the nozzle to gain improved results and maximum efficiency from the system.

The whole assembly of the desired rotor with the shaft coupling is shown in detailed design of Figure 7-31.

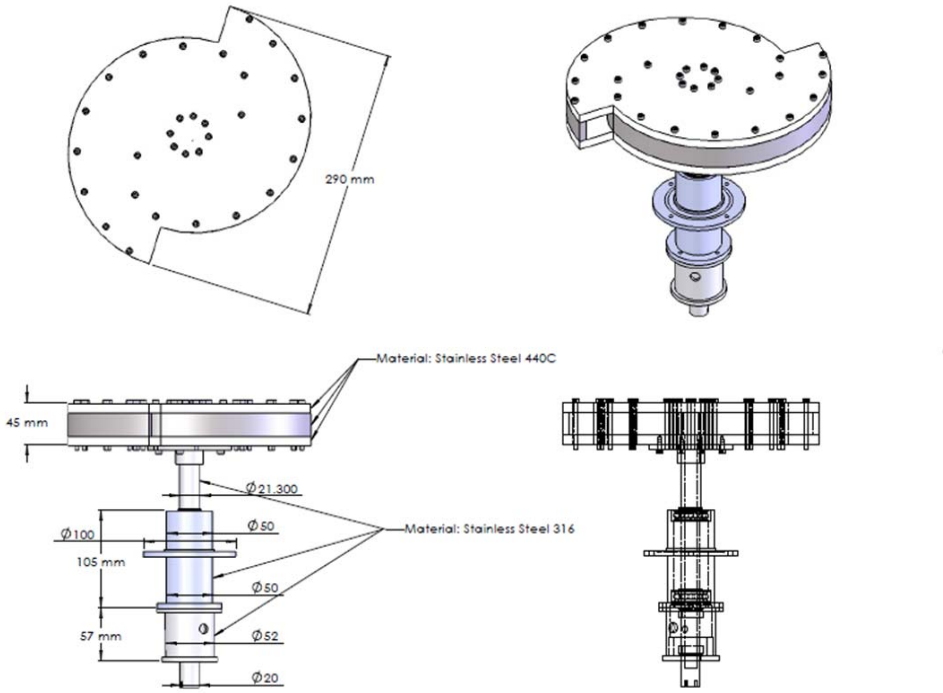

Figure 7-31 Assembly of the split rotor drawing

7.3.2 Advanced rotor

As shown in Figure 7-32 the second sample turbine design was made from two pieces and was made from high strength 7000 series aluminum alloy. Both the top and bottom plates were machined to form the circular converging-diverging (C-D) section of the nozzle. The profile of the C-D section has been developed based on the design of a single phase reaction turbine proposed by Fabris [101]. The C-D section is longer to allow flashing to happen in the nozzle and more curved to minimise flow separation (liquid and vapour separation) while the turbine is rotating. The new nozzle design was manufactured and tested under similar condition to those observed at geothermal sites (90 - 110°C).

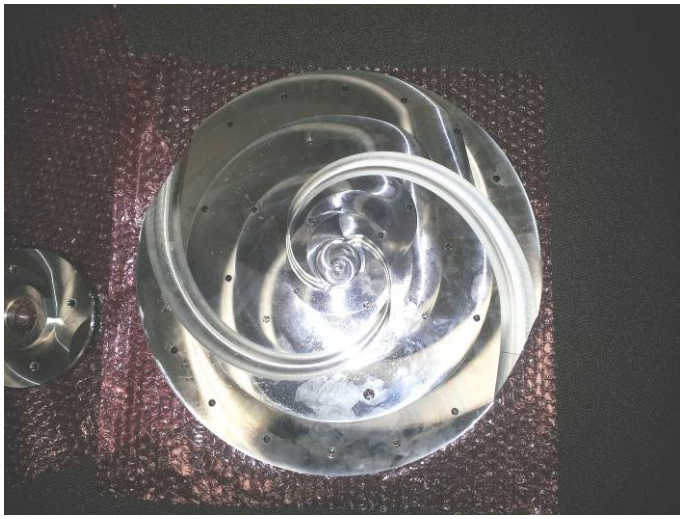

Figure 7-32 Advanced rotor

Figure 7-33 below shows the drawing of the top and bottom plates of the advanced rotor with 400 mm diameter.

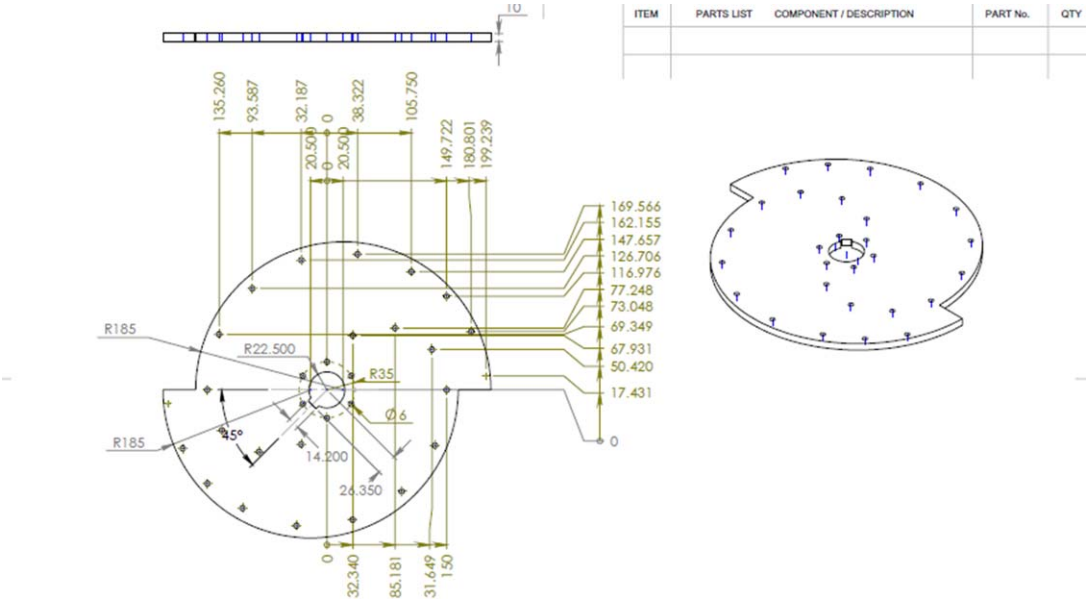

Figure 7-33 Bottom plate of advanced rotor drawing

Also the new design has been applied to the advanced rotor drawing based on the achievement data from experimental tests has been shown in the following figure.

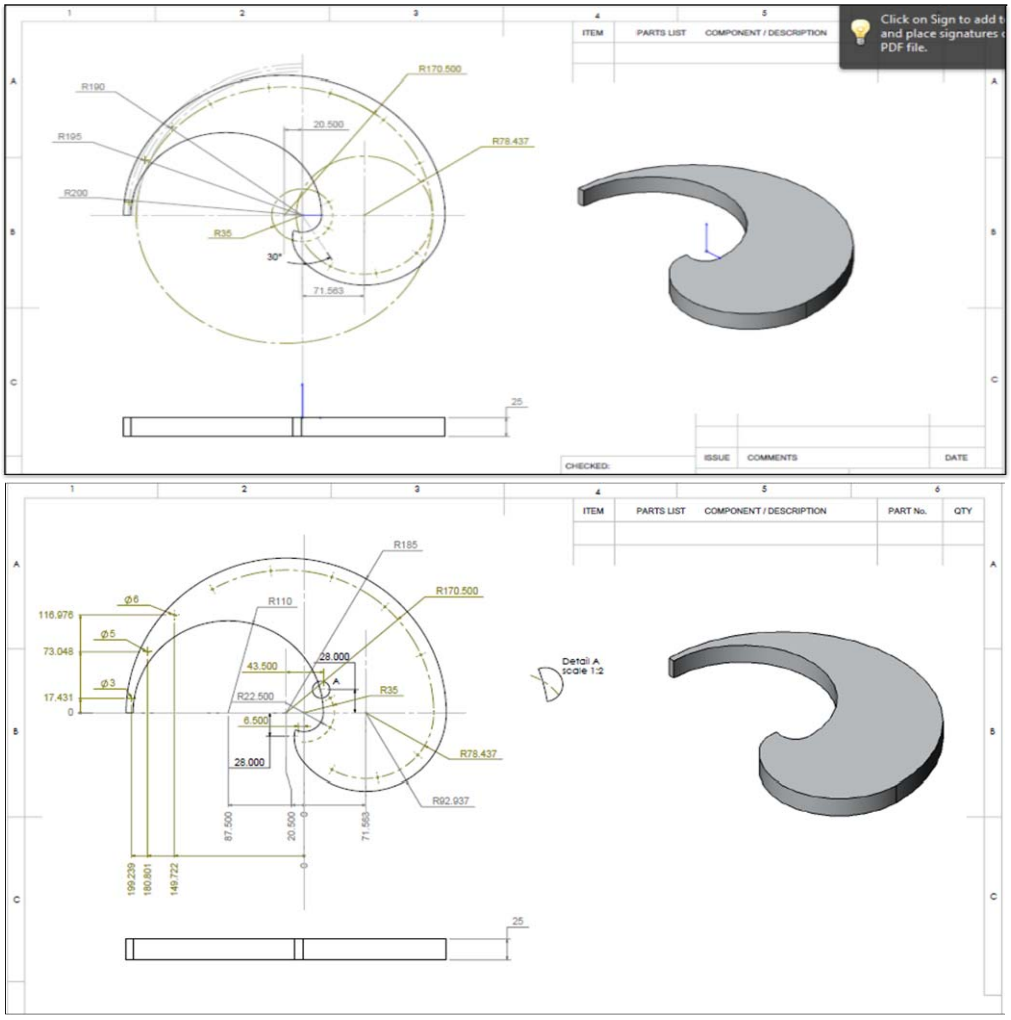

Figure 7-34 Advanced rotor mid plates drawing

As it can be seen from the drawing, for the new design there are no inserts considered for the nozzles. The orifice size is approximately 3 mm based on the best results which have been achieved from the split turbine.

7.3.3 RMIT rotor

Based on the results that have been obtained from testing the first two sample turbine designs, a third and the final rotor has been designed with the optimum nozzle size, throat length and flow pattern. This design of the rotor has been designated the RMIT rotor.

This 300mm diameter rotor was designed and manufactured from Aluminum with a 2mm throat and an efficient pattern flow for the fluid.

Figure 7-35 shows a three dimensional drawing of the RMIT rotor with a designed groove geometry which has been described in chapter 5.

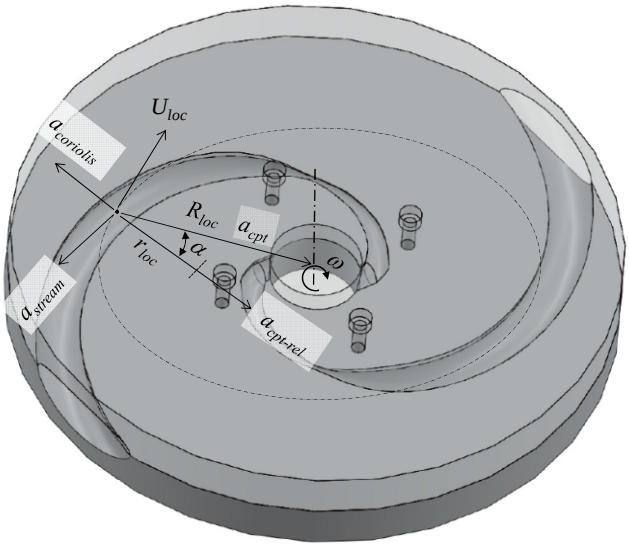

Figure 7-35 Drawing of RMIT rotor

This rotor was the latest design and has demonstrated the best performance of CDP. The results are discussed in detail in the next chapter.

7.4 Condenser

As has been described in the detail design of the appropriate condenser for CDP in Chapter 4, Section 6, the 3 layer condenser has been manufactured as shown in the following Figures.

Figure 7-36 First layer of the condenser

The first layer consisted of 500mm spiral length of the mild steel welded tube with an overall diameter of 500 mm and tube diameter of the stainless steel coil of 25 mm.

The second layer as shown in Figure below consisted of 500mm spiral length of the mild steel welded tube with overall diameter of 400 mm and tube diameter of stainless steel coil of 25 mm.

Figure 7-37First and second layers of the condenser

The third layer has been made from a500 mm spiral length of the mild steel weld tube with an overall diameter of 300 mm and coil diameter of 25mm.

Figure 7-38Third layer of the condenser

Therefore the total configuration of the CDP condenser is as shown in following Figure.

Figure 7-39 Condenser configuration of CDP

This design is based on the available cooling water flow of approximately 12 LPM of mains water.

7.5 Brine and fresh water tank

In order to collect the fresh water and separately the brine which were produced in the process, a brine tank has been designed as shown in Figure 7-40.

Figure 7-40 Brine tank

This tank has two connections of which one is connected to the first part of the rotor and condenser set in which the more saline water sits after the phase change process. This water flows to the brine tank through under gravity and starts filling up the brine tank during the process. The second connection guides the brine water to the drain bore which continuously delivers the water to the brine and for further need, the external pump has been provided to carry on more water for longer experiments.

Figure 7-41Configuration of brine system

The produced fresh water has been collected in the same container as the third shelf of turbine and condenser set as the vapour condense through the designed condenser. As shown in Figure 7-41, A transparent tube has been incorporated in order to indicate the level of fresh water production and therefore the amount of the available fresh water after each experiment.

Figure 7-42 Fresh water measurement

After finishing each experiment the amount of the fresh water which has been produced was measured after which the fresh water was drained through the appropriate valves and the tank emptied ready for the next experiment.

Figure 7-43 Fresh water collector valves

7.6 Instrumentation, measurement devices and transducers

For each individual test procedure the required input and output variables were measured and recorded.

One of these parameters for the CDP tests is temperature measurement which consist of the temperature of the hot feeding water, temperature of the cooling water flow in and out, temperature of the water at the nozzle inlet, temperature of the fluid at the exit of the nozzle and the inside temperature of the set up tank.

All of the temperatures were measured using copper-aluminum thermocouples which were attached to the desired points, using the proper insulation to ensure accurate temperatures. In order to maximise accuracy of the results, all the thermo couples were calibrated using the same hot and cold water and monitoring the digital data on the data logger.

Another required parameter is the flow rate of the water which consists of the hot feed water flow rate from the heat source to the CDP system and the flow rate of the cooling water in and out. These flow rates were measured through a mechanical flow meter mounted in the line of the feeding water and cooling water. These measured data were monitored throughout the experiment and the average of them has been used for analysis of the experimental data.

The next measured parameter was the pressure which included inlet pressure of the feed water and the operating pressure of the system .

The inlet pressure of the hot water was measured using a pressure transducer attached to the feed water line.

Figure 7-44 Pressure transducerfor water inlet

As it has been shown in the Figure 7-44 , this 2200 series universal industrial pressure transducer operates over the range of input pressure of 0-25 bar absolute. The supply voltage range is 10-15 VDC. The output voltage range is 100 mV which convert to the pressure using the calibration supplied by the manufacturer .

The vacuum pressure inside the chamber was measured using two different devices in order to maximise measurement accuracy.

The first device was a mechanical pressure gauge which showed the inside pressure of the chamber and was used to monitor development of the vacuum and the progress of the experiment.

The second device was the pressure transducer attached to the inlet of the chamber providing the measurement in a voltage format which was converted to pressure using the manufacturers calibration. These data were monitored and recorded by the data logger constantly during each experiment.

Figure 7-45 Pressure transducer for vacuum chamber

This pressure transducer had a pressure range of 0-600 bar gauge and absolute formats with 0-5 V output and 0.15% accuracy.

The next parameter was the rotational speed of the rotor which was monitored continuesly through the test procedure. This speed was measured using an electrical speed sensor whihc utilised marks on the rotating shaft in order to accurately and constantly measuring the pulses and convert them to the proportional rotational speed using the calibrationprovided by the supplier. This sensor also attached to the data logger system in order to record and save the RPM for the entire process.

7.7 Data acquisition system

Important test parameters, including feed water flow rate, fresh water production rate, and pressure inside the chamber were measured using appropriate transducers. As illustrated in Figure 7-46, which shows some of the essential exterior components, the test data were stored in a data logger in a flash memory card

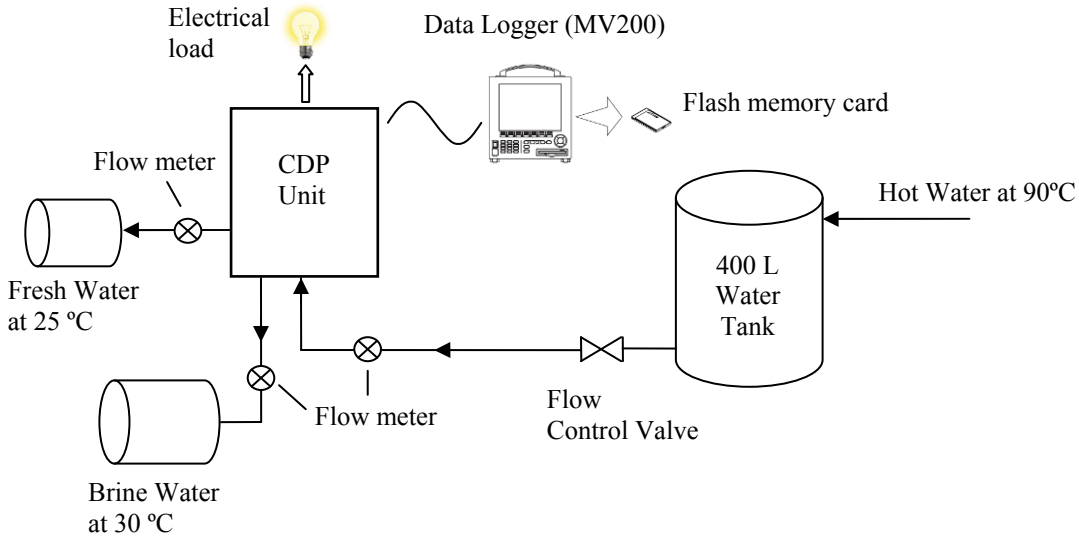

Figure 7-46 Schematic diagram showing the test configuration for the CDP unit

Key parameters of each experiment could be constantly observed from the data logger shown in Figure 7-47 , which allowed the system performance to be displayed.

Figure 7-47 Data logger system

This data logger incorporated a memory card which could save the data through each experiment and then convert to Excel format for the further analysis of the experimental results.

7.8 Test procedure and data collection

Several different two-phase turbines were tested under a variety of operating temperatures and their performance characteristics are presented below.

In order to operate the lab scale CDP at RMIT University, first the vacuum for the chamber should be established using a vacuum pump as an approximate pressure of 5 kPa. This vacuum creation arrangement is shown in following Figure.

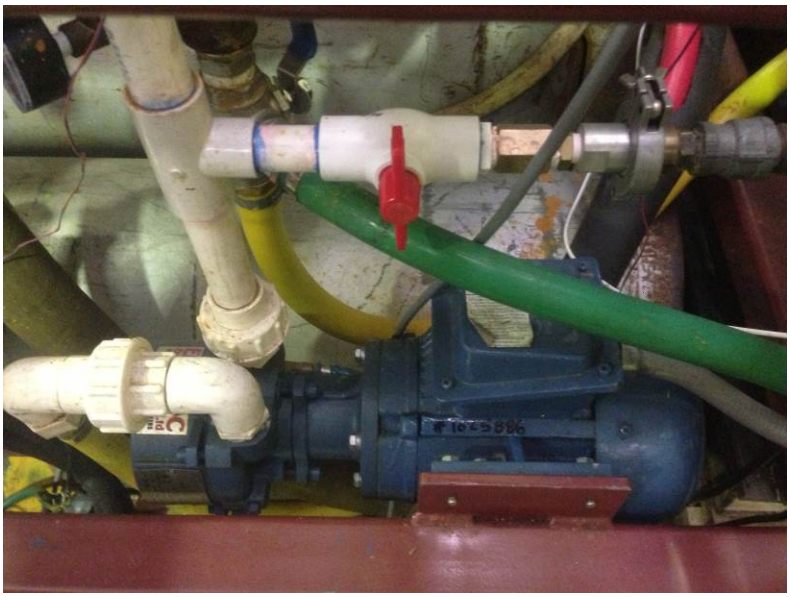

Figure 7-48 Vacuum pump

Then the cooling water flow should start in the condenser to build up the cooling capacity required for the system. When the desire pressure and temperature are reached, the valve for introducing the feeding water is opened.

The specific configurations were determined as shown in following Figure to let the water flow through the shaft and the rotor either to the old CDP set up or new CDP set up using hot water tank as a heat source or boiler as a heat source.

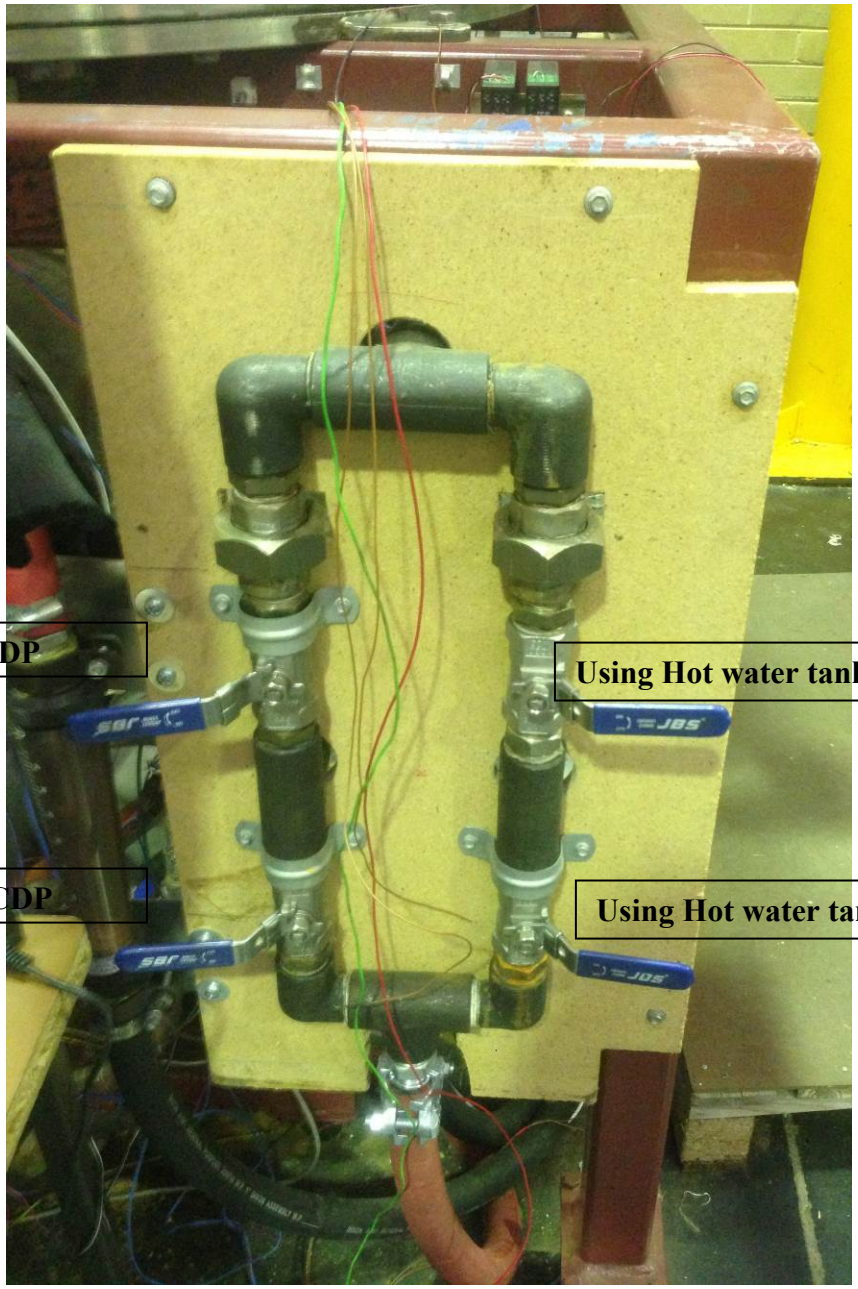

Figure 7-49Valve arrangement for feeding water system

After the desired hot water started flowing through the rotor, initially because of the friction of the seals and also the cooled system, some of the hot water goes through the turbine and nozzles and after a few minutes, the turbine starts rotating. This rotation will increase until the turbine reaches a steady state condition which depends on the pressure, temperature, mass flow rate of the water, cooling capacity and also the mechanical efficiency of the system, bearings and mechanical seals. Therefore, after some time

performance reduces and as soon as the fall off starts, the feed water valve of the is closed to the system in order to let the turbine decrease its speed by the friction in the system. For this part, the main valve which has been used for feeding water to the rotor through the rotating shaft has been used as shown in Figure 7-50.

Figure 7-50 Inlet hot water valve to vacuum chamber

In this way, the amount of mechanical available power can estimated from the acceleration and deceleration process of the turbine. All the data will be measured through the measurement devices connected to the data logger in order to record the data for the further analysis as has been shown and described in the previous section.

When the rotor comes to a stop, the cooling water valve is closed and after monitoring the amount of fresh water production and terminating the saving procedure of the data from data logger, the drain valve for fresh water was opened to drain the water and then release the vacuum in the system to cool it down and ready for the next set of experiments.

Chapter 8 Experimental results, discussion and validation of the computer model

8.1 Introduction

Dynamic tests have been performed using different nozzles at different positions inside the newly designed rotor of the CDP. For this purpose, 3 different sized nozzles of 5mm, 4mm and 5mm diameter have been investigated at 2 positions with one close to the inlet (30mm from the centre) and the other close to the exit (90mm from the centre). Details of the rotors investigated in this chapter are provided in Chapter 7 Section 3.

The rotor investigated in this series of tests was 0.4 m in diameter, made from stainless steel and as shown in Figure 8-1. The principal mass moment of inertia for this turbine has been both measured and calculated through experiment and computer analysis as described previously and was 0.21 kg/m^3.

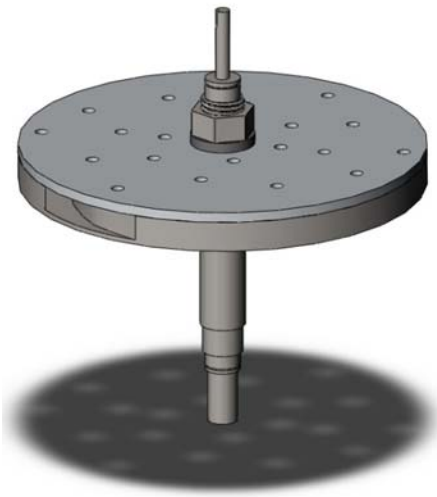

Figure 8-1 Stainless steel turbine

As has been described in the section concerned with estimation of the power output, the power developed has been measured for each of the experiments with different nozzles and positions.

8.2 Split rotor

Figure 8-2 shows the performance of the rotor using a 5 mm nozzle. The figure shows the change in rotational speed of the turbine for positions of the nozzle both closer to the inlet and closer to the exit with corresponding flow rates of hot feed water at a temperature of 99 °C.

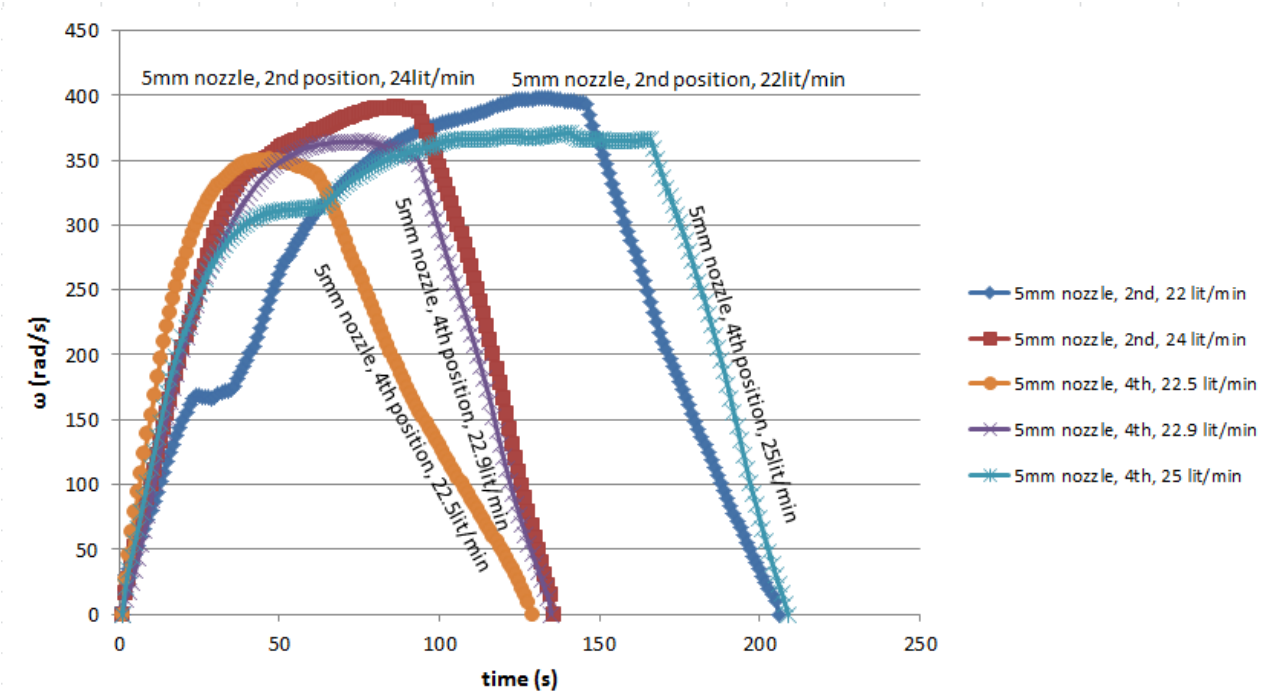

Figure 8-2 Rotational speed VS time for 5mm nozzle

As can be seen from the graphs, the rotor could achieve higher speed when the nozzle was closer to the inlet compared with when it was closer to the exit. The maximum speed obtained was 4100 rpm. The graph also shows that there is an optimum feed water flow rate corresponding to each configuration of the nozzles. The tests were repeated to establish the reliability and repeatability of the results which were found to be reasonably consistent

Figure 8-3 shows the rotor power for the stated rotor and nozzle conditions as a function of rotational speed. The power graphs produced are based on the discussion in Chapter 4. Also a sample calculation for the final design of the RMIT rotor is included at the end of this chapter.

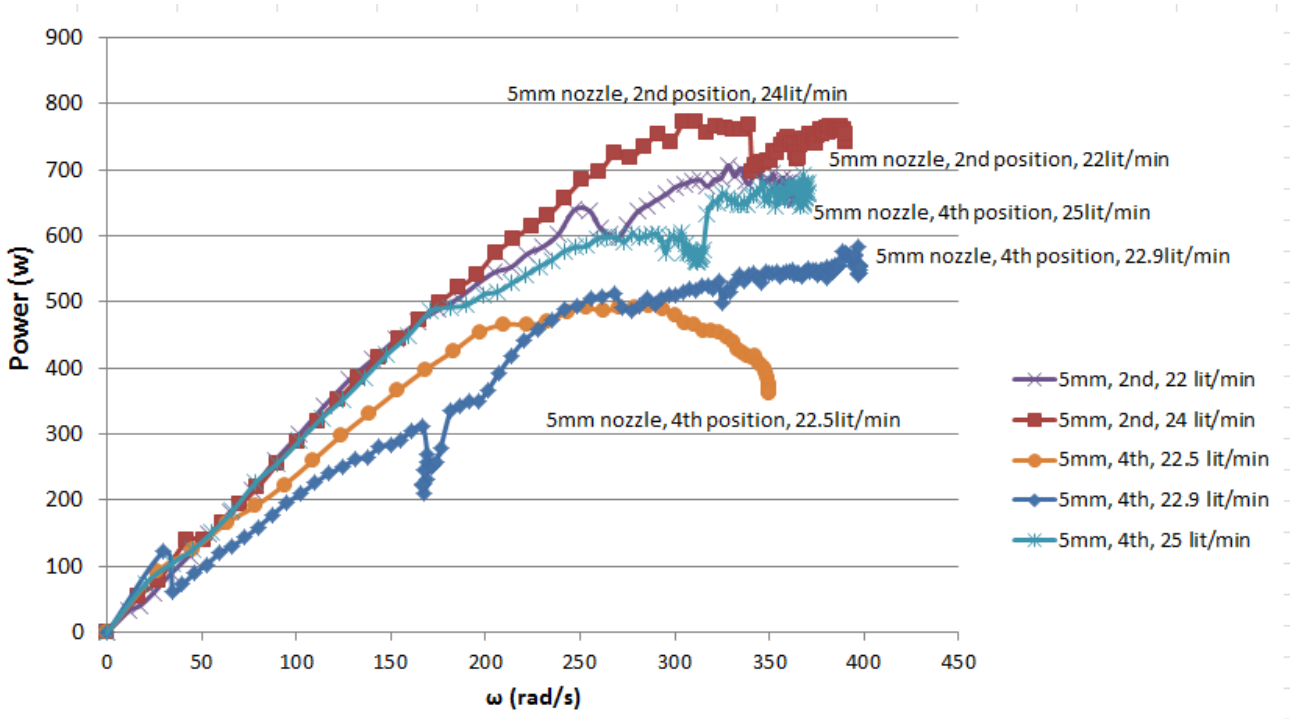

Figure 8-3 Power generation vs. rotational speed for 5mm nozzle

The results indicate that at each condition, the maximum power was achieved at a specific rotational speed and for higher speeds the extracted power decreased. The power decrease is attributed to friction losses which increase with speed. Also, the maximum power, which was approximately 790 W, was obtained when the nozzle was at the position closer to the inlet. Moreover, the flow rate of the feed water has significant effect on rotor performance. As seen in the graph, higher flow rate produces more power, For example, using the 5mm rotor at the position closer to the exit with 22.5 lit/min of water the power developed was 700 W while using this nozzle at the position closer to the inlet, produced 600 W of power

The second group of tests on the CDP with the stainless steel rotor was carried out with the 4 mm nozzle at the same two positions.

Figure 8-4 shows the change in rotor speed as a function of time.

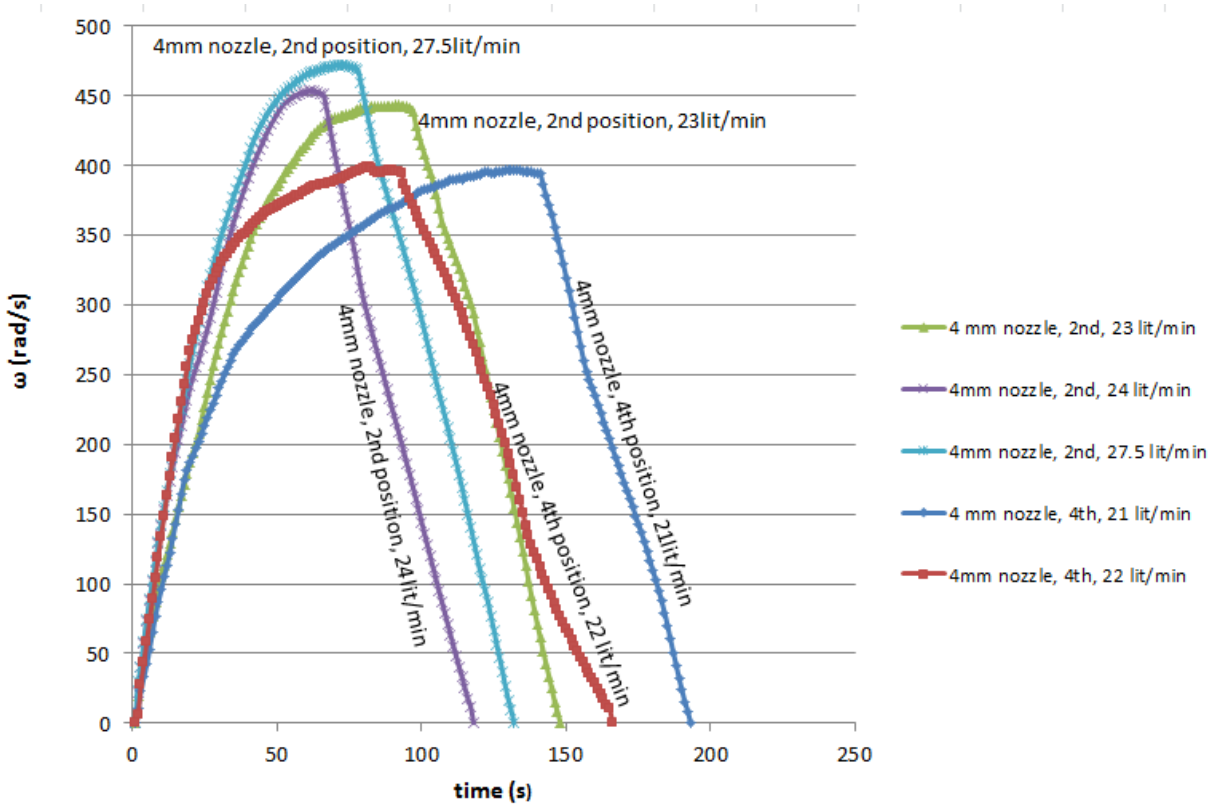

Figure 8-4 Rotational speed VS. time for 4mm nozzle

The results show that with the nozzle at the position closer to the inlet, the turbine achieved higher speed which supports the results from the previous set of experiments. The flow rate of feed water also showed the same effect. In this set of tests, the maximum speed obtained was 4700 rpm when the 4 mm nozzle was at the closer position to the inlet with the hot water flow rate at 27.5 lit/min.

Figure 8-5 indicates the amount of power extracted from the rotor for the different positions of the nozzle and for different flow rates of the inlet water.

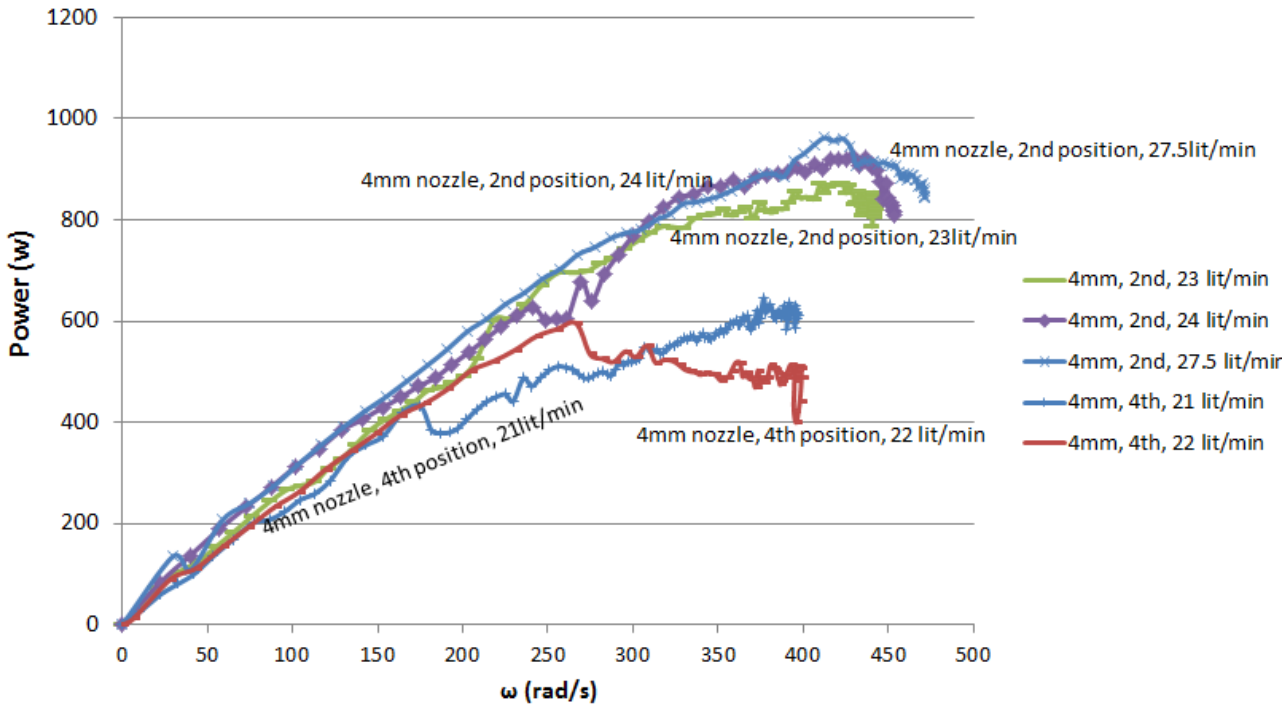

Figure 8-5 Power generation VS. rotational speed for 4mm nozzle

As can be seen from the results, the power production for all the tests showed a similar pattern. The maximum extracted power using the 4 mm nozzle was about 900 W using the nozzle at the position closer to the inlet with 27.5 lit/min of hot water. In addition, similar to the previous outcomes, the feed water flow rate shows its effect on the power generation.

The third group of experiments used similar inlet water temperature to the two previous sets but using a3 mm nozzle at the same two positions.

Figure 8-6 shows the result of rotor speed changes as a function of time for this nozzle and the comparison for the two nozzle positions.

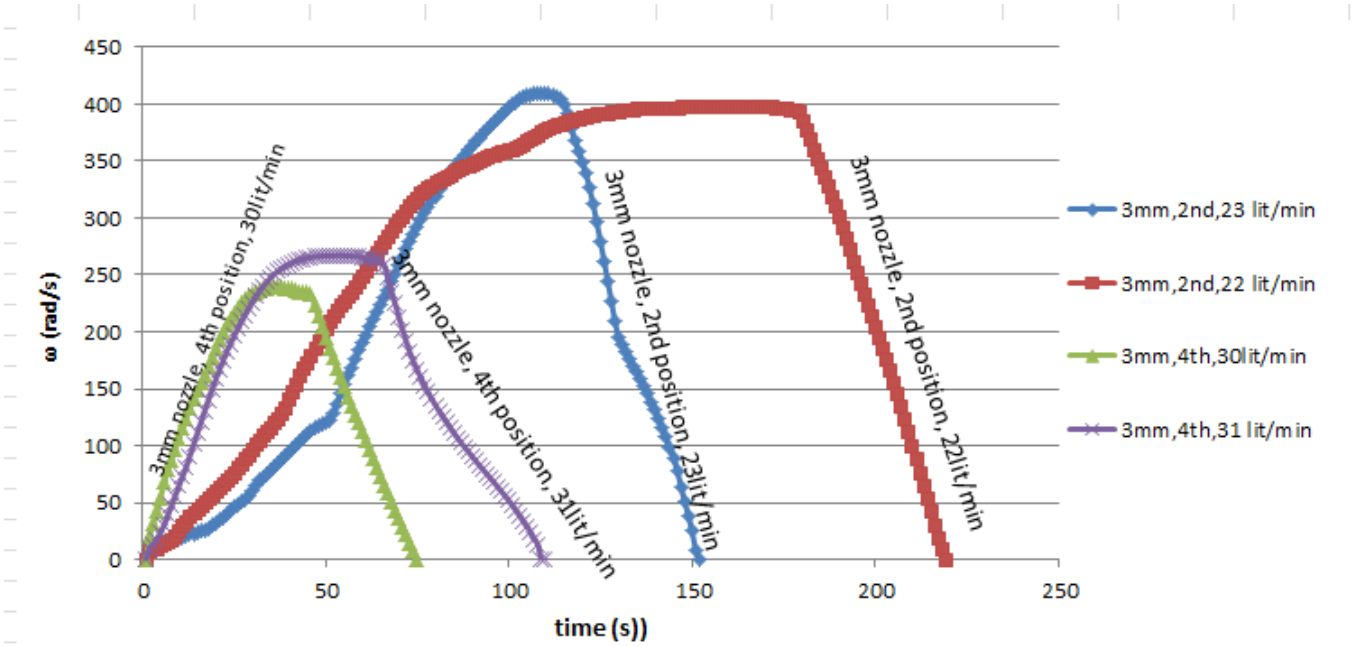

Figure 8-6 Rotational speed VS. time for 3mm nozzle

As with the previous result the maximum rotational speed for the rotor with a 3mm nozzle at the position closer to inlet was approximately 4100 rpm. Using the nozzle in the 4th position and with a very high flow rate of hot water indicated very low speed in comparison. Therefore, it is concluded that having a high flow rate with the small nozzle can create some resistance at the inlet and higher back pressure inside the rotor can cause a reduction in turbine speed. In addition, in this set of case dissimilar to the earlier ones which the valve for the feeding water had been closed as the speed of the rotor starts decreasing to measure the power generated through the procedure which has been described, the open valve has been considered to the full stop of the system in order to see if there is any difference in keeping the turbine rotates at a certain speed. The results show that having the valve open and feeding the water to the system while the rotor is slowing down, does not create higher speed of the rotor but does slow down the rate of decrease of the speed of the turbine. This means that the turbine rotates for a longer period and maintains its speed in a given range for longer. The flow rate of the inlet hot water shows the same effect as in the prior tests in relation to rotor speed.

Figure 8-7 indicates the power generated by the rotor for the 3mm nozzle for different positions and flow rates.

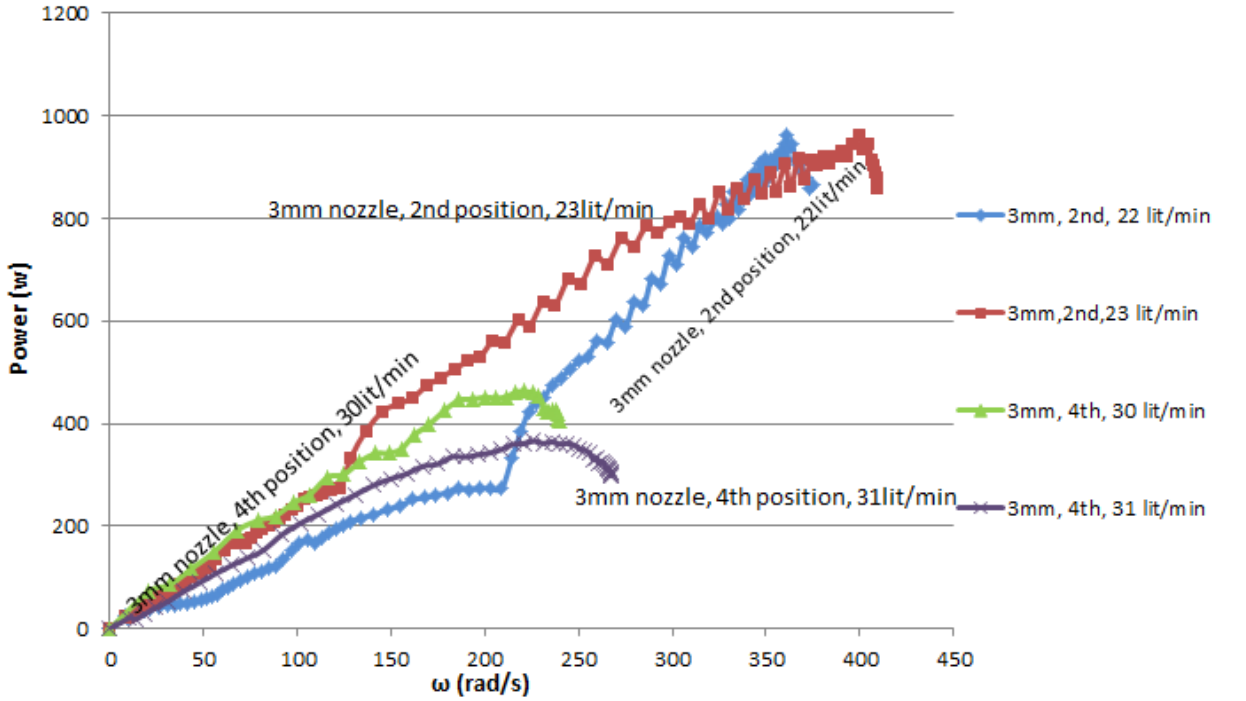

Figure 8-7 Power generation VS. rotational speed for 3mm nozzle

The results show that the maximum power generated from the turbine was approximately 1 kW with the 3mm nozzle at the closer position to the inlet with 23 lit/min of hot water feed .

Similar to the discussion of influence on the turbine speed of having the inlet water valve open , it can be seen that the valve opening does not cause much difference the maximum power generation, although it has the effect of producing more power during the whole test which can be seen by comparing the two tests with the same flow rate and position of the nozzle but with closed valve and opened valve of the inlet water.

8.2.1 Conclusion

It has been shown that more power can be extracted from the rotor by having the nozzle closer to the inlet of the rotor. In order to improve understanding of the effect on power production of using different nozzles sizes at different position of the rotor, the following figure shows a comparison of all the results for all three different nozzles at different positions.

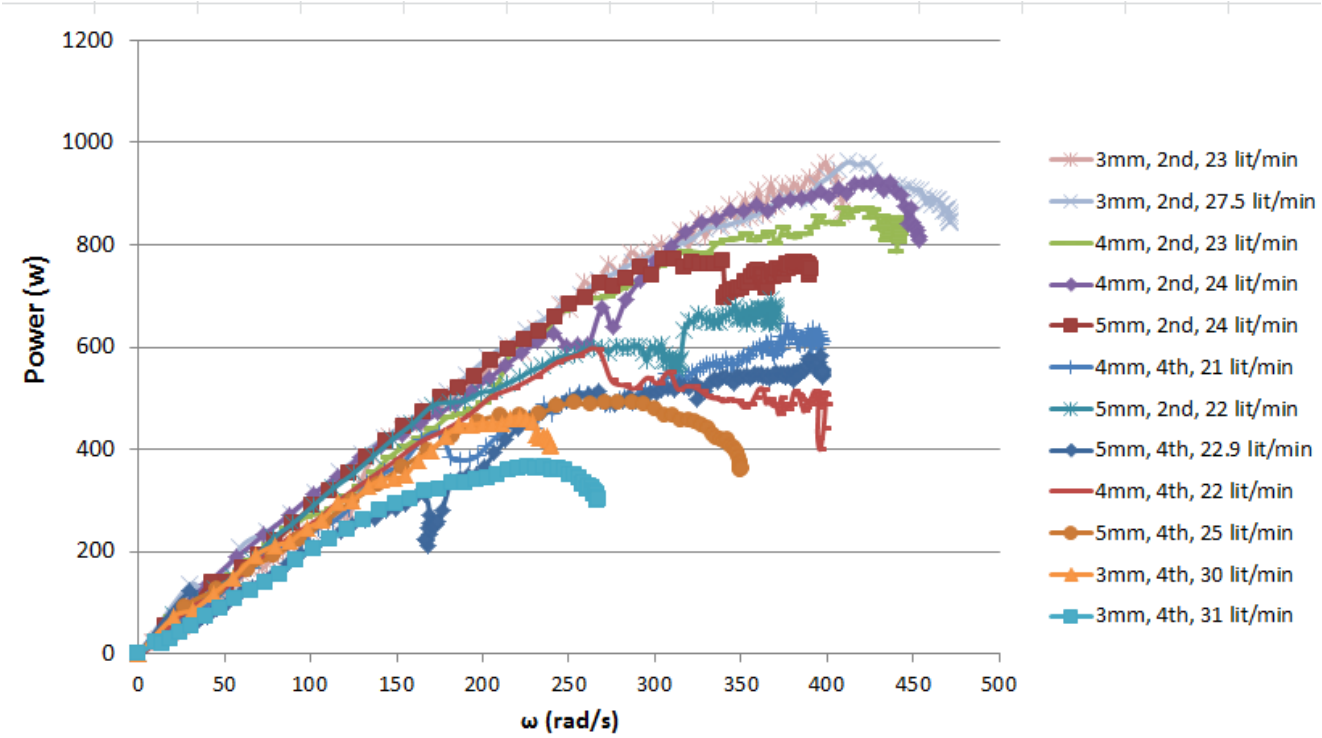

Figure 8-8 Power generation VS. rotational speed all nozzle

The results show that, for the closer position for all the nozzles considered, using the smaller nozzle (3mm) more turbine output power. Comparing the three nozzles at the closer position to the inlet with nominally the same hot water inlet flow rate of approximately 23 lit/min shows a maximum extracted power of 980 W for the 3 mm nozzle, 960 W for the 4 mm nozzle and 600 W for the 5 mm nozzle. Therefore, from the point of power generation the 3 mm nozzle is preferred. However, with a higher hot water flow rate, the extracted power for the 4 mm nozzle was 970 W of which shows the influence of the inlet hot water flow rate. It is concluded that the most efficient nozzle

for the current stainless steel turbine of 0.4 m diameter, is a 3 mm nozzle at 3 mm from the centre of the turbine.

The mechanical power is the total power of the rotor minus the frictional losses in the rotor which can be determined from the deceleration part of the turbine speed profile.

For example, Figure 8-9 shows the power curves for one of the cases which has been studied.

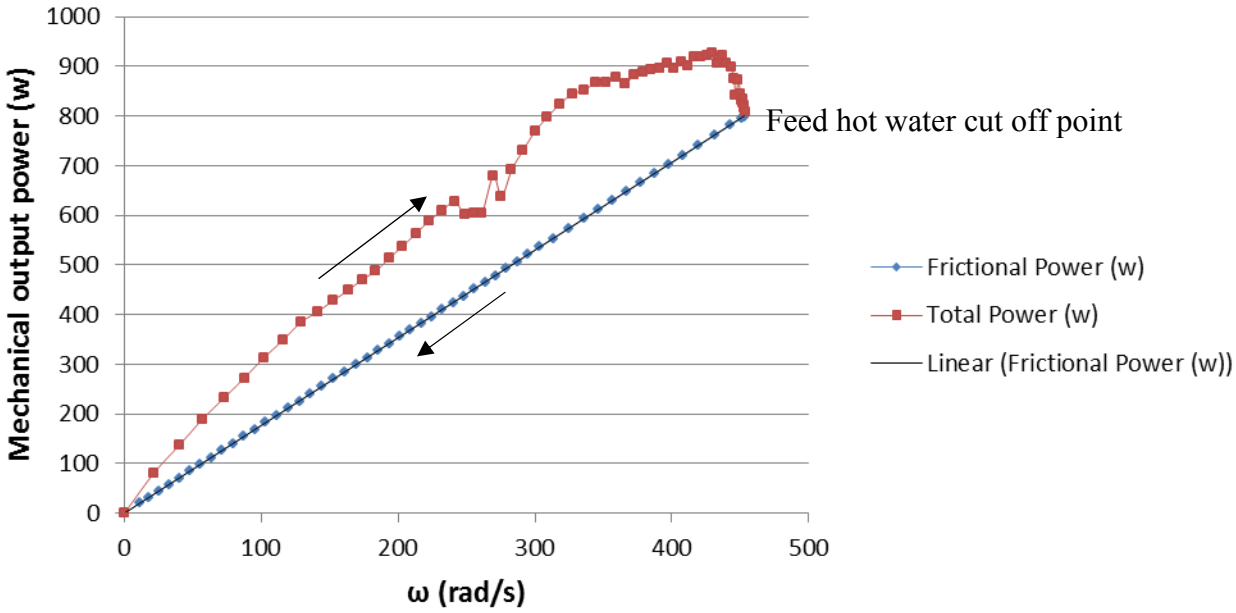

Figure 8-9 Sample of calculating the Mechanical output power

It is seen that the mechanical output power of the system increases up to a certain rotational speed and then starts decreasing because of the continued rise in frictional losses.

Figure 8-10 shows the mechanical output power and the comparison of the best cases for each different nozzle tested in the experiments.

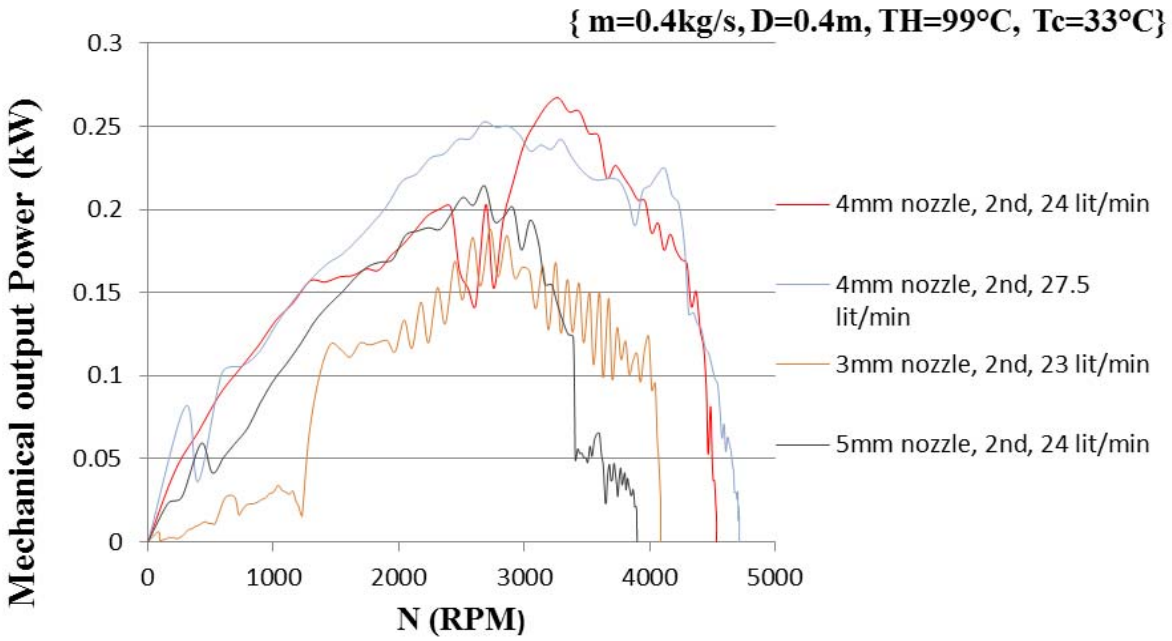

Figure 8-10 Mechanical output power for the examined nozzles at the position closer to the inlet

It can be seen that, although the rotor power was maximum while using the 3mm nozzle at the position near to the inlet, the friction losses were high as well. Consequently, the mechanical output power was minimum. This graph also shows that the most effective nozzle in terms of optimization between the power extracted from the rotor and the frictional losses was the 4 mm nozzle. In this case, the maximum mechanical output power obtained in the experiments was 270 W.

In order to investigate the isentropic efficiency of the designed turbine; the experimental results have been compared with the theoretical results which have been obtained using the developed computer model. Figure 8-11 shows the mechanical output power of the system for different isentropic efficiencies compared with the experimental results.

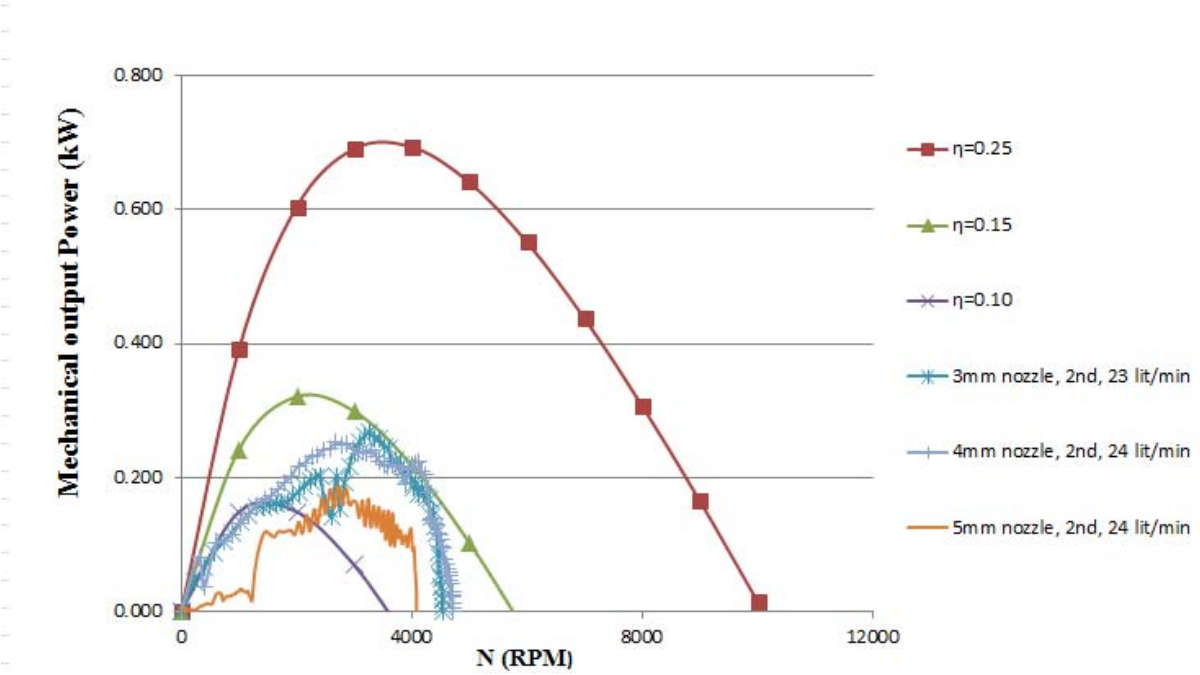

Figure 8-11 Comparison of the experimental and theoretical Mechanical output power for the examined nozzles at the position closer to the inlet

As this figure indicates, for given conditions for the inlet hot water and size of the rotor and nozzles, at the maximum mechanical output power generation, the isentropic efficiency of the designed turbine is approximately 15% at the current stage of development using the split rotor.

The initial torque for the aluminium turbine which was calculated from the experimental results is shown in Figure 8-12.

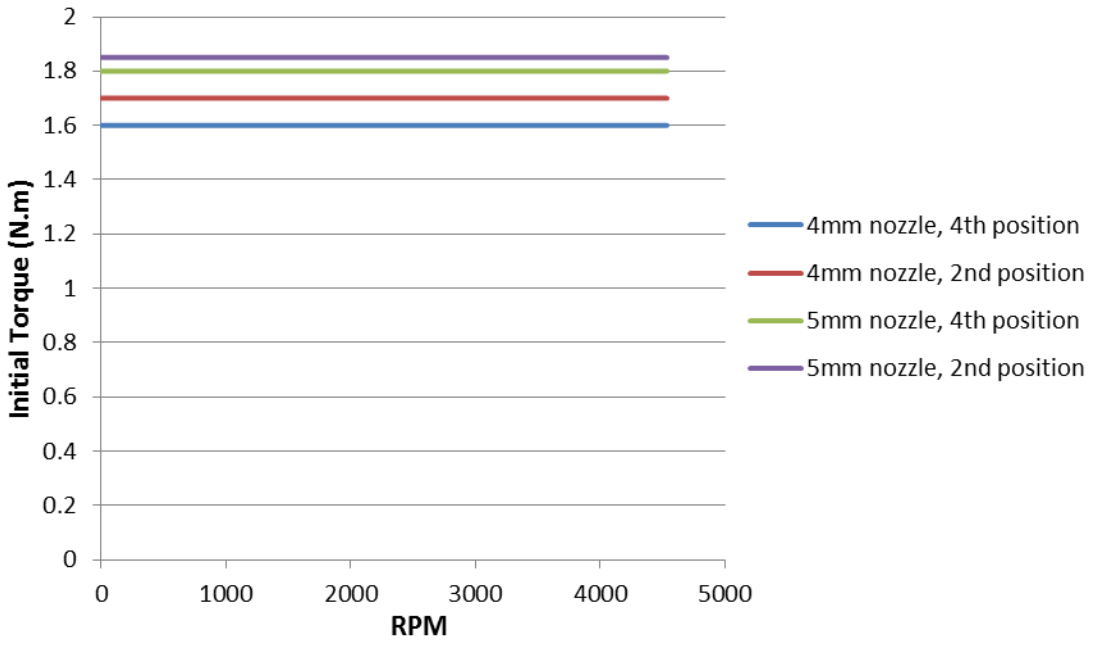

Figure 8-12 Initial torque for the aluminium rotor

As shown in the figure, the initial torque needed for the turbine to start rotating was almost the same for all the conditions through the experiment and was approximately 1.7 N.m.

8.3 Advanced rotor

A new turbine has been designed based on the experimental results and on analytical studies of the flow pattern of the turbine . In this new turbine, a 3 mm orifice of has been used in a converging-diverging form. The rotor has a diameter of 0.4 m and moment of inertia of 0.31 kg/m2.

The results are shown in the following figures.

Figure 8-13 indicates the changes in rotational speed of the turbine as a function of time.

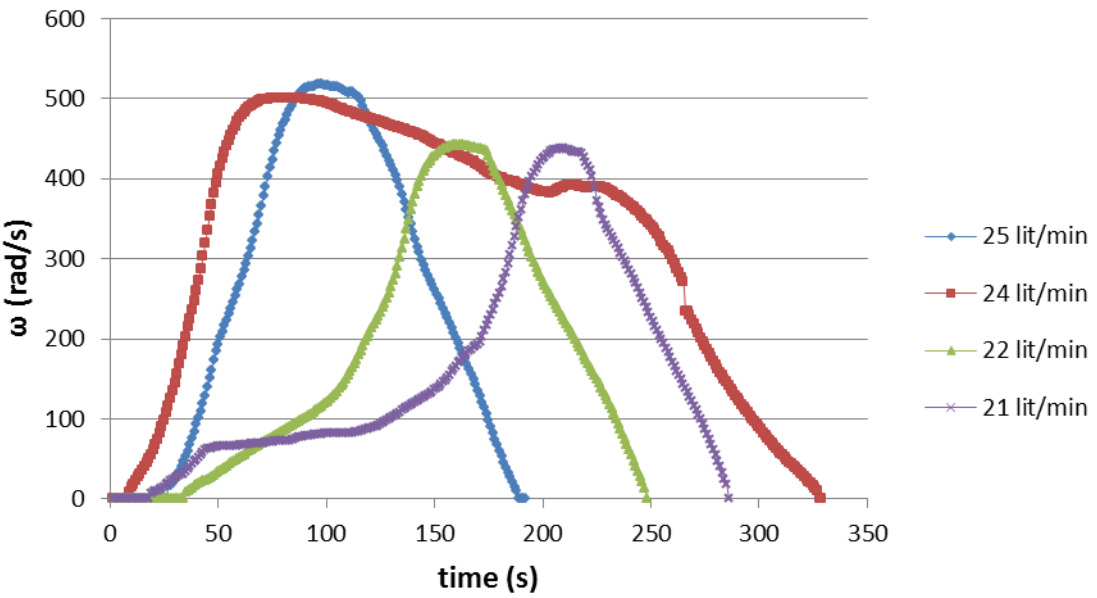

Figure 8-13 Rotational speed VS. time for new designed turbine

As shown in Figure 8.13, the maximum rotor speed is influenced by the flow rate of the feed hot water. The maximum speed obtained was approximately 5100 rpm with 25 lit/min of hot inlet water at 98°C.

Figure 8-14 shows the power extracted from the new design of rotor.

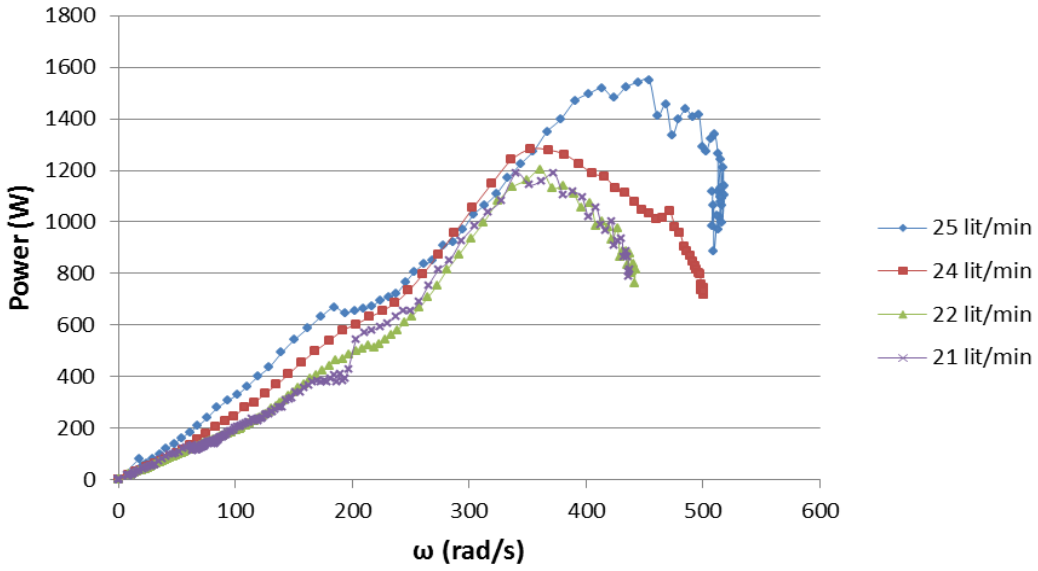

Figure 8-14 Power generation VS. rotational speed for the new design of turbine

It can be seen that with a higher flow rate of inlet hot water, more power can be extracted from the rotor. The maximum power was 1.5 kW associated with a flow rate of 25 lit/min of feed water. It is a large improvement in comparison with the previous rotor with the 3mm nozzle at the position near to the inlet which gave maximum power of 980 W,.

As was analysed for the previous turbine, the mechanical output power for the new turbine has been considered in order to assess the net power output of the turbine. In addition, the isentropic efficiency of the turbine can be estimated through comparison with the developed computer model.

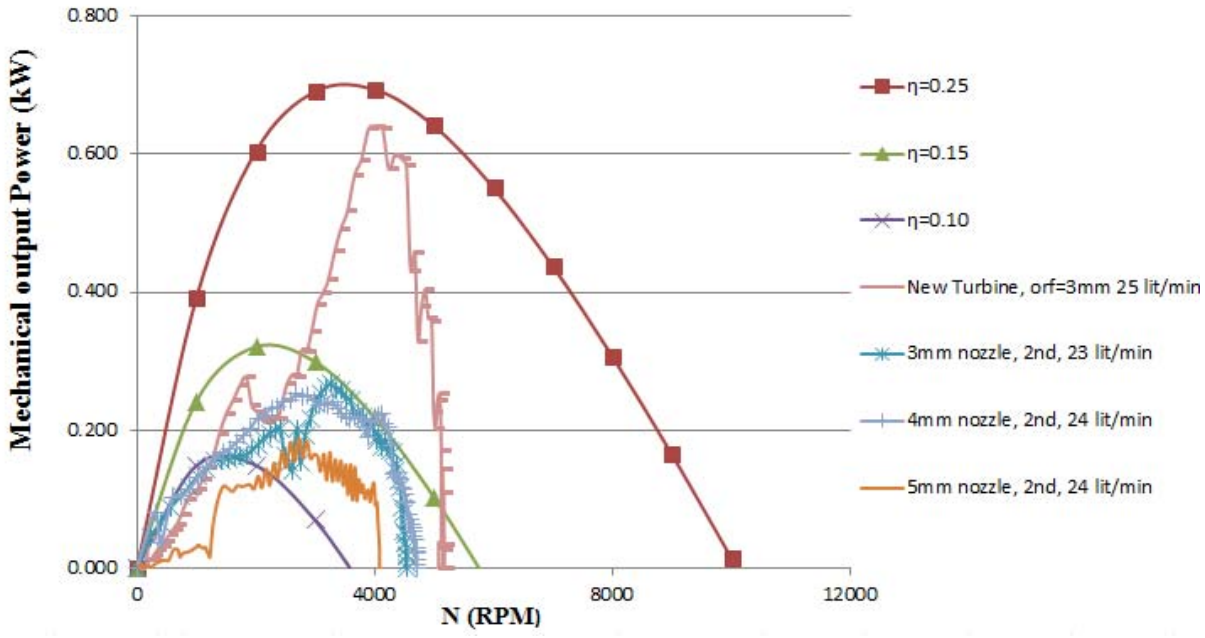

Figure 8-15Comparison of the experimental and theoretical Mechanical output power for the old and new turbine

The results show that the isentropic efficiency of the new turbine was approximately 0.2 which is twice that of the previous turbine. It can be seen that at present the maximum power happens between 3000 to 4000 rpm. So if this turbine was used to produce 50Hz AC power then a suitable gear box must be selected.

The initial torque for the newly designed turbine has been calculated through the deceleration experiment. The results are as follows:

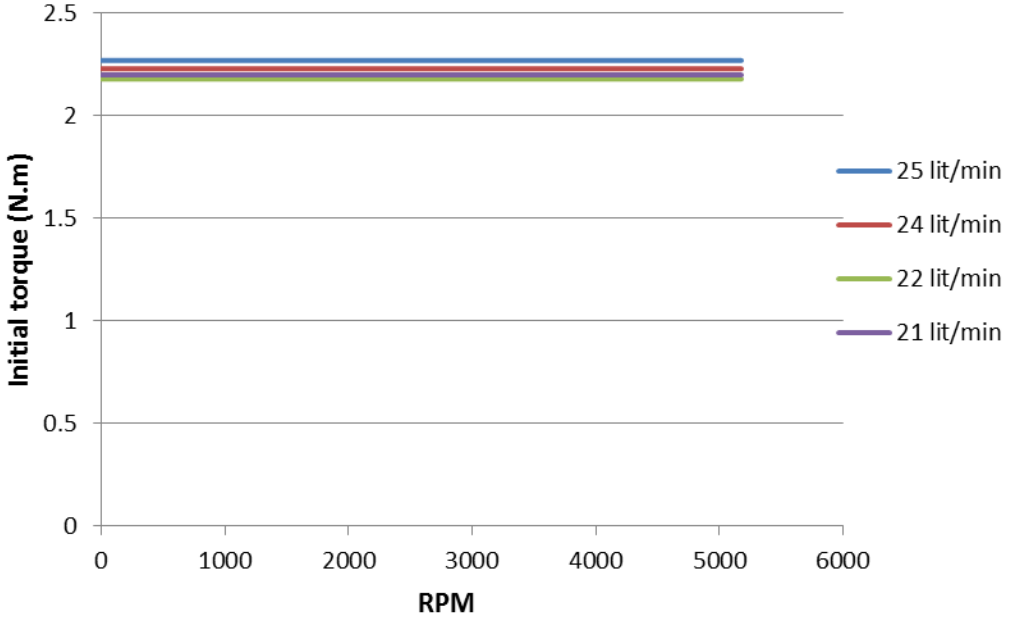

Figure 8-16 Initial torque for the new designed rotor

The isentropic efficiency of the turbine for the tests has been calculated as in the procedure described in Chapter 4 Section 5.

The results for the split turbine and the advanced turbine with a 3 mm throat are shown in Figure 8-17:

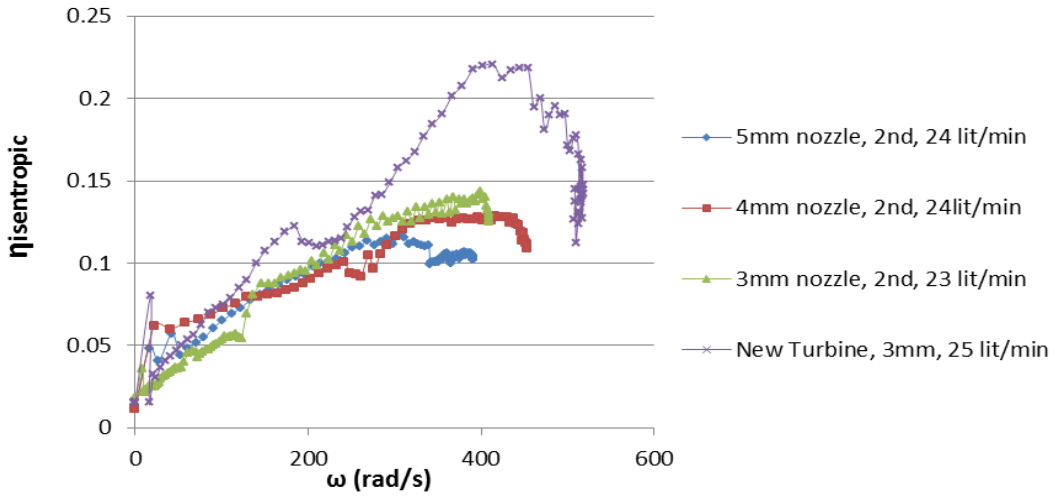

Figure 8-17 Comparison of the experimental isentropic efficiency for the old and new

turbines

From the results it seen that the maximum isentropic efficiency achieved experimentally for the new turbine was approximately 0.23. The earlier turbine, using the 3mm nozzle at the 2nd position of the inserts had maximum isentropic efficiency of 0.15.

Therefore, further experimental tests have been carried out using the advanced turbine with 3 mm throat and a reduced diameter of 1.5 mm. The resulting power output is shown as Figure 8-18.

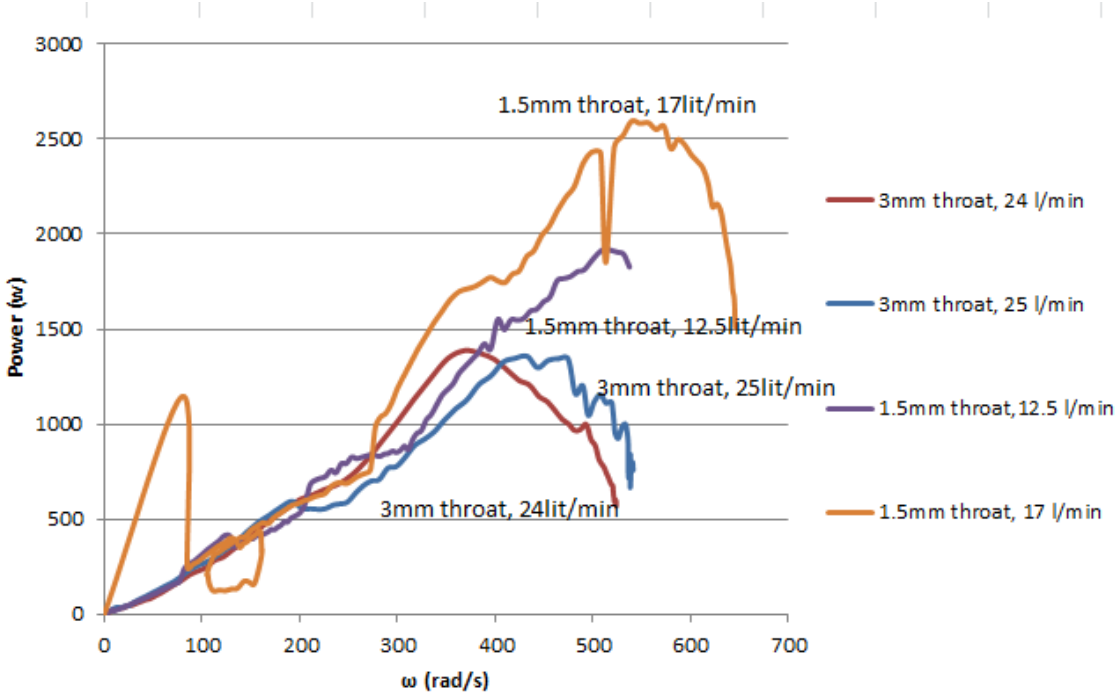

Figure 8-18 Power generation of the advanced rotor for 2 different sizes of throats

It is seen that the 1.5 mm throat provided the maximum power production which was 2.5 kW compared to the 3mm throat which produced 1.4 kW. In addition, the repeatability of the data is indicated by the consistent results obtained through the experiments.

In addition, comparison has been made of the isentropic efficiencies for the same tests.

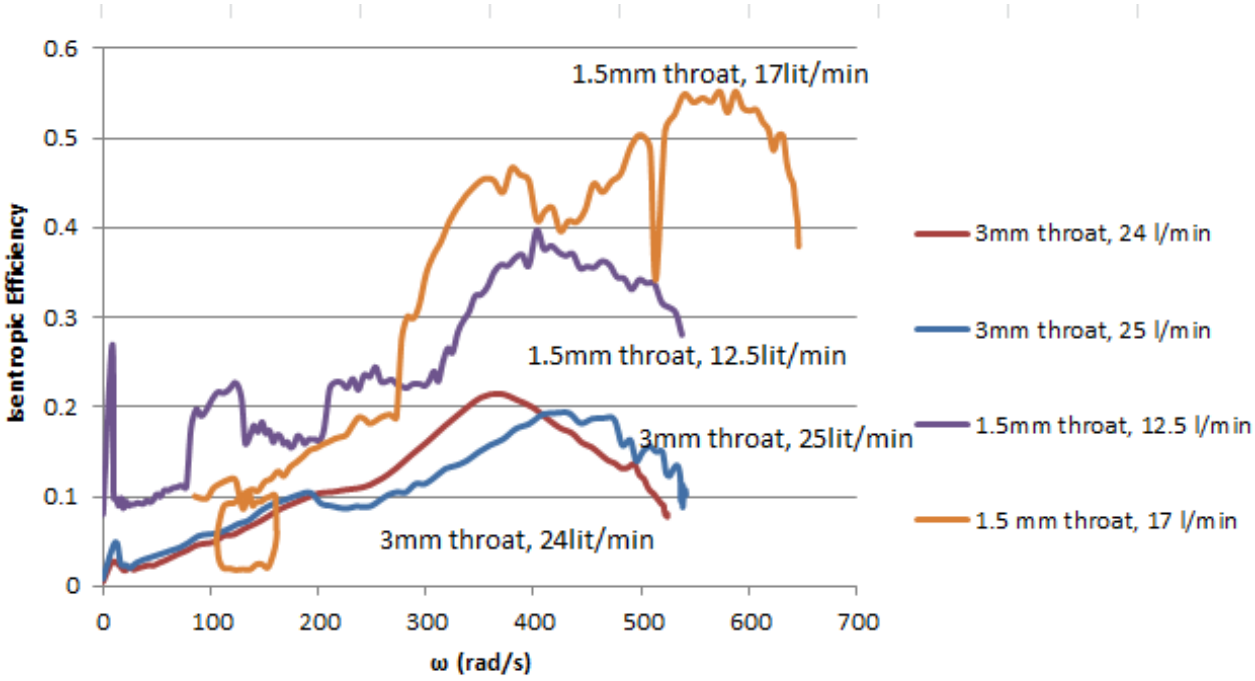

Figure 8-19 Isentropic efficiencies of the advanced rotor for 2 different sizes of throat

It is seen from Figure 8-19 that using the smaller throat gives the highest isentropic efficiency of approximately 55% which is a dramatic improvement. Also it can be seen that this result has been achieved with a smaller flow rate of the feed hot water.

8.4 Conclusion from results for the split and advanced rotor

Based on the developed computer model, the gross power which is the sum of the frictional power and power available for extraction at any given rotational speed, can be calculated based on the turbine specification and inlet conditions.

$$P(\omega) = T_o(\omega) \times \omega + I \times \omega \times \frac{d\omega}{dt} = P_{friction} + P_{inertia} \quad (8.1)$$

Comparison of the different nozzles in the aluminium turbine and also turbine designed on Fabris work is shown in Figure 8-20.

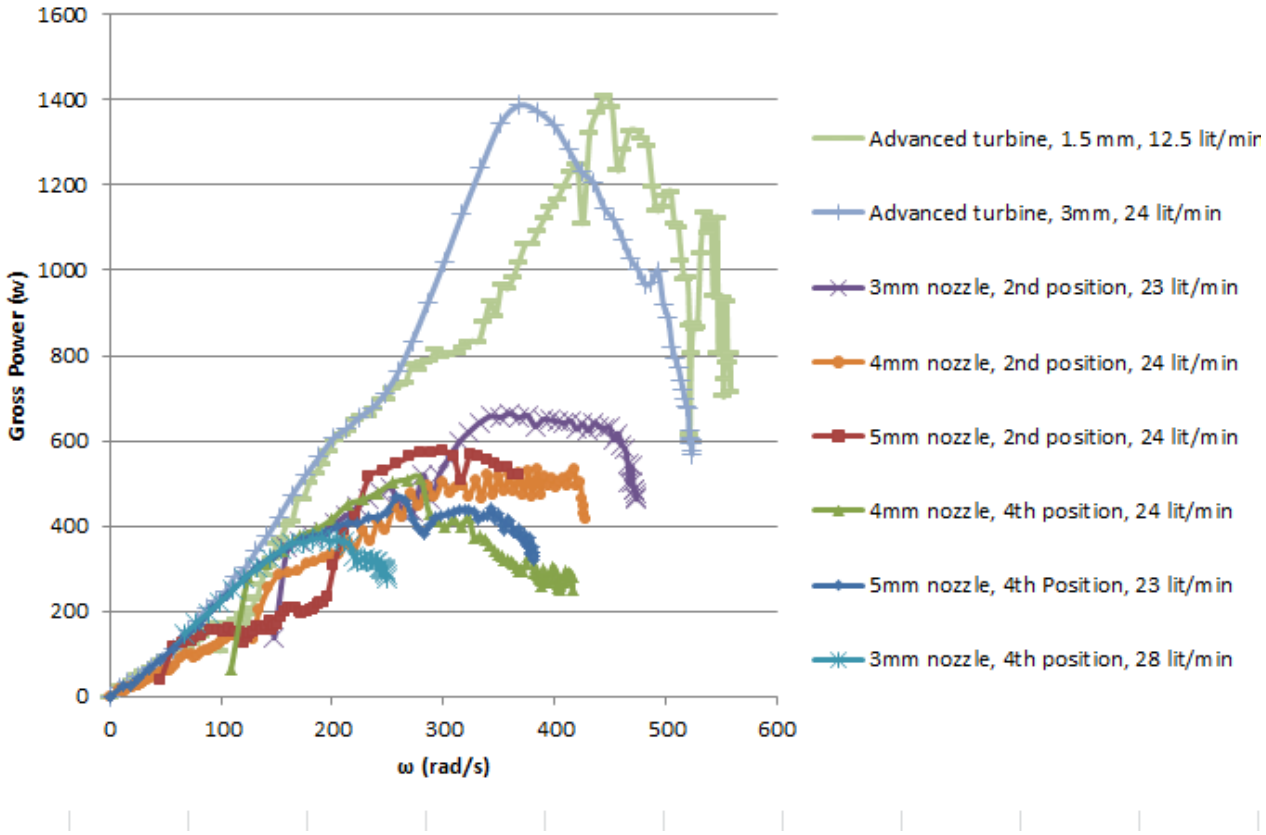

Figure 8-20 Comparison of the gross power for the old and new turbines

It is seen that for the insert nozzles in different positions, having the insert closer to the inlet (2nd position) gave more power generation, of which the maximum was 650 W. On the other hand, using the Fabris turbine with the 3mm throat the maximum power generated was 1.4 kW at approximately 4000 RPM. Having the throat diameter halved, gave maximum power of 1.42 kW at approximately 4700 RPM. In this case, the maximum rotational speed was approximately 6000 RPM. Thus, it can be concluded that having the 1.5 mm throat closer to the inlet with the Fabris profile for the rotor has performed better as a power producer.

Another parameter which can be used as a reliable way of comparing the performance of the turbine in the process of converting the thermal energy to the mechanical energy is the isentropic energy of the nozzle.

In the turbine, considering the thermodynamic process which takes place, the thermodynamic power can be defined as in Equation 8.2:

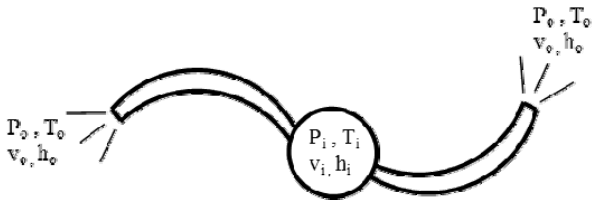

Figure 8-21 Thermodynamic process inside the rotor

$$Thermodynamic\ power = P_{gross} + \frac{1}{2}\dot{m}V_a^2 \tag{8.2}$$

Therefore:

$$\dot{m}(h_i - h_o) = T_o(\omega) \times \omega + I \times \omega \times \frac{d\omega}{dt} + \frac{1}{2}\dot{m}V_a^2 \tag{8.3}$$

In addition the total torque is:

$$T = T_o + I\frac{d\omega}{dt} \tag{8.4}$$

And

$$T = \dot{m} R V_a \tag{8.5}$$

Using the above two equations, the absolute velocity of the mixture at the exit of the nozzle can be calculated as follows:

$$V_a = \frac{T_o + I\frac{d\omega}{dt}}{\dot{m}R} \tag{8.6}$$

Using the calculated absolute velocity and replacing it in the power equation, the real enthalpy of the mixture can be calculated as:

$$h_o = \frac{\dot{m}h_i - (T_o \times \omega + I \times \omega \times \frac{d\omega}{dt} + \frac{1}{2}\dot{m}V_a^2)}{\dot{m}} \tag{8.7}$$

The thermodynamic process of the trilateral cycle has been shown and explained in Chapter 4 Section 5 and has been used to calculate the isentropic efficiency of the system.

The results from the tests performed in conjunction with the developed computer model, enable calculation of the isentropic efficiencies of the different turbines.

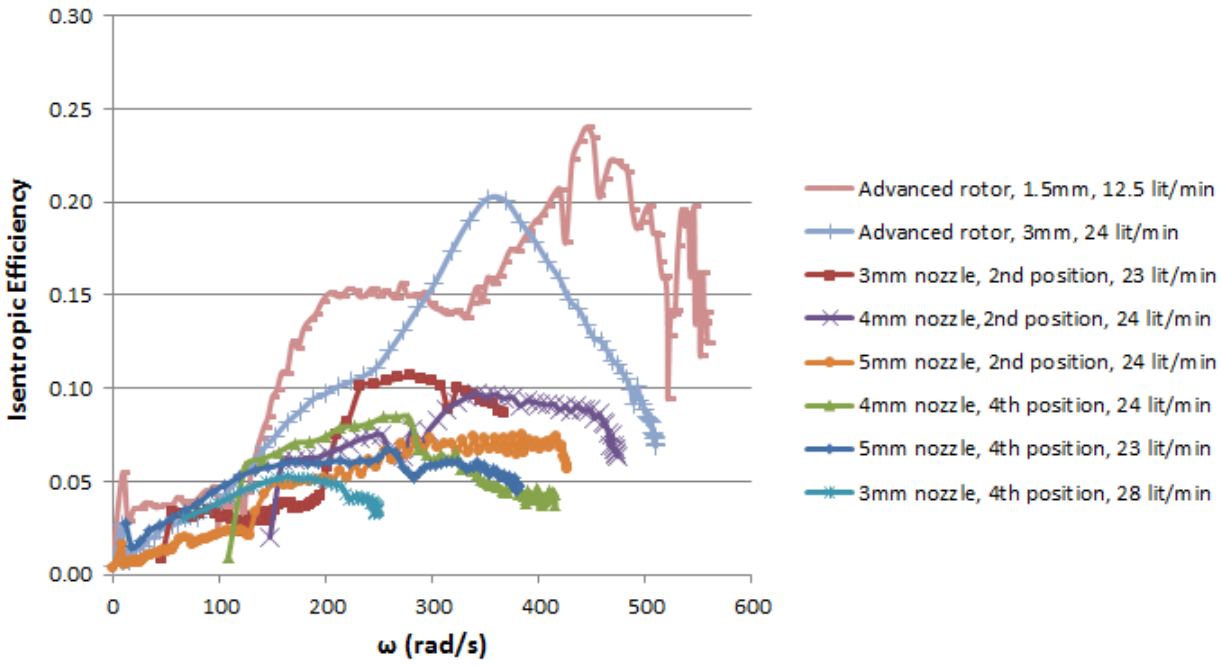

Figure 8-22 Comparison of the experimental isentropic efficiency for the old and new turbines

As seen in Figure 8-22, the maximum isentropic efficiency achieved so far was with the Fabris turbine with 1.5 mm throat close to the inlet. This turbine had 22% isentropic efficiency. For the other turbine, using the nozzles at the 2nd position provided approximately 10% efficiency.

As discussed in the section concerned with the theory of the computer model, the optimum area for the any inlet condition, can be calculated based on the relative velocity of the mixture at the nozzle exit (Vr) and the total volumetric flow rate at the exit). In order to determine how far the designed turbine was from the optimum calculated situation, the ratio of calculated optimum nozzle area to the actual area has been defined and the results based on the tests performed are shown in Figure 8-23.

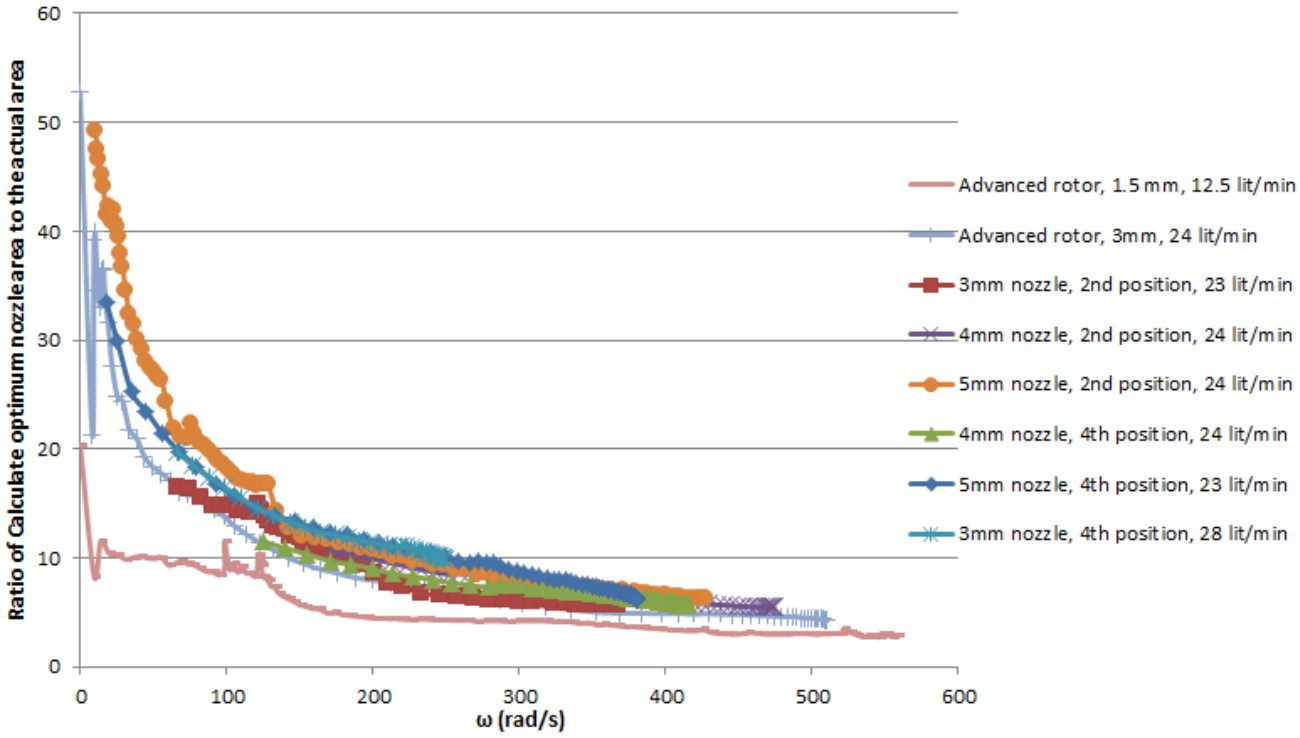

Figure 8-23 Comparison of the ratio of calculate optimum nozzle area to the actual area for the old and new turbines

Figure 8.23 shows that in the best case there is a factor of approximately 5 times difference between the calculated optimum area and the actual area. This difference decreases as the speed increases which indicates that maintaining the turbine rotation at high speed makes its operation closer to the optimum case.

The other efficiency which can be compared for different cases is the thermodynamic efficiency of the system which is based on the thermodynamic power with substraction of the total pumping power for brine and fresh water.

$$\eta_{Thermodynamic} = \frac{P_{gross} + \frac{1}{2}\dot{m}V_a^2 - P_{pump}}{Thermal\ Energy\ in} = \frac{T_o(\omega) \times \omega + I \times \omega \times \frac{d\omega}{dt} + \frac{1}{2}\dot{m}V_a^2 - \dot{V}\Delta P}{\dot{m}C_p\Delta T} \quad (8.8)$$

The thermodynamic efficiency of the system based on the experiments is shown in Figure 8-24

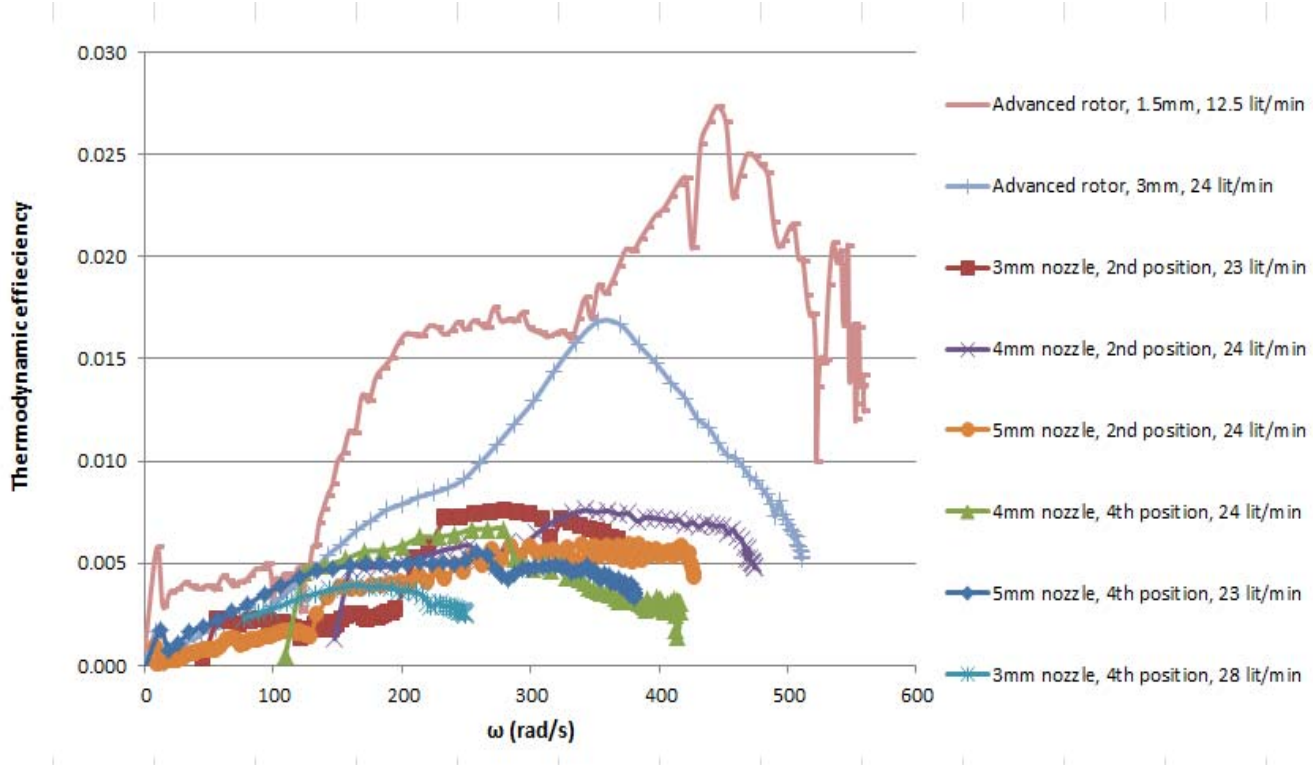

Figure 8-24 Comparison of the Thermodynamic efficiency of the system for the old and new turbines

As Figure 8-24 shows, the maximum thermodynamic efficiency for the Fabris turbine with 1.5 mm throat was approximately 2.7% and compared to the old turbine was approximately 0.5% higher.

In order to gain a better perspective on the state of development of the system, a ratio has been defined of the ideal trilateral efficiency to the thermodynamic efficiency of the system.

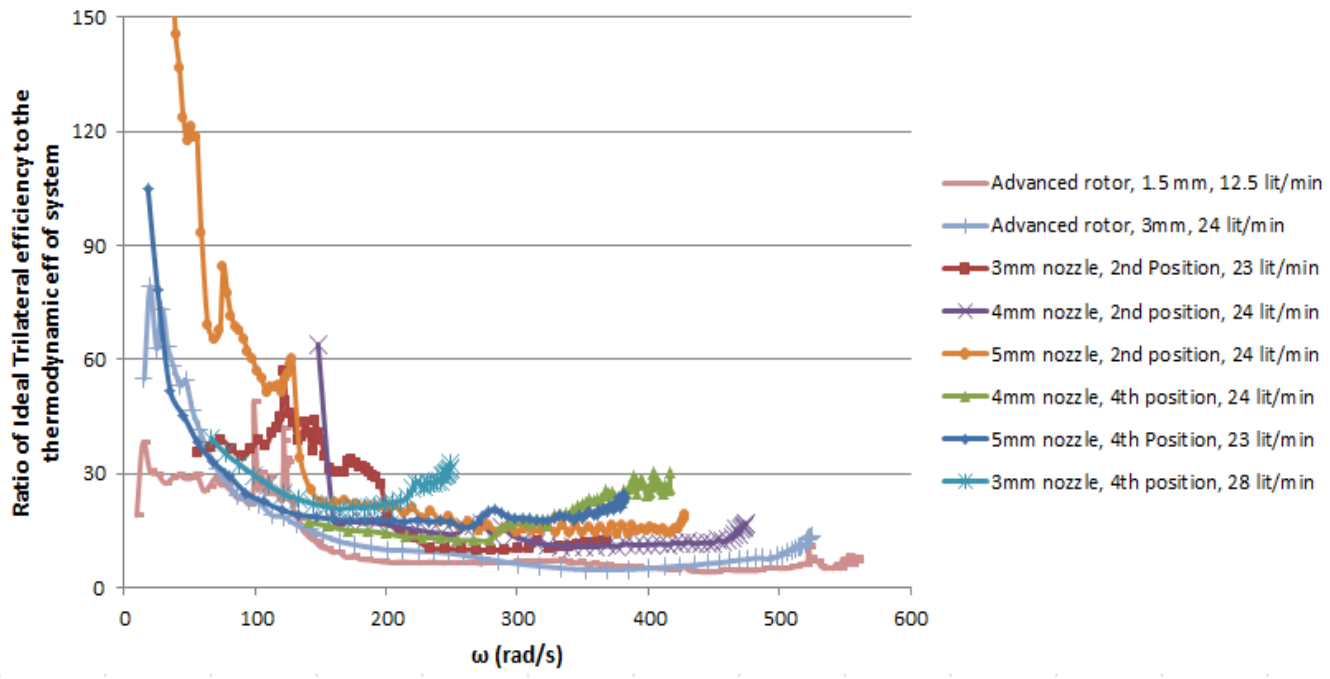

Figure 8-25 Comparison of the ratio of ideal trilateral efficiency to the thermodynamic efficiency of the system for old and new turbines

It can be seen that, using the best performed rotor in the CDP showed more than 5 times under the ideal trilateral efficiency for the same thermal condition.

8.5 Introducing a pin into the front of the throat to enhance the flashing flow

Based on the literature study that has been carried out on flashing phenomena in stationary nozzles, the idea of using a pin in front of the throat in order to stimulate flash boiling for the two phase flow in the rotary nozzle has been developed and applied to the split rotor for further analysis.

From experimental tests on the split rotor, the best option considered was to investigate inserting a pin in front of the throat. Therefore, tests were conducted using an insert with the 3 mm diameter orifice, for which the rotor gave best performance when the insert was positioned at location 2

A calibrated thermocouple was placed approximately 15 mm in front of the turbine nozzle exit to measure the temperature of the fluid leaving the turbine. Measurement of the nozzle exit temperature showed that the fluid leaving the turbine was always at a higher temperature than the saturation temperature corresponding to the absolute pressure in the flash tank. The temperature of the water leaving the turbine was higher than the saturation temperature at the exit pressure (flash tank pressure). At the same time the temperature of the liquid water which fell to the bottom plate was measured and found to be very similar to the saturation temperature corresponding to the flash tank pressure. From these two observations it was concluded that flashing of the feed water happened incompletely inside the turbine nozzle as expected. A spray / atomization nozzle was made by adding a flat head pin in front of the orifice throat to increase the surface area of liquid to improve flashing.

As shown in Figure 8-26, a 2.5 mm diameter flat head pin was placed in line with the orifice throat of the brass insert at 4mm distance. This was done to break the feed water jet and create a spray. The turbine with the brass insert placed at location 2 was tested to estimate the performance. The feed water was maintained under local atmospheric pressure and supplied as sub-cooled hot water to the turbine, while the pressure in the flashing tank was maintained at approximately 6 kPa absolute for all the tests.

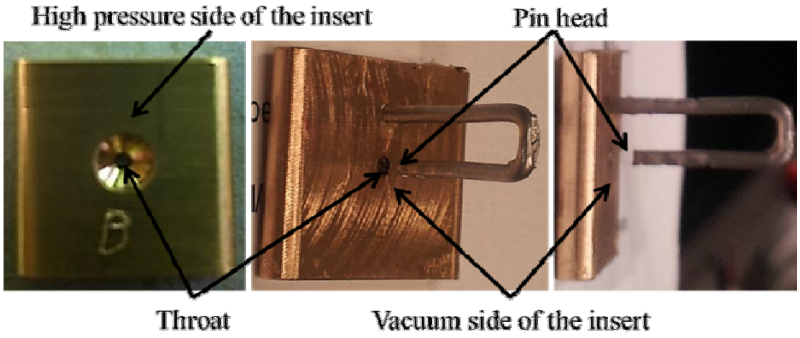

Figure 8-26 Insert and pin set-up

The first experiment on this rotor was performed with no pin in front of the orifices and both nozzles fully open. As in a further study the pin was used to disrupt the mixture flow, this experiment has been shown as WithOutPin (WOP). A hot water tank has been

used in order to supply the hot water. The test has been performed twice in order to assure the repeatability of the data and to validate the developed computer model.

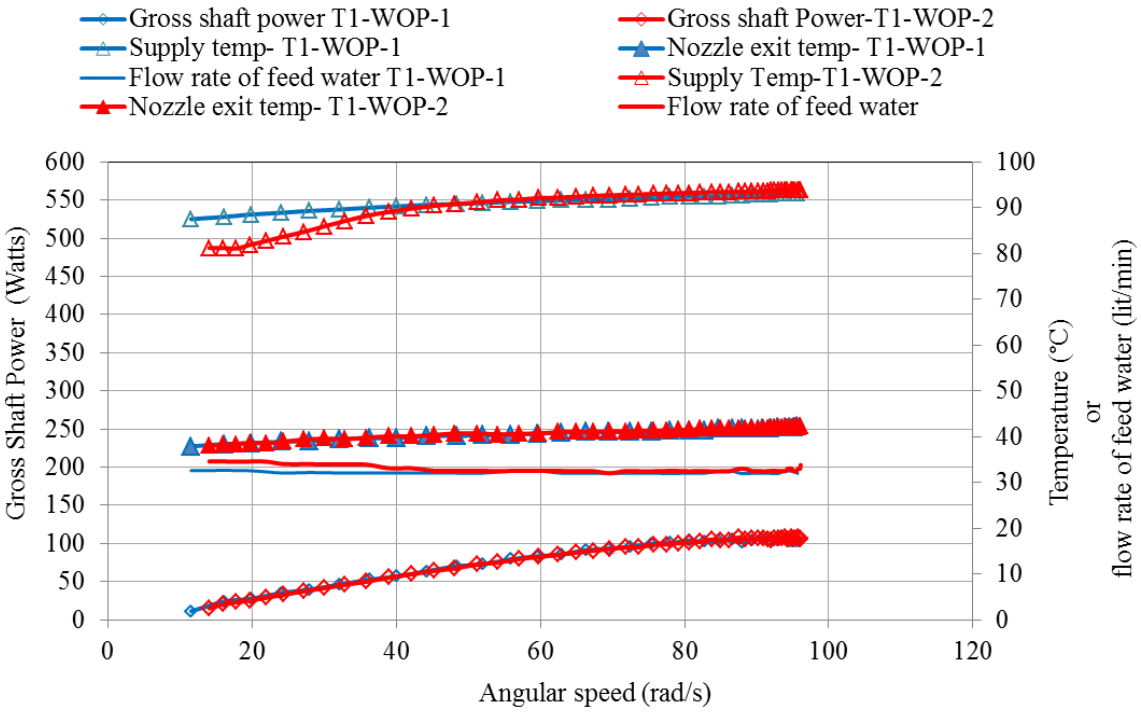

Figure 8-27 Gross power versus angular velocity for split rotor without using pin

It is seen that, for a flow rate of 30 lit/min, the turbine reached 900 rpm with the inlet temperature at 92 °C and the nozzle exit temperature at 40 °C. It can be concluded that the cooling capacity of the system was insufficient for such a flow rate of feed water. The repeatability of the data and results is demonstrated through these graphs which have a good match

As in the previous test, isentropic efficiency and the ratio of the ideal trilateral efficiency to the thermodynamic efficiency have been considered to gain more insight into the performance.

.

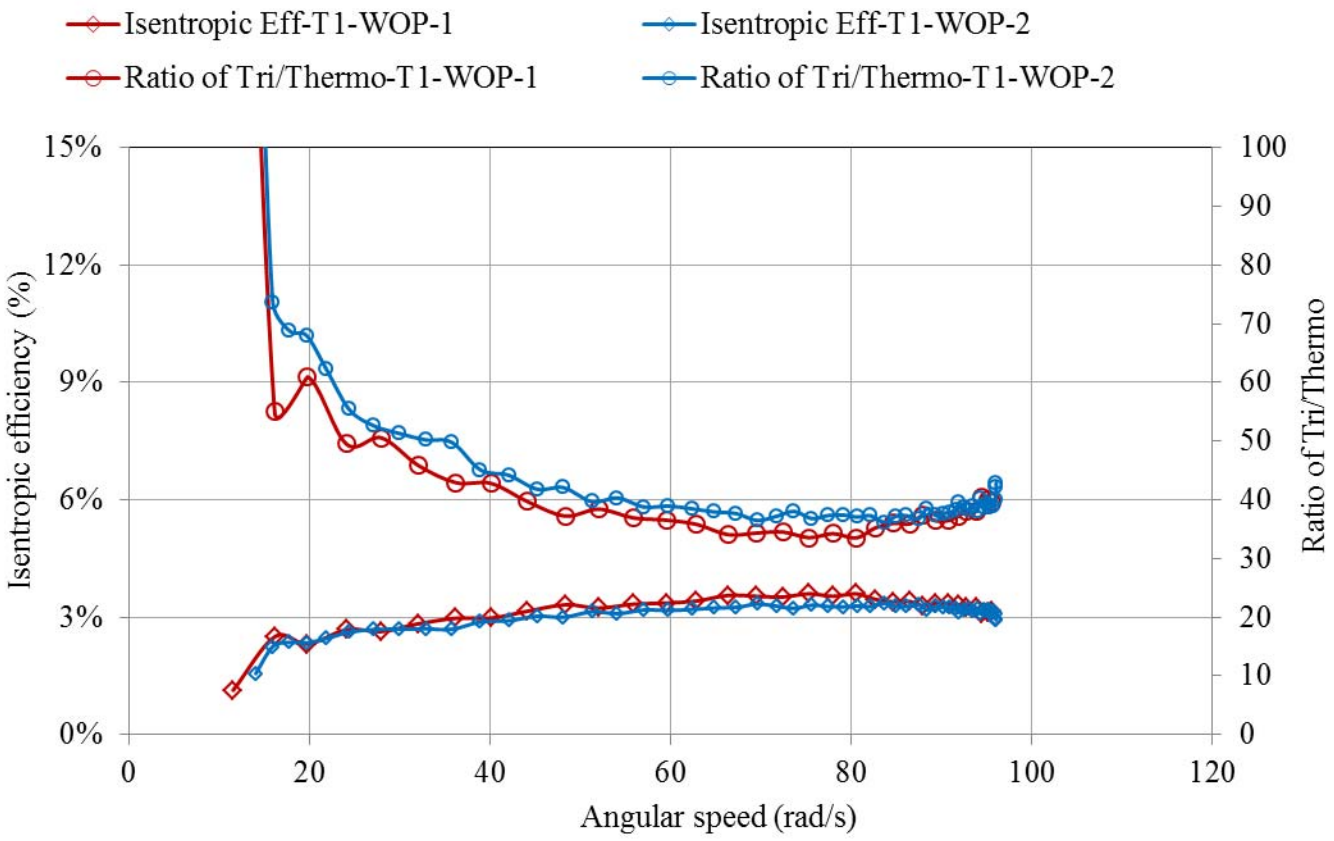

Figure 8-28 Isentropic efficiency and ratio of trilateral efficiency/thermodynamic efficiency for split rotor without pin

As the graph shows, the isentropic efficiency using this turbine was approximately 4 % and the ratio was quite high compared to the previous test, with the thermodynamic efficiency almost 40 times off the ideal case. Again, the results show the repeatability of the validated computed model.

Figure 8-29 shows the fresh water production of the system.

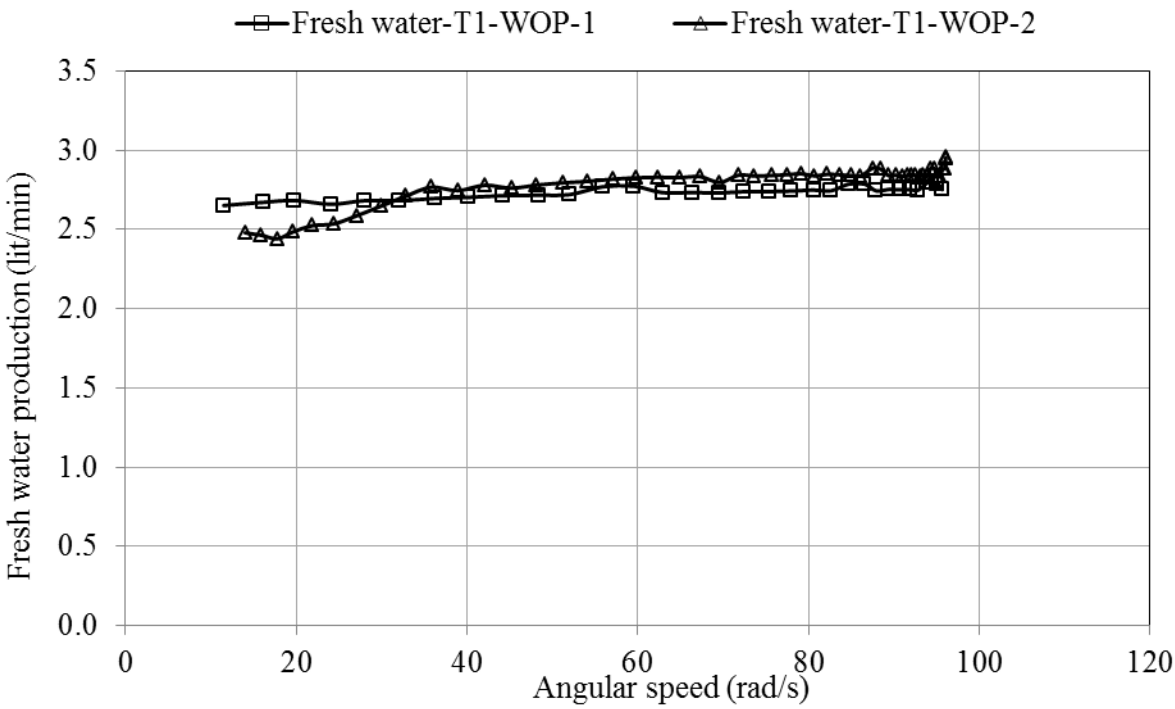

Figure 8-29 Fresh water production of split rotor without pin

The fresh water production was 2.8 lit/min of fresh water which was approximately 7% of the feed water.

The next experiment was carried out using this rotor with the condition of two nozzles fully open with a 3mm pin in front of the orifice (as shown in Figure 8-26) to help the separation of the mixture flow and again using hot water tank as the supply feed water. Figure 8-30 shows the gross power produced vs. rotational speed. Also, the temperatures of the inlet and outlet of the turbine are shown.

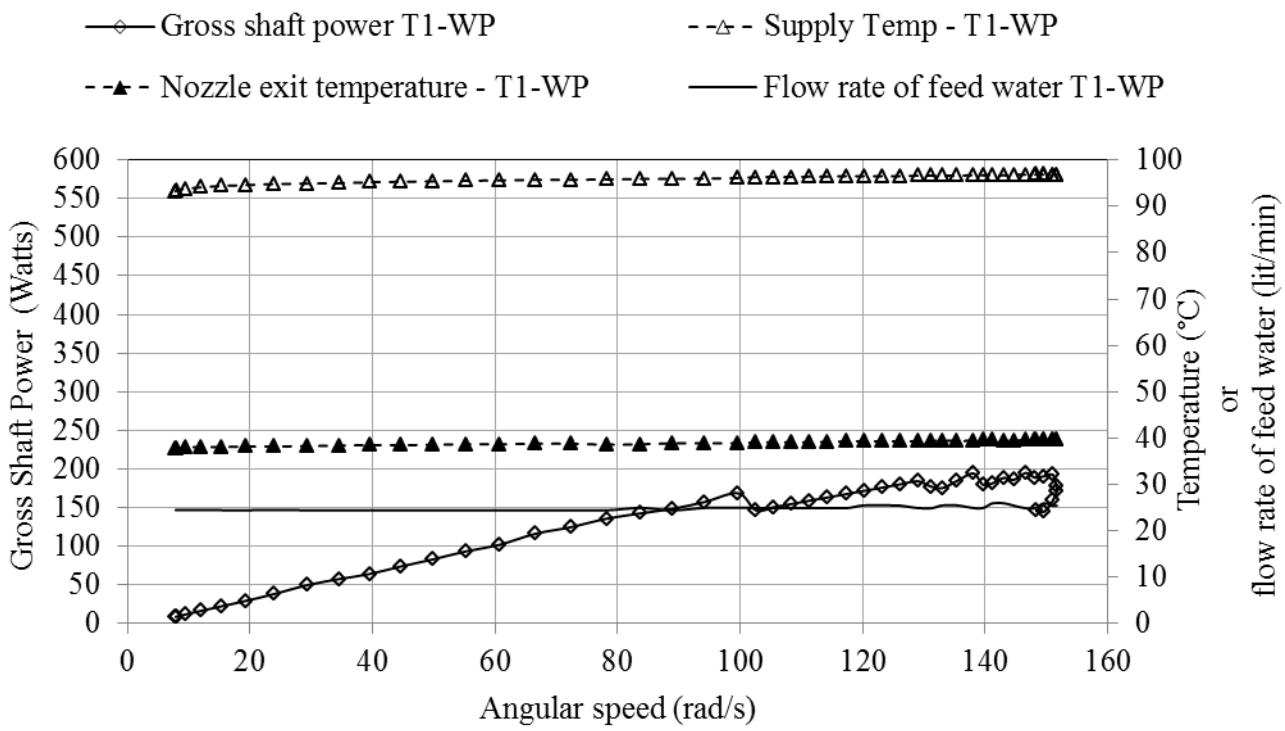

Figure 8-30 Gross power, nozzle exit temperature, supply temperature and flow rate for split rotor with pin in front of throat versus angular speed

It is seen that the flow rate of the feed water was approximately 25 lit/min and the gross shaft power produced was approximately 200 W at 1500 rpm. The inlet temperature of the hot water was 98 °C and the temperature of the mixture at the exit from the nozzle was 37 °C.

Figure 8-31 shows both the isentropic efficiency of this rotor and the ratio of the ideal trilateral cycle to the thermodynamic efficiency of the system in order to improve understanding of the performance of the system.

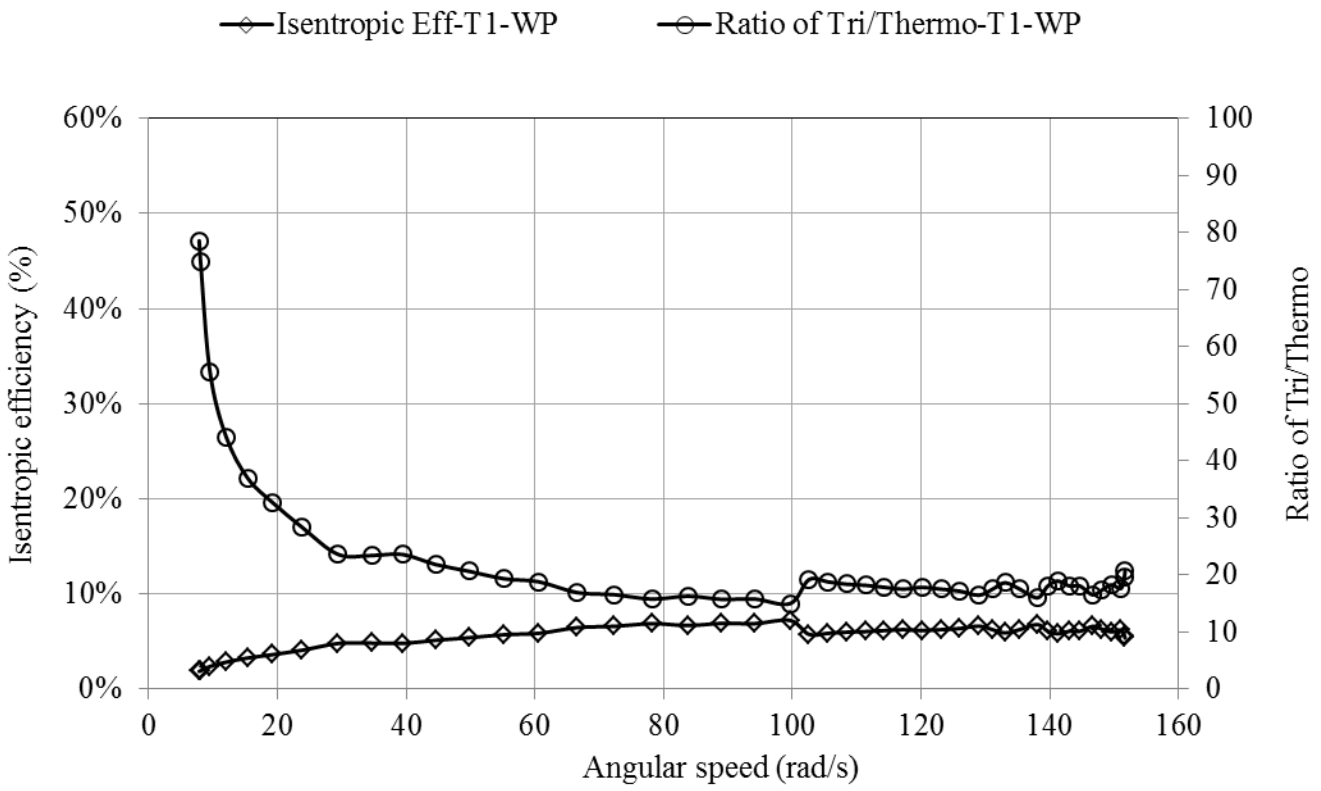

Figure 8-31 Isentropic efficiency of split rotor with pin, the ratio of the ideal trilateral cycle to the thermodynamic efficiency versus angular velocity

This results shows 9% isentropic efficiency while the minimum ratio was 20 which is attributed to the low speed of the system as it was not able to accelerate and the results show that the thermodynamic efficiency of the system was 20 times more the trilateral efficiency of the system based on theoretical analysis.

In addition, Figure 8-32 shows the fresh water production of the system using this rotor.

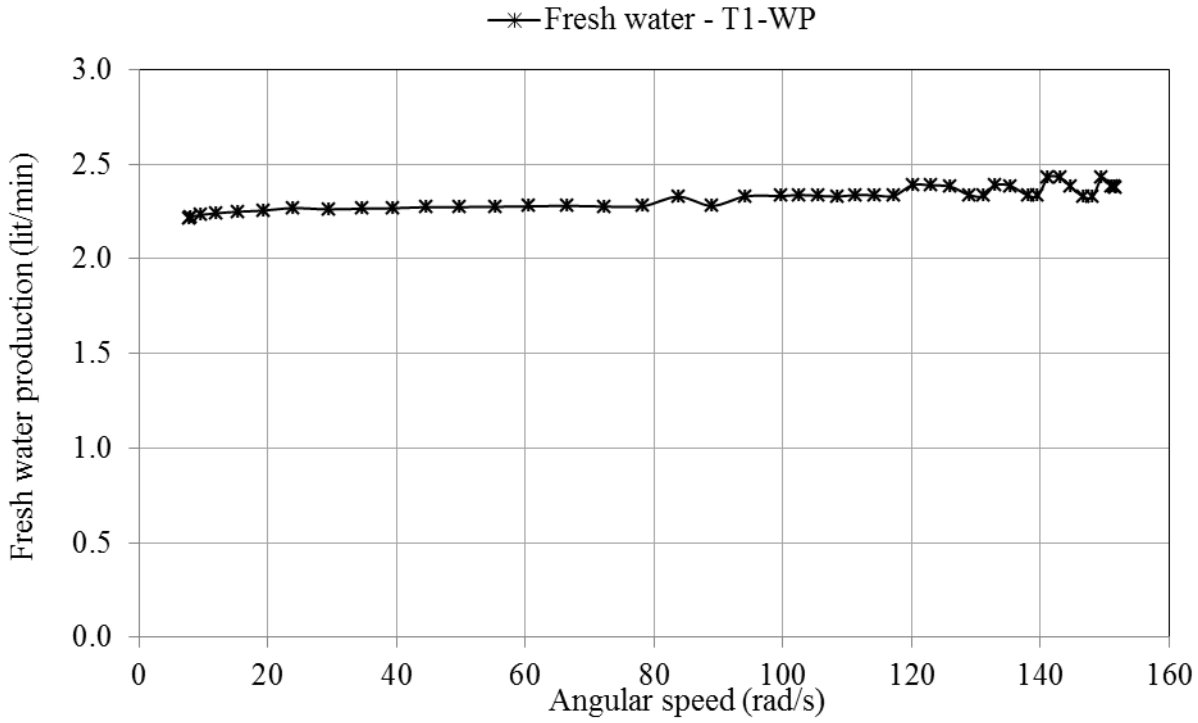

Figure 8-32 Fresh water production of split rotor with pin in front of the throat

Which shows 2.4 lit/min of fresh water production corresponding to 10% of the feed water.

The next experiment, which was carried out using the first RMIT rotor, was putting the sharp pin just inside the orifice while both nozzles were fully open. Again, a hot water tank supply was used.

Figure 8-33 shows the results for two tests under the same conditions for gross shaft power, temperature of the inlet and outlet and the flow rate of the feed water vs rotational speed.

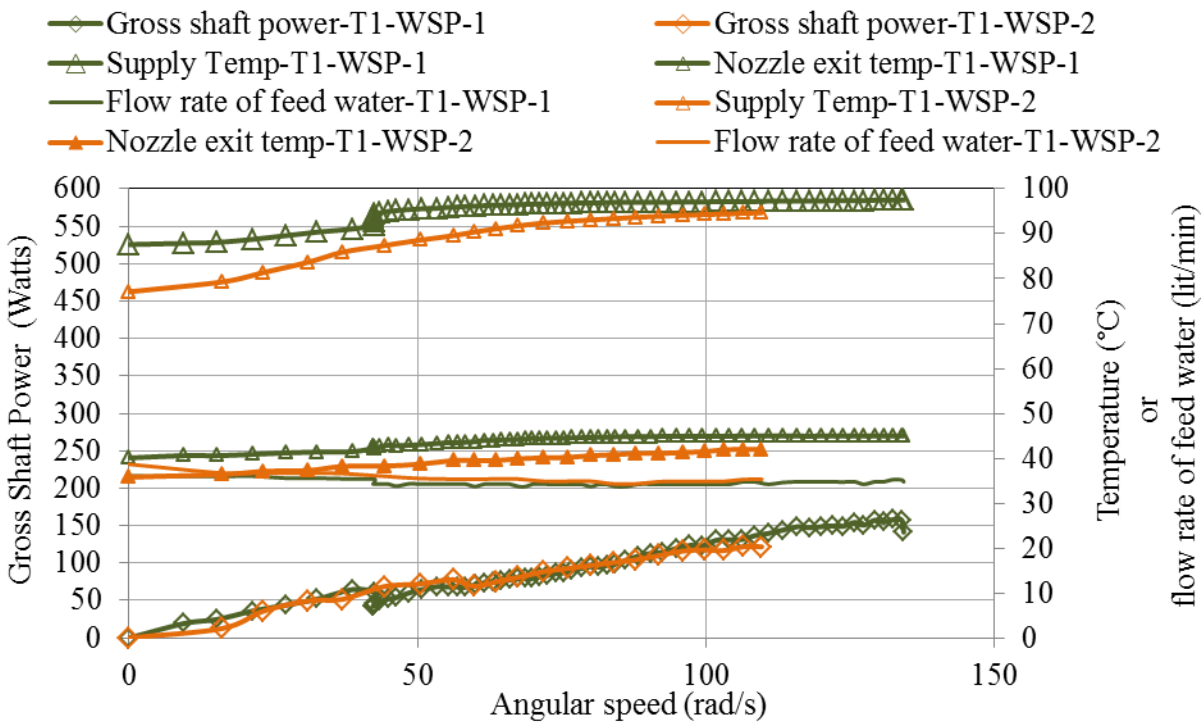

Figure 8-33 Gross power, nozzle exit temperature, supply temperature and flow rate of split rotor with sharp pin in front of throat versus angular speed

As shown, the gross shaft power for the flow rate of 30 lit/min of hot feed water was 150 W at 1300 rpm while the inlet temperature was 99°C and the temperature of the mixture at the exit of the nozzle was approximately 40°C which was low because of the low rotational speed.

Figure 8-34 shows the isentropic efficiency and the ratio of thermodynamic efficiency to the trilateral efficiency for this case.

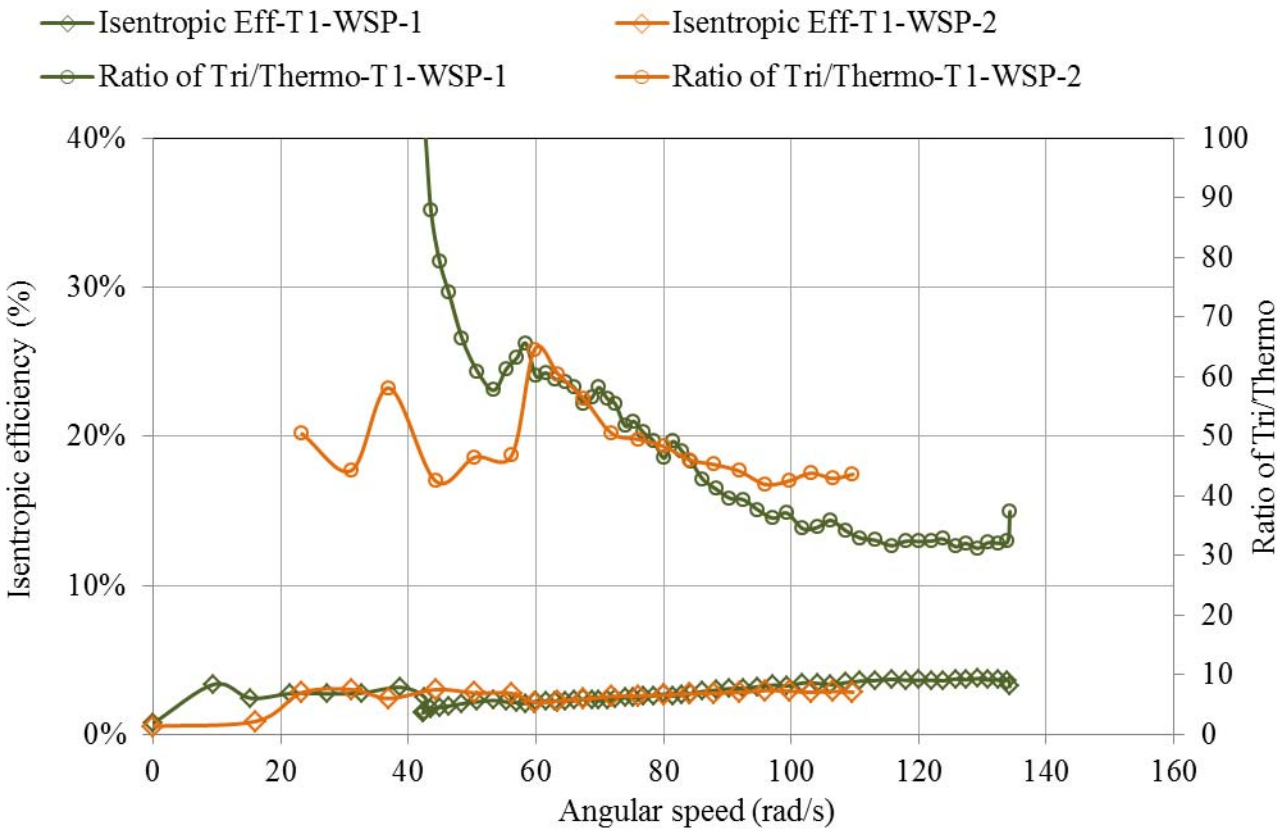

Figure 8-34 Isentropic efficiency of split rotor with sharp pin, the ratio of the ideal trilateral cycle to the thermodynamic efficiency versus angular velocity

As shown, the isentropic efficiency calculated based on the computer model is approximately 5 % for this turbine while the thermodynamic efficiency of the turbine is about 30 times less than theoretical ideal trilateral efficiency.

The fresh water production of the system using this turbine was approximately 11% as in Figure 8-35.

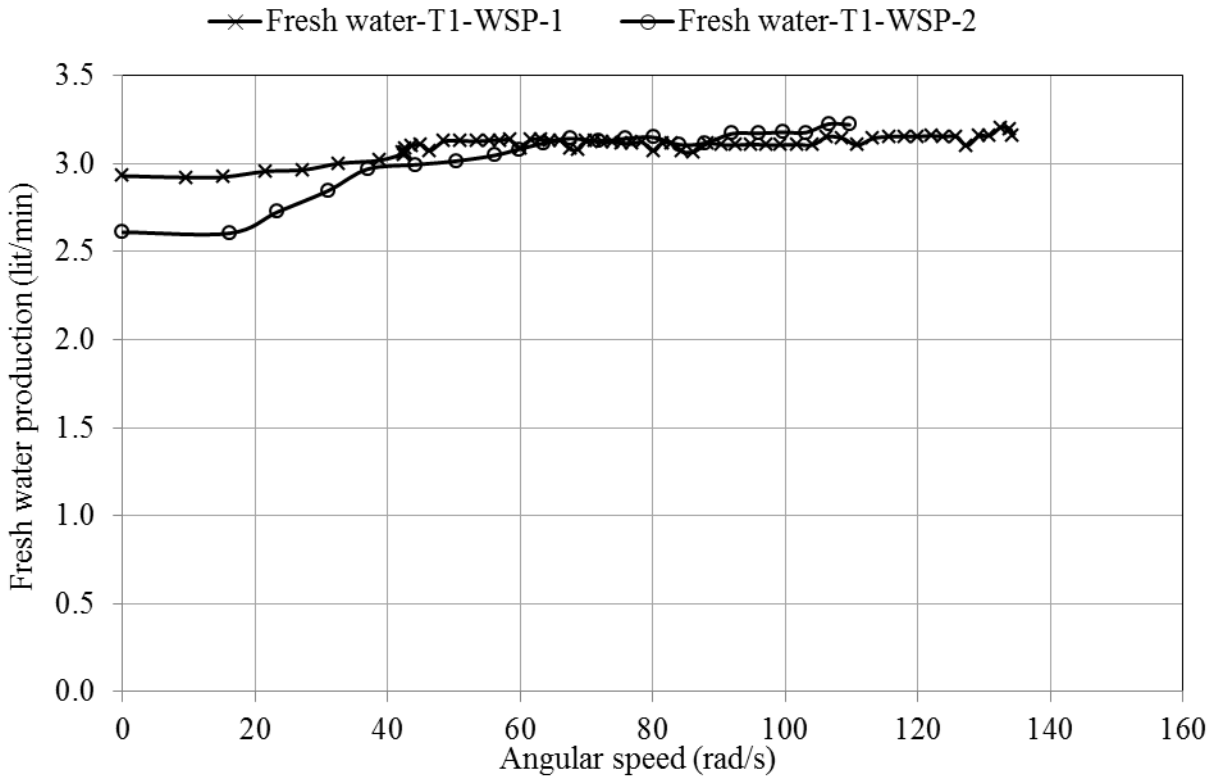

Figure 8-35 Fresh water production of split rotor with sharp pin in front of the throat

It can be seen that almost 3.2 lit/min of fresh water was produced which is more than in previous configurations.

Figure 8-36 shows the acceleration and deceleration of the rotor tested without pin, with pin and with a sharp pin.

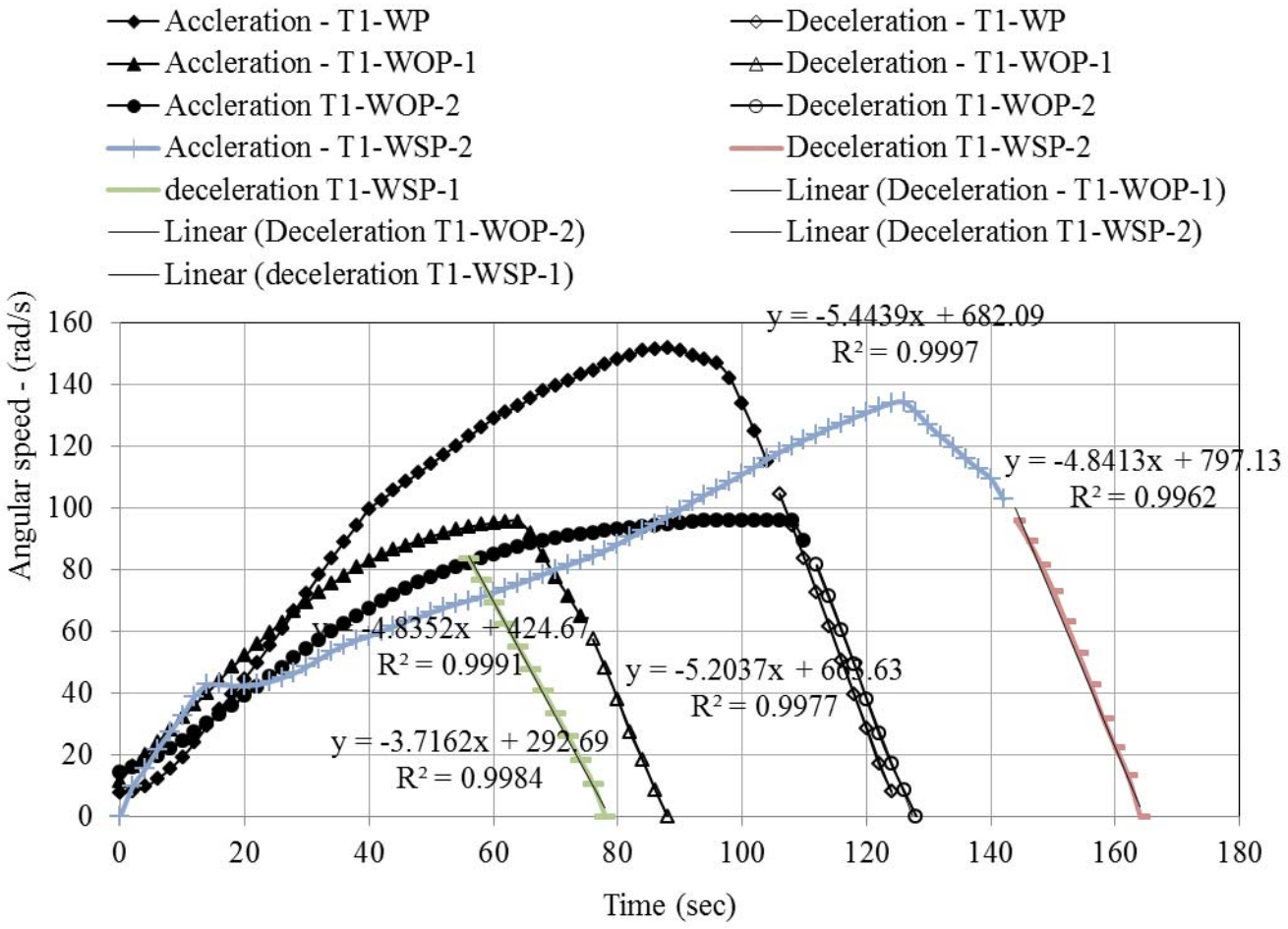

Figure 8-36 Angular velocity versus time

All the curves follow the same pattern in acceleration and deceleration.

It can be seen from Figure 8-36 that the rotor with the pin has higher speed than the turbine without a pin. The deceleration rate of both rotors was approximately 4.2-4.3 m/s2. Further from the following figures it can be seen that the rotor with pin produced more power and had higher isentropic efficiency than the rotor without pin. It can be seen that the feed water flow rate for the rotor without pin was approximately 19LPM, while that for the turbine with pin is around 15LPM, i.e. approximately 20% drop in the feed water flow rate. The drop in the feed water flow rate through the rotor with pin is not attributed to the obstruction caused by the pin, but to the increase in back pressure associated with the increase in volume flow rate caused by higher phase change within

the diverging section of the turbine nozzle. This implies that the pin helps the feed water jet to break into small drops as it comes out of the throat and helps in the evaporation / phase change process by providing extra surface area. It can be seen that the power output of the turbine increased from approximately 95 to 160 W, i.e. approximately 70% improvement in the power output. The isentropic efficiency has increased from only 3% to 6%, which is almost a doubling of the output. Average fresh water production was measured to be approximately 1.42 L/min (i.e. x = 0.0747) for the turbine without pin and 1.18 L/min (i.e. x = 0.0786) for the turbine with pin. Addition of the pin helped early atomization of the hot working fluid jet and delayed the separation of the liquid and vapour and has helped to improve the efficiency of the rotor.

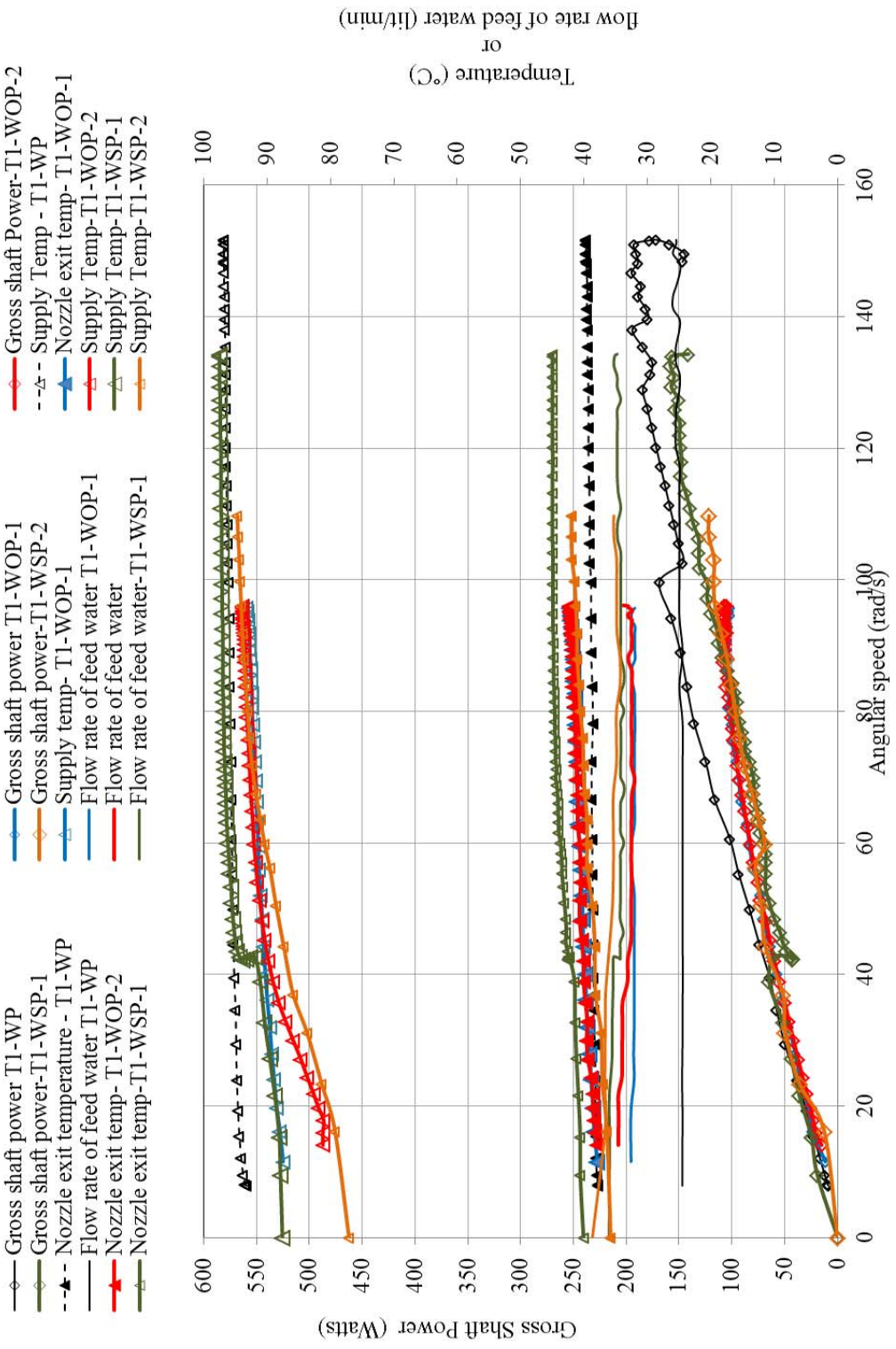

Figure 8-37 Comparison of the gross power production results for the split rotor

In Figure 8-37, it can be seen that for all the cases, the input heat (temperature difference between the inlet and outlet) was almost same. Therefore considering the gross shaft power, using the turbine with 2.5 mm orifice and having a pin in front of it provided better performance.

This conclusion can be also drawn based on the efficiencies of these different turbines.

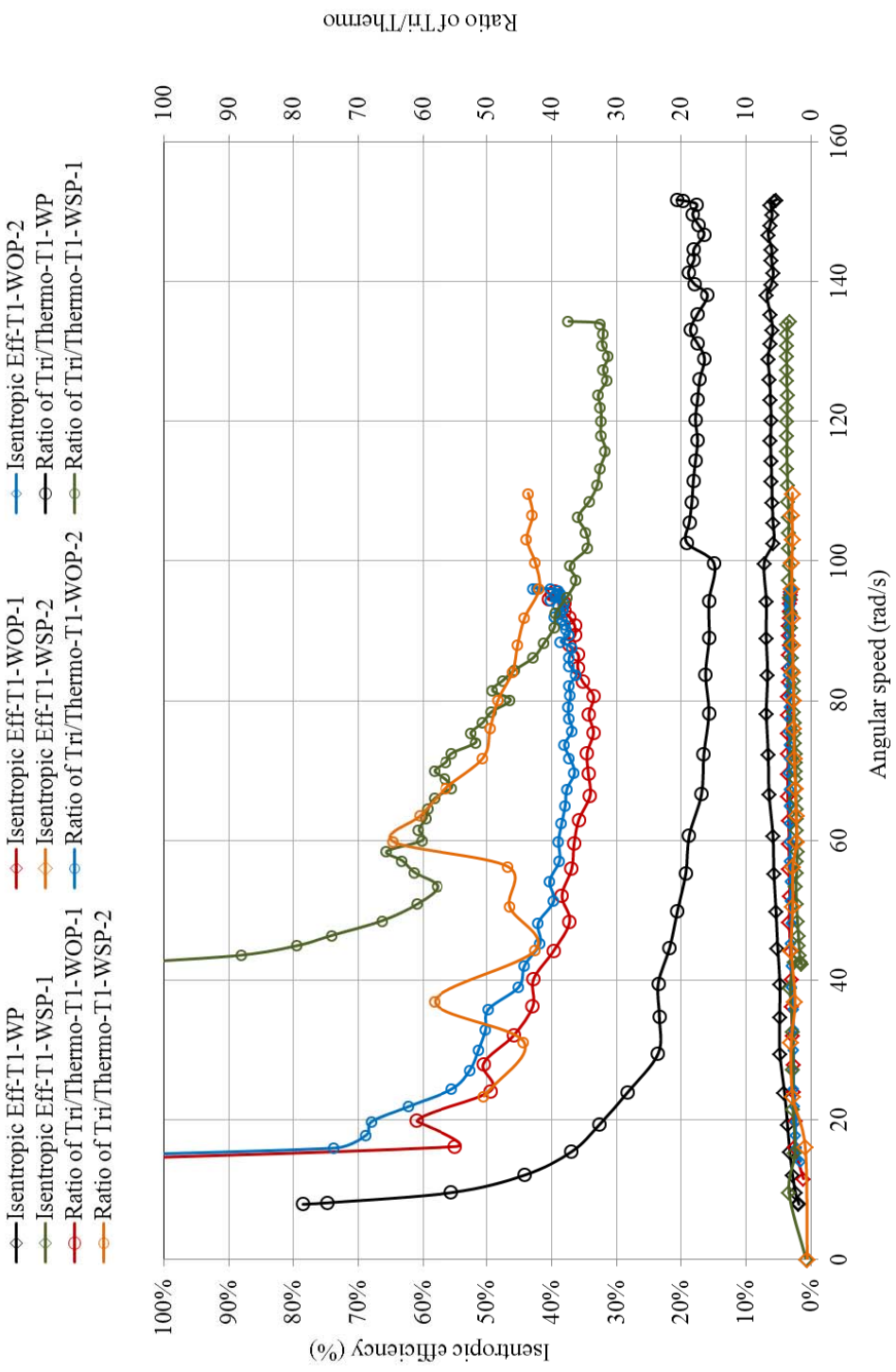

Figure 8-38 comparison of the isentropic efficiency and ratio of tri/thermo for split rotor

The isentropic efficiency was approximately 9% when the pin was used in front of the orifice and the thermodynamic efficiency was 20 times away from the trilateral efficiency which is much less than in the two other cases.

The fresh water production for these tests is shown on the following graph, which in each case was approximately 10% of the feed water.

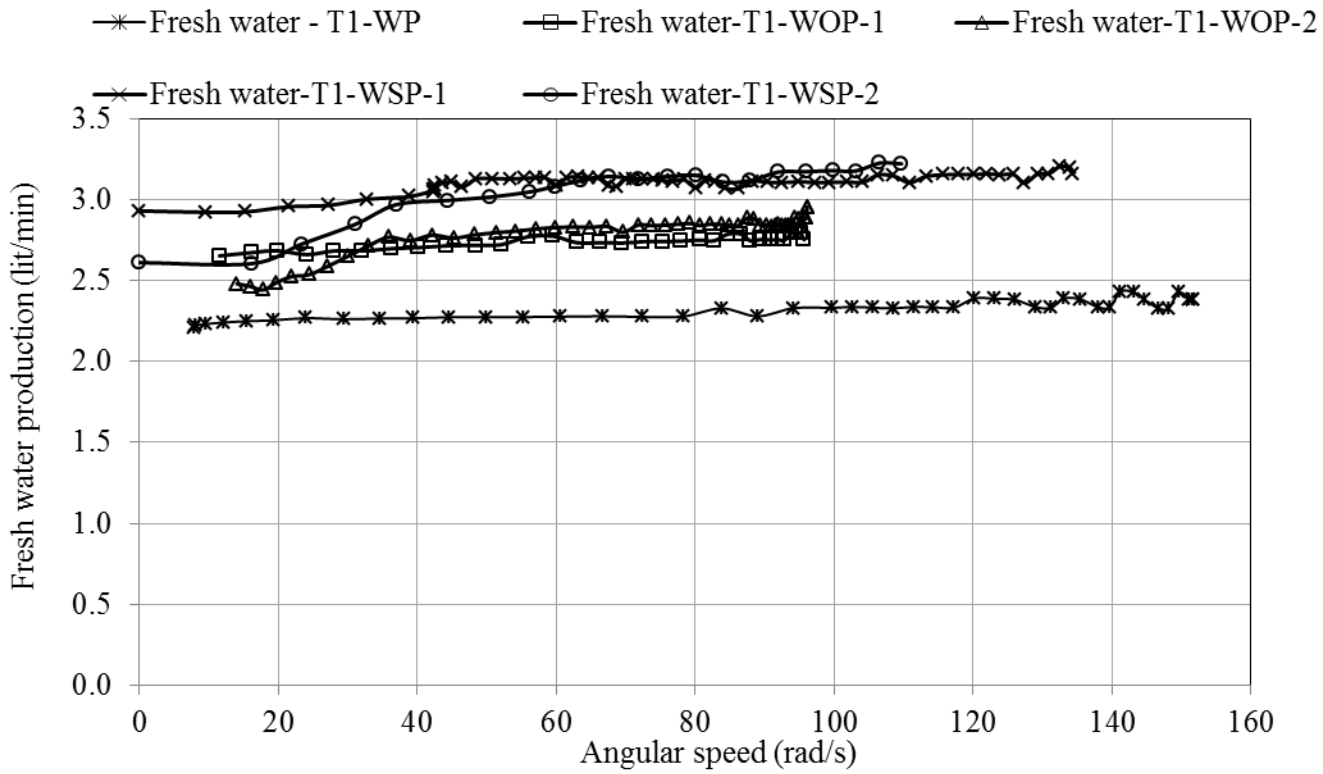

Figure 8-39 Comparison of fresh water production for split rotor.

8.6 RMIT rotor

The first design of RMIT rotor was based on the results from experiments and is as has been described in chapter 7 section 3.3.

. This rotor was made from 7075-T6 series aluminium alloy to withstand the centrifugal forces that are generated at high rotational speeds. The rotor assembly was made from two plates with curved nozzle grooves machined as mirror images. The rotor had outer diameter of approximately 300mm and total thickness of approximately 40 mm. The rotor was attached with a flanged coupling to a hollow shaft that carried the hot feed

water. The throat had a cross sectional diameter of 2mm and the nozzle exit diameter was 25 mm.

By using the boiler as a hot water source, this rotor could reach a maximum angular velocity of 7500 RPM . The figure shows the gross shaft power and the feed water flow rate and temperature as well as the temperature at the exit of the nozzle.

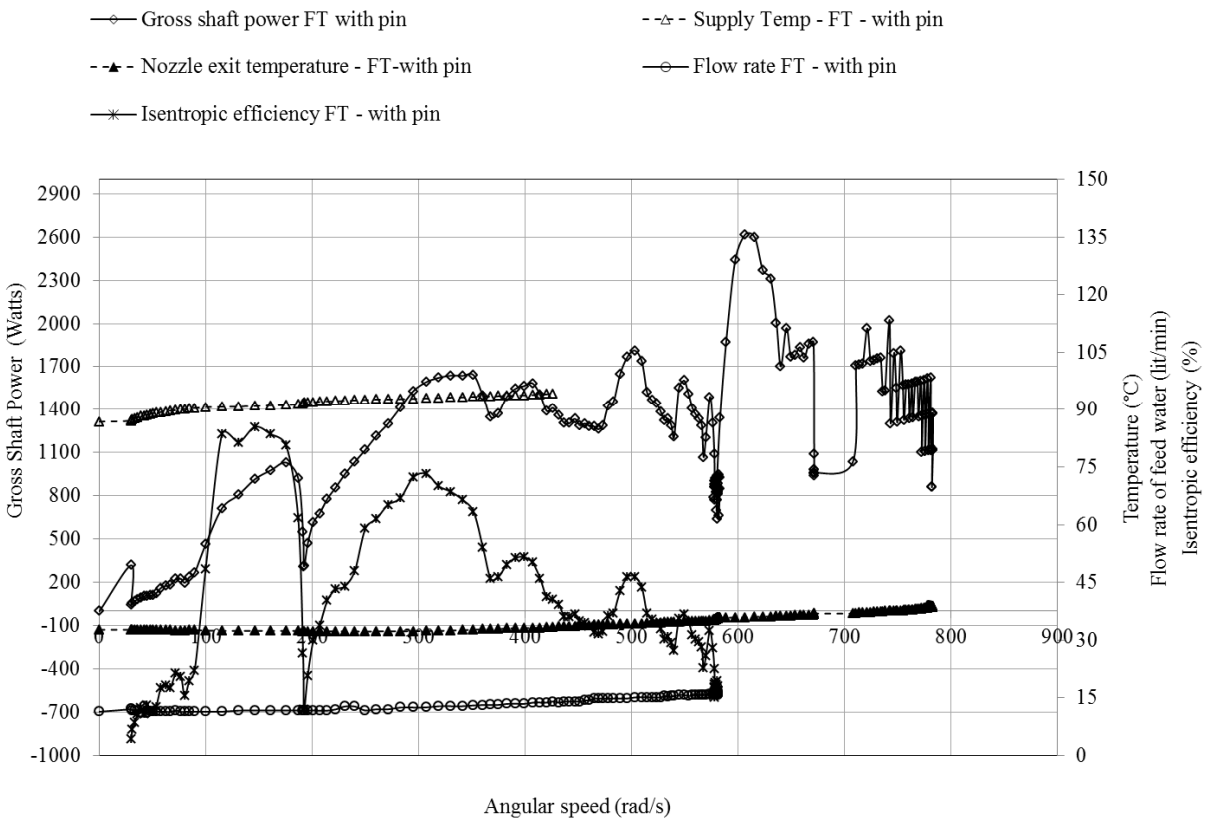

Figure 8-40 Gross power, isentropic efficiency, nozzle exit temperature, supply temperature and flow rate versus angular velocity using RMIT rotor with a pin in front of the throat

The results achieved using a pin in front of the throat were very impressive. The gross shaft power went up to 2.6 kW at 6000 RPM. And the rotor could accelerate to 8000 RPM which was a big improvement.

After the significant improvement of the results using the new design for the RMIT rotor, in order to enhance the higher rotational speed the second design of RMIT rotor has been developed for a 300 mm diameter rotor. The throat was located at 59 mm from the centre of the rotor in order to generate enough centrifugal pressure to prevent unexpected

boiling before the throat which could cause choking. The mass moment of inertia of this turbine shaft assembly was estimated to be 0.12 kg-m².

Using the test procedure discussed previously this rotor was tested for a range of feed water supply temperatures. For all tests the rotor was allowed to accelerate to the maximum rotational speed while the driving temperature difference was maintained as near a possible to constant. The rotor was allowed to decelerate from the top speed by stopping the feed water supply. The acceleration and deceleration rates were monitored, recorded and analyzed to estimate the gross shaft power produced by the rotor.

Figure 8-41 shows the acceleration and deceleration curves for the rotor with feed water temperature maintained below 100°C. It is noted that the slope of the deceleration curve is directly proportional to the dynamic frictional losses present in the rotary system that exerts load on the turbine. Figure 8-41 shows that the slope of deceleration is approximately 5.2rad/s². The main frictional load arises from bearings and the mechanical seal and the load exerted by the mechanical seal is a function of pressure difference, rotational speed and operating temperature.

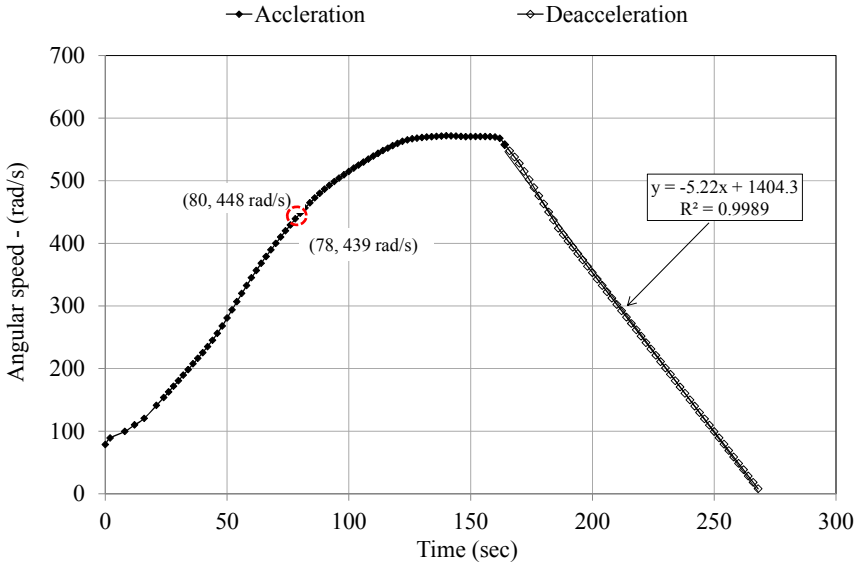

Figure 8-41 Experimental acceleration and deceleration curves with feed water supply temperature below 100°C during first test

Here calculations are shown for a sample data point $(\omega = 448 rad/s)$. Angular speed was recorded by the data logger at 2 second intervals. The rate of acceleration was calculated and shaft power was calculated using equation 16. A sample calculation of shaft power

for one data point on the acceleration curve from Figure 8.41 is shown below, where the work extracted was zero,

$$\dot{W}_{st}(\omega) = I_T \times \omega \times \left[\frac{d\omega}{dt}\right]_{dece} + I_T \times \omega \times \left[\frac{d\omega}{dt}\right]_{acc} + \dot{W}_{ex}$$

$$\dot{W}_{st}(\omega) = 0.12 \times 448 \times [5.22]_{dece} + 0.12 \times 448 \times \left[\frac{(448-439)}{(80-78)}\right]_{acc} + 0$$

$$\dot{W}_{st}(\omega) = 522.55 \quad Watts$$

A calibrated thermocouple was placed approximately 15 mm in front of the rotor nozzle exit to measure the temperature of the fluid leaving the turbine. Measurement of the nozzle exit temperature showed that the fluid leaving the turbine was at approximately 1°C higher temperature than the saturation temperature corresponding to the absolute pressure in the flash tank. At the same time the temperature of the liquid water that dropped to the bottom plate was measured and it was very similar to the saturation temperature corresponding to the flash tank pressure. From these two observations it was concluded that the flashing of the feed water was not happening completely inside the turbine nozzle as had been expected. There seemed to be a delay in the flashing caused by highly sub-cooled water before the throat due to centrifugal pressure. From Figure 8-42 and Figure 8-43 it can be seen that at angular speed of 448 rad/s, the feed water temperature was 97.5°C, the nozzle exit temperature was 42.65°C, and the feed water flow rate was 13.95 L/min. The following are the saturated properties of the feed water at the supply temperature of 97.5°C:

$\rho_{f2} = 960.14 kg/m^3$; $h_{f2} = h_2 = 408.6 \times 10^3 J/kg$, $s_{f2} = s_2 = 1.2787 \times 10^3 J/kg.K$.

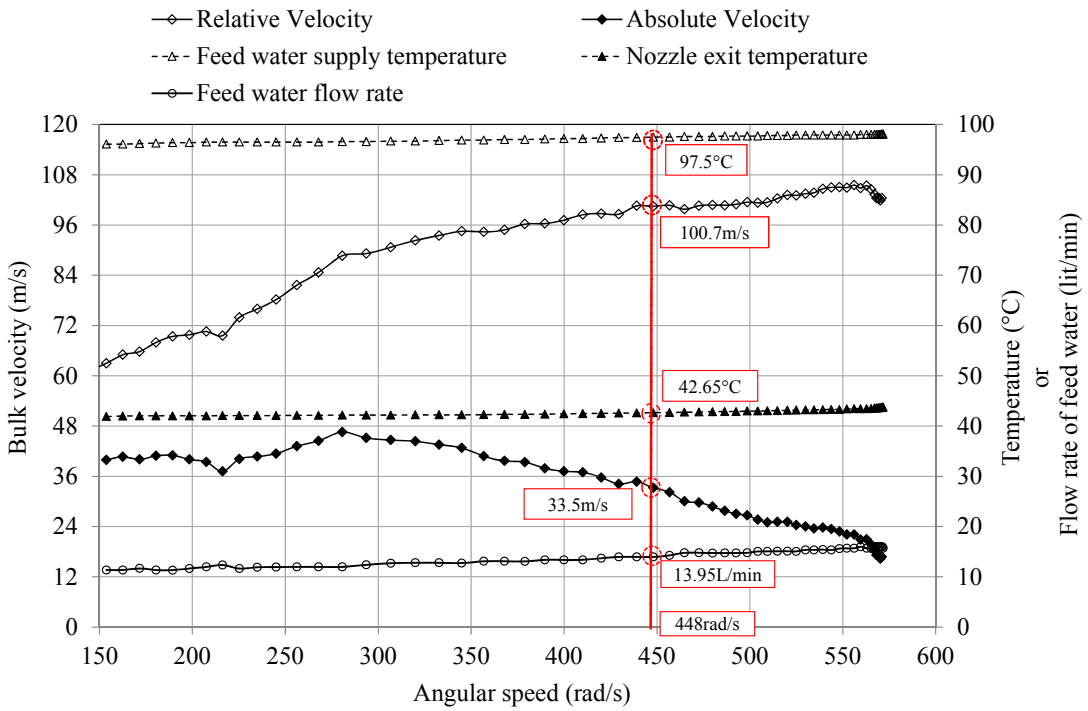

Figure 8-42 Experimental estimations of relative and absolute velocities, feed water flow rate and nozzle exit temperature with the feed water supply temperature below 100°C during the first test

Therefore, feed water mass flow rate was $\dot{m}_{fw} = 0.233 kg/s$,

$$T_{st}(\omega) = \frac{P_{st}(\omega)}{\omega} = \frac{522.55}{448} = 1.17 N.m$$

$$Also,\ \ T_{st}(\omega) = \dot{m}_{fw} \times V_a \times R$$

$$\therefore V_a = \frac{T_{st}(\omega)}{\dot{m}_{fw} \times R} = \frac{1.17}{0.233 \times 0.15} = 33.48 m/s$$

$$V_r = V_a + U = 33.48 + 448 \times 0.15 = 100.68 m/s$$

And,

$$h_{3'} = h_2 - \frac{\left(\dot{W}_{st} + \frac{1}{2} \times \dot{m} \times V_a^2\right)}{\dot{m}} = 408.6 \times 10^3 - \frac{\left(522 + \frac{1}{2} \times 0.233 \times 33.47^2\right)}{0.233} = 405.8 \times 10^3 J/kg$$

Following are the saturated properties of the feed water at nozzle exit temperature of 42.65°C:

$$h_{f3} = 178.6 \times 10^3 J/kg;\ h_{fg3} = 2399.7 \times 10^3 J/kg;$$

$$s_{f3} = 0.6077 \times 10^3 J/kg.K;\ .\ s_{fg3} = 7.598 \times 10^3 J/kg.K$$

The quality of the mixture at the nozzle exit is estimated from the estimated specific enthalpy at the exit as follows,

$$x_3^{'} = \left(\frac{h_3^{'} - h_{f3}}{h_{fg3}} \right) = \frac{(405.8 - 178.6) \times 10^3}{2399.7 \times 10^3} = 0.09467 = 9.467\%$$

An ideal turbine would have an isentropic expansion process as shown in Figure 2, $s_2 = s_3 = 1.2787 \times 10^3 \, J / kg.K$, therefore the quality of mixture at the nozzle exit and the specific enthalpy at point 3 for an ideal turbine are calculated as follows,

$$x_3 = \left(\frac{s_3 - s_{f3}}{s_{fg3}} \right) = \frac{(1.2787 - 0.6077) \times 10^3}{7.598 \times 10^3} = 0.08831 = 8.831\%$$

$$h_3 = h_{f3} + x_3 \times h_{fg3} = 178.6 \times 10^3 + 0.08831 \times 2399.7 \times 10^3$$

$$h_3 = 390.52 \times 10^3 \, J / kg$$

Therefore, isentropic efficiency of the turbine at an angular speed of 70.23rad/s is calculated as below,

$$\eta_{isen} = \frac{(h_2 - h_{3'})}{(h_2 - h_3)} = \frac{(408.55 - 405.8) \times 10^3}{(408.55 - 390.5) \times 10^3} = 0.1514 = 15.24\%$$

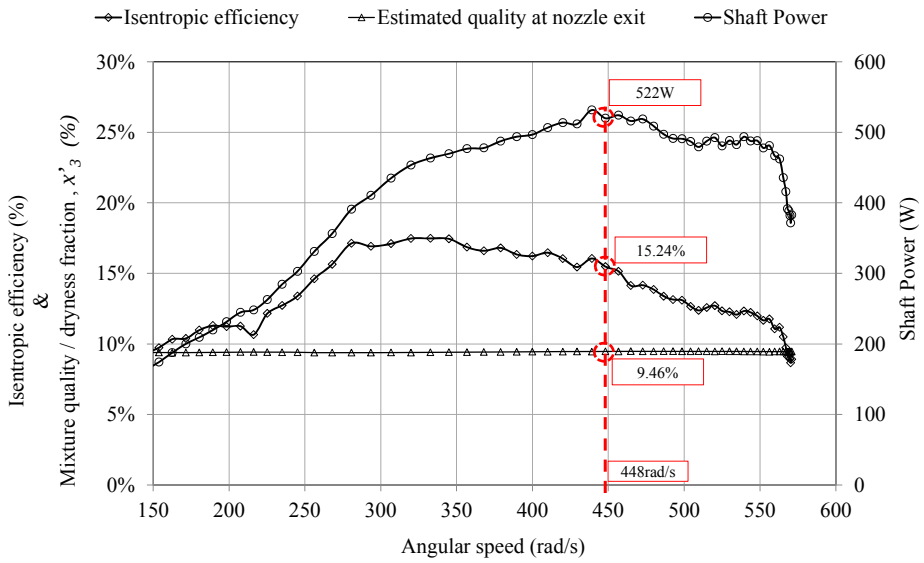

Figure 8-43 Experimental estimation of shaft power and isentropic efficiency of the curved nozzle turbine with feed water supply temperature below 100°C during the first test

It is noted that the feed water flow rate and temperature were measured before the fluid entered the rotating turbine shaft and it was still a sub-cooled liquid. It can be seen from Figure 8.42 that with increase in the rotational speed the mass flow rate of the feed water increased due to centrifugal pumping. At the same time the relative velocity of the working fluid (water) at the exit of the turbine nozzles also increased, while the driving temperature difference was maintained close to 55°C. With increase in the rotational speed of the turbine the absolute velocity decreased and hence the torque produced by the turbine decreased. It can be seen from Figure 10 that the maximum shaft power produced by the second turbine for feed water temperature of below 100°C was approximately 525 W with an isentropic efficiency of approximately 16%. The maximum isentropic efficiency is estimated to be 17.5%. Although the efficiency of the second turbine is still 6 times lower than the ideal isentropic efficiency, it is a big improvement over the first curved nozzle turbine design mentioned in part A of this thesis. The average quality of the mixture at the nozzle exit was estimated to be 0.09434, i.e. average fresh water production of approximately 1.31 L/min.

With increase in the rotational speed, the mass flow rate of the feed water increased which increased vapour production and the cooling load on the condenser. The condenser used had cooling capacity of approximately 55kW. It was observed that beyond 13L/min of feed water flow rate the cooling load on the condenser exceeded the condenser cooling capacity and this caused the flash tank pressure to increase. Hence there was increase in the nozzle exit temperature while the feed water supply (inlet) temperature was constant. This caused drop in the driving temperature difference which in turn caused the shaft power and isentropic efficiency of this turbine to drop.

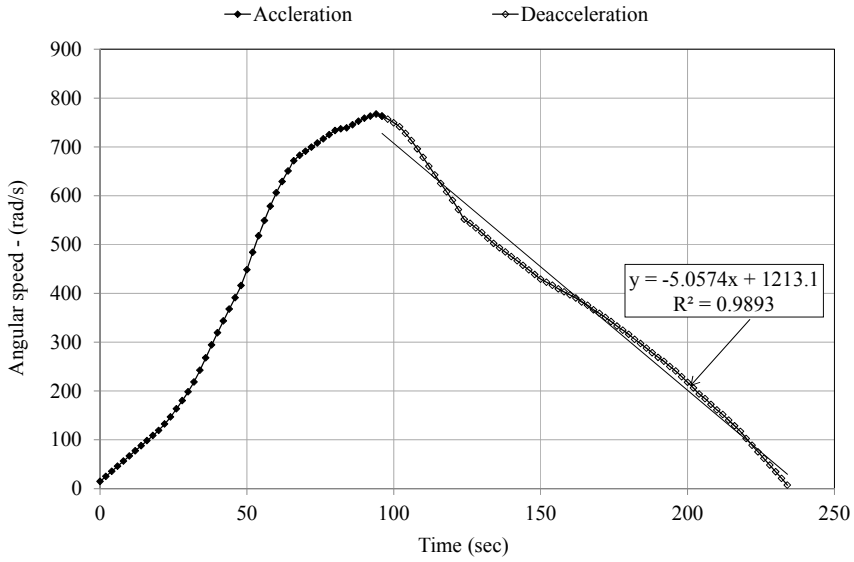

Figure 8-44 Experimental results of acceleration and deceleration of the turbine during the second test for above 100°C feed water supply temperature

It can be seen from Figure 8-44 that with feed water temperature above 100°C the turbine accelerated faster and achieved higher speeds. The rotor assembly decelerated at similar rates for both tests with below and above 100°C feed water temperatures. From Figure 8-42 , Figure 8-43, Figure 8-45 and Figure 8-46 it can be seen that with higher feed water supply temperature the same turbine produced higher power at higher efficiency. The increase in the isentropic efficiency can be attributed to the increase in driving temperature difference. The highest feed water temperature was 119°C while the lowest feed water temperature was 107°C. On an average there was a driving temperature difference of approximately 68°C available during the test with the highest temperature difference of around 79°C and lowest 65°C. The bulk relative velocity of the working fluid was maintained close to 147 m/s while the feed water temperature was close to 116°C and the angular speed of the turbine increased from 483 rad/s to 600rad/s. It can be seen from Figure 12 that the bulk relative velocity of the two-phase fluid dropped as there was a sharp drop in the driving temperature difference because of increase in the flash tank pressure and decrease in the feed water temperature. The feed water flow rate continued to increase with the increase in the rotational speed. When the feed water flow rate went beyond 15 L/min the condenser/heat sink used was not capable of providing enough cooling. This caused the pressure in the flash tank to rise, which caused the nozzle exit temperature to rise and in turn reduced the driving temperature difference. It

is observed that at 483 rad/sec the turbine had an isentropic efficiency of approximately 25% and produced shaft power of approximately 1330W. The driving temperature difference at this point was 79°C and the feed water flow rate was approximately 14.49L/min. The maximum rotational speed of the turbine was recorded to be approximately 764rad/s (i.e. 7300rpm).

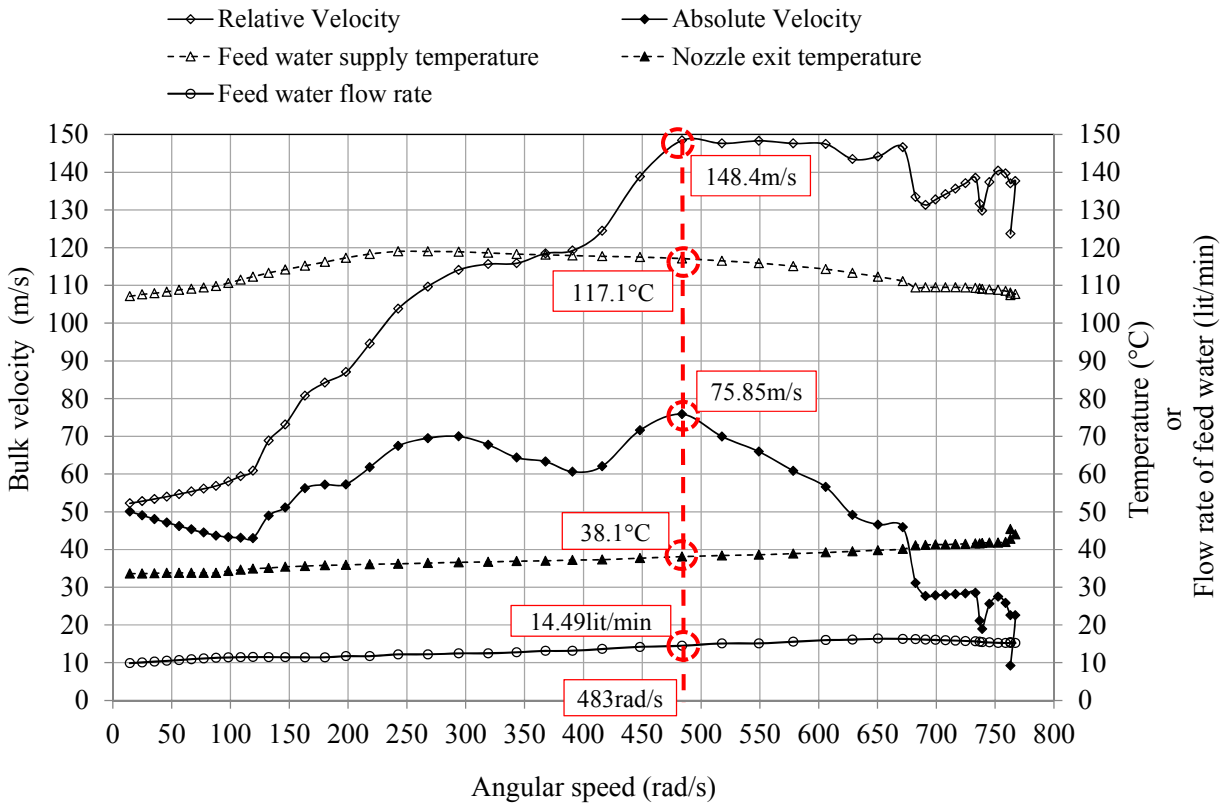

Figure 8-45 Experimental results showing relative and absolute velocities, driving temperature difference and feed water flow rate during second test

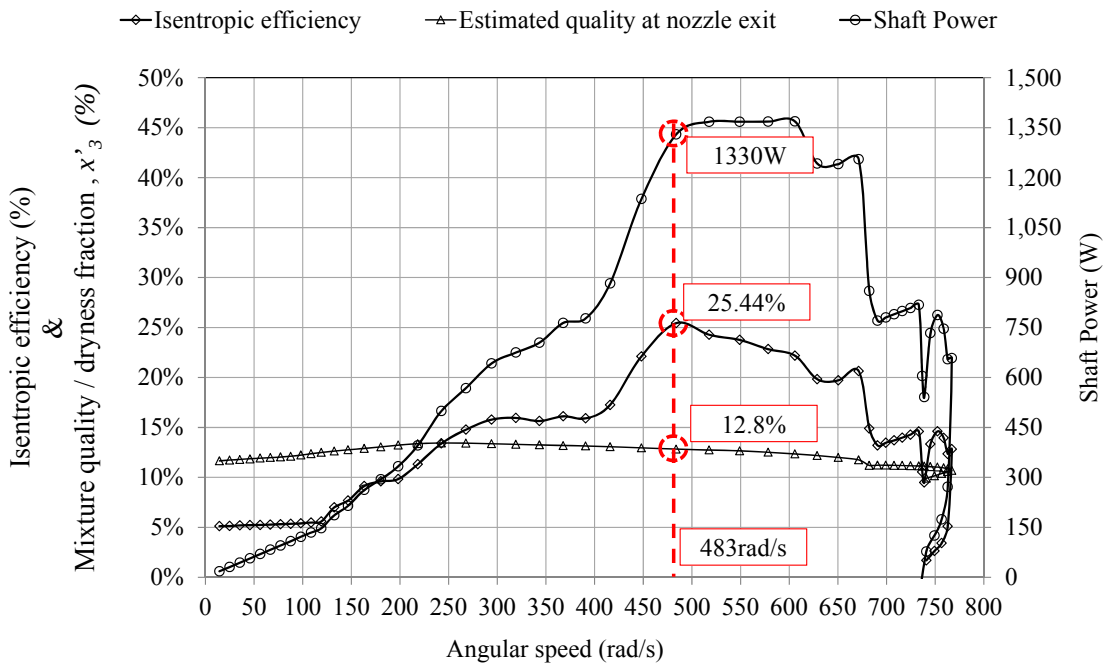

Figure 8-46 Experimental results showing isentropic efficiency and shaft power during second test

The average quality of the mixture at the nozzle exit was estimated to be approximately 0.01201, i.e. average fresh water production of around 1.62 L/min. The quality of the mixture at the nozzle exit did not remain constant and changed as the pressure in the flashing tank changed. The turbine used had a curved nozzle with the optimal curvature estimated for a speed of 20,000rpm. Because of limitations posed by the condenser cooling capacity and auxiliary power losses within the CDP system, the turbine did not reach this high speed. The best efficiency of this turbine is estimated to be around 25% at 483rad/s (i.e. around 4614rpm). And it is expected that if this turbine rotates faster while the flashing tank pressure is maintained even at higher rotational speeds then the turbine efficiency will be much higher.

8.7 Conclusion

The results obtained were as follows,

1. When the turbine was supplied with feed water at 97.5°C it had a maximum isentropic efficiency of approximately 17% and the maximum shaft power was

approximately 525W. The average feed water flow rate was 13.95L/min Average fresh water production for first test was measured to be 1.22 L/min.

2. The power output of the turbine was observed to be highest (1330W) when the feed water temperature was approximately 117°C and the corresponding isentropic efficiency of the turbine was approximately 25%. The average feed water flow rate was around 13.69L/min and the average fresh water production was measured to be around 1.51 L/min. It is noted that the nozzle curvature used in this study was optimal for 20,000rpm (2093rad/s) and hence at lower rotational speed the turbine had lower efficiency.
3. It is observed that the turbine efficiency increased with increase in the turbine rotational speed. With the experimental facilities used the turbine speed was limited to approximately 7300rpm for the following reasons,

- High mechanical frictional load due to mechanical seals requiring higher torque to overcome this friction and hence speed was limited.
- At high speed there was a sharp increase in the feed water flow rate which upsets the balance of heat supply to the CDP and heat removed from CDP which caused the pressure in the flash tank to rise and hence reduced the driving temperature and in turn reduced the turbine speed.

Chapter 9 Theoretical and experimental aspects of gas removal from geothermal water

9.1 Introduction

Geothermal fluids contain Non-Condensable Gases (NCGs) in various quantities. NCGs may have significant impact on the performance of power generation systems which use geothermal waters. In the situation where geothermal water is used as the working fluid in an expander for power generation [102], NCGs present in water can increase the pressure in the condenser and therefore decrease the thermodynamic efficiency of the power generator.

Depending on the source, the fraction of the NCGs in geothermal water can vary from less than 0.2% by mass to greater than 12% by mass [103]. It is important that the selected NCG removal process is appropriate to the concentration of NCG in the source as the removal process uses a large amount of auxiliary power [104]. By using an appropriate NCG removal process the overall performance of the power plant can be improved [105].

The common NCGs present in geothermal water are a mixture of CO2, H2S, H2, Hg, NH3 and CH4 [106]. The most prevalent gas is carbon dioxide constituting approximately 95% by weight of the mixture [104].

The following are some of the NCG removal methods used in industrial processes:

1. Extraction using commercially available vacuum pumps [107].
2. Steam ejectors used in order to create a vacuum which assists in the removal of NCGs [108].
3. Not allowing NCGs to enter the system: this can be achieved by degasification of the source fluid before it enters the system[109].
    a. Degasification by pressure reduction, as the quantity of a dissolved gas in a liquid is proportional to its partial pressure.

b. Degasification by temperature increase. In some cases, however, the solvent and/or the solute decompose, react with each other, or evaporate at high temperature and the rate of removal is less controllable.

R. Angulo et.al have been working on removal of NCG from flash geothermal steam. They have considered condensation and re-evaporation of the steam in a heat exchanger, upstream of a power plant [103]. The main component of their system was a vertical shell and tube heat exchanger with 50 titanium tubes. Steam was fed into the shell side of the heat exchanger. This flowed upwards and most of the steam condensed on the walls of the tubes. The non-condensable gases, together with a small amount of steam were vented through a purge line located at the upper part of the shell. The condensate flowed into a transfer tank, which acted as a steam seal, and finally, into a storage tank, operated at a lower pressure than the shell side. In this way, a temperature difference was created between the incoming steam and the stored condensate. From the bottom of the storage tank, a pump transferred condensate to the flood box, from which it flowed inside the tubes. The latent heat of the incoming steam was transferred, causing a portion of the condensate to be evaporated, thus producing steam with a low gas content that was discharged at the upper part of the storage tank. The nominal capacity of their equipment was 0.4 tonne per hour of steam which resulted in achievement of a mean value of 94% for gas removal efficiency by their system. They also found that non-condensable gas removal efficiency was found to depend on the fraction of steam vented with the non-condensable gases [103].

N. Yildirim Ozcan and G. GokcenIn have studied the net power output and specific steam consumption of a single-flash geothermal power plant which depended on the separator pressure, NCG fraction and wet bulb temperature of the environment. Three different conventional gas removal options were considered, which were a two-stage steam jet ejector system, a two-stage hybrid system and a two-stage compressor system. They found that increasing the NCG fraction decreases, by different amounts, the net power output for each option regardless of separator pressure. It was concluded that in relation to sensitivity of geothermal power plant performance to the NCG fraction, the compressor system is the most efficient and robust system where the influence of the NCG fraction is limited. On the other hand, steam jet ejectors are highly affected by

increasing NCG fraction since the driving steam flow rate to the steam jet ejectors is directly related to NCG fraction [104].

E. E. Michaelides has investigated influence of non-condensable gases on turbine work, turbine efficiency and extraction work. For his study, as carbon dioxide constituted the major fraction of the non-condensable gases with its concentration always more than 85%, he assumed that the mass of non-condensable gases can be replaced by an equivalent mass-fraction of CO2. Therefore he assumed that an ideal gaseous mixture of CO2 and steam enters the turbine. He concluded that the presence of non-condensable gases in geothermal steam power plants has an adverse effect on the net work produced. This is attributed both to the decrease of the turbine work and to the power supplied to the gas-extraction equipment. In his study, liquid brine is supplied to a primary flashing chamber where a small reduction of pressure releases most of the CO2 and some steam. This mixture passes through an atmospheric turbine and is vented to the surroundings. The remaining brine, free of most of the CO2, is flashed and supplies a condensing turbine with steam containing a only small amount of CO2. He showed that with a mass fraction of 0.2 of CO2, 50% more work is needed compared to a conventional dual-flash system [105] .

In this section, a liquid water ejector is investigated for achieving vacuum removal of NCGs as an alternative to using conventional vacuum pumps or steam ejectors. The main motivation for investigating a water ejector is that it is passive in operation (i.e. no moving parts) has low cost and is easy to maintain. As this type of vacuum device requires a continuous water flow, it could be used in a system which also uses water cooled condensers [102]. This would eliminate the need for additional pumps.

Ejectors are a very simple and practical solution to many pumping problems in various industries worldwide and typically their range of application is overlooked. They can be used alone or in multiple stages to create a range of vacuum conditions as well as being operated in transfer and mixing functions [110]. They are most commonly used to pump gases and vapours out of confined spaces in order to lower the pressure below ambient pressure. The simplicity and the passivity of these vacuum systems make the use of this

device highly desirable in order to increase the viability of sustainable vacuum processes for removing NCGs.

There have been many studies on liquid to liquid ejectors and steam jet ejectors, but few on ejectors where the motive fluid is water and suction fluid is gas and which are usually termed eductors [110]. An experimental feasibility study on using eductors to remove NCGs has been done by Anna Khaghani et al. [111]. This paper further investigates the performance of commercially available eductors and compares it with that of commercial available vacuum pumps.

9.2 Theoretical Analysis and calculation of minimum energy required to remove and exhaust NCG

In this section attempts are made to calculate the theoretical minimum energy required to remove non condensable gases from geothermal systems. Here the theoretical minimum specific energy consumption (J/kg) for this degassing process is calculated by considering the thermodynamic processes involved (adiabatic or isothermal), the pressure and temperature of the geothermal system and the atmospheric pressure to which the NCGs are exhausted. The required theoretical minimum specific energy consumption is subsequently used as a benchmark to compare available vacuum systems from the points of performance and sustainability.

Clearly the system with lowest specific energy consumption will be the most desirable in terms of environmental sustainability.

9.2.1 Ideal vacuum machine

The vacuum process can be idealised as increasing the pressure of the extracted gas from a lower pressure (P_{tank}) to atmospheric pressure (P_{atm}) by using a piston and cylinder device as shown in Figure 9-1.

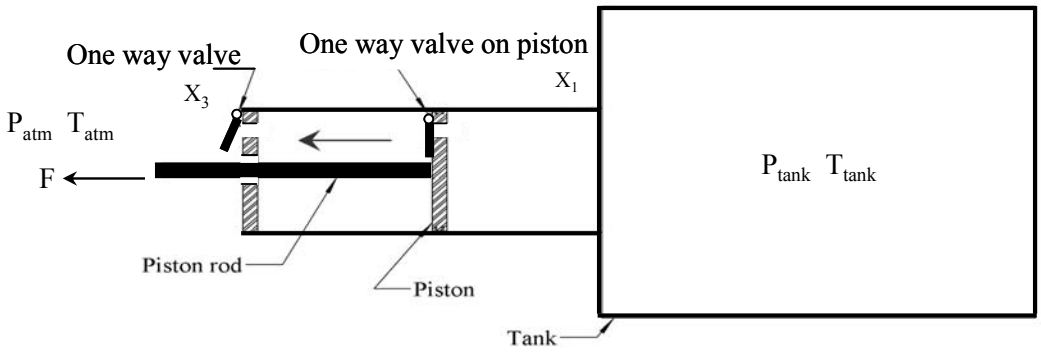

Figure 9-1 Vacuum Process.

If we consider the vacuum process as seen in the P-V diagram in Figure 9-2 the work done to push 1 kg of air from the tank at a pressure of P_{tank} to atmospheric pressure, P_{atm} , can be calculated as below [108].

$$W_{1-2} = \int_{x_1}^{x_2} (p - p_{\tan k}) A.dx = \int_{V_1}^{V_2} (p - p_{\tan k}) dV \tag{9.1}$$

In which W_{1-2} is the work done to pull the piston from position X_1 to position X_2 and A is the area of the piston.

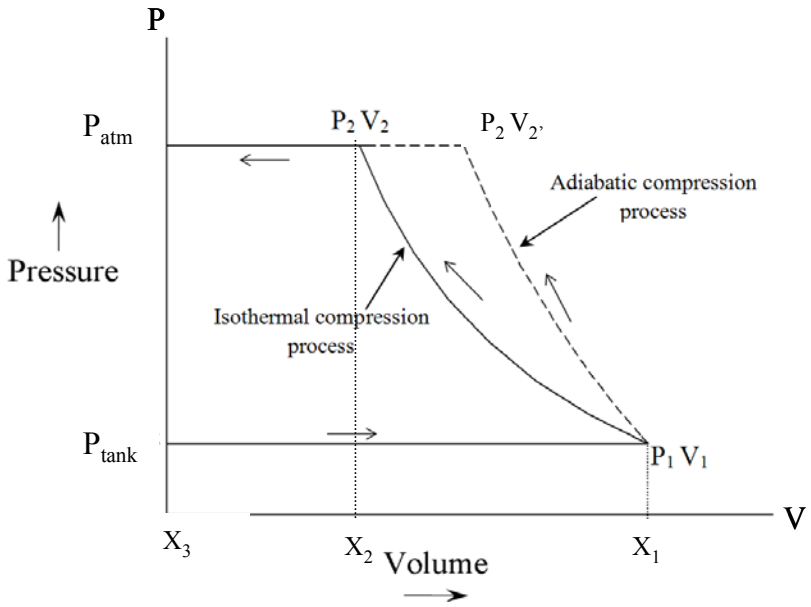

Figure 9-2 P-V diagram for isothermal and adiabatic vacuum process.

Assuming that the air is an ideal gas and that the process is isothermal [108]:

$$PV = mRT = \text{Constant} \tag{9.2}$$

The work done in this isothermal process can be written:

$$\begin{aligned} W_{1-2} &= \left(\int_{V_1}^{V_2} \frac{mRT_{\tan k}}{V} dV \right) - P_{\tan k}(V_2 - V_1) = mRT_{\tan k} \ln(\frac{V_2}{V_1}) - P_{\tan k}(V_2 - V_1) \\ &= mRT_{\tan k} \ln(\frac{P_1}{P_2}) - P_{\tan k}\left(\frac{mRT_{\tan k}}{P_2} - \frac{mRT_{\tan k}}{p_1} \right) = mRT_{\tan k}\left(\ln(\frac{P_1}{P_2}) - \frac{P_{\tan k}}{P_2} + \frac{P_{\tan k}}{p_1} \right) \end{aligned} \tag{9.3}$$

By assuming $P_1 = P_{tank}$ and $P_2 = P_{atm}$, the work required becomes:

$$W_{1-2} = mRT_{\tan k}\left(\ln(\frac{P_{\tan k}}{P_{atm}}) + 1 - \frac{P_{\tan k}}{P_{atm}} \right) \qquad [J] \tag{9.4}$$

In addition, there will be extra work needed to push the compressed air out of the cylinder and into the atmosphere. For an isothermal process, this is shown as W_{2-3}:

$$W_{2-3} = mRT_{\tan k}(\frac{P_{\tan k}}{P_{atm}} - 1) \qquad [J] \tag{9.5}$$

By combining Eqs. (9.4) and (9.5) the total work done in the process becomes:

$$W_{iso} = mRT_{\tan k} \ln(\frac{P_{\tan k}}{P_{atm}}) \qquad [J] \tag{9.6}$$

Therefore, the specific work needed to extract unit mass of air from tank pressure ($P_{\tan k}$) and deliver it to the atmospheric in an isothermal process can be calculated as:

$$w_{iso} = \frac{W_{iso}}{m} = RT_{\tan k} \ln(\frac{P_{\tan k}}{P_{atm}}) \qquad [J/kg] \tag{9.7}$$

The change of the specific work with respect to the tank pressure ($P_{\tan k}$) can be written as:

$$\frac{dw_{iso}}{dP_{\tan k}} = RT_{\tan k}\left(\frac{1}{P_{\tan k}}\right) \tag{9.8}$$

A similar derivation can be made for the case of adiabatic compression. However, as shown in Fig.9.2 the isothermal process offers a lower work requirement for extracting unit mass of air from a tank and raising its pressure in order to deliver it to the atmospheric.

Accordingly, Eq. (9.7) is used to calculate the minimum energy required in the vacuum process and it is also used to calculate the efficiency of the vacuum devices considered in this research, including eductors and vacuum pumps.

To complete the picture the thermodynamics of an adiabatic process instead of isothermal can be also considered as:

$$PV^{\gamma} = \text{Constant} \tag{9.9}$$

Considering this process, the work needed to change the pressure of 1 kg of NCG from $P_{\tan k}$ to P_{atm} can be calculated as:

$$w_{adia} = RT_{atm}\left[\frac{\left(\frac{P_{atm}}{P_{\tan k}}\right)^{1-1/\gamma} - \gamma}{1-\gamma} - \left(\frac{P_{atm}}{P_{\tan k}}\right)\left(\frac{P_{\tan k}}{P_{atm}}\right)^{1/\gamma}\right] \qquad [J/kg] \tag{9.10}$$

As represented schematically in Fig. 9.2, the adiabatic process of gas removal would require more work. The required theoretical power for these processes is:

$$Power = w_{iso/adia} \frac{dm}{dt} \tag{9.11}$$

The theoretical power required for gas removal can be calculated by multiplying the desired mass flow rate of the gas ($\dot{m}$, (kg/s)) and the specific energy given by Eq. (9.7):

$$\dot{W}_{minimum} = \dot{m} \times w_{iso} \tag{9.12}$$

Eq. 12 represents the minimum power required for the vacuum process.

As will be shown later, in practice the energies consumed by eductors and by vacuum pumps are substantially greater. One of the main purposes of the present paper is to compare the efficiencies of eductors and vacuum pumps in removing NCGs from geothermal waters against a benchmark of the theoretical power calculated in Eq. (9.12).

For this purpose the efficiency of the actual vacuum process can be defined:

$$\eta_{actual} = \frac{Electric \quad power}{\dot{m} \times w_{iso}} \tag{9.13}$$

In Eq.(9.13) the numerator (electric power) is the electrical power consumed by the motor in the case of a vacuum pump ($I \times V$) or the electrical power required by the motor driven pump used to creating the pressure difference in the case of an eductor (see section 9.2).

The power required by a conventional vacuum machine is usually provided in the supplier's specifications and can also be calculated by multiplying the measured values of electrical current and voltage. For the case of an eductor the pump power can be defined as:

$$Pump \quad Power = \frac{\dot{V} \Delta P}{\eta_{pump} \times \eta_{motor}} \tag{9.14}$$

In Eq.(9.14), $\dot{V}$ is the volume flow rate of water in m^3/s as a primary fluid and ΔP is the pressure difference across the eductor in Pa. Also η_{pump} refers to the mechanical efficiency of the pump and η_{motor} corresponds to the electrical efficiency of the pump motor. These efficiencies are in the order of 60% and 80% respectively. In the present analysis a combined efficiency of 50% is considered for the water pump (i.e. motor and pump combined).

9.2.2 Ejectors

A single stage ejector (sometimes also known as an eductor or jet pump) in its most basic form contains an actuating nozzle, suction chamber and a diffuser as shown in Figure 9-3. The primary fluid (which can be liquid, vapour or another gas) flows through a tube which converges to a driving nozzle making the fluid accelerate and decrease in pressure due to the venturi effect [112]. Upon exiting the driving nozzle the fluid is at a high velocity and a very low pressure and it entrains the stagnant secondary fluid into its flow within the suction chamber.

The mixture of primary and secondary fluids is then accelerated into the converging section of the ejector due to the rapid increase in velocity as the pressure decreases. As the mixture travels through the diffuser its pressure rises as the cross sectional area increases and the velocity consequently decreases [113].

The basic concept for an eductor involves taking a high pressure motive fluid and accelerating it through a tapered nozzle. This fluid then enters a secondary chamber where friction force between the molecules of it and a secondary fluid (gas) causes this secondary fluid to be entrained. These fluids are intimately mixed together and discharged from the eductor [114].

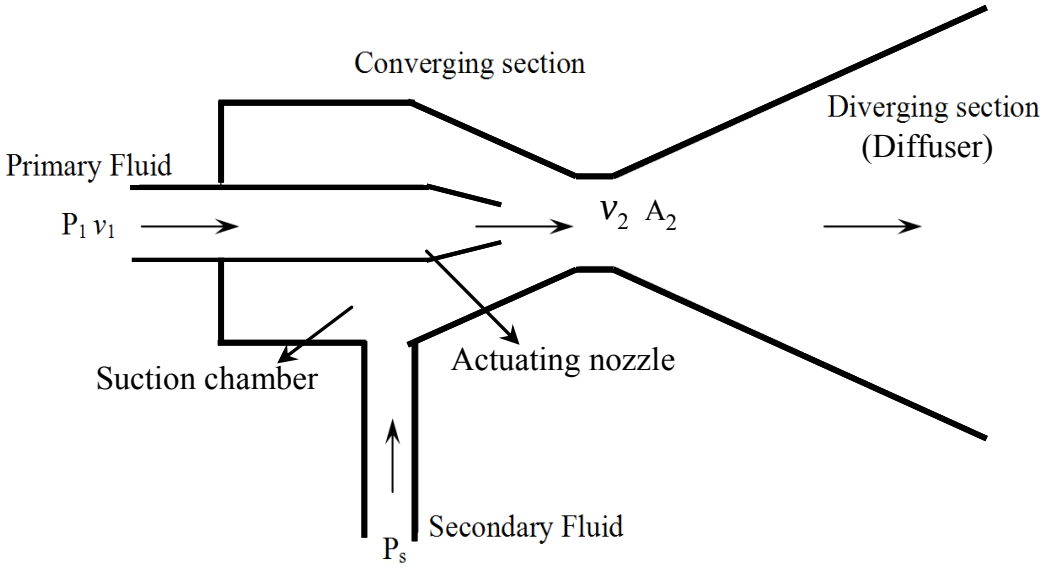

Figure 9-3 Schematic of Ejector.

As P1, Ps and v_1 are known for a specific situation; the velocity of fluid exiting the active nozzle v_2 can be calculated using the Bernoulli equation.

$$\frac{P_1}{\rho_l}+\frac{v_1^2}{2}=\frac{P_s}{\rho_l}+\frac{v_2^2}{2} \tag{9.15}$$

Also:

$$v_2=\frac{\dot{V}}{A_2} \tag{9.16}$$

$$v_1=\frac{\dot{V}}{A_1} \tag{9.17}$$

Using the above equations, Eq. (9.15) can be written as:

$$P_1-P_s=\frac{\rho_l \dot{V}_l^{\,2}}{2A_2^{\,2}}\left(1-\frac{D_2^{\,4}}{D_1^{\,4}}\right) \tag{9.18}$$

Where D_1 and D_2 are the inlet diameter of eductor and exit diameter of the nozzle respectively and A_1 and A_2 are the corresponding cross sectional areas.

Knowing the geometric parameters D_1 and D_2, Eq.18 provides a basis from which the minimum suction pressure (Ps) can be calculated for any given upstream pressure and volumetric flow rate of the primary fluid.

The power consumed by the eductor can be calculated by knowing the pressure of the primary fluid (upstream), its volumetric flow rate, and the pressure of the atmosphere into which the air water mixture is exhausted.

$$Power = \dot{V} \times \Delta P = \dot{V} \times (P_1 - P_{atm}) \tag{9.19}$$

The pumping power needed to run an eductor and its efficiency can be determined experimentally by measuring parameters including the volumetric flow rate of the primary fluid and the inlet and the discharge pressures.

Assuming values for the mechanical efficiency of the pump and the electrical efficiency of the pump motor, the electrical power consumed to create the suction effect may be calculated from Eq. (9.14).

9.2.3 Commercially available vacuum pump

The operating process for a commercially available vacuum pump is shown in Figure 9-4. where the vacuum pump consumes electrical power in order to exhaust the air from the tank and deliver it at atmospheric pressure.

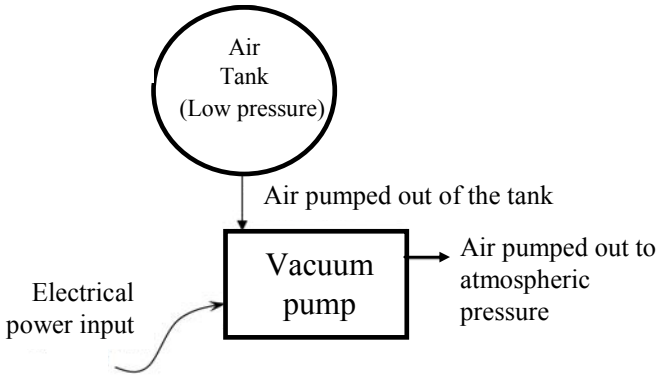

Figure 9-4 Schematic of a vacuum pump

The electrical input power is calculated by:

$$Power_{in} = VI \tag{9.20}$$

The mass flow rate of the air can be calculated using the measured volumetric air flow rate at the outlet using Eq. (9.21):

$$\dot{m}_{air} = \frac{\dot{V}_{air} P_{atm}}{RT_{atm}} \quad kg/s \tag{9.21}$$

The Specific Energy Consumption (SEC) is therefore calculated as:

$$\text{Specific Energy Consumption} = \frac{Power_{in}}{\dot{m}_{air}} \tag{9.22}$$

9.3 Experimental analysis

9.3.1 Comparison of the measured performance of commercial vacuum pumps with that of an ideal vacuum machine

In this section attempts are made to determine the efficiency of the commercially available vacuum machines. In order to do this, the specific electric power consumed by the machine to achieve a certain level of vacuum is compared with that of an ideal vacuum system.

The power of a commercially available vacuum pump was measured as illustrated in Figure 9-5. The inlet pressure of the air was controlled by a pressure control valve to assess the performance of the vacuum pump at different pressures. A vacuum gauge with uncertainty of $\pm 1\%$ was used for measuring the pressure in the range of 0-100 kPa. The atmospheric pressure in the laboratory was measured using a standard barometer. The absolute pressure was then calculated from:

$$P = P_{atm} + P_{gauge} \tag{9.23}$$

The current and voltage were recorded in order to determine input power for each stage using a voltmeter with uncertainty of $\pm 1.5\%$ and an ammeter with uncertainty of $\pm 2.5\%$. Although its influence was minor, adjustments were made to take into account the power factor. The volume flow rate of the extracted air was measured by using a TSI 4000 series flow meter with uncertainty of $\pm 2\%$ which was designed for a variety of gas flow measurement applications in the range of 0-300 lit/min.

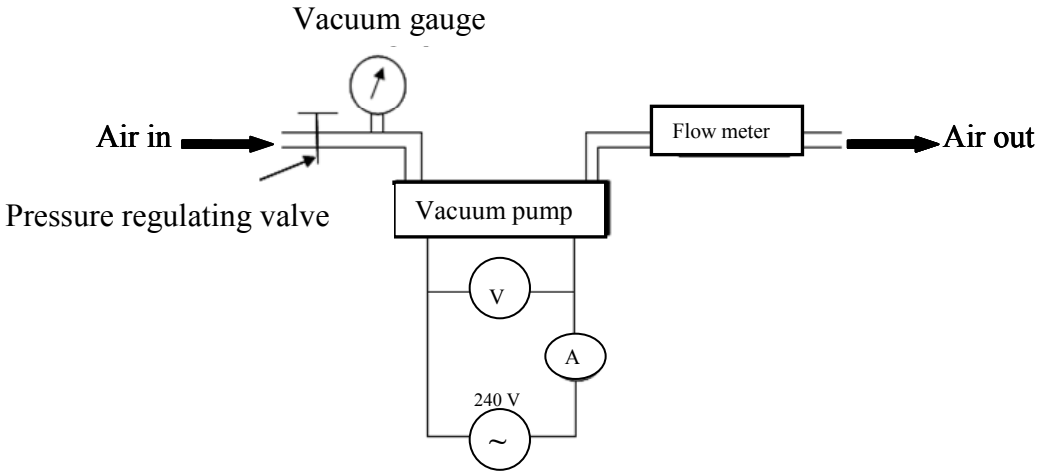

Figure 9-5 Schematic set up for the vacuum pump.

The arrangement of the experiment is shown in Figure 9-6. This experiment was conducted for both increasing and decreasing ranges of openings of the pressure regulating valve (fully open to fully clos) providing corresponding vacuum pressures from atmospheric pressure to the minimum achievable vacuum pressure and back to atmospheric pressure. For each operating condition, current (I), voltage (V), pressure at

the inlet and outlet of the vacuum pump (Pa), the flow rate of air (Lit/min) and atmospheric pressure (Pa) were recorded for use in performance analysis.

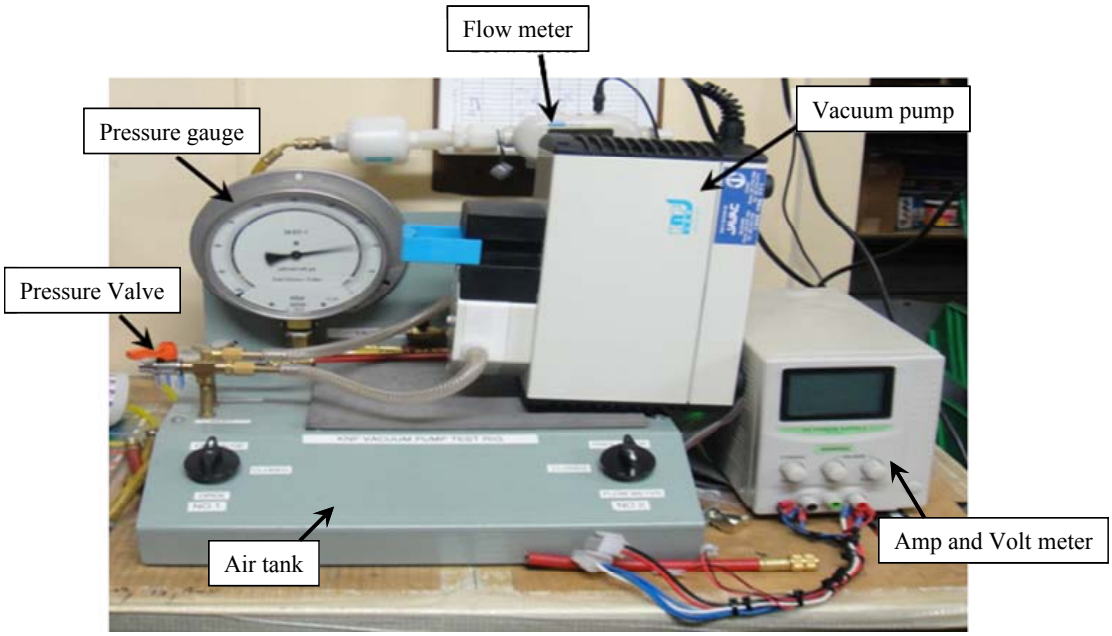

Figure 9-6 Experimental set up for vacuum pump performance analysis.

The recorded experimental data for two of the tests are shown in Table 9-1.

Test 1 (atm to min vacuum pressure)						Test 2 (min vacuum to atmospheric pressure)					
Patm (kPa)	Ttank (°C)	Ptank (kPa)	$\dot{V}$ (lit/min)	V (volts)	I (Amps)	Patm (kPa)	Ttank (°C)	Ptank (kPa)	$\dot{V}$ (lit/min)	V (volts)	I (Amps)
100	16	100	22	248.5	1.2	100	17.4	10	0.75	248.5	1.2
100	16	90	18.5	248.5	1.2	100	16.9	20	2.45	248.5	1.2
100	16	80	15.7	248.5	1.2	100	16.6	30	4.35	248.5	1.2
100	16.2	70	13.5	248.5	1.2	100	16.5	40	6.42	248.5	1.2
100	16.2	60	11.03	248.5	1.2	100	16.4	50	8.80	248.5	1.2
100	16.3	50	8.74	248.5	1.2	100	16.4	60	11.15	248.5	1.2
100	16.5	40	6.3	248.5	1.2	100	16.3	70	13.31	248.5	1.2
100	16.8	30	4.25	248.5	1.2	100	16.3	80	15.45	248.5	1.2
100	17	20	2.45	248.5	1.2	100	16.1	90	17.68	248.5	1.2
100	17	10	0.68	248.5	1.2	100	16	100	21.6	248.5	1.2

Table 9-1 Experimental data for commercially available vacuum pump for 2 tests.

Specific energy consumption of the vacuum pump at each air supply pressure was calculated from:

$$SEC_{vacuum\ machin} = \frac{electrical\ power\ consumed\ by\ the\ machine}{\dot{m}_{air}} \tag{9.24}$$

The results are shown in Figure 9-7.

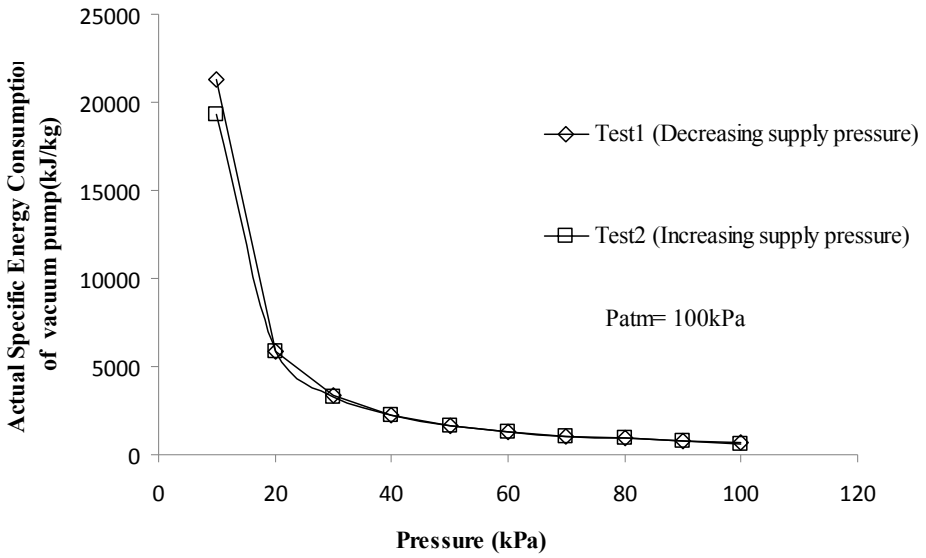

Figure 9-7 Experimental Specific Energy Consumption for two tests on a commercial vacuum pump as a function of supply air.

This is the preferred parameter for comparison of theoretical and measured data. The graph in Figure 9-7 shows close agreement between the results obtained during a reducing pressure test (Test 1) and an increasing pressure test (Test 2). It can be seen that the specific energy consumption for the vacuum pump increases as the inlet pressure is reduced.

9.3.2 Comparison of performance of a vacuum pump with an ideal vacuum machine

Based on the manufacturer's data sheets for the vacuum pump, which relate the flow rate of the entrained air to the suction pressure, theoretical analysis has been performed by assuming the vacuum pump to be ideal. The theoretical work and power for the isothermal and adiabatic processes are calculated by using Eqs. (9.7), (9.11) and (9.10) respectively.

The graphs of theoretical specific work and theoretical power for the isothermal and adiabatic processes for a commercial vacuum pump are shown in Figure 9-8 and Figure 9-9 respectively and these figures can be compared to the measure values

By using Eq. (9.24) the theoretical specific energy consumption was calculated and is plotted in Figure 9.8.

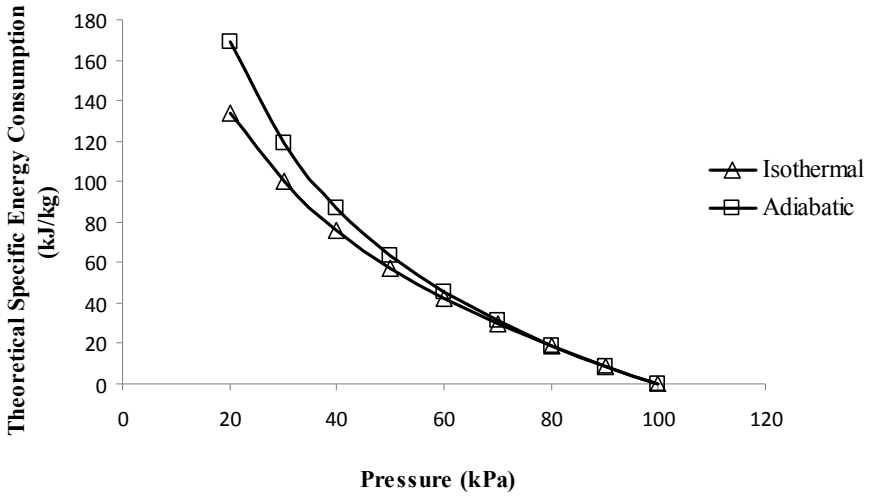

Figure 9-8 Comparison of Theoretical Specific Energy Consumption for Isothermal and Adiabatic vacuum process

It is evident that the adiabatic work is greater than the isothermal work and both increase with decreasing inlet pressure. This is because work in adiabatic vacuum processes is higher than that in isothermal processes. Practical processes lie somewhere between the isothermal and adiabatic processes.

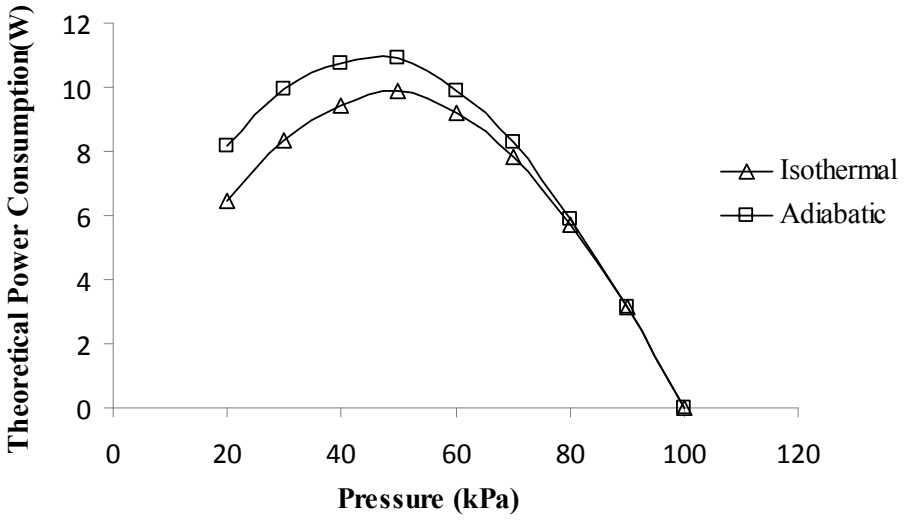

Figure 9-9 Comparison of theoretical power for Isothermal and Adiabatic vacuum process of an ideal vacuum machine with the capacity of the vacuum pump under consideration

It can be seen that by decreasing the pressure, the theoretical power initially increases before decreasing.

Figure 9-10 shows the specific energy consumption from an experimental test on a vacuum pump and compares it with the theoretical analysis for both adiabatic and isothermal processes as calculated from Eq. (9.7).

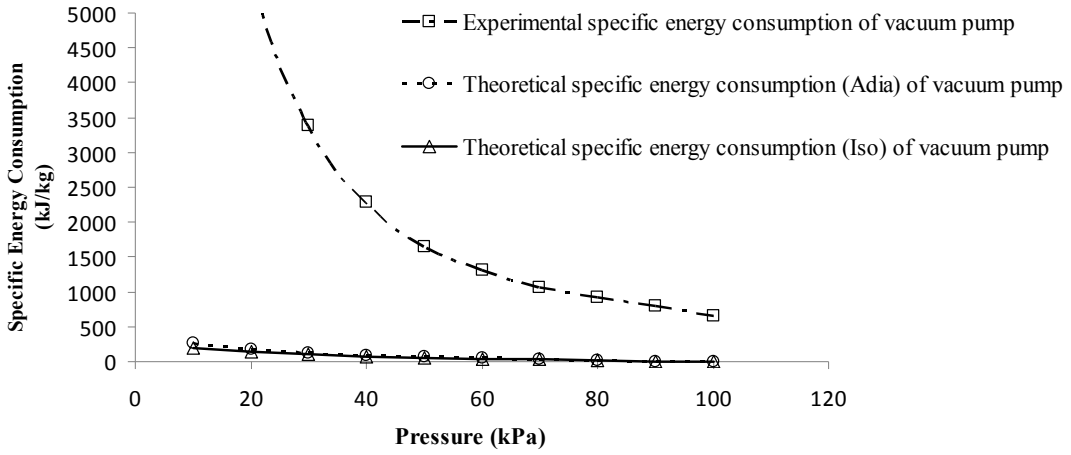

Figure 9-10 Comparison of Experimental and Theoretical Specific Energy Consumption for vacuum pump.

It can be concluded that at high pressure the theoretical and experimental specific energy consumptions become closer. However, as the pressure is decreased the experimental energy consumption rises up dramatically, because of the reduced mass flow rate of air, whereas the energy consumption of the vacuum pump is has much less variation.

Relating the SEC by theoretical analysis to that from experimental data as shown in Figure 9.10, the efficiency of the vacuum pump may be expressed as,

$$\eta_{vacuum\ pump} = \frac{Theoretical \quad SEC}{Experimental \quad SEC} \tag{9.25}$$

Figure 9-11 shows the efficiency of a commercial vacuum pump by considering the vacuum process as an isothermal process or as an adiabatic process.

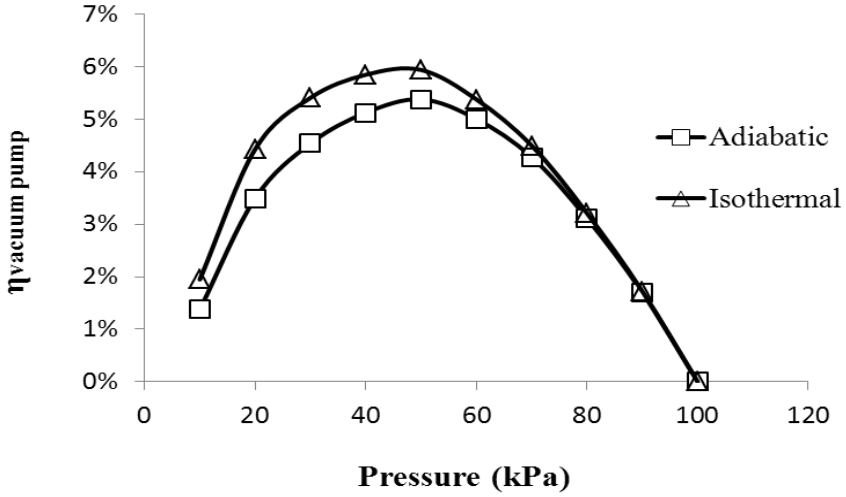

Figure 9-11 Relative efficiency of a commercial vacuum pump.

For a vacuum pump the energy consumption is close to constant because of the characteristics of the pump motor. An ideal vacuum machine will consume very little energy at atmospheric pressure at the inlet even though pumping a large amount of air. From Figure 9-11, it can be seen that the efficiency of the typical vacuum pump tested was maximum at 50 kPa and achieved a value of 5.8%.

Figure 9-12 compares the measured data with the data provided by a commercial vacuum pump manufacturer.

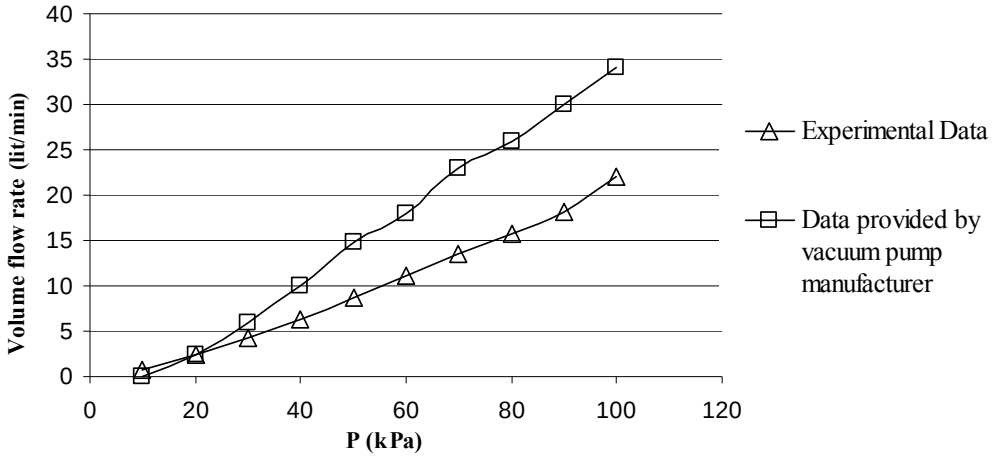

Figure 9-12 Comparison of experimental and supplied data for a commercially available vacuum pump.

9.3.3 Comparison of theoretical and measured results for a commercially available water-gas ejector (eductor)

Here the results from a series of tests on two commercially available eductors are presented. The main purpose of the tests was to determine the specific energy consumption of an eductor at different suction pressures and to compare the results with the performance of a commercially available vacuum pump as presented in Figure 9-11. Furthermore the performance of eductors is assessed against that of an ideal vacuum machine and conclusions have been drawn concerning the efficiency of an eductor as a possible sustainable candidate for removal of non-condensable gases from geothermal water.

In order to gain better understanding of eductor design and to establish the influence of different geometric parameters of an eductor on its efficiency, several performance tests on available eductors were conducted.

Testing an off the shelf eductor was initially planned in order to validate the theory of the base calculations on which the rest of the project will be later built. The suction ability of the nozzle was to be determined and a realistic potential volume of displaced air to be identified. The vacuum ability of a single phase ejector was investigated experimentally in order to find out whether or not it would be sufficient to evacuate and sustain the low pressure required.

A schematic of the eductor test rig is shown in Figure 9-13. The test facility consisted of a water supply reservoir, a water pump, a flow meter, a pressure regulating valve, a pressure gauge, an eductor, a vacuum gauge and an air tank. The ejector is water driven and in the converging section, pressure drop occurs. The air from the tank, as the secondary fluid, is entrained by the water jet. In the diverging section the mixture pressure increases and it is vented to atmosphere.

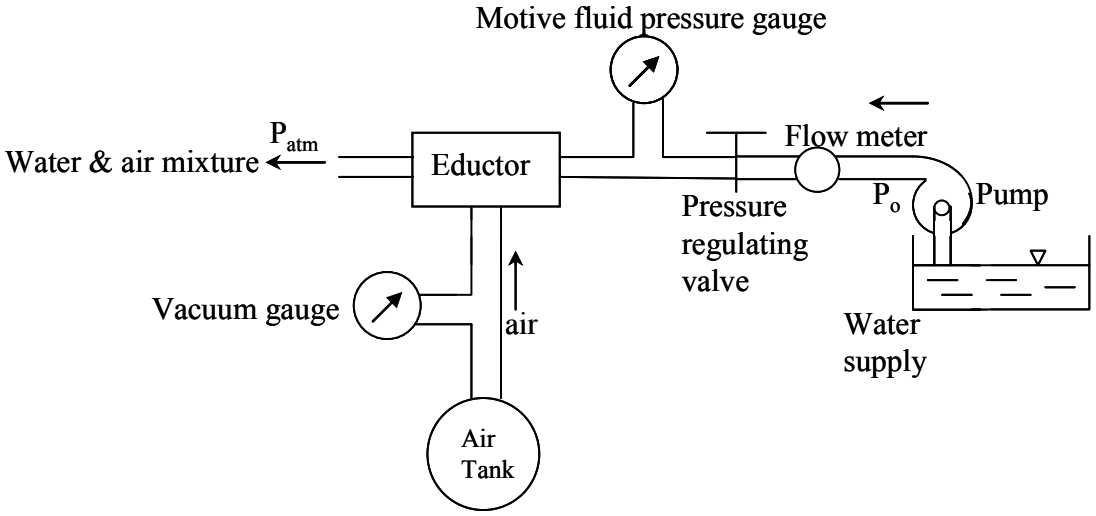

Figure 9-13 Schematic of the experimental set up for the eductor.

In this experiment use was made of a 20 litre tank equipped with a vacuum gauge. The 550 watt water pump could produce a head of 600kPa pressure and could deliver 55 lit/min of water. The flow rate of the system was measured by a flow meter with the accuracy of 0.1%. Also, by using a bucket and stop watch method for measuring the flow rate of the water at the outlet, the accuracy of the flow meter was assessed. The supply water pressure to the eductor was measured using a pressure gauge (0-500 kPa) with uncertainty of $\pm$ 1%.

In this experiment two eductors were used. The first ejector (here we call it eductor 1) was originally used to create a vacuum using steam as the primary fluid, but was driven by water flow in the current tests. The second ejector (here we call it eductor2) was a commercially produced device to create vacuum using liquid water as the motive fluid. In Figure 9-14 both ejectors are shown.

(a) (b)

Figure 9-14 The two eductors used in the experiments (a).eductor 1 (b).eductor 2

The test procedure started with the air tank pressure equal to the atmospheric pressure and at this stage the pump was started and the flow of water through the eductor caused the pressure in the tank to be decreased. Data were gathered on the water flow rate, pressure of the primary fluid as it entered the eductor measured by the pressure gauge, as well as tank pressure as functions of time. This process continued until there was no further reduction in the tank pressure. At this stage the setting of the pressure regulating valve as shown in Figure 9-13 was changed and then the above process of data collection was repeated.

Test results:

Table 9-2 shows the experimental data during the tests on the eductors at different motive fluid pressure.

Pmf=300kPa					Pmf=200kPa				
Patm(kPa)	Ttank (°C)	Ptank(kPa)	Time(s)	$\dot{V}$ (lit/min)	Patm(kPa)	Ttank (°C)	Ptank(kPa)	Time(s)	$\dot{V}$ (lit/min)
100	16.2	100	0	0	100	16.5	100	0	0
100	16.2	91	6.54	0.22	100	16.5	91	5.78	0.163
100	16.2	86	15.46	0.22	100	16.5	81	16.57	0.163
100	16.2	81	17.52	0.22	100	16.6	71	32.98	0.163
100	16.3	71	29.72	0.22	100	16.6	61	58.63	0.163
100	16.4	66	37.22	0.22	100	16.6	56	74.92	0.163
100	16.4	61	45.66	0.22	100	16.6	51	93.34	0.163
100	16.5	56	55.88	0.22	100	16.6	46	114.25	0.163
100	16.5	51	68.06	0.22	100	16.6	41	140.33	0.163
100	16.5	46	81.91	0.22	100	16.6	36	170.49	0.163
100	16.7	41	98.28	0.22	100	16.7	31	202.25	0.163
100	17	36	117.29	0.22	100	16.7	26	241.12	0.163
100	17	31	140.09	0.22	100	16.7	21	290.15	0.163
100	17	26	167.80	0.22	100	17	16	369.10	0.163
100	17	21	202.71	0.22	100	17	11	499.57	0.163
100	17	16	249.07	0.22	100	17	8	1079.03	0.163
100	17.3	11	315.84	0.22	100	17.1	6	1800.00	0.163
100	17.3	6	460.77	0.22					
100	17.5	5	514.27	0.22					
100	17.5	4	603.47	0.22					
100	17.5	3	703.12	0.22					

Table 9-2 Experimental data for eductor at two different motive fluid pressure.

In Figure 9-15 test results for the two eductors 1 and 2 for the maximum motive fluid pressure are shown. In this figure the drop of the tank pressure is presented as a function of time for the two eductors 1 and 2.

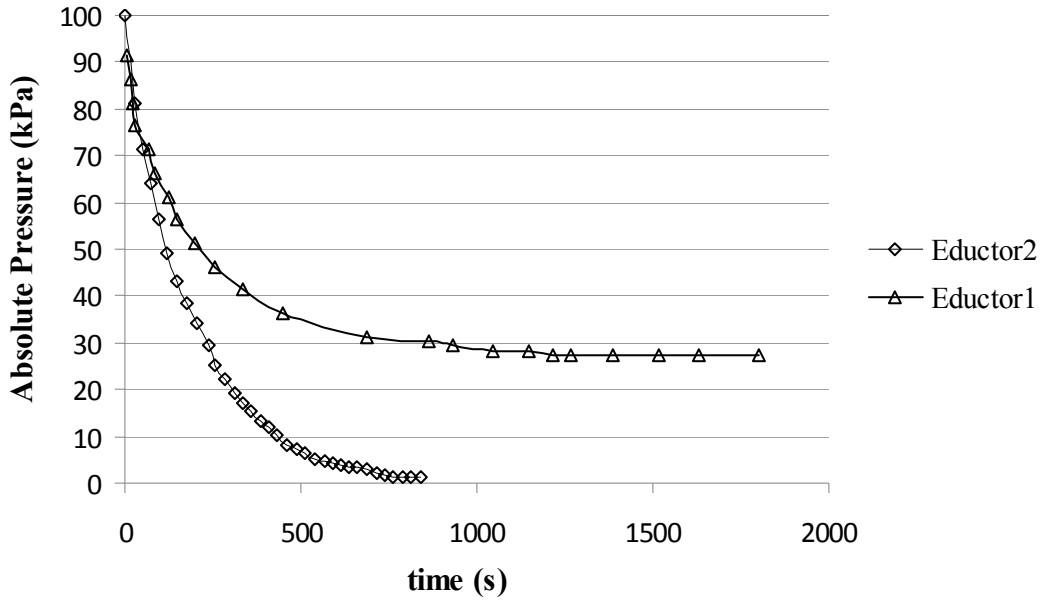

Figure 9-15 Vacuum ability of two ejectors.

It can be seen that eductor 1 which was originally designed and limited to use steam as its primary fluid cannot reduce the tank pressure to the required low level. In this case the eductor has been able to reduce the pressure of the tank to only 27 kPa. However, eductor 2 which was originally been used to use water as primary fluid has achieved very low pressure (almost 2 kPa) in the tank in less time.

Test results are shown in Figure 9-16 for eductor 2 for different primary fluid pressures. In this figure the drop of the tank pressure is shown as a function of time.

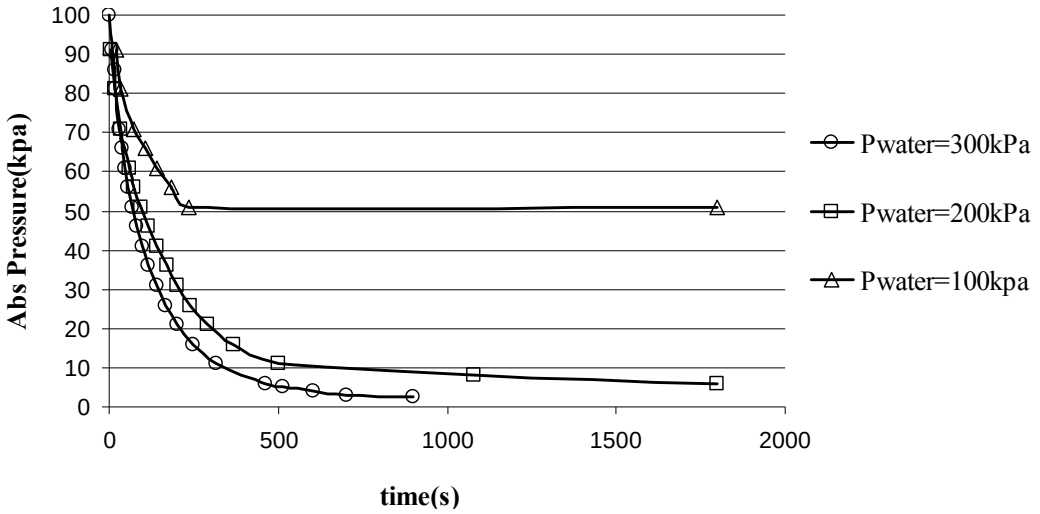

Figure 9-16 Pressure drop in the tank using eductor 2 for different primary fluid pressure

9.3.3.1 Estimating the specific energy consumption of the eductors

Energy is required to produce the suction effect of an eductor and the amount of energy consumed for unit of mass of air will be a good measure of viability of the proposed system for degassing geothermal water. In order to calculate the specific energy consumption of this device for various motive fluid pressures and different ambient pressures, it is necessary to know the mass flow rate of air ($\dot{m}_{air}$). However direct measurement of mass flow rate of air was very difficult, so an indirect method to estimate the mass flow rate of air out of the tank was used. Following are the equations used for indirect estimation of mass flow rate.

For an ideal gas, we have:

$$P_{\tan k} V_{\tan k} = m_{\tan k} R T_{\tan k} \tag{9.26}$$

From Eq.26:

$$m_{\tan k} = \frac{P_{\tan k} V_{\tan k}}{R T_{\tan k}} \tag{9.27}$$

By differentiating Eq(9.27):

$$\frac{dm_{\tan k}}{dt} = \frac{V_{\tan k}}{RT_{\tan k}} \cdot \frac{dP_{\tan k}}{dt} \tag{9.28}$$

The mass flow rate of air ($\dot{m}_{air}$) out of the air tank and into the eductor is related to $m_{\tan k}$ and time as follows,

$$\dot{m}_{air} = -\frac{dm_{\tan k}}{dt} \tag{9.29}$$

By combining Eqs. (9.28) and (9.29):

$$\dot{m}_{air} = -\frac{V_{\tan k}}{RT_{\tan k}} \cdot \frac{dP_{\tan k}}{dt} \tag{9.30}$$

Using Eq(9.30), knowing the volume of the tank, the tank temperature and using data available from Figure 9.16 the mass flow rate of the air ($\dot{m}_{air}$) can be estimated. Evidently $\frac{dP_{\tan k}}{dt}$ is not readily available from Fig. 16 and it must be approximated by using the data in Figure 9.16. However, considering the exponential decay of the pressure in the air tank, it was thought better to perform curve fitting using an exponential function and using the resulting equations to approximate the variation of tank pressure with time.

Considering the data in Figure 9.16, it has been concluded that the variation of $P_{\tan k}$ with time is best presented by the following function:

$$P_{\tan k} = f(t) = P_f + (P_o - P_f)e^{-\alpha t} \tag{9.31}$$

In Eq. (9.31) P_f is the lowest pressure achieved in the tank and P_o is the initial tank pressure which is same as atmospheric pressure. Also, α is a parameter which needs to be determined.

Therefore, to find the best corresponding curve, α must be found by minimizing the value of parameter D defined below.

$$D = \sum_{i=1}^{n} [\, f(t_i) - P_i]^2 = \sum_{i=1}^{n} [\; P_f + (P_o - P_f)e^{-\alpha t} - P_i]^2 \tag{9.32}$$

By minimizing the value of Eq. (9.32) α can be calculated for different pressures of motive fluid. This was done by varying α, examining the values of D and looking for its minimum.

The results of the curve fitting exercise are shown in Figure 9-17, where the actual data and the curves of best fit are presented for three different upstream pressures of the eductor.

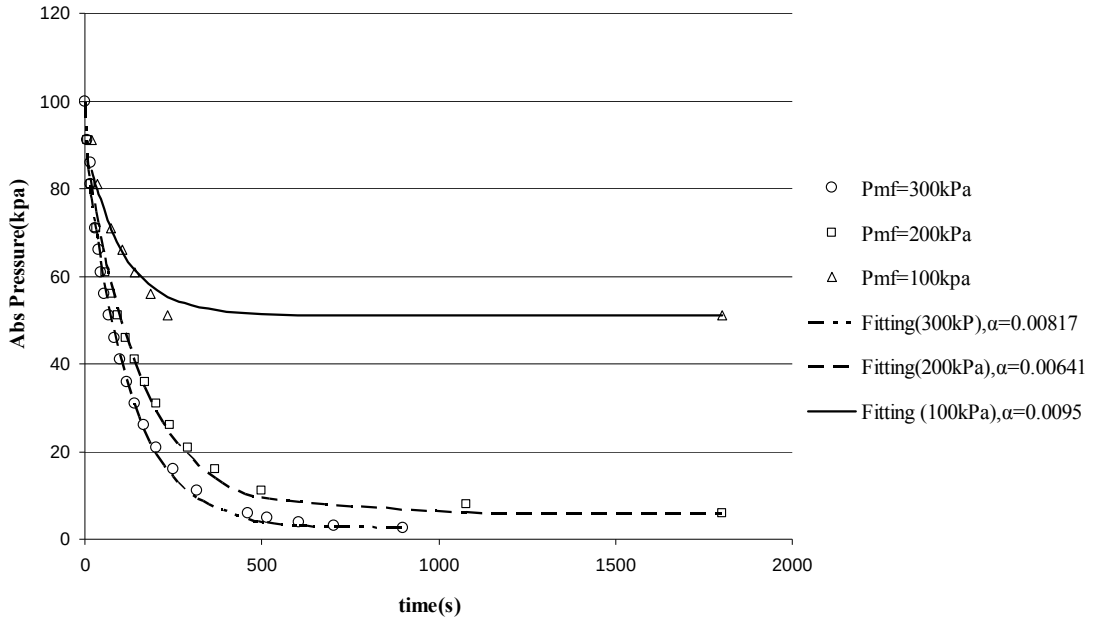

Figure 9-17 Fitting curves for pressure drop in 2nd ejector in different motive fluid pressures

Figure 9-17 indicates reasonable agreement between the curves obtained from the derived equation for pressure drop for different motive fluid pressures and those from the actual data.

The value of $\frac{dP_{\tan k}}{dt}$ can be calculated by taking the derivative of Eq. (9.31) as below,

$$\frac{dP_{\tan k}}{dt} = P_f \alpha e^{-\alpha t} \tag{9.33}$$

From Eq. (9.33) the value of $\frac{dP_{\tan k}}{dt}$ is calculated for each motive fluid pressure at any time using the corresponding value of α. Mass flow rate of the air ($\dot{m}_{air}$) is calculated using Eq. (9.30).

The specific energy consumption of the eductor ($SEC_{eductor}$) is calculated from Eqs. (9.14) and (9.22).

In Figure 9-18 the $SEC_{eductor}$ is shown for three different motive fluid pressures. On the same figure, the SEC of an ideal vacuum machine is also shown.

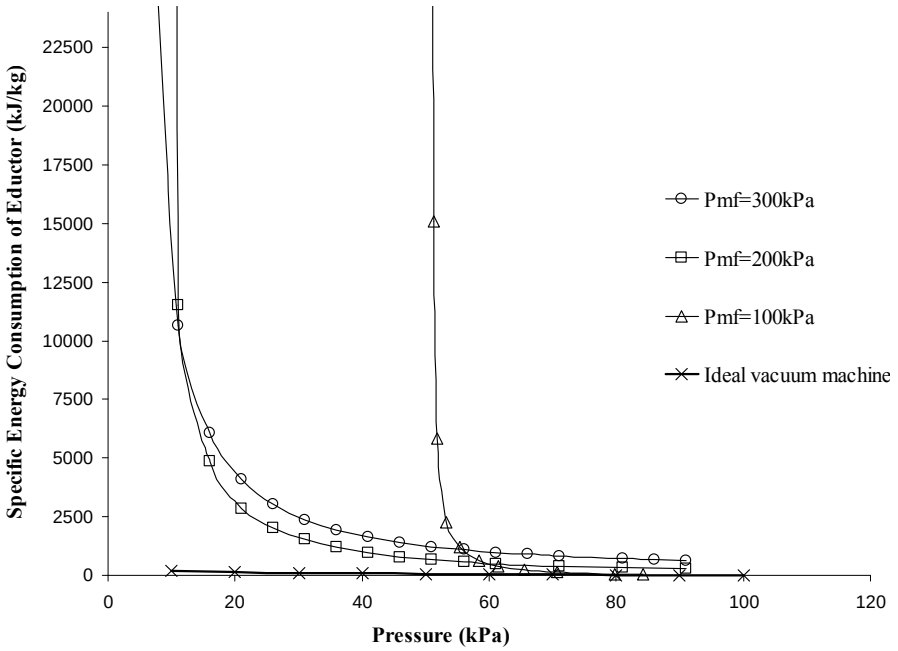

Figure 9-18 Experimental and theoretical specific energy consumption for eductor in different motive fluid pressure

As it can be seen from Figure 9-18, when the pressure of the tank decreases the specific energy consumption increases noticeably for eductors. In addition, decrease in motive fluid pressure has a direct effect of increasing the specific energy consumption of the eductor. It can also be seen that at high tank pressure and lower vacuum levels the

theoretical specific energy consumption is close to experimental results for the eductor. However, as the pressure of the tank is reduced, the discrepancy increases. This is because of the small amount of the air which remains in the tank at low pressure.

The efficiency of the eductor at any point can be calculated using Eq. (9.13). Figure 9.19 shows the efficiency curves of the 2nd eductor estimated using experimental results combined with Eq. (9.15). In Eq. (9.18) the pumping power is estimated using the measured mass flow rate of water and the pressure drop across the eductor and considering an overall efficiency of 0.5 for water pump.

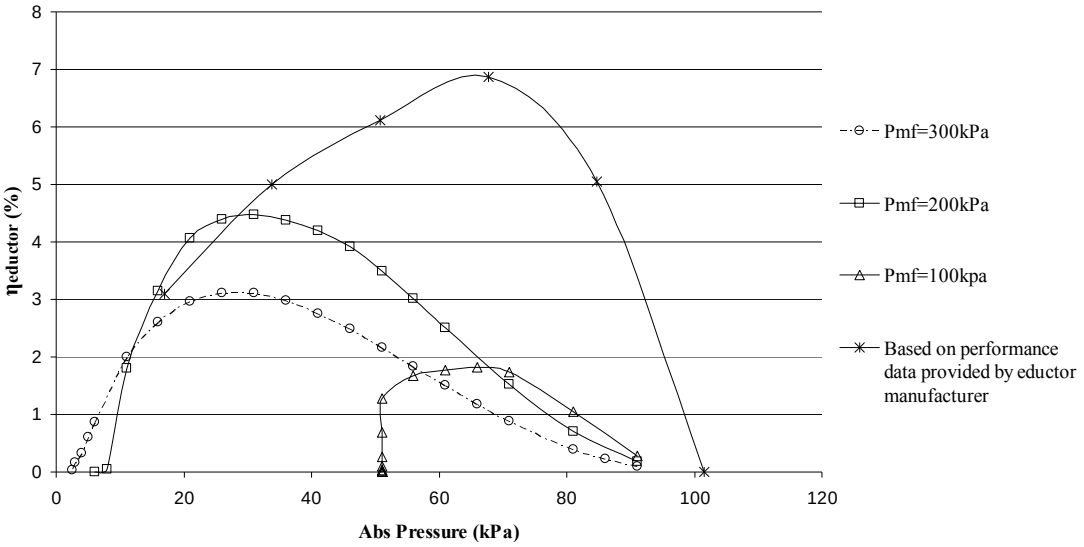

Figure 9-19 Efficiency of the eductor for different motive fluid pressure

It can be deduced from Figure 9-19 that the eductor has a maximum efficiency at a particular motive fluid pressure which in this case is 200 kPa. In the same figure the efficiency of the eductor is presented using the data available from the manufacturer.

9.4 Comparison of performance of the vacuum pump and the eductor

In order to make sensible comparison of the performances of the vacuum pump and eductor, Figure 9-20 shows the specific energy consumption of the vacuum pump and eductor at three different motive fluid pressures.

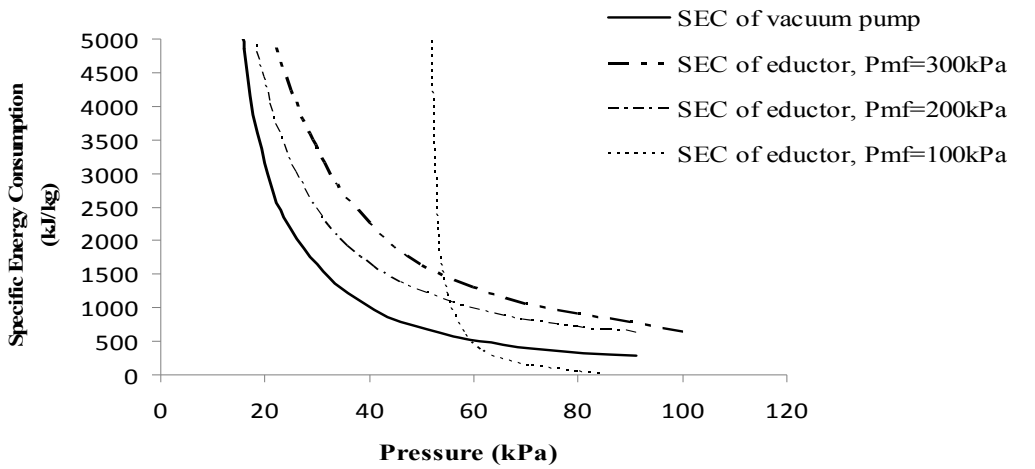

Figure 9-20 Comparison of specific energy consumption for eductor performing in different motive fluid pressure and the commercial vacuum pump

In addition the efficiency curves of the vacuum pump and the 2nd eductor are shown in Figure 9-21 using experimental results and Eq. (9.15). The error analysis show 1.03% uncertainty for the efficiency of the vacuum pump and 1.65% uncertainty for the efficiency of the eductor. It can also be seen that at pressures below 20kPa (abs) the ejector has higher efficiency then a commercially available mechanical vacuum pump.

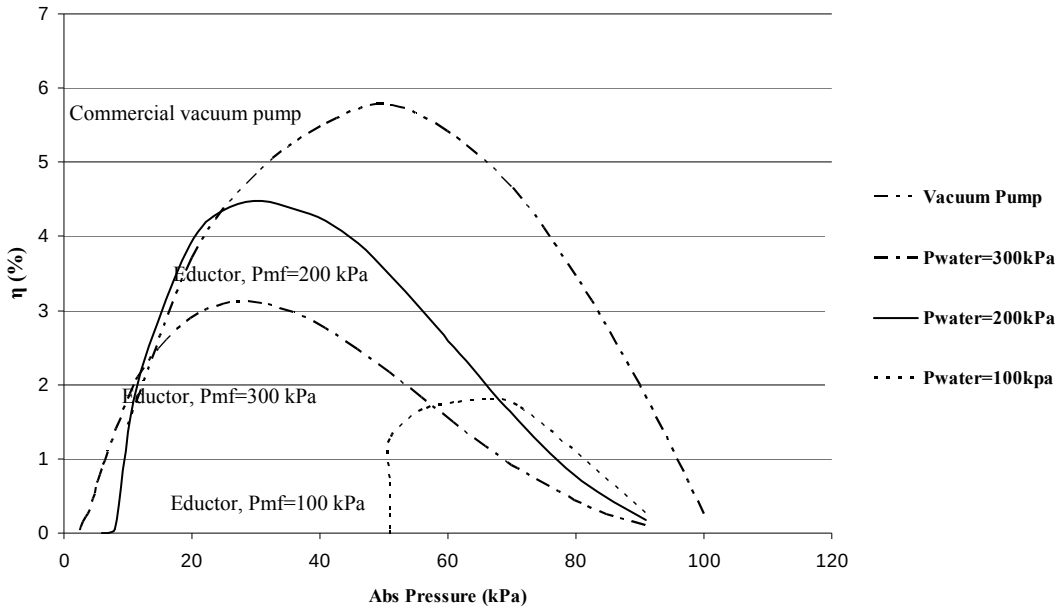

Figure 9-21 Comparison of efficiencies for the commercial vacuum pump and the eductor for different motive fluid pressure

9.5 Discussion of results

Theoretical and experimental results for SEC show close agreement at high tank pressure for both vacuum pump and eductor. However, at low pressure the disparity between the theoretical and experimental results increases. This is attributed to the smaller amount of air left in the tank as the tank pressure decreases while the vacuum ability of these devices remains constant during the whole process. Therefore for the geothermal applications in which running water is available[102], eductors can be installed to remove non condensable gases. This will have a significant effect on reducing the parasitic losses by removing the need for a vacuum pump.

Experimental results on a commercially available vacuum pump indicate that the maximum efficiency of 5.8% is achievable at approximately 50 kPa tank pressure . Below this pressure the performance of the vacuum pump decreases.

It also can be seen from experimental results on available eductors that using the proper design for eductors through choice of motive fluid and geometry can have a significant improvement on their performance. As the experiments indicate by using the eductor which was mainly designed for using liquid (water) as motive fluid, lower absolute

pressure in the tank was achieved compared to that achieved by an eductor which was designed originally for using steam as a motive fluid. Additionally, there will be an optimum motive fluid pressure for a particular eductor to get the best efficiency. For example, the examined water-gas eductor had a best performance at motive fluid pressure of 200kPa. In this case the maximum efficiency of 4.4% was achieved for a 30kPa tank vacuum pressure whereas with the same eductor performing at 300kpa motive fluid pressure, the highest efficiency of 3.1% was achieved for a tank vacuum pressure of 25kPa. The eductor was only 1.9% efficient when it performed at motive fluid pressure of 100kPa at almost 65kPa air pressure.

Considering the optimum condition for the performance of the eductor, it can be concluded that the eductor is less efficient than the commercially available vacuum pump at high pressures.

9.6 Conclusion and future work

Considering the theoretical and experimental results, it can be concluded that two phase eductors can be utilised to remove NCGs from geothermal waters as a sustainable technology. However they are less efficient than the commercial vacuum pump at higher pressures, but have shown better performance than vacuum pumps at low pressures.

Therefore, the water-gas eductor is suitable for removing NCGs where a continuous water flow is available and the vacuum to be maintained is low. In addition, there is the simplicity of the eductor design with no moving parts, rugged construction, large volume capability, maintenance free operation, low cost and long life.

As the efficiency of the available methods for removing non condensable gases from geothermal water is not very high, further research and work is needed to make them more efficient. Furthermore, for future work the efficiency of the water-gas ejector can be increased since there is large potential for improving the performance of the two phase ejector compared to that of a vacuum pump by making changes to the geometry of the ejector and optimising the design.

Chapter 10 Economics of combined desalination and power generation (CDP) for dual geothermal application and preliminary design of CDP technology demonstration for a geothermal site

10.1 Introduction

In this chapter the economics of combined desalination and power generation (CDP) for a geothermal site are investigated. Considering different scenarios of electrical energy and fresh water produced, the economic prospects of CDP as a source of power and fresh water utilising hydrothermal are evaluated.

In addition, a preliminary design and cost of construction of a 20 kW CDP unit considered as a case study for technology demonstration are presented,

10.2 The characteristics of the geothermal site for demonstration unit

In this chapter two cases are considered for using the CDP unit. The first case is a full-scale geothermal power plant with an electrical capacity of 3 MW . The available data indicate that the geothermal waters (hydrothermal) are saline (up to 2% salt) and have a temperature in the range of 90to 150°C at depths of 2 km to 4 km, and a potential flow rate of 130 L/sec.

The second case is a demonstration power plant with an electrical capacity of 20 kW, with liquid water at 125 °C provided from the bore on the site. The flow rate of the water that travels into the CDP unit would be around 1.05 kg/s, which is less than 1% of the hot water available from the bore.

10.3 Preliminary investigation of technical feasibility and economics of a full-scale CDP unit

For a full-scale unit at the geothermal site the following assumptions will be made as it was discussed as a result of chapter 8. :

- Hot water flow rate of 130 L/s at a temperature of 150 °C.
- Isentropic efficiency of the turbine 50%, Mechanical efficiency 80% and the Electrical efficiency 90%.
- Fresh water recovery ratio of 20%.
- Condenser temperature of 40 °C

10.3.1 Condenser, turbine and generator capacities and costs

Based on the assumptions, the capacity of the condenser will be: (150-40)*4.2*130 = 60,000 kW or 60 MW. On the basis of off-the-shelf components, its cost would be be $0.5 million.

Considering T_h=150 °C and T_c =40 °C, the trilateral efficiency of the system will be about 0.12. Therefore turbine output power can be estimated based on isentropic, trilateral, mechanical and electrical efficiencies as:

Turbine output power = 60 MW *(0.12)*(0.5)*(0.8)*(0.9)

= 3 MW of electric power.

Generator cost approximately will be $100 000 and turbine costs will be $500 000

Total plant cost including condenser, generator and turbine costs will be $2 million. This does not include the bore cost and reflects the cost of the above ground equipment. Assuming a bore cost of $15 million, the total cost will be $17 million which gives the $ 6500/kW with capacity factor of almost 1 as it operates all the time which is much higher than the wind farms or photovoltaic sites considering their capacity factor of 0.25.

10.3.2 Fresh water and electrical energy output and income

The above calculations result in 72 000 kWh per day of electrical energy. Assuming a cost of 20 cents per kWh, this would be equivalent to $15 000 per day income .

Fresh water will be 130*0.2*86400/1000= 2200 cubic meters per day. Assuming a water price of $5 per m^3 , this will bring in a revenue of $11 000 per day.

Thus by considering the $ 15000 per day of electricity and $ 11000 per day of fresh water, the income will be $ 26000 per day, which is $10 million yearly.

By considering the yearly running costs for wages of 5 people and maintenance of $1 million the total net yearly income will be 365 *(26 000) - 1000000 = 9 000 000 = $9 million.

Having the above information leads to access to the total cost and payback period based on yearly income, plant and bore costs.

Total cost= Plant capital+ Bore capital (10.1)

Payback period=(Plant capital+ Bore capital) / yearly income

It should be noted that the bore cost is the only uncertainty Therefore, in the economic analysis of payback period is defined as a function of bore cost.

Figure 10-1 shows the 2 scenarios of best and worst condition, these 2 considered scenarios are as below:

Scenario 1: Water price $ 5/ m^3

Electricity price $ 0.2/ kWhr

Net yearly income: $ 9 million

Scenario 2: Water price $ 2/ m^3

Electricity price $ 0.1/ kWhr

Net yearly income: $ 3.5 million

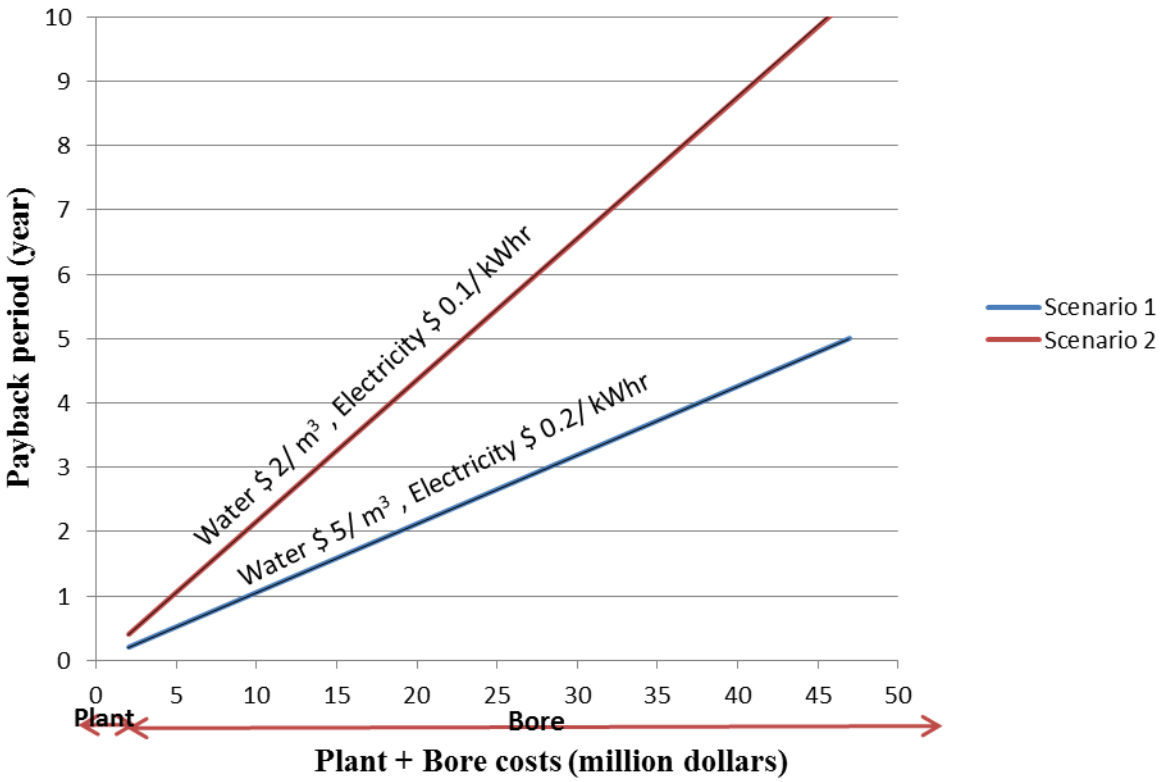

Figure 10-1 Payback period of CDP unit for the full scale geothermal site for 2 scenarios

The payback period depends on the bore cost at a time for any geothermal site. As an example, it can be seen from the figure that in the best condition (Scenario 1) the payback period will be in 2 years if plant and bore cost $ 20 million whereas for the worse case (Scenario 2) this payback period will be 4 years. It should be mentioned that out of this $ 20 million, only 10% is the plant cost and the rest would be the bore cost.

10.4 Predicted performance of demonstration CDP unit at geothermal site

For the 20 kW geothermal power plant with access to 125 °C of liquid water, the performance of the proposed CDP system can be enhanced through the developed computer model, which has been described in chapter 5. The input of the computer model would be inlet temperature of feed water 125°C at the flow rate of 1.05 kg/s. Saturation temperature at the exit of the nozzle as 35 °C and the diameter of the rotor as 0.4 m.

Using the computer model, the following graphs show the performance of the system. Figure 10-2 shows the power generation of the CDP based on the rotational speed for different isentropic efficiency.

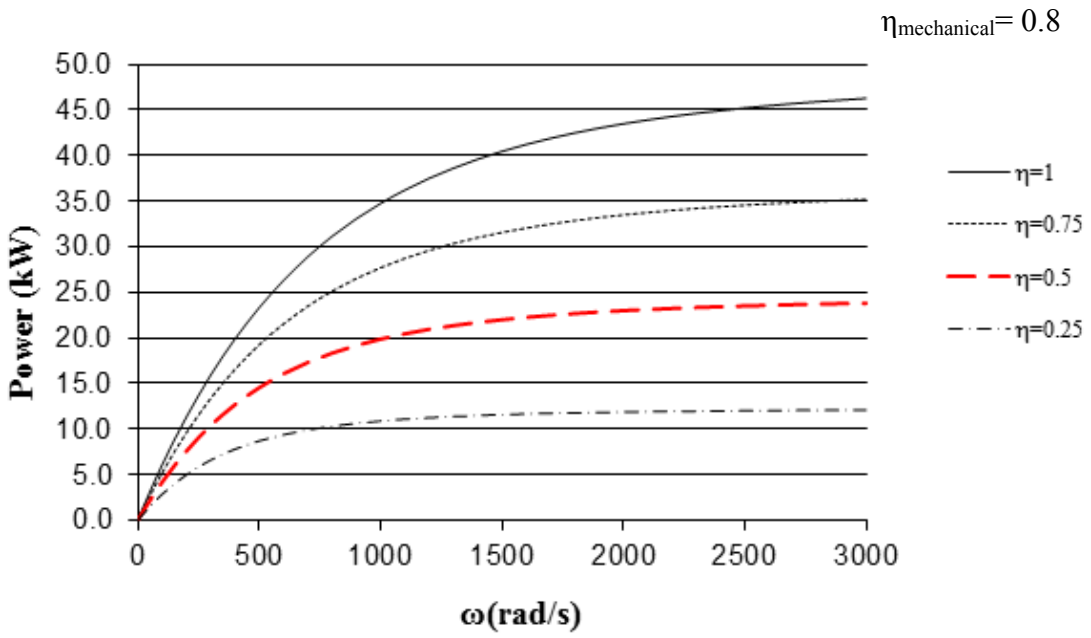

Figure 10-2 Power generation of proposed CDP system for different isentropic efficicencies

As it can be seen from this figure, for an isentropic efficiency of 50% for the system at a rotational speed at 10 000 RPM leads to the generation of 20 kW of power, as required for the demonstration power plant.

As the other output of the CDP system, the fresh water production has been shown in Figure 10-3 for the same demonstration unit characteristics.

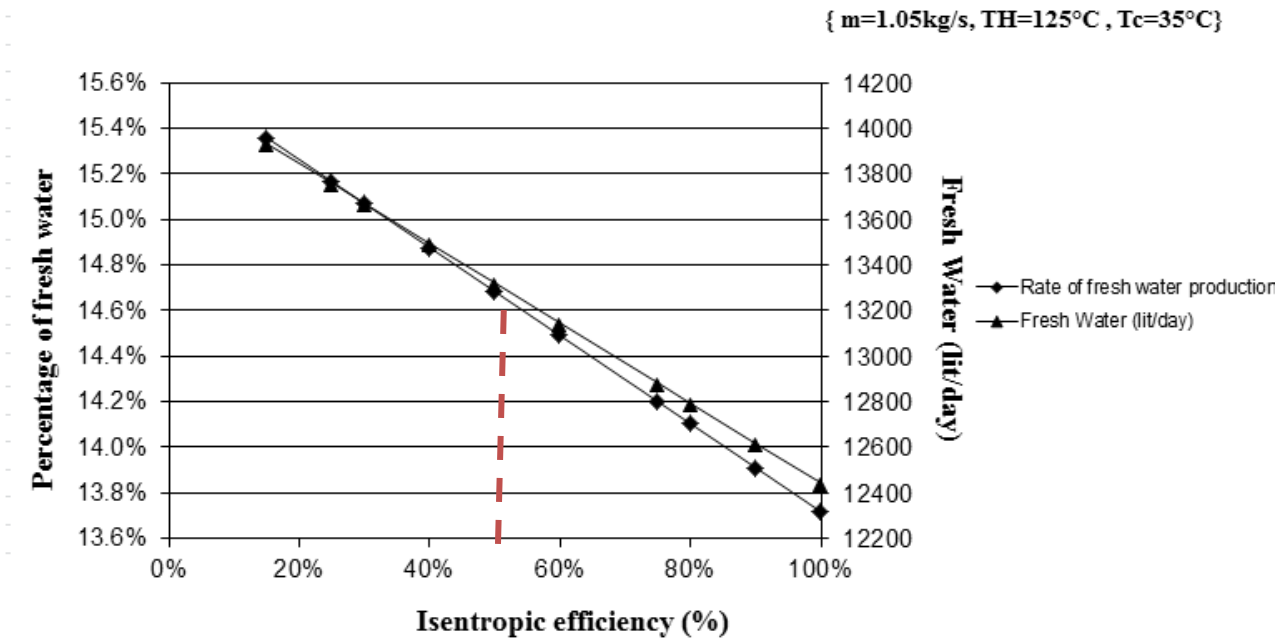

Figure 10-3 Fresh water production for different Isentropic efficiency

For an assumed isentropic efficiency of 50%, the fresh water production will be 13321.1 L/day, which is 0.5 m^3/hr. This is about 14.7% as fresh water, which is a great enhancement compare to the very first design.

10.5 Design of the demonstration CDP unit and its cost analysis

Based on the discussion in the previous section and also the characteristic of the 20 kW pilot plant, a new design for the CDP system has been developed and is described here.

Figure 10-4 shows the proposed arrangement of the 20 kW dual geothermal system for fresh water production and power generation. The DC generator in the system is mounted on the top outside the flashing chamber and hence does not require water proofing. A mechanical seal on the generator shaft and the top plate of the flashing tank helps to maintain the vacuum in the system. This mechanical seal is water cooled with water continuously sprayed at the interface of the rotating carbon and stationary ceramic surface of the mechanical seal. There is another mechanical seal at the inlet to prevent unnecessary feed water leak into the bearings and intern into the flashing chamber. The flashing chamber would be made out from 20 inch diameter schedule 20 stainless steel pipe and the height of the flashing chamber will be 0.4m.

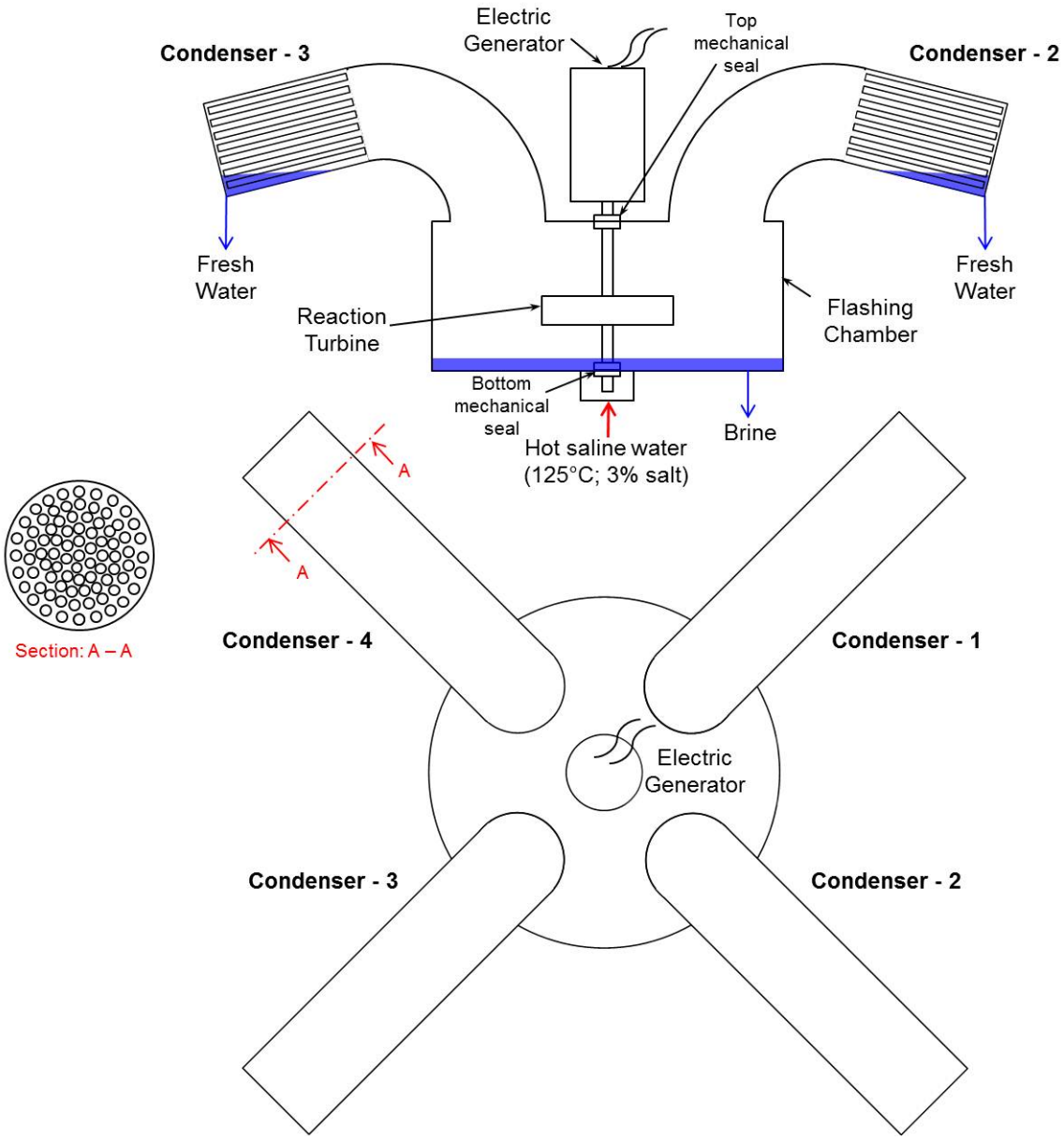

Figure 10-4 Schematic of the 20kW technology demonstration dual geothermal system

The cost of the flashing chamber plus bottom plate with mounting arrangement for turbine and top plate with mounting arrangement for condenser similar to the laboratory scale prototype as shown in the appendix would be about $20,000. The rotary system that supports the turbine, shaft and the generator would cost about $8,000. These costs are based on the experience gained through the development of the laboratory scale prototype. Frame to support and ground the system would cost about $10,000.

The given or assumed conditions are:

- Temperature of the saline geothermal feed water = 125°C
- Flashing tank pressure = 5.6kPa Absolute; corresponding saturation temperature of water = 35°C
- Available driving temperature difference = 90°C
- Diameter of the turbine = 0.4m
- Rotational speed = 10,000rpm
- Isentropic efficiency = 50%
- Electrical power output = 20kW
- Mechanical to electrical energy conversion efficiency = 80%
- Estimated boundary conditions:
- Mass flow rate of the saline geothermal feed water = 1.05 kg/sec
- Total thermal energy supplied = 400kWt
- Fresh water production = 0.5m3/h
- Minimum volume of fresh water collection tank = 0.1 m3 = 100L

A 100 L stainless steel tank that can withstand vacuum of 5 kPa absolute pressure will cost about $5,000.

About 3.2 m3 of brine will be produced every hour and a brine storage tank made out of stainless steel with at least 0.6m3 of volume will be required that can withstand vacuum of 5kPa absolute. This would cost about $6,000.

Two submersible water pumps with delivery head of 15m of water would be required to pump out the fresh water and brine from the vacuum pressure to ambient pressure. These submersible water pumps would cost about $2800 each ($5,600 total).

The fresh water pump should be capable of handling a maximum volume flow rate of 0.6 m^3/hr at delivery head of 15 m or about 147 kPa. While the brine pump should be capable of handling a maximum flow rate of 3.5 m^3/hr at delivery head of 15 m or about 147 kPa.

The operation of these pumps should be regulated with level sensors in the fresh water and brine tanks.

The calculated geometry of the turbine is:

- Total nozzle throat area = 110mm2
- Throat diameter of 2 circular nozzles = 8.4mm
- Distance of the throat from the centre = 50mm
- Total nozzle throat area = 13000mm2
- Exit diameter of 2 circular nozzles = 91mm
- Total thickness of the turbine = 110mm
- Cost of turbine made from aluminium alloy 7000 series will be about $10,000.
- Condenser design:
- Condenser type: shell and tube
- There will be 4 shell and tube heat exchangers (condensers) each with 100kW cooling capacity, i.e. total 400kW cooling capacity.
- Tube carrying cooling water and vapour condensing on the outside.
- Shell and tube material: Stainless steel 316
- Thermal conductivity of the stainless steel = 15W/m°C
- Stainless steel tube diameter = 25mm
- Tube wall thickness = 1mm
- Shell diameter = 300mm
- Tube orientation vertical
- Cooling water inlet temperature = 25°C
- Cooling water mass flow rate per heat exchanger (condenser) = 3kg/s
- Therefore cooling water outlet temperature = 34°C

- Surface area of each heat exchanger (condenser) required to achieve cooling effect of 100kW for the present system = 10m2
- 87 tubes branches with 25mm OD and 1.5m long with single header will be required to provide 10m2 of cooling surface. With total length of stainless steel tube for 100kW heat exchanger would be about 130m.
- Total pressure drop in each condenser = 40kPa

Pumping power consumed by each condenser = 200W with 60% pump efficiency, hence total pumping power loss equal to about 800W.

Each heat exchanger (condenser) will cost about $10,000 including the connecting elbow. So the total of cost of the condensers is about $40,000.

Miscellaneous expensed associated with manufacturing of such a system could be assumed to be about $5000.

So to fabricate a 20 kW dual geothermal system that would produce 12 m^3/day of fresh water and 480 kWh of energy would cost about $105,000. This is assuming that the bore exists and hot geothermal water is accessible for the CDP.

10.6 Conclusion

It is possible to desalinate geothermal water and produce power simultaneously from hydrothermal resources in Victoria at the depth of 4 km and the temperature of 150 °C. The technology is simple and reliable. It has been estimated that from the typical bore with the flow of 130 L/sec will produce of enough electricity and fresh water for consumption of a 4000 houses and 10,000 people.

Total installation cost of such a system is estimated to be less than 20,000 includes bore cost. However the plant cost would not be more than 10% of it.

Depending on the price of water and electricity, considering $ 15 million bore cost, the pay back period will be less than 5 years.

Chapter 11 Conclusion and recommendation

11.1 Conclusion

In the conclusion of this thesis, it can be said that for global sustainable development it is very important to utilise renewable energy resources with low greenhouse gas emissions. Additionally there is a huge technically exploitable geothermal hydropower potential available throughout the world, if utilized this can represent a significant fraction of the present global electricity consumption.

From the theoretical and experimental analysis, it is seen that the idea of utilizing the total flow system for power generation has potential of producing more power per bores especially in the geothermal site as the most cost is drilling the bore. Therefore, the maximum of the heat need to be used from the source. Using total flow idea for the geothermal from hydrothermal water for producing fresh water and power generation does not need an extra heat exchanger for providing the desired temperature and it does not need another working fluid like ORC systems.

This research was the very first study of using total flow technology in reaction turbines for geothermal energy for dual application of generating power as well as fresh water. In addition, as in the total flow system, geothermal water expands when there is stationary nozzle available, the problems of erosion of the material has been faced. Therefore, the theoretical and experimental analysis of removing non condensable gases from geothermal water has been studied and the results proved the promising sustainable method of removing these gases before hot water enters the system to eliminate the erosion problems as well as increasing the efficiency. It has been observed the power produced by the machine drops by increasing the pressure. As the NCGs cause the raise in pressure, removing them from the geothermal water also leads to increasing the performance of the system.

Based on the theoretical and experimental study on removing the Non Condensable Gases (NCGs) from geothermal waters in the most sustainable way, it has been proved that two phase eductors (water-gas) can be utilised to remove NCGs from geothermal waters where a continuous water flow is available and the vacuum to be maintained is

low. However they are less efficient than the commercial vacuum pump at higher pressures, but have shown better performance than vacuum pumps at low pressures.

Considering the reaction turbine also made the effect of erosion much less compare to impulse turbine where the water flow hits the blades compare to reaction turbine where the outward flow of the water makes the rotation.

A new reaction turbine design with nozzle guide vanes made from multiple semi-circles, which is relatively easy to manufacture has been developed and tested experimentally. The interchangeable semi-circular nozzle guide vanes and throat inserts make this turbine design adaptive to any change in the load requirements. Experiments with five different turbine nozzle configurations were carried out for initially sub-cooled hot water to improve overall turbine performance. The turbine inlet pressure was equal to local atmospheric pressure and the inlet temperature was around 96°C. The turbine was placed in a flashing tank that maintained under vacuum pressure of around 6 kPa absolute. The turbine had two semi-circular nozzles with throat diameter of 2.5mm and exit area of each nozzle was 660mm².

The results obtained were as follows,

1. It was observed that the flow rate was dependent on the rotational speed and position of the throat. The feed water flow rate was observed to be highest when the brass insert was placed at insert far from the inlet, while lowest when the brass insert was placed at location closer to the inlet.
2. The power output of the turbine was observed to be highest when the brass insert was placed at insert located far from the inlet and lowest when brass insert was placed at closer to the inlet. While the isentropic efficiency of the turbine was observed to be highest when brass insert was placed at the position far from inlet. The isentropic efficiency of the turbine for this location (3.1%) was observed to be 20% higher than rest of the insert locations.
3. A 2.5 mm diameter flat head pin was placed in line with the orifice of the brass insert at 4mm distance and the brass insert was placed at location far from the inlet. For turbine with pin the feed water flow rate decreased by around 20% as

compared to the turbine without pin. Further it was observed that the rotational speed of the turbine with pin increased by around 50% as compared to the turbine without pin.

4. Finally it was observed that the output power and isentropic efficiency of the turbine with pin increased by 70% and 100% respectively as compared to turbine without pin. And the average fresh water production was estimated to be around 7.5% of the feed water flow rate.
5. It can be concluded that adding a pin in front of the throat helped to create spray of hot working fluid in the diverging section of the turbine helps to improve the turbine performance. The turbine under investigation has low isentropic efficiency of around 6% and the authors are conducting further research to improve turbine design to achieve better performance.

The produced fresh water is 0.2 liter of fresh water per liter of salty water which is a recovery ratio of 20%.

Although the efficiency of the Rankine system is more than Trilateral cycle, considering total flow system and trilateral cycle as a thermodynamic process in the system proves that there are more amount of useful energy per unit of mass of feed hot geothermal water is achievable compare to Organic Rankin Cycle. Example: For constant driving temperature difference, in the case of total flow system the total energy that could be utilised per kL is around 6kWh while for a conventional ORC this is 1.5kWh, which is about 5 times.

The economics of the proposed system designed looks very promising, as the main cost of such a system will be the bore cost. Bore cost plays important roles in the total cost whereas the plant cost is the small percentage.

In summary, the combined desalination and power generation has been achieved simultaneously for the first time through this study. The theoretical analysis using in developing the computer model to design the desired unit has been proved by the several experimental tests on different nozzle and turbine geometry and design.

The aim of this research to develop a low cost and high performance simple reaction two phase flow turbine has been achieved with fulfillment of all task oriented objectives. In the final conclusion of this thesis it can be confidently said that a Combined Desalination and Power generation (CDP) design is very flexible, it has good energy conversion efficiency and is an economic alternative to commercially available system for use in low-medium temperate of geothermal resources for production of power and fresh water.

11.2 Future work

Future research should investigate following,

1. Influence of higher rotational speeds on the performance of the turbine and this could be achieved by having large condenser which can handle the cooling loads even at higher rotational speed.
2. It was seen that the performance of non-optimized curved nozzle improved when a pin was added in front of the nozzle throat. So it would be interesting to find out the influence on performance of adding a thin wire / pin around nozzle throat section in the present design of the turbine.
3. The investment on the study of two phase flow nozzle geometry will be beneficial for achieving and improving the isentropic efficiency beyond 50%.
4. Investigation on the experimental analysis of the two phase flow rotating nozzle will be beneficial for validating the theoretical model.
5. Develop computer model to predict the performance of a two phase flow considering the phase change in rotating nozzle for CDP system.
6. It should be noted that condensation of water vapour and removal of non-condensable gasses is very critical for optimal operation of CDP. And as a rule of thumb the future researchers and/or CDP system designers should make sure they use a condenser with cooling capacity at least twice the required cooling load.

7. Performing the experimental tests on higher temperature by upgrading the water heating system. Due to the safety issues, this phase might need to be done in the industry,

References

1. Barbier, E., *Geothermal energy technology and current status: an overview.* Renewable and Sustainable Energy Reviews, 2002. **6**(1-2): p. 3-65.
2. Barry A Goldstein, T.H., *Australian Geothermal Implementing Agreement Annual Report*, 2006, Australian Geothermal Energy Group.
3. CONTI, J.J., HOLTBERG, P.D., & BEAMON, J.A, *Annual Energy Outlook* 2008, Energy Information Administration US Department of Energy
4. Sternberg, R., *Hydropower: Dimensions of social and environmental coexistence.* Renewable and Sustainable Energy Reviews, 2008. **12**(6): p. 1588-1621.
5. Blanco, J., et al., *Review of feasible solar energy applications to water processes.* Renewable and Sustainable Energy Reviews, 2009. **13**(6–7): p. 1437-1445.
6. UNDP, *energy and the challenge of sustainability*, 2000, World energy assessment: New York.
7. I, D., *Potential solutions. Energy Sources, Part A: Recovery, Utilization, and Environmental Effects* Environmental issues, 2001(23): p. 83–92.
8. Yuksel, I. and K. Kaygusuz, *Renewable energy sources for clean and sustainable energy policies in Turkey.* Renewable and Sustainable Energy Reviews, 2011. **15**(8): p. 4132-4144.
9. Fridleifsson, I.B., *Geothermal energy for the benefit of the people.* Renewable and Sustainable Energy Reviews, 2001. **5**(3): p. 299-312.
10. Kralova I, S.J., *Biofuels-renewable energy sources : A review.* Journal of Dispersion Science and Technology, 2010(31): p. 409-425.
11. Khan, M.J., M.T. Iqbal, and J.E. Quaicoe, *River current energy conversion systems: Progress, prospects and challenges.* Renewable and Sustainable Energy Reviews, 2008. **12**(8): p. 2177-2193.
12. Khennas, S. and A. Barnett, *Chapter 313 - Micro-hydro power: An option for socio-economic development*, in *World Renewable Energy Congress VI*, A.A.M. Sayigh, Editor. 2000, Pergamon: Oxford. p. 1511-1517.
13. Bartle, A., *Hydropower potential and development activities.* Energy Policy, 2002. **30**(14): p. 1231-1239.
14. Clarke, M., *Desalination for the Power Industry (Applications, efficiencies and costs)*, 2006, M.E.T.T.S. Pty. Ltd.: Brisbane.
15. Shafiullah, G.M., et al., *Prospects of renewable energy – a feasibility study in the Australian context.* Renewable Energy, 2012. **39**(1): p. 183-197.
16. Zhao, Y., A. Akbarzadeh, and J. Andrews, *Simultaneous desalination and power generation using solar energy.* Renewable Energy, 2009. **34**(2): p. 401-408.
17. Hung, T.-C., *Waste heat recovery of organic Rankine cycle using dry fluids.* Energy Conversion and Management, 2001. **42**(5): p. 539-553.

18. A.Kalina, *Combined cycle and waste-heat recovery power systems based on a novel thermodynamic energy cycle utilizing low-temperature heat for power generation*, in *ASME Joint-Power-Generation-Conference*1983.

19. Y Zhao, A.A., J Andrews. *Combined Water Desalination and Power Generation Using a Salinity Gradient Solar Pond as a Renewable Energy Source*. in *Solar World Congress*. 2007. Beijing, China.

20. Fabris, G., *Two-phase reaction turbine.*, 1999, US.

21. Fabris, G., *Two-Phase reaction Turbine*, 1993: US.

22. Fabris, G., *Two phase flow turbine for cogeneration, geothermal, solar and other applications'*, 2006, FAS Engineering.

23. Y Zhao, A.A., *Simultaneous Desalination and Power Generation using Solar Energy,.* Renewable Energy, 2008. **34**(2): p. 401-408.

24. Y Zhao, A.A., J Andrews. *Combined Water Desalination and Power Generation Using a Salinity Gradient Solar Pond as a Renewable Energy Source*. in *Proceedings of the Solar World Congress*. 2007. Beijing, China.

25. J Leblanc, A.A., J Andrews. *Modelling Solar-Thermal Desalination Systems*. in *43rd ANSES Conference*. 2005. Dunedin, New Zealand.

26. M. Bryson, A.A., C. Dixon. *Applying the Trilateral Flash Cycle to the Portland Geothermal Resource to Produce Power*. in *41st ANZSES Conference*. 2003. Melbourne, Australia.

27. Hung, T.-C., *Waste heat recovery of organic Rankine cycle using dry fluids.* Energy Conversion and Management, 2001. **42**: p. 539-53.

28. A, K. *Combined cycle and waste-heat recovery power systems based on a novel thermodynamic energy cycle utilizing low-temperature heat for power generation*. in *ASME Joint-Power-Generation-Conference*. 1983.

29. Chopra, P.N. *Status of the Geothermal industry in Australia, 2000-2005*. in *World Geothermal Congress*. 2005. Antalya, Turkey.

30. Panwar, N.L., S.C. Kaushik, and S. Kothari, *Role of renewable energy sources in environmental protection: A review.* Renewable and Sustainable Energy Reviews, 2011. **15**(3): p. 1513-1524.

31. Lund, H., *Renewable energy strategies for sustainable development.* Energy, 2007. **32**(6): p. 912-919.

32. Nakicenovic N, G.b.A., McDonald A, *Global energy perspectives*, 1998, Cambridge University Press: Cambridge (UK).

33. Leijon, M., et al., *On the physics of power, energy and economics of renewable electric energy sources – Part I.* Renewable Energy, 2010. **35**(8): p. 1729-1734.

34. Skoglund, A., et al., *On the physics of power, energy and economics of renewable electric energy sources - Part II.* Renewable Energy, 2010. **35**(8): p. 1735-1740.

35. Zhou, W., H. Yang, and Z. Fang, *Wind power potential and characteristic analysis of the Pearl River Delta region, China.* Renewable Energy, 2006. **31**(6): p. 739-753.

36. Canale, M., L. Fagiano, and M. Milanese, *KiteGen: A revolution in wind energy generation.* Energy, 2009. **34**(3): p. 355-361.

37. Joselin Herbert GM, I.S., Sreevalsan E, Rajapandian S, *A review of wind energy technology.* Renewable and Sustainable Energy, 2007(11): p. 117-147.

38. Dahmouni, A.W., et al., *Assessment of wind energy potential and optimal electricity generation in Borj-Cedria, Tunisia.* Renewable and Sustainable Energy Reviews, 2011. **15**(1): p. 815-820.

39. Keyhani, A., et al., *An assessment of wind energy potential as a power generation source in the capital of Iran, Tehran.* Energy, 2010. **35**(1): p. 188-201.

40. Leijon, M., et al., *An electrical approach to wave energy conversion.* Renewable Energy, 2006. **31**(9): p. 1309-1319.

41. Falcão, A.F.d.O., *Wave energy utilization: A review of the technologies.* Renewable and Sustainable Energy Reviews, 2010. **14**(3): p. 899-918.

42. Clément, A., et al., *Wave energy in Europe: current status and perspectives.* Renewable and Sustainable Energy Reviews, 2002. **6**(5): p. 405-431.

43. Ozdamar, A., et al., *Investigation of the potential of wind–waves as a renewable energy resource: by the example of Cesme—Turkey.* Renewable and Sustainable Energy Reviews, 2004. **8**(6): p. 581-592.

44. Fridleifsson, I.B. and D.H. Freeston, *Geothermal energy research and development.* Geothermics, 1994. **23**(2): p. 175-214.

45. V, S., *Estimate of the world geothermal potential*, in *Geothermal Training in Iceland 20th Anniversary Workshop*1998: Reykjavik: United Nations University Geothermal Training Programme. p. 111-120.

46. Mock, J.E. and G.V. Beeland, *U.S. department of energy support of growth in industrial use of geothermal energy.* Geothermics, 1992. **21**(5–6): p. 939-946.

47. Bahadori, A., S. Zendehboudi, and G. Zahedi, *A review of geothermal energy resources in Australia: Current status and prospects.* Renewable and Sustainable Energy Reviews, 2013. **21**(0): p. 29-34.

48. Bertani, R., *Geothermal power generation in the world 2005–2010 update report.* Geothermics, 2012. **41**(0): p. 1-29.

49. Lund, J.W., D.H. Freeston, and T.L. Boyd, *Direct application of geothermal energy: 2005 Worldwide review.* Geothermics, 2005. **34**(6): p. 691-727.

50. Lund, J.W., D.H. Freeston, and T.L. Boyd, *Direct utilization of geothermal energy 2010 worldwide review.* Geothermics, 2011. **40**(3): p. 159-180.

51. Lund, J.W., *The USA geothermal country update.* Geothermics, 2003. **32**(4–6): p. 409-418.

52. Fridleifsson, I.B., *Status of geothermal energy amongst the world's energy sources.* Geothermics, 2003. **32**(4–6): p. 379-388.

53. Huttrer, G.W., *The status of world geothermal power generation 1995–2000.* Geothermics, 2001. **30**(1): p. 1-27.

54. Zarrouk, S.J. and H. Moon, *Efficiency of geothermal power plants: A worldwide review.* Geothermics, 2014. **51**(0): p. 142-153.

55. Davidsdottir, B., *Sustainable Energy Development; The Role of Geothermal Power*, in *Reference Module in Earth Systems and Environmental Sciences*. 2013, Elsevier.

56. Goyal, K.P. and T.T. Conant, *Performance history of The Geysers steam field, California, USA.* Geothermics, 2010. **39**(4): p. 321-328.

57. Eltawil, M.A., Z. Zhengming, and L. Yuan, *A review of renewable energy technologies integrated with desalination systems.* Renewable and Sustainable Energy Reviews, 2009. **13**(9): p. 2245-2262.

58. Kalogirou, S.A., *Seawater desalination using renewable energy sources.* Progress in Energy and Combustion Science, 2005. **31**(3): p. 242-281.

59. Khawaji, A.D., I.K. Kutubkhanah, and J.-M. Wie, *Advances in seawater desalination technologies.* Desalination, 2008. **221**(1–3): p. 47-69.

60. Hamoda, M., *Desalination and water resource management in Kuwait.* Desalination, 2001. **138**(1–3): p. 165.

61. Kershman, S.A., J. Rheinländer, and H. Gabler, *Seawater reverse osmosis powered from renewable energy sources - hybrid wind/photovoltaic/grid power supply for small-scale desalination in Libya.* Desalination, 2003. **153**(1–3): p. 17-23.

62. Sauvet-Goichon, B., *Ashkelon desalination plant — A successful challenge.* Desalination, 2007. **203**(1–3): p. 75-81.

63. Glater, J., *The early history of reverse osmosis membrane development.* Desalination, 1998. **117**(1–3): p. 297-309.

64. DiPippo, R., *Ideal thermal efficiency for geothermal binary plants.* Geothermics, 2007. **36**(3): p. 276-285.

65. Dowd, A.-M., et al., *Geothermal technology in Australia: Investigating social acceptance.* Energy Policy, 2011. **39**(10): p. 6301-6307.

66. Curran, G., *Contested energy futures: Shaping renewable energy narratives in Australia.* Global Environmental Change, 2012. **22**(1): p. 236-244.

67. de Moel, M., et al., *Technological advances and applications of geothermal energy pile foundations and their feasibility in Australia.* Renewable and Sustainable Energy Reviews, 2010. **14**(9): p. 2683-2696.

68. Shahiduzzaman, M. and K. Alam, *Changes in energy efficiency in Australia: A decomposition of aggregate energy intensity using logarithmic mean Divisia approach.* Energy Policy, 2013. **56**(0): p. 341-351.

69. Effendi, P. and J. Courvisanos, *Political aspects of innovation: Examining renewable energy in Australia.* Renewable Energy, 2012. **38**(1): p. 245-252.

70. Hasan Chowdhury, S. and A. Maung Than Oo, *Study on electrical energy and prospective electricity generation from renewable sources in Australia.* Renewable and Sustainable Energy Reviews, 2012. **16**(9): p. 6879-6887.

71. Lindal.B., *Industrial and other applications of geothermal energy, In Geothermal Energy: Review of Research and Development*, 1973, UNESCO: Paris. p. 135-148.

72. Guo, T., H.X. Wang, and S.J. Zhang, *Fluids and parameters optimization for a novel cogeneration system driven by low-temperature geothermal sources.* Energy, 2011. **36**(5): p. 2639-2649.

73. Abbott, M., W.C. Wang, and B. Cohen, *The long-term reform of the water and wastewater industry: The case of Melbourne in Australia.* Utilities Policy, 2011. **19**(2): p. 115-122.

74. M.Oreijah, et al., *Expander Modelling in Binary Cycle Utilizing Geothermal Resources for Generating Green Energy in Victoria, Australia.* Procedia Engineering, 2012. **49**(0): p. 316-323.

75. Nelson, T., et al., *An analysis of Australia's large scale renewable energy target: Restoring market confidence.* Energy Policy, 2013. **62**(0): p. 386-400.

76. King, R.L., Ford, A.J., Stanley, D.R., Kenley, P.R., and Cecil, M.K., *Geothermal resources of Victoria a discussion paper*, D.o.I.T.a.R.a.t.V.S.E. Council, Editor 1985.

77. *Victorian desalination plant is completed*, 2013: Membrane Technology. p. 6-7.

78. M. Bryson, A.A., C. Dixon, *Applying the Trilateral Flash Cycle to the Portland Geothermal Resource to Produce Power.* 41 ANZSES Conference, 2003: p. 228-238.

79. Phillpot, S.R., *A course in thermodynamics.* Materials Today, 2006. **9**(4): p. 57.

80. M, L., *Kreisprozess mit Flashverdampfung im Arbeitsraum einer Kolbenmaschine.* VGB PowerTech. Int J for Electricity Heat Generation 2007(7): p. 92-97

81. Zamfirescu C, D.I., *Thermodynamic analysis of a novel ammoniaewater trilateral Rankine cycle.* Thermochimica Acta 2008(447): p. 7-15.

82. Koglbauer G, S.B., Wendland M, Fischer J, *Arbeitsmedien für Niedrigtemperatur-ORC-Prozesse.* Symposium Energie innovation, 15. - 17 Februar 2006, TU Graz, Verlag der TU Graz, 2006(ISBN 3-902465-30-1).

83. Smith, I., Stosic, N. and Aldis, C., *Trilateral Flash Cycel System - A High Efficiency Power Plant For Liquid Resources.* Journal of Power and Energy, 1995.

84. DUNCAN, W.J., THOMAS, A.S., YOUNG D, *Mechanics of Fluids*

1970: Edward Arnold.

85. WHITE, F.M., *Fluid Mechanics*. 1986, New York: McGraw-Hill Book Company.

86. DAUGHERTY, R.L., INGERSOLL, A.G, *Fluid Mechanics with engineering applications*. 1954: McGraw-Hill Book Company.

87. SHEPHERD, D.G., *Principles of turbomachinery*. 1956: MacMillan company.

88. Brown, R.a.J.L.Y., *Sprays formed by flashing liquid jets.* AIChE Journal, 2004

8: p. 149-153.

89. Austin, A.L.a.A.W.L., *A status report on the development of the Total-Flow concept*, 1978, Lawrence Livermore Laboratory geothermal energy program. p. 77.

90. Kitamura, Y., H. Morimitsu, and T. Takahashi, *Critical superheat for flashing of superheated liquid jets.* Industrial & engineering chemistry fundamentals, 1986: p. 206-211.

91. Gopalakrishna, S., V.M. Purushothaman, and N. Lior, *An experimental study of flash evaporation from liquid pools.* Desalination, 1987(65): p. 139-151.

92. Ohta, J., T. Fujii, K. Akagawa, and N. Takenaka, *Performance and flow characteristics of nozzles for initially subcooled hot water (influence of turbulence and decompression rate).* International Journal of Multiphase Flow, 1993(19): p. 125-136.

93. Bunch, T.K., A.A. Kornhauser, and M.P. Alexandrian. *Efficiency of a flashing flow nozzle*. in *Energy Conversion Engineering Conferenc*. 1996. the 31st Intersociety.

94. Mutair, S. and Y. Ikegami, *Experimental study on flash evaporation from superheated water jets: Influencing factors and formulation of correlation.* International Journal of Heat and Mass Transfer, 2009. **52**(23–24): p. 5643-5651.

95. Fabris, G., *Two-phase reaction turbine, in Other Information*, 1999: PBD: 1 Oct 1999.

96. Date, A., et al., *Experimental performance of a rotating two-phase turbine for initially sub-cooled hot water for combined desalination and power generation: Part A.* Applied Thermal Engineering, 2014. **Submitted**

97. Fabris, G., *Two-phase reaction turbine.* , 1993: United States.

98. Vahaji, S., et al., *Experimental Analysis of Two-phase Flow nozzle for Desalination and Power Generation System.* Procedia Engineering, 2012. **49**(0): p. 324-329.

99. Date, A. and A. Akbarzadeh, *Design and analysis of a split reaction water turbine.* Renewable Energy, 2010. **35**(9): p. 1947-1955.

100. Date, A. and A. Akbarzadeh. *Design analysis and investigation of a low head simple reaction water turbine*. in *43rd ANZSES conference*. 2005. Dunedin, New Zealand.

101. Fabris, G.D.D., Glendale, CA,, *Two-phase reaction turbine.* , 1993: United States.

102. Bai, F., et al., *Novel System for Combined Power Generation and Water Desalination Using Renewable Energy.* 2010.

103. Gunerhan, G.G., *An upstream reboiler design for removal of noncondensable gases from geothermal steam for Kizildere geothermal power plant, Turkey.* Geothermics, 1999. **28**(6): p. 739-757.

104. Angulo, R., et al., *Developments in geothermal energy in Mexico--part six. Evaluation of a process to remove non-condensable gases from flashed geothermal steam upstream of a power plant.* Journal of Heat Recovery Systems, 1986. **6**(4): p. 295-303.

105. Yildirim Ozcan, N. and G. Gokcen, *Thermodynamic assessment of gas removal systems for single-flash geothermal power plants.* Applied Thermal Engineering, 2009. **29**(14-15): p. 3246-3253.

106. Bidini, G., U. Desideri, and F.D. Maria, *A single flash integrated gas turbine-geothermalpower plant with non condensable gas combustion.* Geothermics, 1999. **28**(1): p. 131-150.

107. Florescu, N.A., *some theoretical and experimental observations on the ultimate vacuum obtainable in vapour pumps.* Vacuum, 1954. **4**(1): p. 30-39.

108. R.Sonntag, C.B., and G.Van Wylen, *Fundamentals of Thermodynamics*, 2002, John Wily & sons,Inc.

109. Coker, A.K., *Ejectors and Mechanical Vacuum Systems, in Ludwig's Applied Process Design for Chemical and Petrochemical Plants* 2007: Burlington. p. 525-573.

110. H.G. Elrod, J., *The theory of ejectors*, 1954, ASME transactions. p. A 170.

111. Khaghani, A., A. Date, and A. Akbarzadeh. *Sustainable noncondensable gas removal from geothermal waters*. in *Solar 2010 Conference*. 2010. Canberra, Australia.

112. Kandakure, M.T., V.G. Gaikar, and A.W. Patwardhan, *Hydrodynamic aspects of ejectors.* Chemical Engineering Science, 2005(60): p. 6391-6402.

113. Ouzzane, M.a.Z.A., *Model development and numerical procedure for detailed ejector analysis and design.* Applied Thermal Engineering, 2003(23): p. 2337-2351.

114. Zhu. Y, W.C., Changyun.W, Yanzhong.L, *Numerical investigation of geometry parameters for design of high performance ejectors.* Applied Thermal Engineering, 2009(29): p. 898-905.